Title
New insights into North America-Pacific plate boundary deformation from Lake Tahoe, Salton Sea and Southern Baja California

Author
Brothers, Daniel Stephen

Publication Date
2009

Peer reviewed|Thesis/dissertation

UNIVERSITY OF CALIFORNIA, SAN DIEGO

New Insights into North America-Pacific Plate Boundary Deformation from Lake Tahoe, Salton Sea and Southern Baja California

A dissertation submitted in partial satisfaction of the requirements for the degree

Doctor of Philosophy

in

Earth Sciences

by

Daniel Stephen Brothers

Committee in charge:

Graham M. Kent, Chair
Neal W. Driscoll, Co-Chair
Jeffrey M. Babcock
Yuri Fialko
Alistair J. Harding
David T. Sandwell
Larry Smarr

2009

The Dissertation of Daniel Stephen Brothers is approved, and it is acceptable in quality and form for publication on microfilm:

____

____

____

____

____

____

Chair

____

Co-Chair

University of California, San Diego

2009

To my parents, Wayne and Kristine Brothers

“Far beyond the sprawl of suburban America, where success and failure collide, and where utopia and the apocalypse meet to dance a dirty tango. It’s a special place...”

From Plagues and Pleasures on the Salton Sea

Table of Contents

List of Figures

List of Tables

Acknowledgements

My experience as a graduate student surpassed all of my expectations primarily because of the great people at Scripps that helped make my work so enjoyable. I would like to thank my advisors Graham Kent and Neal Driscoll for providing interesting research projects, freedom to pursue my personal research interests and opportunities to travel around the world for fieldwork. I would like to thank them for an overall great experience during the last five years. The best thing about these guys is that when I leave Scripps, I'll take a couple of great friends and colleagues with me for rest of my career. The same goes for Alistair Harding and Jeff Babcock, who spent tremendous amounts of time helping me at sea and at Scripps. I learned a great deal from Alistair during my final year and I really appreciate his patience. While working with these (four) guys I experienced the true meaning of teamwork, which can be hard to find in academia. Great things can be accomplished if people with different areas of expertise come together as a team and really strive to bring out each other's strengths, rather than weaknesses. I also learned how important it is to laugh and enjoy life, even as a scientist. I hate to say it, but Neal has made me laugh more than any other person. Graham is a close second. There truly is nothing better than spending a career trying to understand how our planet works, especially if it involves spending time out at sea. Lastly, I'll miss the foosball matches in Neal's lab. I did win a few, but I also learned that in foosball success comes with age.

I would like to thank my former officemates Jeff Dingler and JJ Becker. They also knew how to make me laugh. JJ happens to be one of the most generous people that I know, for which I am extremely grateful. Thanks to my fellow Driscoll lab mates, particularly Liz Johnstone for being a great friend and for selflessly sacrificing her time to help me in the field. I look forward to collaborating with all of you in the future. I would like to thank Ernest Aaron, Mark Gibaud and Martin Rapa of the OBS lab for their help out at sea and at Scripps. I'd like to thank to John Kleppe at Fallen Leaf Lake for the hospitality and advice over the years. We shared some very exciting discoveries up on that little lake.

I would like to thank my family and closest friends for their support and encouragement all these years. I am very fortunate to have such supportive and amazing parents. Thanks to my good pal, Redd. We shared some of our finest moments during the last five years. One of my luckiest experiences at Scripps was meeting my beautiful, future wife, Cathy Preston. I owe her tremendous gratitude for helping me stay balanced and for helping me through the ups and downs. I can't believe how fortunate I am to have her in my life. We have a lot to look forward to.

Lastly, I would like to thank Alan Jaffe for financial support during my final year. I can't express how incredible it is to meet someone as generous and sincere as Alan.

The text and figures from chapter 2, in part of in full, is a reprint of the material as it appears in: Brothers, D.S., Kent, G.M., Driscoll, N.W., Smith, S.B., Dingler, J.A., Harding, A.J., Seitz, G.G., Karlin, R., and Babcock, J.M., 2009, New constraints on earthquake history and slip-rates on the West Tahoe-Dollar Point Fault, Lake Tahoe Basin, CA: Bulletin of the Seismological Society of America, v.99, no. 2A, p. 499-519. dissertation author was the primary researcher and author and the co-authors listed in this publication directed and supervised the research which forms the basis for this chapter.

The text and figures from chapter 4, in part of in full, is a reprint of the material as it appears in: Brothers, D.S., Driscoll, N.W., Kent, G.M., Harding, A.J., Babcock, J.M., and Baskin, R.L., 2009, Tectonic evolution of the Salton Sea inferred from seismic reflection data: Nature Geoscience, v.2, p. 581-584. The dissertation author was the

primary researcher and author and the co-authors listed in this publication directed and supervised the research which forms the basis for this chapter.

The text and figures from chapter 5 are being prepared for publication in: Brothers, D.S., N.W. Driscoll, G.M. Kent, A.J. Harding, J.M. Babcock and R.L. Baskin, In Prep, Late Holocene earthquake and sedimentary history beneath the Salton Sea, Southern California: Bulletin of the Seismological Society of America. The dissertation author was the primary researcher and author of the submitted work. The co-authors directed and supervised that research, which forms the basis for this chapter.

The text and figures from chapter 6 are being prepared for publication in: Brothers, D.S., A.J. Harding, G.M. Kent and N.W. Driscoll, In Prep, 2-D seismic reflection and wide-angle refraction constraints on the crustal structure of southern Baja California: Journal of Geophysical Research. The dissertation author was the primary researcher and author of the submitted work. The co-authors directed and supervised that research, which forms the basis for this chapter.

Vita

2001-2003	Undergraduate Reserach Assistant Department of Geological Sciences University of Colorado, Boulder
2003	IRIS Intern University of Texas Institute for Geophysics
2004	Bachelor of Arts, Geology University of Colorado, Boulder
2009	Doctor of Philosophy, Earth Sciences Institute of Geophysics and Planetary Physics Scripps Institution of Oceanography University of California, San Diego

Publications

Brothers, D.S., Driscoll, N.W., Kent, G.M., Harding, A.J., Babcock, J.M., and Baskin, R.L., 2009, Tectonic evolution of the Salton Sea inferred from seismic reflection data: Nature Geoscience.

Brothers, D.S., Kent, G.M., Driscoll, N.W., Smith, S.B., Dingler, J.A., Harding, A.J., Seitz, G.G., Karlin, R., and Babcock, J.M., 2009, New constraints on earthquake history and slip-rates on the West Tahoe-Dollar Point Fault, Lake Tahoe Basin, CA: Bulletin of the Seismological Society of America.

Abstract of the Dissertation

New Insights into North America-Pacific Plate Boundary Deformation from Lake Tahoe, Salton Sea and Southern Baja California

by

Daniel Stephen Brothers

Doctor of Philosophy in Earth Sciences

University of California, San Diego, 2009

Graham M. Kent, Chair

Neal W. Driscoll, Co-Chair

Five studies along the Pacific- North America (PA-NA) plate boundary offer new insights into continental margin processes, the development of the PA-NA tectonic margin and regional earthquake hazards. This research is based on the collection and analysis of several new marine geophysical and geological datasets. Two studies used seismic CHIRP surveys and sediment coring in Fallen Leaf Lake (FLL) and Lake Tahoe to constrain tectonic and geomorphic processes in the lakes, but also the slip-rate and earthquake history along the West Tahoe-Dollar Point Fault. CHIRP profiles image vertically offset and folded strata that record deformation associated with the most recent event (MRE). Radiocarbon dating of organic material extracted from piston cores constrain the age of the MRE to be between 4.1–4.5 k.y. B.P. Offset of Tioga aged glacial deposits yield a slip rate of 0.4–0.8 mm/yr. An ancillary study in FLL determined that submerged, in situ pine trees that date to between 900-1250 AD are related to a medieval megadrought in the Lake Tahoe Basin. The timing and severity of this event match medieval megadroughts observed in the western United States and in Europe.

CHIRP profiles acquired in the Salton Sea, California provide new insights into the processes that control pull-apart basin development and earthquake hazards along the southernmost San Andreas Fault. Differential subsidence (>10 mm/yr) in the southern sea suggests the existence of northwest-dipping basin-bounding faults near the southern shoreline. In contrast to previous models, the rapid subsidence and fault architecture observed in the southern part of the sea are consistent with experimental models for pull-apart basins. Geophysical surveys imaged more than 15 ~N15°E oriented faults, some of which have produced up to 10 events in the last 2-3 kyr. Potentially 2 of the last 5 events on the southern San Andreas Fault (SAF) were synchronous with rupture on offshore faults, but it appears that ruptures on three offshore faults are synchronous with Colorado River diversions into the basin.

The final study was used coincident wide-angle seismic refraction and multichannel seismic reflection surveys that spanned the width of the of the southern Baja California (BC) Peninsula. The data provide insight into the spatial and temporal evolution of the BC microplate capture by the Pacific Plate. Seismic reflection profiles constrain the upper crustal structure and deformation history along fault zone on the western Baja margin and in the Gulf of California. Stratal divergence in two transtensional basins along the Magdalena Shelf records the onset of extension across the Tosco-Abreojos and Santa Margarita faults. We define an upper bound of 12 Ma on the age of the pre-rift sediments and an age of ~8 Ma for the onset of extension. Tomographic imaging reveals a very heterogeneous upper crust and a narrow, high velocity zone that extends ~40 km east of the paleotrench and is interpreted to be remnant oceanic crust.

1

Introduction

1.1 MARINE GEOPHYSICS TO STUDY PLATE BOUNDARY PROCESSES

Our understanding of the physical processes that control continental margin development and evolution is still emerging, in part, due to an absence of data needed to answer several fundamental, but unresolved questions. Studies along the Pacific- North America (PA-NA) plate boundary offer an ideal opportunity to study a continental system that has undergone all three styles of margin deformation since the mid-Miocene: convergent, transform and divergent. Continental crust does not behave rigidly, but deforms over broad regions. To understand the dynamics of tectonic processes we must first define the kinematics and how strain is partitioned across the plate boundary. We examine both ancient and modern boundary architectures to address how past processes influence the modern day kinematics. This research uses several new geophysical and geological datasets to address fundamental, but unresolved questions: (1) How and why is strain partitioned along the PA-NA margin and (2) what are the associated earthquake hazards along active fault systems. Regions undergoing transtension appear to be partitioned into strike-slip and dip-slip domains. The scale-dependency of strain partitioning are partially related to lithospheric structure and pre-existing fabrics formed during earlier tectonic episodes. High-resolution seismic reflection data provide important constraints on active, near surface processes whereas the lower resolution, deeper penetrating seismic data provide information on crustal-scale deformation and long-term tectonic evolution of a region. The following paragraphs introduce our research objectives and briefly summarize the significant results from five separate, but related projects that are described in the forthcoming chapters.

Chapters 2 and 3 present new data from the Walker Lane Belt (WLB; Figure 1), an actively deforming tectonic province situated between the relatively stable Sierra Nevada microplate on the west and the central Great Basin to the east (Argus and Gordon, 2001; Stewart, 1988). The WLB is a complex zone of dextral transtension responding to the oblique-divergent motion of the Sierra Nevada microplate relative to the central Great Basin (Unruh et al., 2003). Geodetic studies have detected 9–13 mm/yr of mostly dextral shear partitioned across numerous strike-slip, dip-slip, and oblique-slip faults in the WLB, which accounts for ~25% of the total plate motion across the PA-NA margin (Hammond and Thatcher, 2004, 2007). Geodetic studies indicate that the majority of WLB extension (between 2–3 mm/yr) is focused around the eastern margin of the Sierra Nevada. In an effort to characterize Holocene faulting, slip-partitioning and geomorphic processes along the eastern margin of the Sierran microplate, we conducted a suite of studies in Lake Tahoe and Fallen Leaf Lake. Chapter 2 is focused on constraining the geomorphic expression, slip-rate and earthquake history along the West Tahoe-Dollar Point Fault, an active normal fault that bounds the western margin of the Lake Tahoe Basin (Brothers et al., 2009b). We conducted multidisciplinary field studies that included seismic CHIRP surveys and sediment coring Fallen Leaf Lake and Lake Tahoe along with onshore reconnaissance mapping of fault scarps. The study was one of first to use marine paleoseismic techniques to constrain the timing and magnitude of Holocene earthquakes on an active fault system. The data show that faulting in the Lake Tahoe Basin accommodates a significant percentage (~50%) of extension across the WLB. Chapter 3 is a hydroclimatic study of the Fallen Leaf Lake watershed. The discovery of medieval aged pine trees standing upright, but fully submerged in Fallen Leaf Lake motivated a sidescan sonar survey to image lakefloor morphology. We discovered submerged paleoshorelines that are indicative of large lake level fluctuations during the late Holocene. This study provided the first conclusive evidence for severe and prolonged medieval drought in the Lake Tahoe Basin and demonstrated that alpine lakes similar to Fallen Leaf Lake may contain important, high fidelity paleoclimate proxies that constrain the late-Holocene hydroclimatic variability of the Sierra Nevada.

The next two chapters (4 & 5) explore transtensional faulting in the Salton Trough, California, where transpression of the San Andreas fault system transitions at its southern tip into the Gulf of California ridge-transform system. The Salton Sea covers the northernmost transtensional boundary of the Gulf of California system where dextral strain is transferred from the San Andreas Fault southwestward to the Imperial Fault. These fault system carry between 50-80 % of the PA-NA plate motion at this latitude. Both chapters are based on the results of comprehensive seismic CHIRP surveys in the Salton Sea that enabled us to define the late-Holocene stratigraphic framework, basin architecture and paleoseismic history of the San Andreas Fault-Imperial Fault pull-apart basin. Chapter 3 presents the first direct imagery of the fault structure, deformation patterns and extension rates in the Salton Sea (Brothers et al., 2009a). Based on the results of CHIRP sub-bottom imagery, we developed a new tectonic model for the crustal deformation along southernmost San Andreas fault system. The data provide a rare opportunity to look at how strain is partitioned between normal, oblique and strike-slip faults in a pull-apart basin and show a large component of extension that produces rapid subsidence in the southern sea. Chapter 5 builds on the results of Chapter 4 by developing a detailed paleoseismic history on several normal faults mapped in the Salton Sea. This chapter develops the methodology behind marine paleoseismology and its application to normal faults. By deconvolving coseismic offset and timing from the stratigraphic cross sections, we were able to identify at least ten earthquakes on three faults during the last 2-3 thousand years. This represents one of the largest event-records for any fault system in North America. Earthquakes on faults in the Salton Sea appear to be modulated by changes in vertical stress (e.g., floods from the Colorado River) and faults in the sea have the potential to alter the state of stress on the southernmost San Andreas Fault, which is considered to be overdue for a large magnitude earthquake (Philibosian, 2007). Chapters 2, 4 and 5 highlight the use and advantages of using high-resolution marine geophysical methods to study deformation rates, fault behavior and sedimentation history in subaqueous environments.

The final chapter (6) examines how the Baja California microplate (Figure 1), a continental plate fragment, has been rifted from mainland Mexico and subsequently captured by the Pacific plate over a time span of ~10-15 Ma (Lonsdale, 1991; Michaud et al., 2006; Stock and Lee, 1994). The capture of continental microplates at subducting margins is controlled in some fashion by the underlying oceanic slab, possibly through basal traction across the plate interface (Nicholson et al., 1994). Understanding the dynamics of microplate capture requires knowledge of the plate kinematics leading up to capture, the geometry and rheology of the slab/upper plate interface and the lithospheric architecture of the microplate. To address these questions, we analyzed 2-D crustal-scale seismic refraction and reflection data that spanned the Baja California microplate (Figure 1). Seismic reflection profiles constrain the upper crustal structure and deformation history along fault zone on the western Baja margin and in the Gulf of California. The refraction data image crustal and upper mantle velocity structure and revealed that a fragment of the formerly subducting Farallon plate remains beneath the western margin of the peninsula. A narrow high-velocity zone extending at least 50 km east of the western edge of the continental shelf suggesting that enigmatic post-subduction volcanism may be related to the presence of relic Farallon slab beneath Baja California. The results point to the importance of slab traction in the opening of the Gulf of California rifted margin, but also raise questions regarding the magnitude and timing of dextral shear along the Baja California continental margin.

1.2 REFERENCES

Argus, D.F., and Gordon, R.G., 2001, Present tectonic motion across the Coast Ranges and San Andreas fault system in central California: Geological Society of America Bulletin, v. 113, p. 1580-1592.

Brothers, D.S., Driscoll, N.W., Kent, G.M., Harding, A.J., Babcock, J.M., and Baskin, R.L., 2009a, Tectonic evolution of the Salton Sea inferred from seismic reflection data: Nature Geoscience.

Brothers, D.S., Kent, G.M., Driscoll, N.W., Smith, S.B., Dingler, J.A., Harding, A.J., Seitz, G.G., Karlin, R., and Babcock, J.M., 2009b, New constraints on earthquake history and slip-rates on the West Tahoe-Dollar Point Fault, Lake Tahoe Basin, CA: Bulletin of the Seismological Society of America.

Hammond, W.C., and Thatcher, W., 2004, Contemporary tectonic deformation of the Basin and Range province, western United States: 10 years of observation with the Global Positioning System: Journal of Geophysical Research-Solid Earth, v. 109, p. 10.1029/2003JB002746.

—, 2007, Crustal deformation across the Sierra Nevada, northern Walker Lane, Basin and Range transition, western United States measured with GPS, 2000-2004: Journal of Geophysical Research-Solid Earth, v. 112, p. -.

Lonsdale, P.F., 1991, Structural patterns of the Pacific floor offshore of Peninsular California: in Dauphlin, J. P., and Simoneit, B. R. T., eds., The Gulf and Peninsular Province of the Californias: American Association of Petroleum Geologists Memoir, v. 47.

Michaud, F., Royer, J.Y., Bourgois, J., Dyment, J., Calmus, T., Bandy, W., Sosson, M., Mortera-Gutierrez, C., Sichler, B., Rebolledo-Viera, M., and Pontoise, B., 2006, Oceanic-ridge subduction vs. slab break off: Plate tectonic evolution along the Baja California Sur continental margin since 15 Ma: Geology, v. 34, p. 13-16.

Nicholson, C., Sorlien, C.C., Atwater, T., Crowell, J.C., and Luyendyk, B.P., 1994, Microplate Capture, Rotation of the Western Transverse Ranges, and Initiation of the San-Andreas Transform as a Low-Angle Fault System: Geology, v. 22, p. 491-495.

Philibosian, B., 2007, Paleoseismology of the San Andreas Fault at Coachella, California: Master's Thesis, University of Oregon.

Stewart, J.H., 1988, Tectonics of the Walker Lane belt, western Great Basin –Mesozoic and Cenozoic deformation in a zone of shear. In: Ernst, W.G. (Ed.): Metamorphism and Crustal Evolution of the Western United States. Rubey, v. VII.

Prentice-Hall, Englewood Cliffs, NJ, p. 683-713.

Stock, J.M., and Lee, J., 1994, Do Microplates in Subduction Zones Leave a Geological Record: Tectonics, v. 13, p. 1472-1487.

Unruh, J., Humphrey, J., and Barron, A., 2003, Transtensional model for the Sierra Nevada frontal fault system, eastern California: Geology, v. 31, p. 327-330.

Figure 1-1: Regional map of the Pacific-North American plate boundary. Numbered yellow boxes mark the study areas: (1) Lake Tahoe Basin and Walker Lane Belt (WLB) described in chapters 2 and 3; (2) Saltton Trough in chapters 4 and 5; (3) Baja California Sur in chapter 6. Abbreviations: JFP, Juan De Fuca plate; SN, Sierra Nevada microplate; SAF, San Andreas Fault; BC, Baja California; GoC, Gulf of California; FP, Farallon Plate; EPR, East Pacific Rise. Purple shades represent areas undergoing transtension, red shades are areas undergoing transpression. Black lines are major faults (active and inactive) and the thick red lines are active spreading boundaries. Large black arrows mark the plate motion vectors.

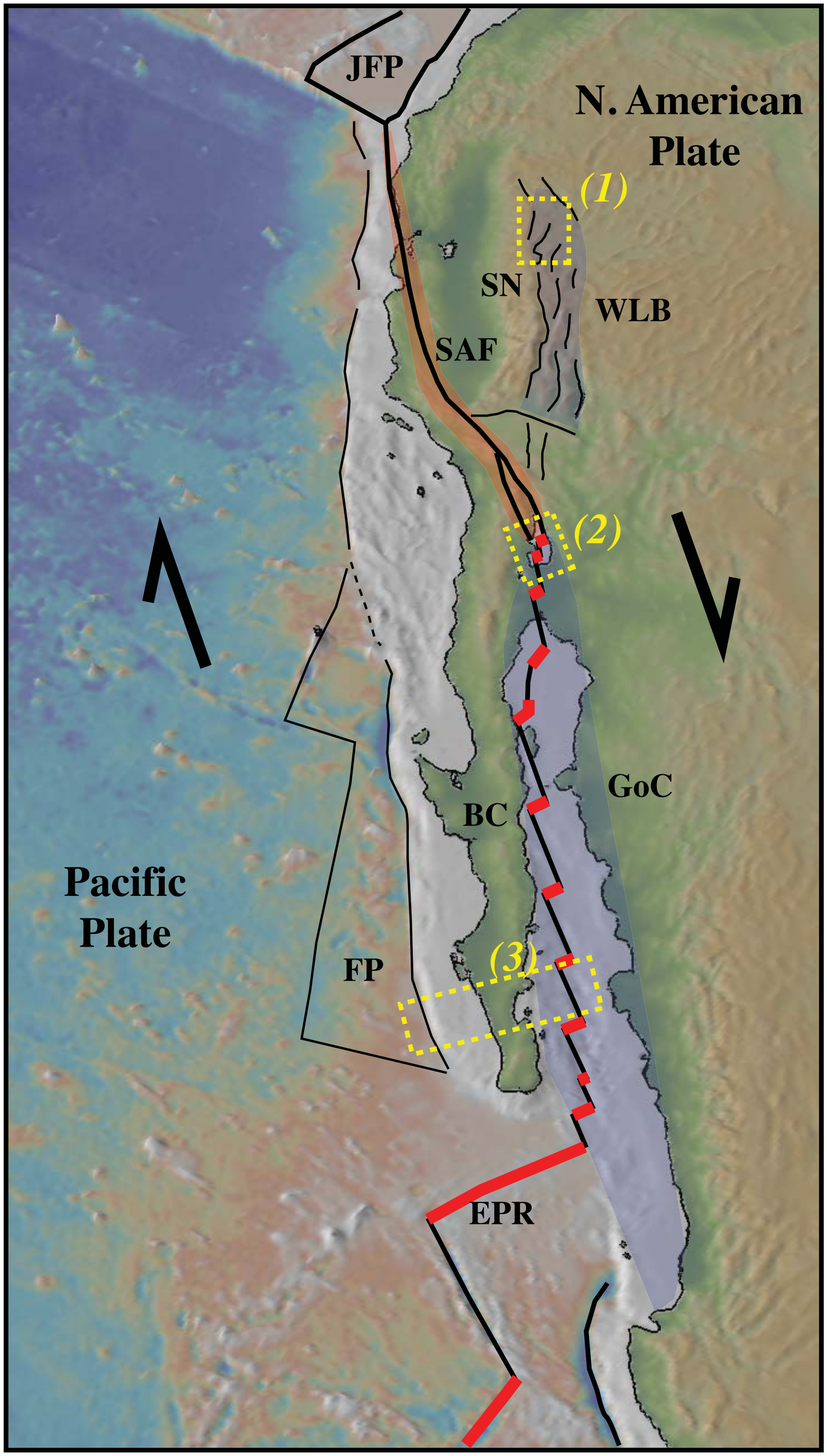
JFP
N. American
Plate
(1)
SN
WLB
SAF
(2)
GoC
BC
Pacific
Plate
(3)
FP
EPR

2

New Constraints on Deformation, Slip Rate, and Timing of the Most Recent Earthquake on the West Tahoe–Dollar Point Fault, Lake Tahoe Basin, California

Bulletin of the Seismological Society of America, Vol. 99, No. 2A, pp. 499–519, April 2009, doi: 10.1785/0120080135

New Constraints on Deformation, Slip Rate, and Timing of the Most Recent Earthquake on the West Tahoe–Dollar Point Fault, Lake Tahoe Basin, California

by Daniel S. Brothers, Graham M. Kent, Neal W. Driscoll, Shane B. Smith, Robert Karlin, Jeffrey A. Dingler, Alistair J. Harding, Gordon G. Seitz, and Jeffrey M. Babcock

Abstract High-resolution seismic compressed high intensity Radar pulse (CHIRP) data and piston cores acquired in Fallen Leaf Lake (FLL) and Lake Tahoe provide new paleoseismic constraints on the West Tahoe–Dollar Point fault (WTDPF), the westernmost normal fault in the Lake Tahoe Basin, California. Paleoearthquake records along three sections of the WTDPF are investigated to determine the magnitude and recency of coseismic slip. CHIRP profiles image vertically offset and folded strata along the southern and central sections that record deformation associated with the most recent event (MRE) on the WTDPF. Three faults are imaged beneath FLL, and the maximum vertical offset observed across the primary trace of the WTDPF is ~3.7 m. Coregistered piston cores in FLL recovered sediment and organic material above and below the MRE horizon. Radiocarbon dating of organic material constrained the age of the MRE to be between 3.6 and 4.9 k.y. B.P., with a preferred age of 4.1–4.5 k.y. B.P. In Lake Tahoe near Rubicon Point, approximately 2.0 m of vertical offset is observed across the WTDPF. Based on nearby core data, the timing of this offset occurred between ~3–10 k.y. B.P., which is consistent with the MRE age in FLL. Offset of Tioga-aged glacial deposits provides a long-term record of vertical deformation on the WTDPF since ~13–14 k.y. B.P., yielding a slip rate of 0.4–0.8 mm/yr. In summary, the slip rate and earthquake potential along the WTDPF is comparable to the nearby Genoa fault, making it the most active and potentially hazardous fault in the Lake Tahoe Basin.

Introduction

The Lake Tahoe Basin (LTB) is one of several fault-controlled basins within the northern Walker Lane deformation belt (Unruh *et al.*, 2003). Based on westward dipping lake deposits and the structural tilt of the Carson Range, the LTB appears to be an asymmetric half-graben (Hyne *et al.*, 1972; Schweickert *et al.*, 1999; Surpless *et al.*, 2002; Dingler, 2007) separating the Sierra Nevada Range to the west from the Carson Range to the east (Fig. 1). Extension occurs along three primary normal fault systems: the West Tahoe–Dollar Point fault (WTDPF), the Stateline–North Tahoe fault (SLNTF), and the Incline Village fault (IVF). Each fault exhibits down-to-the-east normal displacement during the last 10 k.y. (Dingler, 2007). Until recently, geologic slip rates, earthquake timing, and magnitude estimates across faults in the LTB were poorly constrained. Offshore swath bathymetry and compressed high intensity Radar pulse (CHIRP) sub-bottom surveys combined with cores and onshore paleoseismic excavations have defined the regional distribution of faults and the first precise estimates on slip rates (Gardner *et al.*, 2000; Kent *et al.*, 2005; Dingler, 2007). Despite such advances, one of the most active, but poorly understood, structures is the north–south striking WTDPF (Fig. 1). Along strike fault morphology (Fig. 1), large cumulative displacement beneath Lake Tahoe and vertically offset Pleistocene glacial moraines in the southern LTB indicate the WTDPF has a relatively high slip rate. Nevertheless, relaxed scarp profiles measured south of Lake Tahoe suggest the fault has not experienced a ground-rupturing event for several thousand years.

In 2006, we acquired CHIRP sub-bottom data and piston cores along the southern section of the WTDPF between Emerald Bay and Christmas Valley to define the age, coseismic offset, and rupture length of the most recent event (MRE; Fig. 2). High-resolution marine geophysics provides an opportunity not only to identify offset strata associated with individual earthquakes, but also to define the regional fault architecture in an area that is inaccessible by traditional onshore methods. Our results, combined with previous sub-

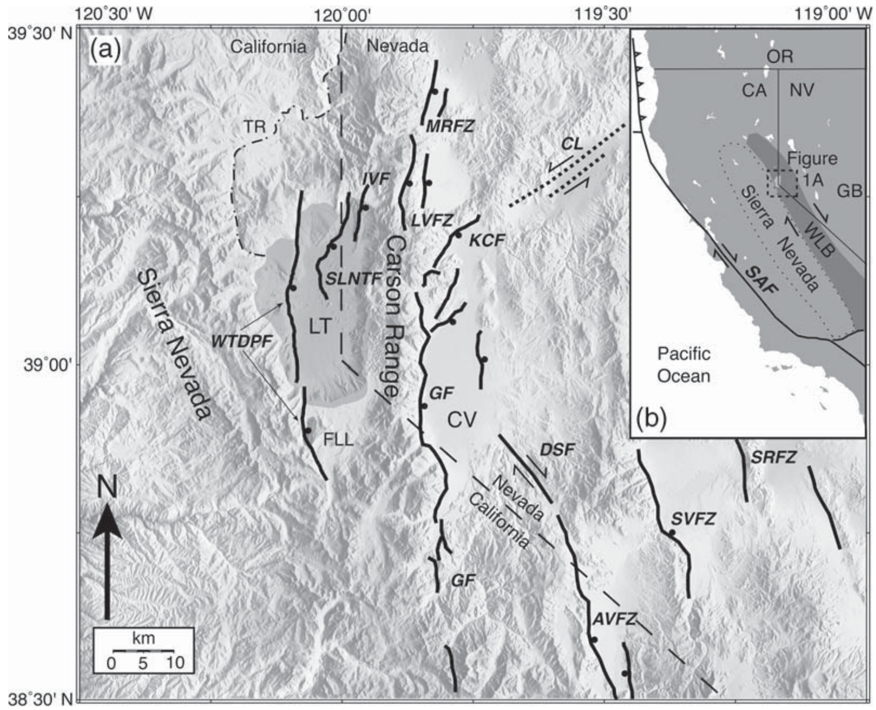

Figure 1. (a) Generalized fault and shaded relief map of eastern California and western Nevada. The LTB lies between the Sierra Nevada and Carson Ranges. Lake Tahoe (LT) and FLL are shaded gray. Solid black lines are active fault systems; dashed black lines are inferred faults. Abbreviations: West Tahoe–Dollar Point fault, WTDPF; Stateline–North Tahoe fault, SLNTF; Incline Village fault, IVF; Genoa fault, GF; Mount Rose fault zone, MRFZ; Little Valley fault zone, LVFZ; Carson Lineament, CL; Kings Canyon fault, KCF; Deep Springs fault, DSF; Antelope Valley fault zone, AVFZ; Smith Valley fault, SVF; Smith Range fault zone, SRFZ; Truckee River, TR; and Carson Valley CV. (b) Simplified plate boundary highlighting the San Andreas fault (SAF), Walker Lane belt (WLB; shaded gray area), Sierra Nevada block (thin dashed line), and the Great Basin (GB).

bottom and piston core data collected in Lake Tahoe (Dingler, 2007), indicate the WTDPF is the most active and hazardous fault in the LTB. The relatively high slip rate and rupture potential of the WTDPF provides essential information for geohazards assessments, including probability estimates for a future, large-magnitude event.

Quaternary Geology and Tectonics

Walker Lane

The Walker Lane belt (WLB) is an actively deforming tectonic province situated between the relatively stable Sierra Nevada microplate on the west and the central Great Basin to the east (Stewart, 1988; Argus and Gordon, 2001). The WLB is a complex zone of dextral transtension responding to the oblique-divergent motion of the Sierra Nevada microplate relative to the central Great Basin (Fig. 1b; Bennett *et al.*, 2003; Oldow, 2003; Unruh *et al.*, 2003). A suite of geodetic studies have detected 9–13 mm/yr of mostly dextral shear partitioned across numerous strike-slip, dip-slip, and oblique-slip faults in the Walker Lane, accounting for ~25% of the total plate motion between the North American and Pacific plates (Hearn and Humphreys, 1998; Dixon *et al.*, 2000; Svarc *et al.*, 2002; Bennett *et al.*, 2003; Hammond and Thatcher, 2004, 2007).

Lake Tahoe is within the northern WLB, which consists of a series of north–south trending, normal fault bounded mountain ranges, northwest striking dextral faults, and northeast striking sinistral faults (Faulds *et al.*, 2005). At the latitude of Lake Tahoe and east of the Sierra Nevada Range the topography is dominated by several uplifted mountain ranges (Wassuk, Singatse, Pine Nut, and Carson) that are bounded by north–south striking normal faults. Although Surpless *et al.* (2002) document larger cumulative offset along normal fault systems to the east than those to the west, geodetic studies indicate that the majority of extension (between 2–3 mm/yr) is focused around the Sierra Nevada frontal fault system. Near Lake Tahoe, the Sierra Nevada frontal fault system splays into two extensional domains separated by the Carson Range: the LTB and Carson Valley (Unruh *et al.*, 2003). Measured geodetic rates across the LTB

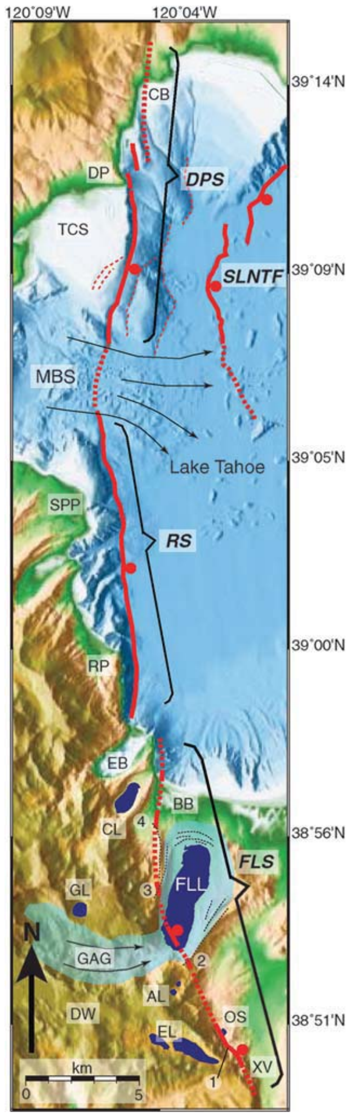

Figure 2. Map showing the three sections of the WTDPF (solid red lines—where known, and dashed red lines—where inferred): Dollar Point section (DPS), Rubicon section (RS), and Fallen Leaf section (FLS). Thin dashed red lines surrounding the DPS represent slump scarps. Abbreviations: Christmas Valley, XV; Osgood Swamp, OS; Echo Lakes, EL; Desolation Wilderness, DW; Angora Lakes, AL; Glenn Alpine glacier (also where the present Glen Alpine Creek is sourced), GAG; Gilmore Lake, GL; Cascade Lake, CL; Baldwin Beach, BB; Emerald Bay, EB; Rubicon Point, RP; Sugar Pine Point, SPP; McKinney Bay slide, MBS; Tahoe City shelf, TCS; Dollar Point, DP; and Carnelian Bay, CB. Black arrows represent flow directions for the MBS and GAG (also shaded blue). Dashed black lines surrounding FLL are approximate locations of moraine crests; arcuate crests north of FLL are recessional moraines. Numbered features: (1) photographed scarp in Figure 14, (2) and (3) 2–3 m scarps offsetting Tioga-aged moraine crests on either side of FLL, and (4) 2–3 m meadow scarp.

are poorly resolved due to sparse coverage on the western side of the Basin. Results of geologic and geodetic studies in the region, point to a westward encroachment of extension from the western Basin and Range province into the eastern Sierra Nevada block (Henry and Perkins, 2001; Surpless *et al.*, 2002). The present day Sierra Nevada–WLB boundary is located along the WTDPF. North of the LTB, Global Positioning System (GPS) studies measured ~7 mm/yr of dextral shear across the northern WLB, representing ~15% of the total plate motion (Bennett *et al.*, 2003; Hammond and Thatcher, 2004, 2007). Paleoseismic studies in the northern WLB have uncovered evidence for large-magnitude Holocene ruptures along normal, dextral, and sinistral fault systems, including the IVF (Dingler, 2007), Genoa fault (GF; Ramelli *et al.*, 1999), Pyramid Lake fault (Briggs and Wesnousky, 2004), and the Olinghouse fault (Briggs and Wesnousky, 2005).

Lake Tahoe Basin

The LTB has been tectonically active since at least 3 Ma (Henry and Perkins, 2001; Surpless *et al.*, 2002; Faulds *et al.*, 2005) with extension occurring along a series of east-dipping normal faults. The Quaternary landscape has been shaped by several Wisconsin glacial advances between 79 and 15 k.y. B.P. (Bischoff and Cummins, 2001), forming several moraine-bounded valleys along the range fronts within the LTB. The Sierra Nevada and Carson Ranges are predominantly composed of granodiorite and related metamorphic roof pendants of the Sierra Nevada batholith (Saucedo *et al.*, 2005), but also Miocene and younger volcanic rocks are found in the northern LTB (Birkeland, 1963; Saucedo *et al.*, 2005). Seismic reflection data collected in Lake Tahoe have imaged up to ~300 m of sediment below the lake floor without reaching the acoustic basement (AB, Hyne *et al.*, 1972).

The basin exhibits abundant low-magnitude seismicity (Ichinose *et al.*, 1999, 2003; Smith *et al.*, 2004). New paleoseismic evidence suggests there have been large-magnitude Holocene events (Kent *et al.*, 2005; Dingler, 2007). Late-Pleistocene to present geologic slip-rate estimates were calculated based on offset geomorphic markers observed in sub-bottom CHIRP profiles (Kent *et al.*, 2005; Dingler, 2007). An offset 19.2 ± 1.8 ka wave-cut paleoterrace, which correlates temporally with a 19 ± 1 ka glacial advance during the Tioga glaciation (Phillips *et al.*, 1996), was used to calculate a minimum basin extension rate of ~0.5 mm/yr (Kent *et al.*, 2005). In addition to offshore studies, an excavation across the IVF revealed the first direct evidence for multiple $M \approx 7$ Holocene events in the LTB (Dingler, 2007).

West Tahoe–Dollar Point Fault. The WTDPF is the north–south striking, range bounding normal fault along the western margin of the LTB (Figs. 1 and 2). Most of the fault's length is located beneath Lake Tahoe where, presumably, the cumulative throw is greatest. Swath bathymetry and sub-bottom CHIRP surveys reveal well-defined scarps through debris aprons, slides, and lake bottom sediments (Hyne *et al.*, 1972; Gardner *et al.*, 2000; Kent *et al.*, 2005; Dingler, 2007). We divide the WTDPF into three sections that are defined by apparent discontinuities or geomorphic boundaries (Fig. 2). The Fallen Leaf section extends from Christmas Valley at the south through Fallen Leaf Lake (FLL) and offshore into Lake Tahoe at the western edge of Baldwin Beach. Prior to this study, the Fallen Leaf section was poorly understood. Fault scarps within the transition between the Fallen Leaf and Rubicon sections are not well expressed by the local morphology and may include more than one splay. After an apparent ~1 km northwestward step from below Eagle Point to the base of the submerged slope off Emerald Point, the Rubicon section continues northward to McKinney Bay. Although the trends of the two northern sections are nearly equivalent and evidence for a tectonic boundary has not been observed, we treat the McKinney Bay slide (MBS) as a section boundary because faulting beneath the slide is poorly imaged and scarps have been overprinted or eroded by debris aprons and/or landslides. The southern extent of the Dollar Point section begins at the northern edge of the MBS and continues to the north along the eastern edge of the Tahoe City shelf (TCS) then eventually steps onshore in the vicinity of Carnelian Bay. A series of scarps and offset strata below the TCS appear to be caused by slumping (Dingler, 2007). The total length of the WTDPF is greater than 50 km.

Fallen Leaf Lake. FLL, located ~2 km south of Baldwin Beach, provides another lacustrine environment in which the WTDPF can be imaged using marine seismic methods. FLL is ~45 m higher than Lake Tahoe and fills a narrow moraine-bounded glacial valley (Fig. 2). The overall morphology has been shaped by Pleistocene glaciers sourced in the Desolation Wilderness (Fig. 2) where Tahoe-aged glaciers seem to have been more significant than the more recent Tioga-aged glaciers that merely reworked the inner slopes of Tahoe moraines (Saucedo *et al.*, 2005). The entire valley is bounded on either side by >300 m high-lateral moraines (measured from the lake floor) that extend towards Lake Tahoe for >5 km from the range front. Near its northern shoreline, FLL is bounded by a series of Tioga-aged recessional and terminal moraines that separate it from Lake Tahoe (Saucedo *et al.*, 2005). Based on the dimensions of lateral and end moraines, the Tahoe and Tioga glaciers in Fallen Leaf Valley appear to have been much larger than the adjacent valley glaciers that occupied Cascade Lake and Emerald Bay. Sediment discharge from Glen Alpine Creek, the most significant modern sediment input to FLL, would have been strongly modulated by glacial melt water. Like much of the LTB, glacial morphology, fluvial incision, and dense vegetation surrounding FLL make onshore identification of fault scarps difficult. Offshore geophysical surveys offer an alternative method to study the interactions between tectonic and glacial or fluvial processes.

Methods

Detailed geophysical surveys and field reconnaissance mapping were conducted between Christmas Valley and Emerald Bay in July 2006 (Figs. 2 and 3). Two sub-bottom surveys conducted in FLL and offshore Baldwin Beach in Lake Tahoe employed the Scripps Institution of Oceanography's Edgetech CHIRP profiler. In FLL, the CHIRP profiler was mounted on an aluminum frame held afloat by two inflatable pontoons and towed by a small (~20 × 10 ft) platform barge operated by the Fallen Leaf Marina. More than 40 line-km of data were collected at a constant tow depth of ~1 m. Offshore Baldwin Beach the CHIRP was towed off the stern of the R/V LeConte (operated by University of California, Davis) at 2–3 m below the surface; over 12 line-km of data were collected. All data were digitally recorded in SEG-Y format with real-time GPS navigation recorded with each shot, providing absolute location accuracy to within 5 m. SEG-Y files were processed using SIOSEIS then imported into the Kingdom Suite and Fledermaus software packages for interpretation. The 1–6 kHz swept frequency acoustic source provided sub-bottom penetration to >50 m in lacustrine sediments, but in some places penetration was limited by the AB. All depth conversions assumed a 1500 m/sec sediment velocity unless otherwise stated. Onshore field reconnaissance between Baldwin Beach and Christmas Valley identified scarps along the Fallen Leaf lateral moraines as well as a several kilometer-long scarp south of FLL near Osgood Swamp (Fig. 2). The onshore and offshore results were integrated with datasets collected in 2000, 2002, and 2006 along the Rubicon and Dollar Point sections of the WTDPF (Kent *et al.*, 2005; Dingler, 2007).

During October 2006, five piston cores were collected in FLL (Figs. 3 and 4) from a platform barge using a modified Kullenberg piston corer. The coring device includes an ~250 kg weight stand, a 5 m long, 3 inch diameter core barrel and, depending on the sediment type, typically recovers between 3 and 5 m of sediment. The cores were acquired in the southern half of FLL in the vicinity of the WTDPF in an effort to construct a chronostratigraphic framework that can be used to estimate the timing of the MRE. Each of the piston cores recovered >3.5 m of sediment. Lithologic and magnetic susceptibility logs were produced for all cores. The stratigraphy in all cores except one, PC5, was easily correlated based on color, texture, lithology, and magnetic susceptibility patterns (Fig. 4). Increases in magnetic susceptibility generally reflect increased concentrations of magnetite-rich siliciclastic sediments and may be correlated with periods of increased sediment contribution from the basin margins or in this case from Glen Alpine Creek. Conversely, low magnetic susceptibility appears to correlate with increased amounts of nonmagnetic clays and silts. PC5 was located at a shallower depth along the eastern basin slope. Six detrital wood samples and one organic fiber sample extracted from cores PC3, PC4, and PC5 were radiocarbon dated using an accelerator mass spectrometer. PC5 was the

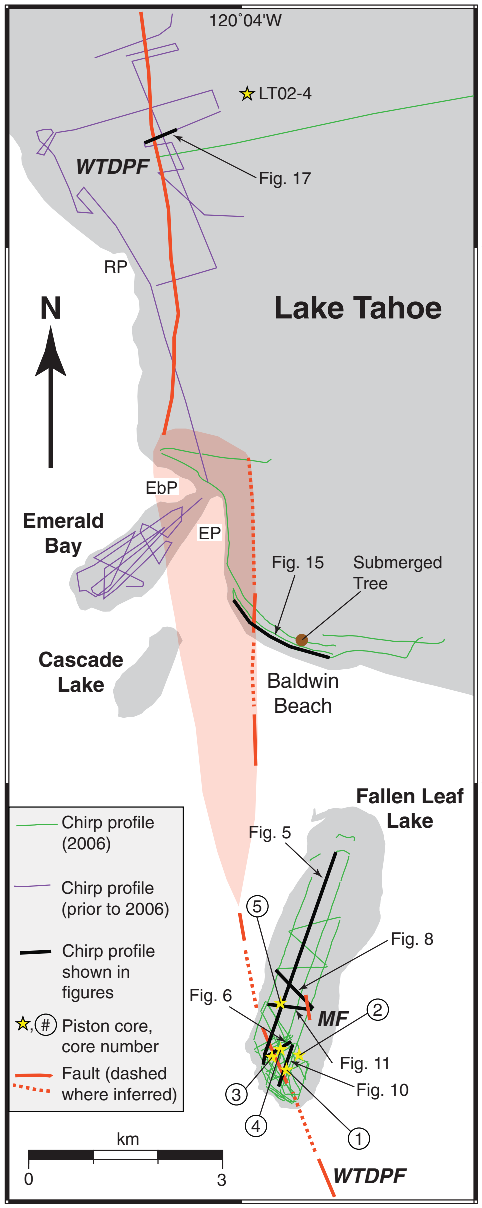

Figure 3. CHIRP profiles and sediment core locations in FLL and southwestern Lake Tahoe. Red lines mark the location of the WTDPF and MF (solid red line—where known, and dashed red line—where inferred). Abbreviations: RP, Rubicon Point; Eagle Point, EP; and Emerald Point, EmP. The submerged tree (brown circle) was sampled and radiocarbon dated to test for coincident timing of its submersion and the MRE on the WTDPF (Table 1). LT02-4 is the location of a piston core used to constrain sedimentation rates near the Rubicon section of the WTDPF shown in Figure 17 (Smith *et al.*, 2007). The precise location of faulting between FLL and EmP is not clear and may be distributed across a complex relay zone (red shaded area).

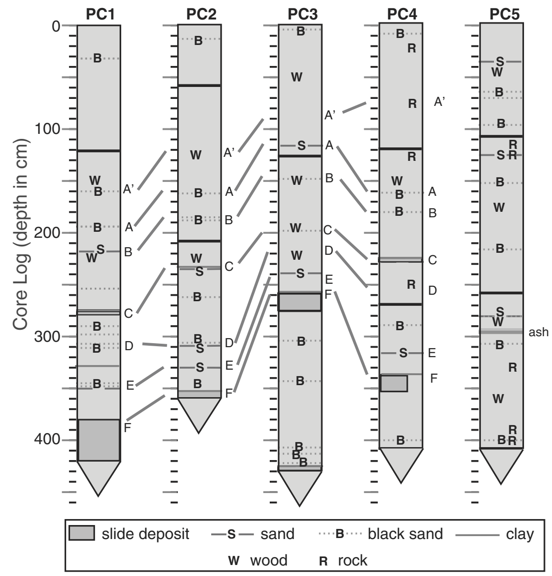

Figure 4. Piston core logs. Stratigraphic correlations are based on color, lithology, and magnetic susceptibility. Note the distinct slide deposit that is recognized in four of the cores. The ash labeled in PC5 is the 7.6–8.0 k.y. B.P. Tsoyowata Ash (Bacon, 1983).

only core that contained the 7.5–8.0 k.y. old Tsoyowata Ash as a chronological marker bed (Bacon, 1983; Sarna-Wojkicki *et al.*, 1991). Once the chronostratigraphy was established based on core data, we correlated distinct marker beds in the cores with corresponding layers in the seismic stratigraphy, allowing us to constrain the age of tectonically offset seismic horizons.

Faulting and Stratigraphic Framework

Fallen Leaf Lake

A high-density grid of sub-bottom CHIRP profiles was collected in the southern portion of the lake surrounding the WTDPF and a less dense grid collected in the northern lake (Fig. 3). The survey afforded three-dimensional, basin-wide correlation between seismic horizons and a nearly complete characterization of recent tectonic, glacial, and sedimentary processes beneath FLL. A low-resolution bathymetric elevation model was constructed by gridding lake-floor elevations measured in the CHIRP profiles. The basin depocenter is in the southern lake and is bounded to the south by a steep, ~100 m high escarpment that trends obliquely to the long axis of the valley and glacial flow direction. The base of the slope and its trend are coincident with the WTDPF, which is delineated by vertically offset and folded lacustrine horizons. In general, horizontally layered lacustrine deposits infill topographic relief in the underlying AB (Fig. 5). Three faults beneath FLL are observed in the CHIRP profiles. Two parallel faults separated by ~80 m trend ~N25˚W along

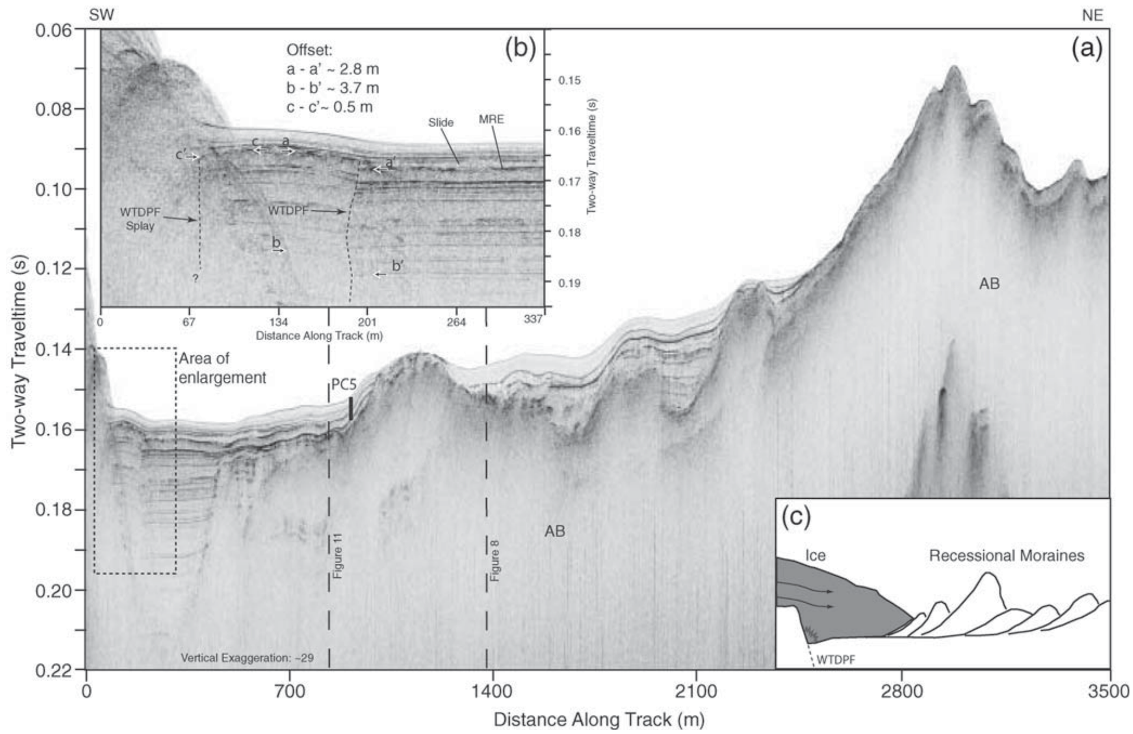

Figure 5. (a) Northeast–southwest tending CHIRP profile spanning over two-thirds of FLL. The WTDPF is seen toward the southern end, adjacent to a steep, fault-parallel escarpment. (b) Enlarged section of the two splays of the WTDPF (dashed box in 5a). Offset across both faults creates anticlinal folding in the sediments. A divergent bed labeled "slide" thickens into the fault and infills accommodation created during the MRE. The slide is an important marker bed that is seen in the seismic stratigraphy and in four of the piston cores (Fig. 4) throughout most of the southern lake. Piercing points (white arrows) on the footwall were selected near the apex of the anticline; beds are assumed to have been deposited approximately horizontal, then were subsequently folded and offset during the MRE. Offset increases with depth from ~2.8 m across the MRE horizon (aa′) to ~3.7 m across horizon bb′ due to increased compaction and dewatering with depth (all travel time to depth conversions assume 1500 m/sec velocity). Piston core PC5 is ~40 m to the west of this profile. (c) Hummocky topography in the acoustic basement (AB) is seen in several profiles. This type of morphology is typical for moraines formed at glacier fronts by temporary still stands or readvancements during an overall glacial retreat. Similar morphology is observed as a series of arcuate recessional moraines between FLL and Lake Tahoe (Saucedo, 2005). The relief toward the southern end of the profile, adjacent to the WTDPF, may be formed by a combination of glacial and tectonic processes, much like a roche moutonée, but glacial plucking may have been facilitated by the location of the fault.

the base of the steep escarpment in the southern lake and project onto scarps mapped on the moraine crests above FLL (Fig. 2). Based on their proximity and synthetic nature, the two faults are collectively referred to as the WTDPF. The third fault, termed the Midlake fault (MF), is located ~1 km to the northeast of the WTDPF (Fig. 3) and is observed in only two profiles.

Coseismic deformations in the shallow sub-bottom are identified as vertically folded strata, but down-section layers show greater separation and exhibit distinct offset, suggesting that extensional fault-propagation-folding has occurred (Gawthorpe *et al.*, 1997; Hardy and McClay, 1999). East-side-down folding (~5 m below the lake floor) demarcates the MRE horizon on both the WTDPF and MF (Figs. 6–8). The MRE horizon on the hanging wall dips into the fault and is overlain by a thin divergent layer that thickens toward the fault reflecting syntectonic deposition and infill of the accommodation created during the MRE. A striking observation is that the MRE horizon and the thin divergent bed overlying the MRE horizon can be traced across both the WTDPF and the MF (Fig. 9). Throughout the southern half of the lake the divergent layer onlaps bathymetric highs and diverges and thickens into lows, ranging in thickness from 0–~1.5 m. Near the southeastern slope, strata beneath the layer abruptly changes in character, where it becomes chaotic and appears to have been disrupted (Fig. 10). Based on acoustic character and core logs (discussed later), we refer to this layer as a slide deposit. The stratal geometry and acoustic character seen in Figures 8 and 11 provide a stratigraphic framework that is used for basin-wide interpretations. The smooth lenticular shaped units labeled A, B, and C in package I thicken away from the bathymetric lows and down lap

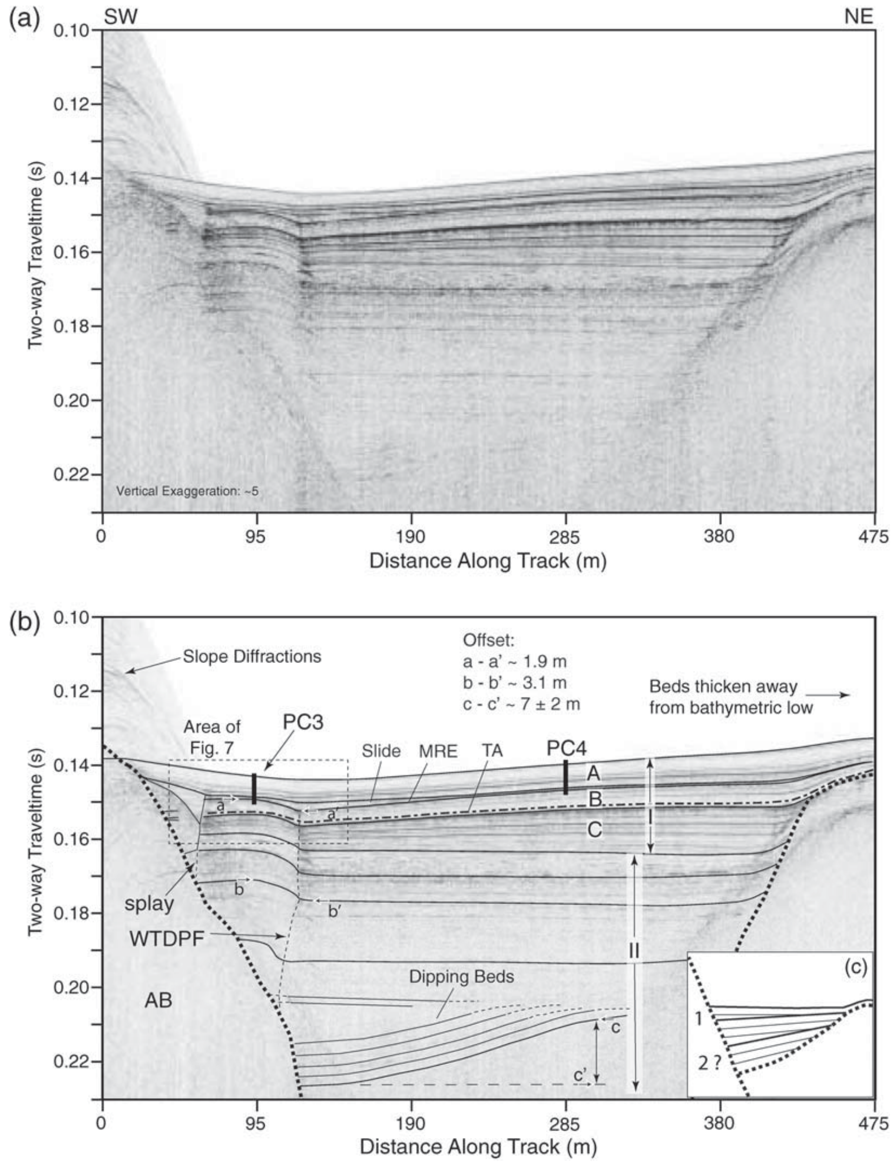

Figure 6. (a) Uninterpreted, and (b) interpreted fault-perpendicular profile. Locations of two nearby cores are projected onto the cross section. Piercing points (white arrows) measure slip that occurred during the MRE. Although offset of the MRE horizon is ~1.9 m then increases to ~3.1 m over deeper horizons, we do not observe stratigraphic evidence for multiple events (e.g., increase in dip or divergence down section) in the upper ~35 m. The deformation resembles a normal fault propagation fold, where offset at depth is attenuated in the shallow, unconsolidated sediments and is expressed as a fold. A slide deposit directly above the MRE horizon infills accommodation created during the MRE. Piston core PC3 sampled the slide near the WTDPF, which is used as a marker bed throughout the lake. Radiocarbon samples from PC3 constrain the timing of the MRE to 4.1–4.5 k.y. B.P. (Table 1). Units A, B and C in section I represent fine-grained layers (low amplitude reflections) that are separated by thin, coarse-grained layers (high-amplitude reflections). The fine-grained layers appear to thicken away from the basin depocenter suggesting current-controlled deposition (see text). The approximate position of the Tsoyowata Ash (dashed line labeled TA; ~7 m depth adjacent to the WTDPF) is correlated from seismic sections near piston core PC5 and provides an independent constraint on sedimentation rate. Section II exhibits more uniform deposition. Faintly imaged strata in the hanging wall dip at ~4°. Assuming the beds were deposited horizontally then subsequently tilted during a penultimate event, the vertical offset is estimated at 7 ± 2 m. (c) Conceptual model for syntectonic deposition, where divergent beds record subsidence along the fault and multiple events can be recognized by increased dip down section.

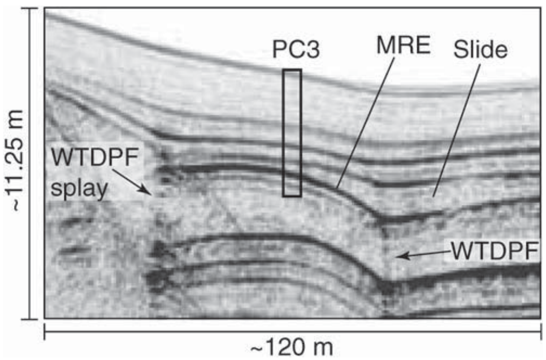

Figure 7. Enlarged section (dashed box) from Figure 6 highlighting the MRE horizon and overlying slide deposit. The two faults are separated by ~60 m. Piston core PC3 sampled material above and below the MRE horizon.

onto underlying beds. In contrast, the intervening layers diverge and thicken into low points along the basin margins. Package II does not exhibit the same geometric relationships and deposition appears more uniform.

Matching cores with the nearby seismic profiles allowed us to define relationships between seismic stratigraphy and the corresponding lithostratigraphy. Distinct marker beds sampled by the cores were traced onto adjacent CHIRP profiles (Fig. 9). Lithostratigraphy documented in all the piston cores except PC5 includes a distinct coarse-grained slide deposit (Fig. 4). At the base of PC1 is a coarse-grained, massive bed that contained several large pieces of wood and twigs, where PC2, PC3, and PC4 sampled the distal, fine-grained extent of the equivalent layer. The coarse-grained slide deposit observed in the cores correlates well with the divergent bed overlying the MRE horizon seen in the seismic profiles (Figs. 6 and 10). All cores except PC5 are within 30 m of a CHIRP profile; PC5 is within 45 m. The horizontal offset may result in a slight mismatch (< 0.5 m) between seismic stratigraphy and core logs. Another potential source for mismatch is overpenetration (< 0.5 m), which was noted during recovery by mud on the weights above the core barrel.

The age of the MRE was estimated by radiocarbon dating organic material from either side of the MRE horizon. The analysis was based solely on radiocarbon data from core PC3 (Fig. 12), which was located nearest the WTDPF. Sediment recovered by PC3 extended > 1.5 m below the MRE horizon and contained abundant organic matter for radiocarbon dating. Four samples (all > 5 mg) were analyzed with an accelerator mass spectrometer (Table 1). The radiocarbon dates were converted to calendar years B.P. using the OxCal 4.0 radiocarbon calibration software and calibration curve IntCal04.14c (Ramsey, 1995, 2001; Reimer *et al.*, 2004). All further discussions will be in terms of calendar years B.P. The sample at 3.40 m depth was anomalously old for its stratigraphic position suggesting it had a long-residence time in the watershed before deposition in FLL and was excluded from the analysis. Of the remaining samples, the deepest and oldest (5.3–5.6 k.y. B.P.) was sampled by the core catcher at a depth of ~4.3 m, meaning the actual depth is between 4.3 and 4.8 m (accounting for possible overpenetration). Dividing the depth range by the age range resulted in an average sedimentation rate adjacent to the WTDPF between 0.8 and 0.9 mm/yr. An independent comparison can be made using the 7.5–8.0 k.y. B.P. Tsoyowata Ash that was sampled at a depth of 2.95 m in PC5 between two thin sand beds (Fig. 4). The relative stratigraphic position of the ash layer can be projected onto the nearest profile (Fig. 11; ~50 m away) and correlated basin wide. The ash is inferred at a depth of 7 ± 2 m adjacent to the WTDPF (labeled TA in Fig. 6), again resulting in an average sedimentation rate of ~1 mm/yr.

The age of the MRE horizon is confined by the age of samples 1 and 3 in PC3 (Fig. 13, Table 1). The absolute lower and upper bounds are 3.6 and 4.9 k.y. B.P. based on the radiocarbon ages, but a more precise estimate was calculated by linearly interpolating the age as a function of depth between samples 1 and 3 (Fig. 13). We assume the slide deposit was emplaced rapidly and removed its thickness from the interpolation. The total thickness between samples after removing the slide is 173 cm (the slide is only ~10% of the total thickness between samples) and the MRE horizon is 65 cm below sample 1. Interpolating the age as a function of depth for both the upper and lower age bounds on each sample confines the MRE to 4.1–4.5 k.y. B.P. Uncertainty in this estimate would be introduced by nonlinear sedimentation rates or nonlinear compaction within the interpolation interval during core collection. However, these effects are not quantifiable with the available data, and we do not observe evidence for either.

Piercing points in the seismic stratigraphy are selected to measure vertical offset (white arrows in Figs. 5, 6, and 8). The 1–6 kHz CHIRP source can resolve layers that are vertically separated by greater than ~0.4 m. Travel-time intervals between piercing points are measured directly then converted to depth intervals by assuming an interval velocity. We use a nominal velocity (1500 m/sec) for all depth conversions to avoid overestimating the offset measurements, and we incorporate a pick error of ± 0.2 m. At greater depths (> 10 m) where compaction and dewatering are likely, it is possible that seismic velocities reach ~1800 m/sec. On the main splay of the WTDPF, deformation within the shallow, poorly consolidated sediments appears to become distributed as folding and possibly minor faulting, which results in an attenuated offset up-section similar to analog models for extensional fault propagation folds (Hardy and McClay, 1999). Offset measurements show a gradual increase in offset with depth from ~2 m over the folded MRE horizon to > 3 m across horizons at depths greater than ~10 m (Table 2; Figs. 5–7). Because we do not observe any stratigraphic evidence (e.g., divergent beds, increasing dip with depth) for multiple events in the upper 0.05 sec (~38 m) of sediment, it is assumed that the deeper measurements provide our best

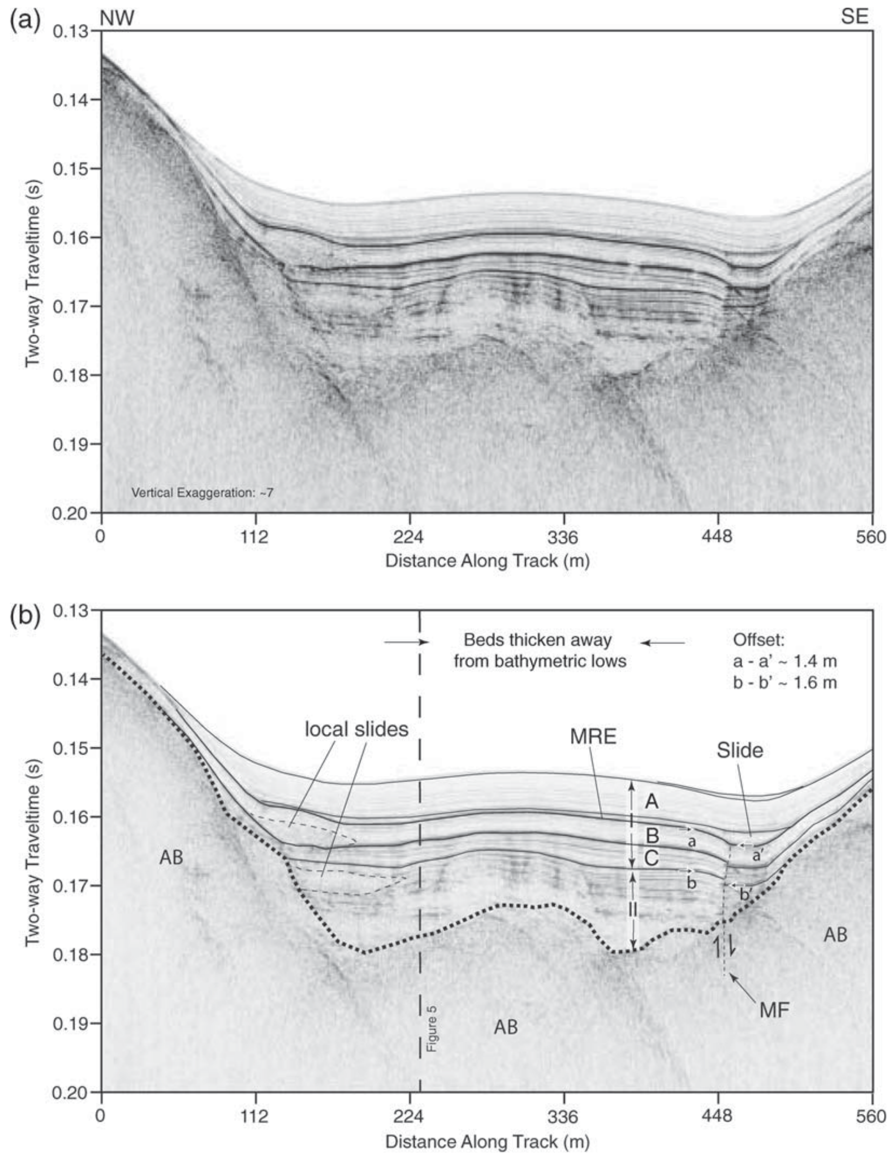

Figure 8. Northeast–southwest oriented profile over the MF and a series of debris slides along the western slope. The MRE horizon and overlying slide are the equivalent layers observed across the WTDPF. Displacement is down-to-the-east and increases from ~1.4 m across the MRE horizon to ~1.6 m down section. Packages A, B, and C represent lenticular shaped drift deposits (low amplitude) that mantle the underlying topography, but also thicken away from the basin margins. Each unit is separated by thin, coarse-grained gravity slides, one of which is the slide directly above the MRE horizon. Contact surfaces between coarse- and fine-grained deposits result in high-impedance (i.e., high-amplitude) boundaries in the seismic stratigraphy.

estimates for coseismic slip that occurred during the MRE. Overall, nine precise measurements across the MRE horizon ranged between 1.5 and 2.8 m and eight measurements across deeper horizons ranged between 3.0 and 3.7 m (Table 2). The secondary splay (Figs. 5–7), located very near the slope break, is evident in six profiles by small synclinal folding and infill above the MRE horizon. Offset measurements over the splay ranged from 0.6 to 1.3 m. Although the nature of the splay is poorly imaged, it is possible that the two faults merge at depth and their slip is additive, increasing the total offset produced during the MRE to between 3.6 and 4.5 m, with an average of ~4.1 m.

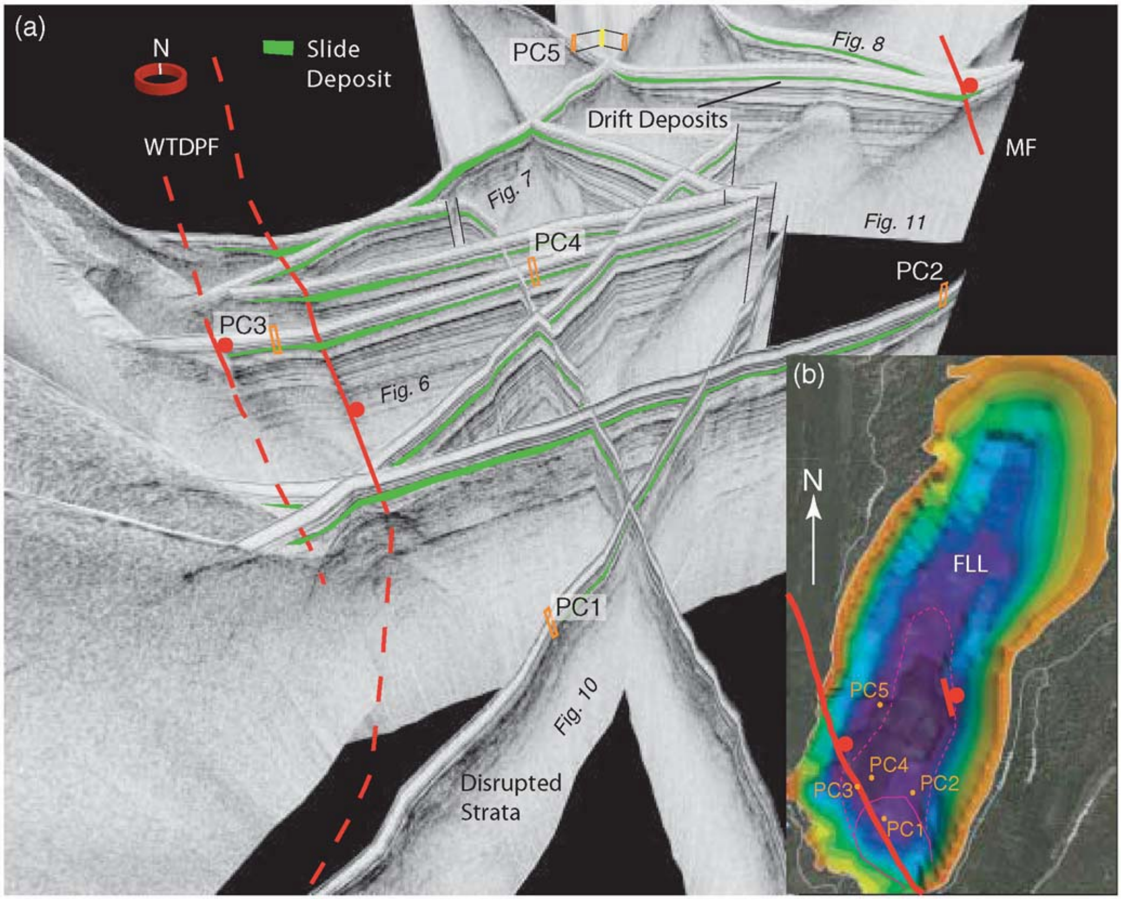

Figure 9. (a) Fence diagram of CHIRP profiles and core locations illustrating the 3-dimensional structure, stratigraphy, and core locations. The diagram illustrates the utility of using acoustic stratigraphy to correlate sediments throughout the basin. PC5 is projected onto the two nearest profiles, but all other cores are within 20 m of the nearest profile. The slide deposit directly above the MRE horizon (green layer) can be traced from its coarse-grained proximal extent to its fine-grained distal reach at the far side of the southern basin. The run-out length is over 1 km. Faults are depicted by red lines (solid red lines, where known and dashed red lines, where inferred). (b) Bathymetric grid of FLL based on CHIRP soundings. Thick red lines are the WTDPF and MF; thin red lines outline the inferred extent of slide deposit (solid red line, proximal and dashed red line, distal).

Approximately 35 m below the lake floor, the stratigraphy abruptly changes in character and has a marked 4° increase in dip toward the fault (Fig. 6). The data quality diminishes down-section due to attenuation and interference from diffractions off the AB and adjacent slopes, but the dipping strata are observed in several profiles and are unlikely to be a three-dimensional artifact or sideswipe from a nearby slope. A dipping horizon that spans the deeper portion of the basin was used as a piercing line and depth was measured at both ends (cc′ in Fig. 6). Some ambiguity exists when picking the edges of the horizon resulting in large uncertainty, but the measured difference is ~7 ± 2 m (Fig. 5).

The MF is observed in two profiles ~1 km northeast of the WTDPF (Figs. 8, 9, and 11). The MRE horizon at the MF was vertically folded by 1.4 m and is overlain by a divergent wedge similar to that observed across the WTDPF. Offset increases slightly down-section to ~1.6 m. The trend of the fault, determined over a length of ~100 m, appears parallel to the WTDPF. However, the nearest profile north of the projected trend lacks convincing evidence for faulting. Farther north, disrupted sediments and slide deposits provide weak evidence for a north–south trending fault.

Onshore Mapping

Onshore field reconnaissance mapping south of FLL, near Osgood Swamp (Figs. 2 and 14), revealed a 2.6 km long section of down-to-the-east fault scarps. The scarps offset

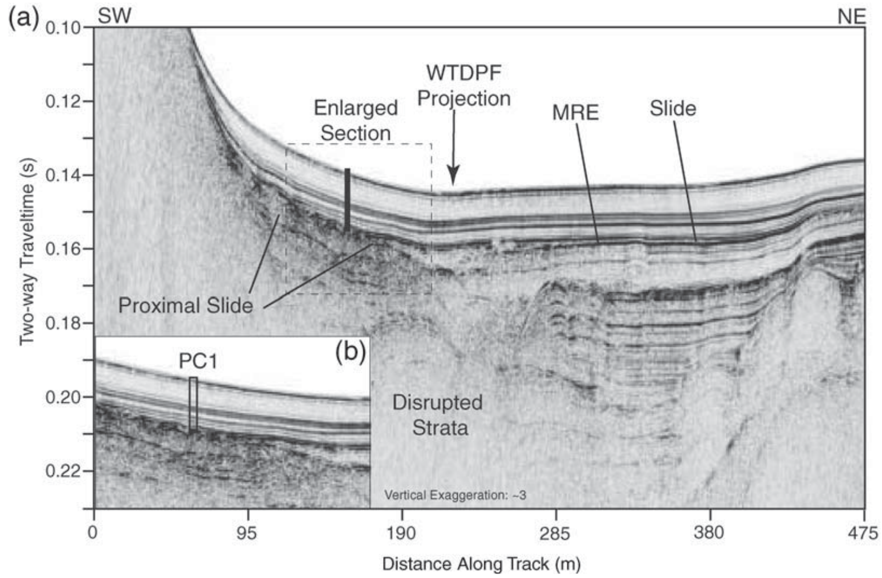

Figure 10. Northeast–southwest oriented type section that confirmed the correlation between the slide material sampled at the base of PC1 (Fig. 4) and highly disrupted, chaotic bedding that grades distally into the divergent bed observed above the MRE horizon.

unconsolidated alluvial and glacial sediments and have relaxed slope profiles. Heights varied depending on the age of the offset material, where some scarps north of Osgood Swamp are 10–15 m high, while others to the south of Osgood swamp are 2–4 m high (Fig. 14). Between Osgood Swamp and Angora Lakes (Fig. 2) steep slopes and dense vegetation preclude identification of the fault. An ~400 m long, ~3 m high scarp was mapped perpendicular to the Angora Ridge moraine crest (Fig. 2) and aligns with the trend beneath FLL and another ~500 m long scarp mapped on the opposite side of FLL valley. North of FLL, the landscape again becomes covered with dense vegetation and complex fluvial and glacial overprint. A potential ~1 km long scarp was mapped ~2 km south of Baldwin Beach along the edge of a small meadow (Fig. 2). The scarp height in the meadow varies between 3 and 10 m depending on the age of the surface material. Overall, the onshore expression of the WTDPF is poorly constrained, particularly in the region between FLL and Lake Tahoe. Because of the complex geomorphology, subsurface studies are needed to discern fault scarps from glacial or fluvial scarps.

Baldwin Beach

CHIRP data collected along the shallow sandy shelf immediately offshore Baldwin Beach (Fig. 3) show evidence for faulted sediments. A tightly folded syncline (Fig. 15) traced between three profiles and trending north–south aligns with pockmarks and possible lake-floor disruption down the adjacent steep basin slope (Dingler, 2007). The deformation is less obvious than in FLL, possibly due to an absence of internal bedding in the unconsolidated, medium- to coarse-grained sand.

Several submerged, but rooted trees have been identified near Baldwin Beach and are thought to reflect climatic variability during the mid-Holocene (Lindstrom, 1990). A sample from the deepest submerged tree (Fig. 3), rooted at ~4 m depth and located to the east of the inferred fault (Fig. 3), was radiocarbon dated (Table 1) to test for coincident timing between the MRE on the WTDPF and the tree's inundation. Its age (5.3–5.6 k.y. B.P.; Table 1) is slightly greater than the MRE age range determined at FLL but is consistent with the range of dates determined by Lindstrom (1990).

Rubicon Point to Dollar Point

Several CHIRP profiles discussed by Dingler (2007) were reexamined to define the Rubicon and Dollar Point sections of the WTDPF. Deformation similar to that in FLL is observed across a CHIRP profile at the base of the shelf offshore Rubicon (Figs. 3 and 16). An ~1.4–2.0 m thick section of nearly transparent, unfaulted material overlies a divergent bed that thickens into the fault and infills the small accommodation (Fig. 17). As in FLL, the divergent bed rests directly above the MRE horizon and has a high-amplitude basal reflector suggesting it is a coarse-grained deposit, possibly a gravity slide. The MRE horizon is offset down-to-the-east by 1.0 m (possibly along a synthetic splay of the WTDPF) but farther down-section the offset increases to 2.0 m. Folding is observed ~150 m east of the main fault with horizons offset vertically up to 0.3 m. A piston core located ~800 m from the eastern end of the profile in Figure 3

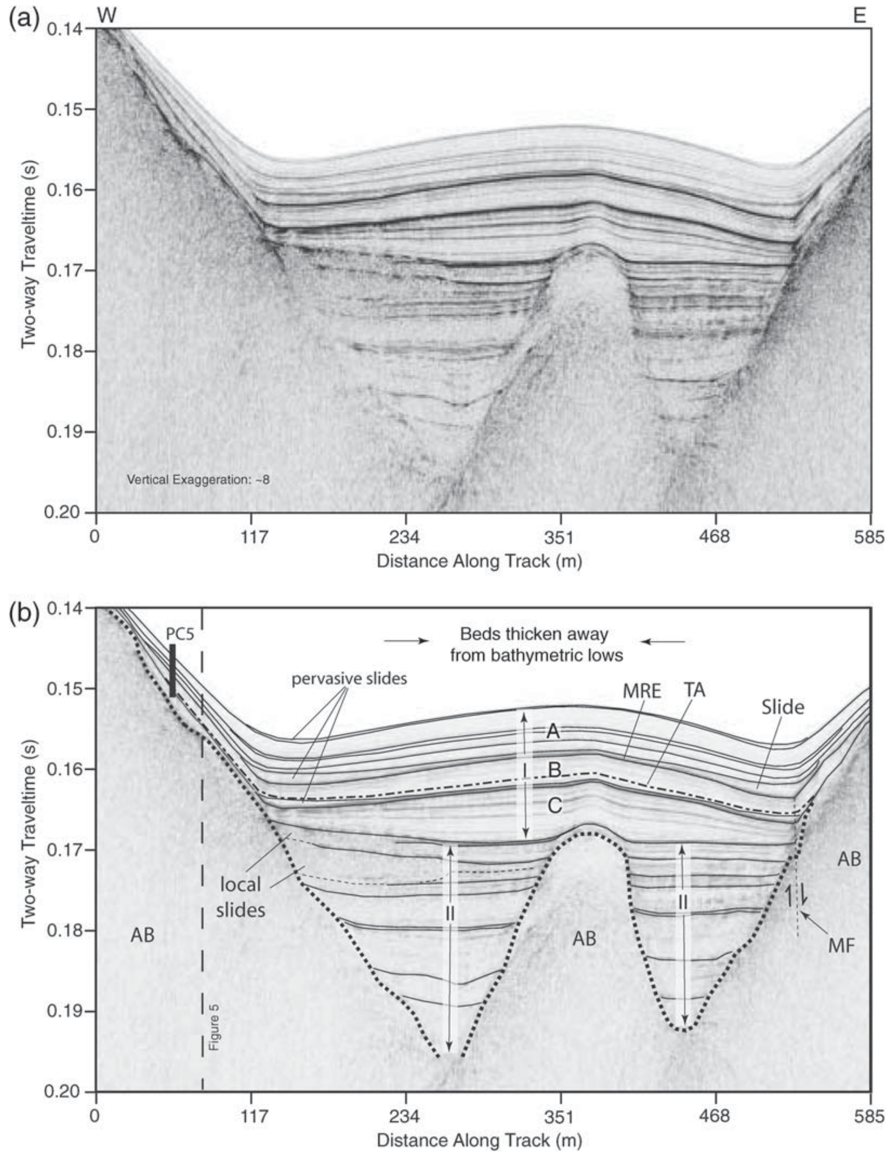

Figure 11. East–west oriented profile highlighting the interplay between current-controlled deposition that forms contourite drifts and down-slope deposits that infill bathymetric low points. Units A, B, and C of section I are separated by coarse-grained slide deposits, resulting in the high-amplitude contacts. The MRE horizon is traced from profiles to the south. Piston core PC5 (~50 m to the north of its projected position shown in the figure) samples the 7.6–8.0 k.y. B.P. Tsoyowata Ash (Fig. 4; Bacon, 1983). The stratigraphic position of the TA is projected onto the seismic section and correlated basin wide. Several thin slides are observed on several profiles, and other local slides are observed to disrupt underlying strata. Evidence for drift deposits is not observed in section II, but small slide complexes are observed along the basin slopes and uniform deposition in topographic lows.

sampled two distinct slide deposits, one at ~0.6 m and the other at ~1.2 m, that have been correlated with several cores to the north and have been dated at 4.1–4.5 k.y. B.P. and 5.3–5.6 k.y. B.P., respectively (Smith *et al.*, 2007). Despite the equivalent age of the upper slide in the core and the MRE timing along the Fallen Leaf section, we cannot verify that the thin slide imaged above the MRE in Figure 17 correlates with the slide in the core because their relationship is speculative. Nevertheless, using this slide as a marker bed provides a minimum sedimentation rate for this area of ~0.1 mm/yr.

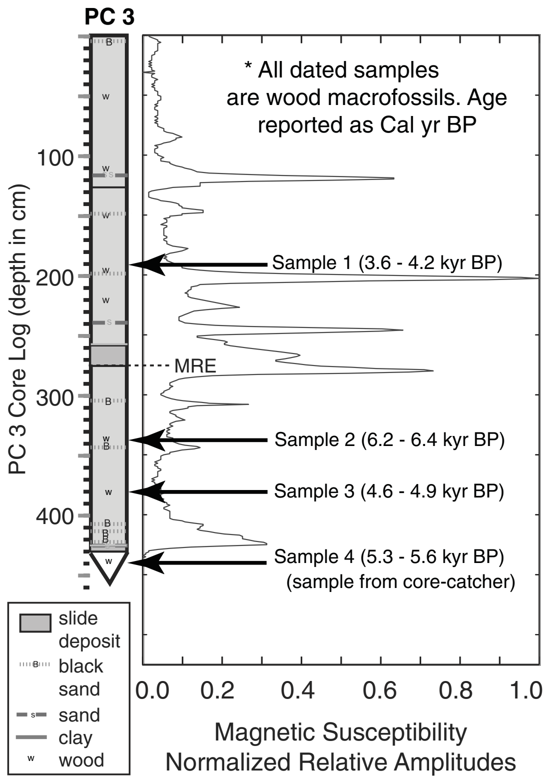

Figure 12. Piston core PC3 lithology and magnetic susceptibility logs. Each of the lithological layers logged can be correlated between all cores except PC5 (Fig. 4). The slide layer, consisting of highly disturbed sand, silt, and clay mixed with several twigs and organics, directly overlies the MRE horizon. Four radiocarbon samples (black arrows; Table 1) were dated to constrain the timing of the MRE. Sample 4, a pine needle, was taken from the core catcher and may have been slightly deeper than 4.3 m due to overpenetration.

The MRE horizon nearest the core in Figure 17 is at ~1.4 m depth, resulting in an age of ~10 k.y. Sedimentation rates may be expected to increase closer to the basin margins, thus reducing the MRE age estimate. Elsewhere in Lake Tahoe sedimentation rates in the upper 2 m have been estimated as high as ~0.4 mm/yr (Smith *et al.*, 2007), which would result in an age for the MRE of ~3.5 k.y. B.P.

Offshore Sugar Pine Point the WTDPF offsets a fan delta forming a 10.5 m high scarp observed in both bathymetry and CHIRP data (Fig. 16 and Fig. 18 for the scarp profile). Just north of Sugar Pine Point, the scarp is ~90 m tall then disappears at the main run-out area of the MBS debris apron. The Dollar Point section begins at the southern edge of the TCS, where the fault has an ~100 m tall scarp and possible slumping and secondary faulting in both the footwall and hanging wall (Fig. 16; Dingler, 2007). The scarp continues along the east edge of the TCS to Dollar Point. The scarps on either side of the MBS are approximately the same height. The age of the MRE is not constrained on this section.

Discussion

Fallen Leaf Lake Morphology and Stratigraphic Character

FLL has formed through a combination of glacial and tectonic forces. The undulating and hummocky nature of the AB imaged in the northern two-thirds of the lake suggests that a series of recessional and lateral moraines create topography that is being filled with lacustrine sediments (Fig. 4). Formation of the steep slope bounding the basin depocenter may have facilitated glacial erosion along the WTDPF. Any preglacial structure in the bedrock, including an increased fracture density due to faulting, may have created a zone of preferential quarrying along the hanging-wall block on the lee side of glacial flow. The glacial history in the LTB provides rough estimates for the sedimentary history in FLL where it is assumed that Tioga glaciation reworked the inner walls of the moraine-bounded valleys and reset lacustrine sedimentation at ~14 ka, when the glaciers recessed (Benson *et al.*, 1998).

The stratigraphy observed in package I (Figs. 6, 8, and 11) reveals that a combination of down-slope and along-slope processes have formed intercalated drift deposits and gravity driven slope deposits. The lenticular beds that thicken toward the center of FLL resemble current controlled deposits that are swept basinward by bottom currents (Driscoll and Laine, 1996). Bathymetric lows along the basin slopes have been filled with coarse-grained beds that onlap the underlying strata. High-amplitude contacts between the lenticular beds and onlapping beds support the notion that coarser-grained down-slope deposits are emplaced on top of finer-grained drift deposits. Contourite drifts are often observed in marine environments along continental margins (Driscoll and Laine, 1996; McGinnis *et al.*, 1997; Faugeres *et al.*, 1999) and in large-scale lacustrine basins (Gilli *et al.*, 2005), but less commonly in small confined basins such as FLL.

The coarse-grained layer above the MRE horizon is observed throughout the southern lake and appears to be a slide deposit. Although disrupted strata beneath the slide (Fig. 10) may be caused by soft sediment deformation during the MRE, the coincidence of coarser-grained (proximal) material in PC1 and the chaotic reflections in Figure 10 suggest the slide source is near the southeastern basin slope (Fig. 9b). The extensive run out (> 1000 m) away from the source region and the absence of coherent internal reflectors indicate the slide deposit was most likely emplaced by a hyperpycnal flow with high velocity. Based on the stratal relationship between the slide and the MRE horizon, it is possible that the slide was triggered by the last major event on the WTDPF. Several smaller slides are identified throughout the basin

Table 1

Radiocarbon Ages Derived from Macrofossil Samples

Location	Lab[*]	Sample Number, Description[†]	Stratigraphic Depth[§] (m)	Lab Identification Number	$\delta^{13}C$[‡]	Uncalibrated ^{14}C Age (yr B.P.)	Calibrated Calendric Age[‖]	% Confidence	Rounded Age[#] (k.y. B.P.)
Core 3 (FLL)	UofA	1, wood	1.90	AA76371	−21.9	3580 ± 110	4159–3585	94.1	3.6–4.2
							4201–4227	1.0	
							4171–4178	0.2	
	UofA	2, wood	3.40	AA76375	−26.3	5506 ± 41	6270–6400	86.5	6.2–6.4
							6214–6242	8.9	
	UofA	3, wood	3.83	AA76374	−25.6	4235 ± 44	4785–4869	45.6	4.6–4.9
							4620–4765	49.8	
	LLNL	4, pine needle	4.30	128008	−25	4795 ± 45	5458–5607	89.3	5.3–5.6
							5331–5375	6.1	
Core 4 (FLL)	LLNL	5, fiber	4.10	128009	−25	7995 ± 40	8717–9008	94.6	8.7–9.0
							8705–8708	0.3	
							8661–8667	0.5	
Core 5 (FLL)	UofA	6, wood	2.36	AA76376	−26.2	6003 ± 48	6730–6975	95.4	6.7–7.0
Baldwin Beach Tree (LT)	LLNL	7, wood	N/A	12628	−25	4705 ± 35	5510–5581	23.1	5.3–5.6
							5438–5485	21.1	
							5321–5420	51.2	

[*]Sample analysis was performed at the University of Arizona Accelerator Mass Spectrometry Laboratory (UofA) and the Lawrence Livermore National Laboratory Center for Accelerator Mass Spectrometry (LLNL).

[†]All samples were larger than 5 mg.

[‡]$\delta^{13}C$ values equal to −25 were not measured, but are the assumed values according to Stuiver and Polach (1977). All other values were measured.

[§]Measured from top of core.

[‖]All dates given as a max–min date range. Raw ^{14}C ages were calibrated using OcCal v4.0.5 (Ramsey, 2001) and the IntCal04 atmospheric curve (Reimer *et al.*, 2004). Calibrated ages are reported as % confidence under the 95% probability distribution.

[#]Rounded ages are reported as a max–min range. Final age ranges are rounded to the nearest 0.1 k.y.

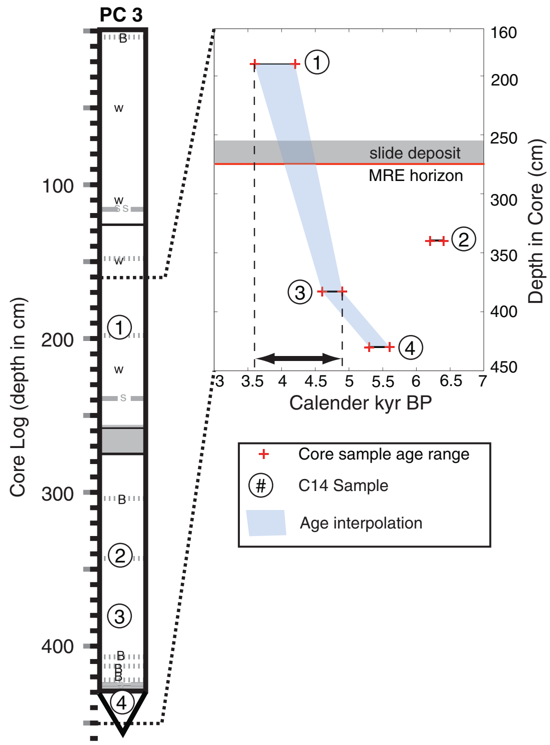

Figure 13. Plot of piston core PC3 sediment depth as a function of age. The age of the MRE was estimated by removing the thickness of the slide then linearly interpolating between samples 1 and 3. Sample 2 appears anomalously old based on its stratigraphic position and was not used in the analysis. The blue region represents the interpolated age range, and the black double-sided arrow indicates the absolute range of ages. The section between samples 1 and 3 is 173 cm and the MRE is at 65 cm after removing the 20 cm thick slide deposit. Interpolating between the upper and lower age ranges results constrains the MRE to between 4.1 and 4.5 k.y. B.P.

based on their acoustic character and range in size from very localized to regional.

Updated Fault Locations

Results from the onshore and offshore fault mapping have improved our understanding of fault locations along the Fallen Leaf section of the WTDPF and add important constraints on the potential rupture length. The southernmost extent of the fault is uncertain as the scarp merges with a steep hillside ~1 km south of Osgood Swamp, but based on the 2–3 m scarp height near this location (Fig. 14), the fault may continue southward for several kilometers. Evidence for faulting offshore Baldwin Beach based solely on CHIRP profiles is ambiguous but, when combined with mapped scarps to the south (meadow scarp) and the lake-floor disruption to the north, suggests that the WTDPF extends offshore near Baldwin Beach. Although the coseismic vertical offset observed in FLL (Table 2) would be sufficient to drown near-shore vegetation situated east of the fault, the age of the submerged tree offshore Baldwin Beach is slightly older than the age estimate of the MRE. Nonetheless, given the timing of the MRE, it is likely that down-to-the-east motion associated with this event played a role in the ultimate preservation of the submerged trees, and we cannot reject the possibility that an older event submerged the trees but did not rupture through FLL. The mapped extent of the MF in FLL is limited but appears to project northward toward the meadow scarp (Fig. 2). We do not observe offset strata in CHIRP data collected in Emerald Bay, but acoustic penetration was limited toward the mouth of the bay by glacial sediment. North of FLL, the fault may trend towards the eastern shore of Cascade Lake, then across the mouth of Emerald Bay into the Rubicon section. The apparent complexity may be due to inconclusive mapping onshore, a relay zone between sections, or the existence of a broader basin-bounding fault zone, in which multiple faults accommodate extension. The fault's proximity to the steep basin slope creates acoustic interference and hinders our ability to image the sub-bottom using the CHIRP system; therefore, the Rubicon and Dollar Point sections are generally delineated by bathymetric expression.

The minimum estimate for the total length of the combined sections, from the southern terminus of our field mapping to where the Dollar Point section steps onshore in Carnelian Bay, is ~46 km. The fault likely extends onshore at least another 5 km north of Carnelian Bay (Saucedo *et al.*, 2005) and possibly a similar amount south of Osgood Swamp, producing a length of ~55 km. Overall, the length and morphology of the WTDFP is strikingly similar to that of the GF (Fig. 19).

Earthquake Timing, Magnitude, and Slip Rates

The MRE age estimates for the Fallen Leaf (4.1–4.5 k.y. B.P.) and Rubicon (~3–10 k.y. B.P.) sections are in rough agreement and imply the fault may rupture as a single strand. Offset measurements should be considered minimum estimates as the apparent offset (based on constant velocity) is expected to increase in the deeper, more compacted, higher velocity sediments. At FLL, the maximum observed offset of the lacustrine sediments is 3.7 m on the main trace and 1.3 m on the secondary splay, producing a maximum possible offset of 5.0 m. The MF has a 1.6 m of offset but remains poorly understood and may have recorded local deformation following an event on the WTDPF. The ~2 m offset observed along the Rubicon section (Fig. 17) is about half the maximum but within the range of offset values measured beneath FLL (e.g., Fig. 5). The fault observed in Figure 17 may represent a splay off the WTDPF, with a second fault along the base of the slope where acoustic diffractions preclude imaging with the CHIRP system. However, along strike variation in slip is common along normal fault ruptures, in particular near geometric complexities (Witkind *et al.*, 1962; Crone *et al.*, 1987; Ramelli *et al.*, 1999). More

Table 2
WTDPF Offset Measurements from Chirp Profiles in Fallen Leaf Lake

	MRE Horizon				Depth Horizon				Secondary Splay				
Profile	Footwall (sec)	Hanging wall (sec)	Offset (m)	±(m)	Footwall (sec)	Hanging wall (sec)	Offset (m)	±(m)	Footwall (sec)	Hanging wall (sec)	Offset (m)	±(m)	Total* (m)
Perp01	0.1570	0.1592	1.7	0.2	0.1661	0.1702	3.0	0.2	0.1536	0.1562	1.0	0.2	4.0
Perp02	0.1530	0.1550	0.15	0.2	?	?	?	?	?	?	?	?	
Perp04	0.1589	0.1617	2.0	0.2	0.1780	0.1827	3.5	0.2	0.1575	0.1583	0.6	0.2	4.1
Perp05	0.1577	0.1604	2.0	0.2	0.1733	0.1779	3.5	0.2	0.1574	0.1584	0.8	0.2	4.3
Perp06	0.1604	0.1631	2.0	0.2	0.1736	0.1776	3.0	0.2	?	?	?	?	
Line4	0.1579	0.1611	2.4	0.2	0.1737	0.1780	3.2	0.2	0.1581	0.1598	1.3	0.2	4.5
Line04all†	0.1589	0.1626	2.8	0.2	0.1875	0.1923	3.7	0.2	0.1585	0.1597	0.8	0.2	4.5
D3L08‡	0.1577	0.1602	1.9	0.2	0.1779	0.1820	3.1	0.2	0.1602	0.1614	0.9	0.2	3.9
Line03b	0.1568	0.1592	1.7	0.2	0.1679	0.1704	3.0	0.7	?	?	?	?	
Measurements			9				8				6		
Average			2.0				3.3				0.9		
Maximum			2.8				3.7				1.3		
Minimum			1.5				3.0				0.6		

Offset is measured at three places: the MRE horizon, a horizon at greater than 10 m depth, and the MRE horizon of the WTDPF splay. Piercing points on either side of the fault are listed as two-way travel times then converted to depth using a constant 1500 m/sec seismic velocity. All uncertainties are the vertical resolution of the CHIRP source. Offset measurements on Line03b (not shown) have higher uncertainty due to chaotic bedding near the fault.

*The sum of measurements across the depth horizon and the secondary splay.

†See Figure 5.

‡See Figure 6.

seismic data and coincident coring are required along the Rubicon and Dollar Point sections to evaluate the precise timing and slip during the MRE.

Length and displacement estimates can be used to reconstruct the rupture magnitude for the MRE. The greatest sources of uncertainty in the magnitude calculation arise from measuring the coseismic slip and the total length of rupture, especially in regions with sparse data coverage such as the two northern sections. However, several factors allow us to calculate a worst case scenario magnitude estimate in which the entire WTDPF ruptured during the MRE: (1) overlap between the MRE timing between the Fallen Leaf and Rubicon sections leads us to believe they could rupture in concert, (2) the Rubicon and Dollar Point sections combined have a linear trend and do not appear to have any major strutural discontinuities that would terminate propagation, (3) thorough-going ruptures are reported on the GF despite a 1.5 km stepover (Ramelli *et al.*, 1999), and (4) ruptures along strike-slip faults suggest the limiting stepover dimension is between 3 and 4 km (Wesnousky, 2006). A range of theoretical moment magnitudes (Hanks and Kanamori, 1979) can be calculated using the minimum slip and minimum rupture length and the maximum slip and maximum rupture length estimates. Assuming all sections rupture concomitantly, we believe the uncertainty in total fault length does not exceed 10 km (20%). However, our maximum slip measurement is along the southernmost 15 km of the fault, which may actually be a better estimate of the average slip because displacement is generally the greatest at fault midpoints (Scholz, 2002). Therefore, we assume slip measured at FLL represents an average value for the entire WTDPF and calculate a theoretical moment magnitude. Using a 4.5 m maximum offset (the combined offset across the WTDPF and secondary splay in FLL), a 55 km fault length and 15 km fault width produces an M 7.33 event. Because we do not understand the nature of the splay and we cannot rule out the possibility for multiple events between the MRE horizon and the deeper offset measurements, a minimum estimate of M 6.81 is calculated using the 2.8 m maximum offset measured across the MRE horizon and a fault length of 15 km for the Fallen Leaf section. However, based on the previous dis-

Figure 14. Photograph of the WTDPF scarp ~500 m south of Osgood Swamp (see Fig. 2 for location). Mapped scarps typically have relaxed profiles with slopes between 20° and 40°, suggesting that significant time has passed since the last surface rupture. White arrow delineates the approximate base of the scarp.

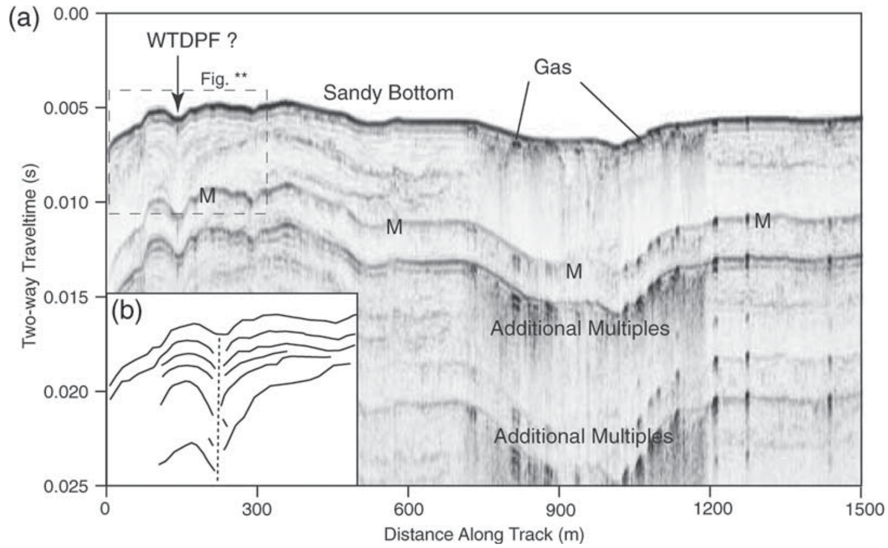

Figure 15. (a) Northwest–southeast oriented profile directly offshore Baldwin Beach (see Fig. 3 for location). Three profiles image a tightly folded syncline that is inferred to be a strand of the WTDPF. Coarse-grained sandy sediments and shallow water multiples limit penetration to ∼4 m below the lake floor. There is no penetration beneath the first multiple (M). (b) Interpreted structure within the dashed box.

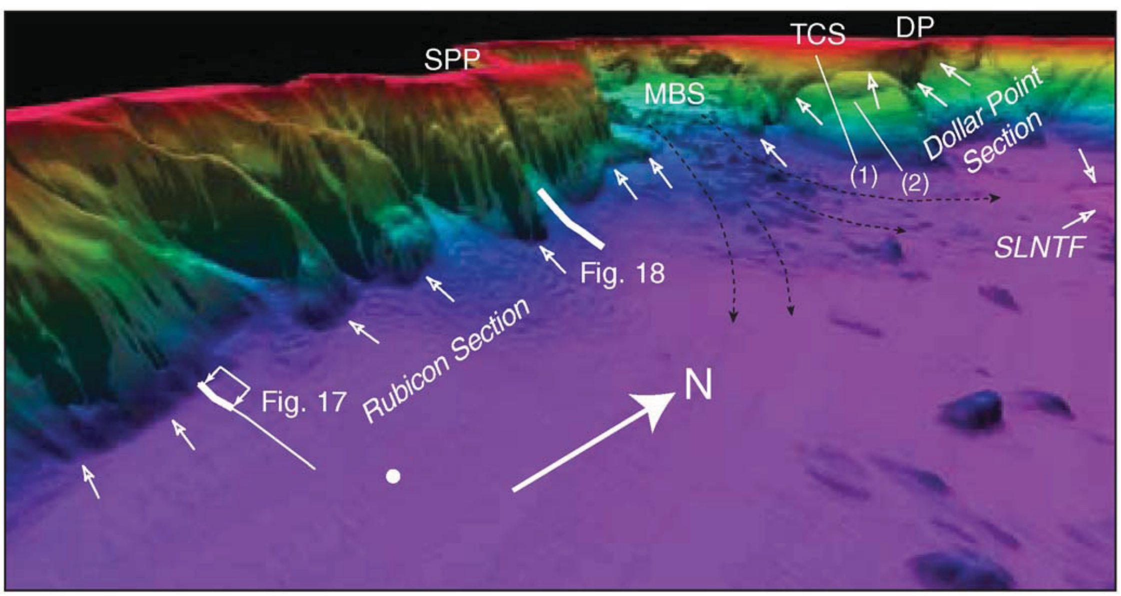

Figure 16. Three-dimensional rendering of Lake Tahoe bathymetry looking northwest along the Rubicon and Dollar Point sections of the WTDPF. Small, open arrows point to fault locations and observed lake-floor scarps; thin black arrows are the approximate transport direction of the MBS debris flow and fan systems. (1) and (2) highlight slumping head scarps and secondary deformation in the hanging wall of the WTDPF. Abbreviations: Sugar Pine Point, SPP; McKinney Bay slide, MBS; Tahoe City shelf, TCS; Dollar Point, DP; West Tahoe–Dollar Point fault, WTDPF; and Stateline–North Tahoe fault, SLNTF.

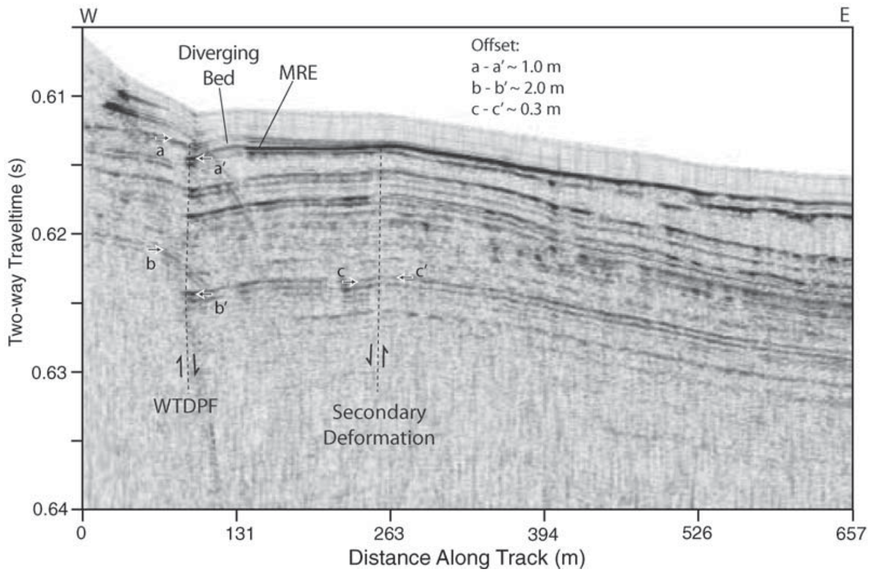

Figure 17. East–west trending profile in Lake Tahoe (see Fig. 3 for location) over the Rubicon section of the WTDPF highlighting offset lake stratigraphy. The MRE horizon is delineated by the sudden change in dip and overlying divergent wedge that thickens into the fault (similar to the deformation observed beneath FLL). Piercing points (white arrows with black interior) measure ~1 m down-to-the-east offset across the MRE horizon (aa′) and up to ~2 m on a deeper horizon (bb′). Note secondary deformation ~150 m to the east of the WTDPF, where bedding dip abruptly changes from down-to-the-west to down-to-the-east and layers are slightly folded (> 0.5 m). This may represent secondary deformation associated with either an antithetic fault or hanging-wall collapse. A piston core ~800 m to the east of this profile (Smith *et al.*, 2007) provides a rough estimate of the sedimentation rates, and an MRE age between ~3.5 and 10 k.y. B.P., which is consistent with the age determined in FLL.

cussion, our best estimate for the magnitude of the MRE employs a fault length of 55 km and an average slip of 3.7 m (the maximum measured across the primary WTDPF splay in FLL), producing an *M* 7.27 event. Using the same parameters

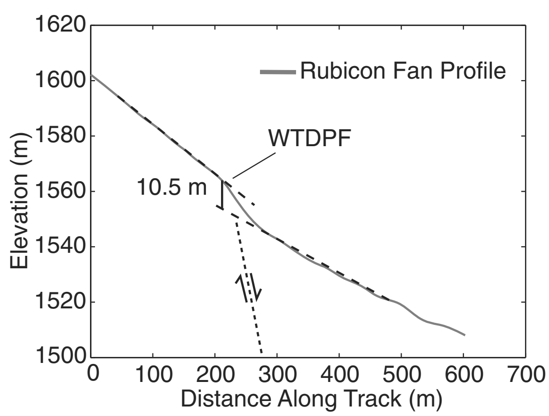

Figure 18. Topographic profile across the Rubicon Fan, offshore Sugar Pine Point (see Fig. 16 for location). A 10.5 m high scarp has formed along the WTDPF and appears to record coseismic deformation since the recession of the Tioga-aged glaciation ~14 ka. 10.5 m slip during this period results in an average slip rate between 0.7 and 0.8 mm/yr.

in an empirical magnitude estimate (Wells and Coppersmith, 1994) produces an event between *M* 6.89 and 7.35. In summary, the MRE magnitude estimates are between *M* 6.8 and 7.3, with the latter being the best estimate. This magnitude range is similar to historical large-magnitude earthquakes in the northwestern Basin and Range (Bell *et al.*, 2004; Wells and Coppersmith, 1994), as well as paleoseismic based estimates for the GF (Ramelli *et al.*, 1999).

Slip rates can be calculated in two ways, both of which involve the timing of Tioga glacial retreat. First, if lacustrine sediments in FLL were deposited after the Tioga glacier receded up the valley, we can apply the age of glacial retreat as an upper bound on the age of the tilted strata in Figure 6. We assume the dipping strata were originally deposited horizontally and then subsequently tilted toward the fault during multiple events. Tioga glaciation ceased in the eastern Sierra Nevada between 13 and 14 k.y. B.P. (Phillips *et al.*, 1996; Clark and Gillespie, 1997; Benson *et al.*, 1998), an age range also supported by climate proxies from piston cores collected in Lake Tahoe (Smith *et al.*, 2007); therefore, the 7 ± 2 m offset measured across the dipping beds produces a minimum late-Pleistocene slip rate between 0.4 and 0.7 mm/yr. The seismic velocity used to convert from travel time to depth in the measured section may be as high as 1800 m/sec, which would increase the offset to ~10.5 m (upper bound) and the slip rate to ~0.8 mm/yr over the last 13 k.y. In the

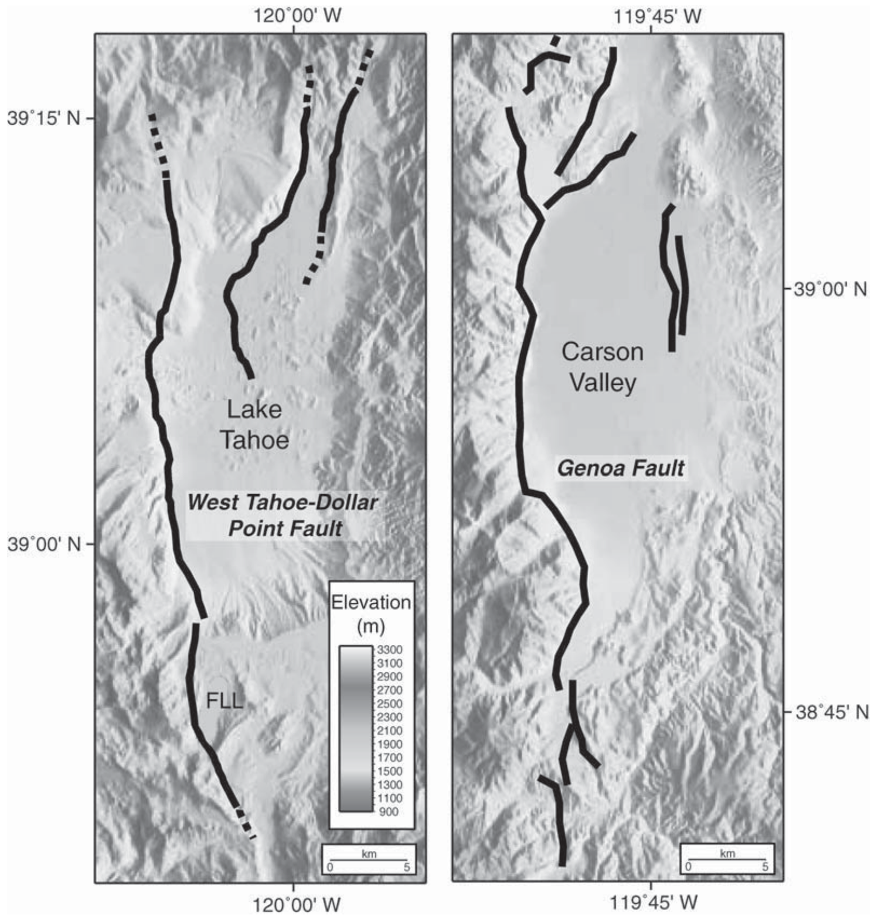

Figure 19. Comparison of the West Tahoe fault and the GF; both faults exhibit similar range front morphology, strike, and length. Together, these faults appear to be accommodating most of the extension (2–3 mm/yr) occurring within the northern Walker Lane at the latitude of Lake Tahoe.

second method, the offset fan surface offshore Sugar Pine Point (Figs. 16 and 18) is presumed to be inactive since the Tioga glacial retreat (Dingler, 2007). The 10.5 m offset (Fig. 18) since 13 k.y. B.P. also produces a maximum vertical slip rate of ~0.8 mm/yr. Overall, these data give rise to a vertical displacement rate between 0.4 and 0.8 mm/yr since the end of Tioga glaciation, which is slightly higher than the 0.5 mm/yr minimum slip-rate estimate (over the last ~20 ka) reported by Kent *et al.* (2005). An extension rate can be estimated from vertical slip rate assuming simple fault geometry. For a 60° dipping normal fault, the vertical deformation rate is transformed into an extension rate between 0.3 and 0.5 mm/yr. The slip rate along the WTDPF may be higher than estimated because the MRE occurred at 4.1–4.5 k.y. B.P. and, presumably, additional strain has accumulated during the quiescent interval. With a slip rate between 0.4 and 0.8 mm/yr, it is possible that ~3 m of elastic strain has accumulated across the WTDPF. Coseismic slip of 3 m on the WTDPF could generate an $M \geq 7$ event. The GF (Fig. 19) has a vertical deformation rate of 2–3 mm/yr over the last 2 k.y. (Ramelli *et al.*, 1999), which can be converted to a 1.2–1.7 mm/yr extension rate (also assuming 60° dip). The combined extension rates of the GF and the WTDPF are consistent with the 2–3 mm/yr GPS derived extension rates across the Sierra Nevada frontal fault zone (Hammond and Thatcher, 2004, 2007).

Earthquake triggering associated with normal fault earthquakes and resulting static stress changes have been used to explain normal fault event sequences (Nostro *et al.*, 1997); therefore, it is important to compare paleoearthquake records between neighboring faults. Events on the IVF and GF at ~500 yr B.P. (Ramelli *et al.*, 1999; Dingler, 2007) suggest a possible relationship in the rupture timing, but the age uncertainty is large and coincident timing could also be related to dynamic and viscoelastic stress changes. We do not observe any evidence for an event 500 yr B.P. along the Fallen Leaf or Rubicon sections of WTDPF. Although the MRE timing along the SLNTF has not been determined, the proximity (~3 km) of the SLNTF to WTDPF suggests either of these faults may adversely affect stress conditions on the other following a large rupture.

Conclusions

Based on fault length and cosesimic slip determined for the MRE, the WTDPF has the potential to generate $M \geq 7.0$ ruptures. The vertical slip rate determined in this study (0.4–0.8 mm/yr) suggests that the WTDPF is amongst the most active normal faults in the western Basin and Range and the northern WLB. With the westward encroachment of extensional faulting since the middle Miocene (Surpless *et al.*, 2002), the faults in the LTB, may eventually take on higher (2–3 mm/yr) slip rates comparable to that of the GF (Ramelli *et al.*, 1999). Although the northern sections require additional studies, and only one paleoearthquake has been precisely identified on the WTDPF, the new constraints on timing and slip across the WTDPF are important for hazard assessment in the LTB as well as Carson City and Reno, Nevada. Beyond the loss of life and damage associated with ground shaking in large earthquakes, Ichinose *et al.* (2000) predict ~10 m high seiche waves in Lake Tahoe can be generated by 2.83 m (average) of coseismic slip on the WTDPF. If the WTDPF were to produce an $M \geq 7.0$ rupture, the resulting seiche waves would present a significant hazard to lakefront areas.

Data and Resources

The authors collected all seismic CHIRP data and piston cores used in this study. To request data, contact author Daniel Brothers.

Acknowledgments

We would like to acknowledge Captain Brant Allen of the Tahoe Environmental Research Center, John Kleppe, John Rich of the Fallen Leaf Marina, Jenna Hill, Leah Hogarth, and Elizabeth Johnstone for their assistance with fieldwork in Fallen Leaf Lake and Lake Tahoe. We would also like to thank Rich Koehler of the University of Nevada, Reno, for thorough and helpful reviews. This project was funded through U.S. Geological Survey National Hazards Reduction Program (USGS NEHRP) Grant Number 06HQGR0064.

References

Argus, D. F., and R. G. Gordon (2001). Present tectonic motion across the Coast Ranges and San Andreas fault system in central California, *Geol. Soc. Am. Bull.* **113,** 1580–1592.

Bacon, C. R. (1983). Eruptive history of Mount Mazama and Crater Lake Caldera, Cascade Range, USA, *J. Volcanol. Geotherm. Res.* **18,** 57–115.

Bell, J. W., S. J. Caskey, A. R. Ramelli, and L. Guerrieri (2004). Pattern and rates of faulting in the central Nevada seismic belt, and paleoseismic evidence for prior beltlike behavior, *Bull. Seismol. Soc. Am.* **94,** 1229–1254.

Bennett, R. A., B. P. Wernicke, N. A. Niemi, A. M. Friedrich, and J. L. Davis (2003). Contemporary strain rates in the northern Basin and Range province from GPS data, *Tectonics* **22,** no. 2, 1008, doi 10.1029/2001TC001355.

Benson, L. V., H. M. May, R. C. Antweiler, T. I. Brinton, M. Kashgarian, J. P. Smoot, and S. P. Lund (1998). Continuous lake-sediment records of glaciation in the Sierra Nevada between 52,600 and 12,500 C-14 yr BP, *Quat. Res.* **50,** 113–127.

Birkeland, P. W. (1963). Pleistocene volcanism and deformation of the Truckee area, north of Lake Tahoe, California, *Geol. Soc. Am. Bull.* **74,** 1453–1463.

Bischoff, J. L., and K. Cummins (2001). Wisconsin glaciation of the Sierra Nevada (79,000–15,000 yr BP) as recorded by rock flour in sediments of Owens Lake, California, *Quat. Res.* **55,** 14–24.

Briggs, R. W., and S. G. Wesnousky (2004). Late Pleistocene fault slip rate, earthquake recurrence, and recency of slip along the Pyramid Lake fault zone, northern Walker Lane, United States, *J.Geophys. Res.-Solid Earth* **109,**. B8402, doi 10.1029/2003JB002717

Briggs, R. W., and S. G. Wesnousky (2005). Late Pleistocene and Holocene paleoearthquake activity of the Olinghouse fault zone, Nevada, *Bull. Seismol. Soc. Am.* **95,** 1301–1313.

Clark, D. H., and A. R. Gillespie (1997). Timing and significance of late-glacial and Holocene cirque glaciation in the Sierra Nevada, California, *Quat. Int.*, **38–9,** 21–38.

Crone, A. J., M. N. Machette, M. G. Bonilla, J. J. Lienkaemper, K. L. Pierce, W. E. Scott, and R. C. Bucknam (1987). Surface faulting accompanying the Borah Peak earthquake and segmentation of the Lost River fault, Central Idaho, *Bull. Seismol. Soc. Am.* **77,** 739–770.

Dingler, J. A. (2007). New geophysical approaches to study neotectonics and associated geohazards, *Ph.D. Thesis*, University of California at San Diego.

Dixon, T. H., M. Miller, F. Farina, H. Z. Wang, and D. Johnson (2000). Present-day motion of the Sierra Nevada block and some tectonic implications for the Basin and Range province, North American Cordillera, *Tectonics* **19,** 1–24.

Driscoll, N. W., and E. P. Laine (1996). Abyssal current influence on the southwest Bermuda Rise and surrounding region, *Mar. Geol.* **130,** 231–263.

Faugeres, J. C., D. A. V. Stow, P. Imbert, and A. Viana (1999). Seismic features diagnostic of contourite drifts, *Mar. Geol.* **162,** 1–38.

Faulds, J. E., C. D. Henry, and N. H. Hinz (2005). Kinematics of the northern Walker Lane: an incipient transform fault along the Pacific–North American plate boundary, *Geology* **33,** 505–508.

Gardner, J. V., L. A. Mayer, and J. E. H. Clarke (2000). Morphology and processes in Lake Tahoe (California–Nevada), *Geol. Soc. Am. Bull.* **112,** 736–746.

Gawthorpe, R. L., I. Sharp, J. R. Underhill, and S. Gupta (1997). Linked sequence stratigraphic and structural evolution of propagating normal faults, *Geology* **25,** 795–798.

Gilli, A., F. S. Anselmetti, D. Ariztegui, M. Beres, J. A. McKenzie, and V. Markgraf (2005). Seismic stratigraphy, buried beach ridges and contourite drifts: the Late Quaternary history of the closed Lago Cardiel basin, Argentina (49 degrees S), *Sedimentology* **52,** 1–23.

Hammond, W. C., and W. Thatcher (2004). Contemporary tectonic deformation of the Basin and Range province, western United States: 10 years of observation with the Global Positioning System, *J. Geophys. Res.-Solid Earth* **109,** B08403, doi 10.1029/2003JB002746.

Hammond, W. C., and W. Thatcher, (2007). Crustal deformation across the Sierra Nevada, northern Walker Lane, Basin and Range transition, western United States measured with GPS, 2000–2004, *J. Geophys. Res.-Solid Earth*, **112,** B05411, doi 10.1029/2006JB004625.

Hanks, T. C., and H. Kanamori (1979). Moment magnitude scale, *J. Geophys. Res.* **84,** 2348–2350.

Hardy, S., and K. McClay (1999). Kinematic modelling of extensional fault-propagation folding, *J. Struct. Geol.* **21,** 695–702.

Hearn, E. H., and E. D. Humphreys (1998). Kinematics of the southern Walker Lane belt and motion of the Sierra Nevada block, California, *J. Geophys. Res.-Solid Earth* **103,** 27033–27049.

Henry, C. D., and M. E. Perkins (2001). Sierra Nevada-Basin and Range transition near Reno, Nevada: two-stage development at 12 and 3 Ma, *Geology* **29,** 719–722.

Hyne, N. J., P. Chelmins, D. S. Gorsline, C. R. Goldman, and J. E. Court (1972). Quaternary history of Lake Tahoe, California–Nevada, *Geol. Soc. Am. Bull.* **83,** no. 5, 1435–1448.

Ichinose, G., J. Anderson, K. Satake, R. Schweickert, and M. Lahren (2000). The potential hazard from tsunami and seiche waves generated by large earthquakes within Lake Tahoe, California–Nevada, *Geophys. Res. Lett.* **27,** no. 8, 1203–1206.

Ichinose, G. A., J. G. Anderson, K. D. Smith, D. dePolo, R. Anooshehpoor, R. A. Schweickert, and M. L. Lahren (1999). The seismotectonics of the 30 October 1998 Incline Village, Nevada earthquakes from regional moment tensor inversion, *Bull. Seismol. Soc. Am.* **70,** 297–305.

Ichinose, G. A., J. G. Anderson, K. D. Smith, and Y. H. Zeng (2003). Source parameters of eastern California and western Nevada earthquakes from regional moment tensor inversion, *Bull. Seismol. Soc. Am.* **93,** 61–84.

Kent, G. M., J. M. Babcock, N. W. Driscoll, A. J. Harding, J. A. Dingler, G. G. Seitz, J. V. Gardner, L. A. Mayer, C. R. Goldman, A. C. Heyvaert, R. C. Richards, R. Karlin, C. W. Morgan, P. T. Gayes, and L. A. Owen (2005). 60 k.y. record of extension across the western boundary of the Basin and Range province: estimate of slip rates from offset shoreline terraces and a catastrophic slide beneath Lake Tahoe, *Geology* **33,** 365–368.

Lindstrom, S. G. (1990). Submerged tree stumps as indicators of mid-Holocene aridity in the Lake Tahoe region, *J. Calif. Gt. Basin Anthropol.* **12,** 146–157.

McGinnis, J. P., D. E. Hayes, and N. W. Driscoll (1997). Sedimentary processes across the continental rise of the southern Antarctic Peninsula, *Mar. Geol.* **141,** 91–109.

Nostro, C., M. Cocco, and M. E. Belardinelli (1997). Static stress changes in extensional regimes: an application to southern Apennines (Italy), *Bull. Seismol. Soc. Am.* **87,** 234–248.

Oldow, J. S. (2003). Active transtensional boundary zone between the western Great Basin and Sierra Nevada block, western US cordillera, *Geology* **31,** 1033–1036.

Phillips, F. M., M. G. Zreda, L. V. Benson, M. A. Plummer, D. Elmore, and P. Sharma (1996). Chronology for fluctuations in late Pleistocene Sierra Nevada glaciers and lakes, *Science* **274,** 749–751.

Ramelli, A. R., J. W. Bell, C. M. dePolo, and J. C. Yount (1999). Large-magnitude, late Holocene earthquakes on the Genoa fault, west-central Nevada and eastern California, *Bull. Seismol. Soc. Am.* **89,** 1458–1472.

Ramsey, C. B. (1995). Radiocarbon calibration and analysis of stratigraphy: the OxCal program, *Radiocarbon* **37,** 425–430.

Ramsey, C. B. (2001). Development of the radiocarbon calibration program, *Radiocarbon* **43,** no. 2A, 355–363.

Reimer, P. J., M. G. L. Baillie, E. Bard, A. Bayliss, J. W. Beck, C. J. H. Bertrand, P. G. Blackwell, C. E. Buck, G. S. Burr, K. B. Cutler, P. E. Damon, R. L. Edwards, R. G. Fairbanks, M. Friedrich, T. P. Guilderson, A. G. Hogg, K. A. Hughen, B. Kromer, G. McCormac, S. Manning, C. B. Ramsey, R. W. Reimer, S. Remmele, J. R. Southon, M. Stuiver, S. Talamo, F. W. Taylor, J. van der Plicht, and C. E. Weyhenmeyer (2004). IntCal04 terrestrial radiocarbon age calibration, 0–26 cal kyr BP, *Radiocarbon* **46,** 1029–1058.

Sarna-Wojkicki, A. M., K. R. Lajoie, C. E. Meyer, D. P. Adam, and H. J. Rieck (1991). Tephrochronologic correlation of upper Neogene sediments along the Pacific margin, conterminous United States, in *Quaternary Non-Glacial Geology: Conterminous United States*, in The Decade of North American Geology, R. B. Morrison (Editor), Geological Society of America, Boulder, Colorado, Vol. **K–2**, 117–140.

Saucedo, G. J., J. D. Little, S. E. Watkins, J. R. Davis, M. T. Mascorro, V. D. Walker, and E. W. Ford (2005). Geologic map of the Lake Tahoe Basin, California and Nevada, California Geological Survey, scale 1:100,000.

Scholz, C. H. (2002). The mechanics of earthquakes and faulting, Second Ed., Cambridge U. Press, Cambridge, UK, 439 pp..

Schweickert, R. A., M. M. Lahren, K. D. Smith, and R. Karlin (1999). Preliminary fault map of the Lake Tahoe Basin, California and Nevada, *Seism. Res. Lett.* **70,** 306–312.

Smith, K. D., D. von Seggern, G. Blewitt, L. Preston, J. G. Anderson, B. P. Wernicke, and J. L. Davis (2004). Evidence for deep magma injection beneath Lake Tahoe, Nevada–California, *Science* **305,** 1277–1280.

Smith, S. B., R. Karlin, G. G. Seitz, and G. M. Kent (2007). Clastic sedimentation in Lake Tahoe as a record for submarine landsliding and seismic shaking (Abstract OS33A-1000), *Eos. Trans. AGU* **88,** OS33A-1000.

Stewart, J. H. (1988). Tectonics of the Walker Lane belt, western Great Basin–Mesozoic and Cenozoic deformation in a zone of shear, in *Metamorphism and Crustal Evolution of the Western United States*, W. G. Ernst (Editor), Vol. **VII,** Prentice-Hall, Englewood Cliffs, New Jersey, 683–713.

Stuiver, M., and H. A. Polach (1977). Reporting of C^{14} data, *Radiocarbon* **19,** no. 3, 355–363.

Surpless, B. E., D. F. Stockli, T. A. Dumitru, and E. L. Miller. (2002). Two-phase westward encroachment of Basin and Range extension into the northern Sierra Nevada, *Tectonics* **21,** no. 1, doi 10.1029/2000TC001257.

Svarc, J. L., J. C. Savage, W. H. Prescott, and A. R. Ramelli (2002). Strain accumulation and rotation in western Nevada, 1993–2000, *J. Geophys. Res.-Solid Earth* **107,** no. B5, doi 10.1029/2001JB000579.

Unruh, J., J. Humphrey, and A. Barron (2003). Transtensional model for the Sierra Nevada frontal fault system, eastern California, *Geology* **31,** 327–330.

Wells, D. L., and K. J. Coppersmith (1994). New empirical relationships among magnitude, rupture length, rupture width, rupture area, and surface displacement, *Bull. Seismol. Soc. Am.* **84,** 974–1002.

Wesnousky, S. G. (2006). Predicting the endpoints of earthquake ruptures, *Nature* **444,** 358–360.

Witkind, I. J., W. B. Myers, J. B. Hadley, W. Hamilton, and G. D. Fraser (1962). Geologic features of the earthquake at Hebgen Lake, Montana, August 17, 1959, *Bull. Seismol. Soc. Am.* **52,** 163–180.

Scripps Institution of Oceanography
University of California, San Diego
9500 Gilman Drive
La Jolla, California 92093-0225
dbrother@ucsd.edu
(D.S.B., G.M.K., N.W.D., J.A.D., A.J.H., J.M.B.)

Department of Geological Sciences/172
University of Nevada, Reno
1664 N. Virginia St.
Reno, Nevada 89557-0138
(S.B.S., R.K.)

Department of Geological Sciences
San Diego State University
5500 Campanile Drive
San Diego, California 92182
(G.G.S.)

Manuscript received 4 January 2008

3

Evidence for Prolonged Medieval Drought in the Lake Tahoe Basin

3.1 ABSTRACT

Evidence for severe and prolonged drought during Medieval times has been observed throughout western North America (Herweijer et al., 2006; Stine, 1994). Here we present evidence for a prolonged and severe drought in the Lake Tahoe Basin (LTB) between 950 – 1250 AD. Submerged trees rooted in situ beneath Fallen Leaf Lake (FLL) have been mapped and sampled using sidescan sonar, manned submersible and ROV dives (Kleppe, 2005). Several trees were radiocarbon dated to ~1250 AD and are positioned upslope of a ~60 m deep submerged paleoshoreline. Older upright and rooted trees (~200 AD, and ~ 1500 BC) may suggest shoreline regression occurred several times during the Holocene. Water-balance calculations based on historical data demonstrate ground water exchange between FLL and Lake Tahoe, which makes FLL very sensitive to changes in precipitation and provides a mechanism to explain prolonged shoreline regression. We have developed a consistent hydrologic model that suggests precipitation was <60% of normal between 950-1250 AD. Assuming long-term (century-scale) hydroclimatic conditions in the FLL watershed are modulated by regional climate patterns, our observations constrain the longevity and magnitude of past drought in the Sierra Nevada Range, a major water resource for California and northwestern Nevada.

3.2 INTRODUCTION

Severe droughts in the western U.S. during the last 200 years are relatively minor when compared to a series of megadroughts that struck between about 900 AD and 1400 AD (Cook et al., 2007; Cook et al., 2004; Herweijer et al., 2007). Evidence for these medieval droughts is recorded at many sites in and adjacent to the central Sierra (Stine, 1994) (e.g., Mono Lake, Tenaya Lake, the West Walker River, and Osgood Swamp), Lake Tahoe (Lindstrom, 1990) and Pyramid Lake (Benson et al., 2002). Ancient tree stumps preserved in river channels and in lakes, radiocarbon dated to the medieval period

(Stine, 1994), suggest they grew during dry periods and were subsequently inundated as climate became wetter. Other studies have documented increased forest fires during the same period (Swetnam, 1993), changes in the regional biota (Mensing et al., 2004) and potential influence on human habitation (Jones and Schwitalla, 2008). Nevertheless, well-preserved records for medieval drought in the Sierra Nevada and their affects on watershed dynamics are sparse. The two most severe and persistent dry periods in the Sierra's instrumented records occurred between 1928 and 1934 (the Dust Bowl period), and 1987-1992, where runoff averaged ~ 70% of "normal". Based on several lines of evidence, the medieval droughts appear to be more severe and of greater duration than any drought period in modern times. Studying prehistoric drought in the Sierras allows us to account for the potential range in magnitude and variability of precipitation.

FLL is a small, but deep (>120 m) lake located 2.2 km south of Lake Tahoe at an elevation of 1945 m (Figure 1). It has a surface area of 5.7 km^2 and drains into Lake Tahoe through Taylor Creek. The lake fills a narrow glacial valley bounded on both the east and west sides by >300 m high-lateral moraines and separated from Lake Tahoe by a series of Tioga-aged recessional and end moraines (Brothers et al., 2009; Saucedo et al., 2005) (Figure 1). Lacustrine sediment has accumulated in the deeper portions of the lake with the steep margins being composed of rocky glacial till. The greatest depths occur adjacent to the West Tahoe-Dollar Point Fault in the southern lake (Brothers et al., 2009). FLL's watershed (including the lake area) is ~43.25 km^2, mostly located in the Desolation Wilderness and enters FLL via Glen Alpine Creek. Most of the basin has been sculpted by Pleistocene alpine glaciations (Birkeland, 1964; McCaughey, 2005) with only ~30% being forested where the remaining portion containing thin soils, granodiorite bedrock and talus slopes. Besides a few small lakes (Figure 1) the rocky nature of the watershed does not provide for much water storage (Hanes, 1981), which leads to Glen Alpine Creek running dry at the end of summer, leaving FLL without a year-round base flow. A small dam controls the outlet of FLL into Taylor Creek and raises the water level ~1.5 meters above its natural sill. Mean annual precipitation is approximately 0.4 m near the dam and may exceed 1.5 m at the top of the basin. Approximately 80% of this precipitation falls as snow in the headwaters of the watershed, where mean (WY 1969-1992) April snowpack water content at Lake Lucille is ~1.5 m (Figure 1).

3.3 GEOMORPHIC AND HYDROCLIMATIC DATA

Our methods offer an effective way to locate, sample and analyze paleoclimate indicators in alpine lakes. To characterize the lakefloor morphology and locate submerged trees, a comprehenive side-scan sonar survey was conducted over FLL. Side-scan data were acquired using an Edgetech 4200 system with GPS navigation to ensure overlapping bottom coverage. The dual frequency (100 and 400 kHz) system provides very high resolution in shallow areas, but also the ability to image the deeper parts of the lake. Individual sonar swaths were processed and digitally merged using xsonar (Danforth, 1997) to produce a seamless, geo-referenced mosaic. The corrected data were mosaiced at 0.2 m resolution and the final images were exported as GeoTIFF files that could be viewed in Google Earth (e.g., Figure 2).

A bathymetric model of the lake bottom was constructed using depths measured from 2-D sub-bottom sonar surveys (Brothers et al., 2009) and overlain with side-scan mosaics to map the distribution of glacial and lacustrine deposits. The sidescan sonar mosaic clearly identifies glacial deposits as high backscatter and the fine-grained lacustrine sediments as low backscatter. Numerous submerged paleoshoreline features can be correlated throughout the lake. Upright trees appear to be acoustic absorbers producing shadows rather than high-amplitude returns. They are invisible to a standard fish finder operating at 50 kHz, offering an explanation for why these ancient, upright, rooted trees were not discovered earlier. At least 80 trees, including the still upright trees, were systematically identified and recorded on the sonar mosaic. Trees were then targeted with the ROV (Video-Ray) and submersible dives. ROV grabs and SCUBA divers collected samples, which were radiocarbon dated at the Lawrence Livermore Center for Accelerator Mass Spectrometry.

A large, downed tree was radiocarbon dated to 1088 ± 64 years and recovered from the lake floor and analyzed at the UNR dendrochronology laboratory (Kleppe, 2005). The recovered tree contained 220 rings. Wood samples from other of the submerged trees were retrieved by SCUBA divers and brought to the Dendrochronology Laboratory (DL) at the University of Nevada, Reno for analysis. In order to date the underwater samples, the DL developed a western juniper (Juniperus occidentalis) tree-ring chronology that spans the period from AD 543 to 2003. Additional tree-ring chronologies were available either from their own studies or from public databases. By means of visual and numerical cross dating, the DL was able to date one of the two underwater samples, i.e., a cross section of a branch cut from one of the submerged ancient upright and rooted trees. Anatomical features of this specimen were consistent with pine species, and a clearly visible continuous sequence of 69 rings was cross-dated with the juniper-derived chronology for the period AD 1085-1153. This initial result shows that it is feasible to obtain tree mortality dates and continuous tree-ring time series from submerged trees in the Sierra Nevada.

A mass water balance for water year (WY) for the FLL Basin can be written in the form:

(1): $\Delta S(y) = P(y) - E_T(y) - R_T(y) - GW(y) - E(y)$

where $\Delta S(y)$ = change in stage, or lake level (m/yr)

$P(y)$ = annual mean precipitation over FLL basin (FLL plus watershed; m/yr)

$E_T(y)$ = evapotranspiration (m/yr)

$R_T(y)$ = flow down Taylor Creek (m/yr)

$GW(y)$ = net ground water flow out (m/yr)

$E(y)$ = evaporation from the lake surface (m/yr)

The above parameters are all referenced to the surface area of FLL and hence the units are shown as flow/surface area/yr ($m^3/m^2/yr = m/yr$). The areas of FLL and its watershed are 5.7 km^2 and 43.2 km^2, respectively. The normalized precipitation $Pi(y)$ for FLL and $PBi(y)$ for the Lake Tahoe Basin is simply the precipitation for each WY divided by the mean annual precipitation between 1969-1992. For example, in Figure 3, the following is used to normalize annual precipitation

[(mean precipitation for the FLL Basin) X (watershed area) / (surface area of FLL)]

where "normal precipitation" is equal to 1.0, which also represents a precipitation value of 10.00 m/yr over the surface area of FLL. In comparison, Trask used the regression equation $R_T(y) = R_T'(y) = 10.19x - 3.46,$ where x is normalized precipitation and y is yield normalized yield for Taylor Creek, to show that for normal precipitation the flow down Taylor Creek equals 6.73 m/yr over the surface area of FLL. The difference of 2.41 m/yr between $R_T(y)$ and the yield $FLY(y)$ is due to the groundwater seepage from FLL.
One can use the terms of equation (1) to write an expression for FLL Basin yield:

(2): $FLL(y) = P(y) - E_T(y) - GW(y) - E(y)$

Trask and Fogg (2007) assumed that $GW(y) = 0$ in the FLL Basin, which makes the yield equal to the Taylor Creek outflow, $R_T(y)$ (Blue line in Figure 3). However, we have shown that *GW(y)* is on the order of $1.5x10^7$ m^3/year; therefore the yield of the FLL Basin is given by :

(3): $FLL(y) = R_T(y) - GW(y) = 10.19x - 5.87$

which simply shifts the blue line downward by a correction value of 2.41 (0.66 of this represents the portion of ground water seepage that is included in the stream flow gage reading, $R_T(y)$, since the gage is located below FLL).

3.4 RESULTS

Between 2007 and 2009, we completed sidescan sonar surveys, remotely operated vehicle (ROV) dives (Kleppe, 2005) and missions aboard the Undersea Voyager Project's manned submersible to map the lake floor and locate ancient trees in FLL. We have identified more than 80 upright and downed trees. Several large, upright trees remain rooted at depths between 10-36 m below the existing lake surface and have been radiocarbon dated between ~1500 BC and ~1250 AD (Table 1), with most clustering between ~1100-1300 AD. Some measure over 30 m tall and have a circumference of over 4.5 m. Detailed inspections of the root structures reveal the upright trees are in situ (Figure 2b). In fact, the root structure of the ancient trees appears almost identical to submerged modern tree stumps. Sidescan and sub-bottom seismic data (Brothers et al., 2009) reveal submerged paleoshoreline morphology throughout the lake margins with no stratigraphic or geomorphic evidence for large slumps, slides or faults that may have transported the trees downslope. The deepest shoreline features are imaged at a depth of ~60 m, or 1882 m in elevation. Interestingly, a medieval (1240 ± 40 A.D.; Benson et al., 2002) tree stump near Rubicon Point, Lake Tahoe is rooted at 1892 m, suggesting Lake Tahoe was also lower at this time. Seismic reflection imagery and bathymetric data in Lake Tahoe show no stratigraphic or geomorphic evidence that Lake Tahoe has dropped more than 10-15 m during the last several thousand years (Dingler et al., 2009). Assuming the Rubicon tree grew a few meters above Lake Tahoe's shoreline, the medieval shorelines in FLL and Lake Tahoe were nearly equivalent.

Prior to this study, FLL has been considered to be hydraulically stable (Hanes, 1981) and relatively insensitive to climatic variability (Trask and Fogg, 2007). Here we show that groundwater flow from FLL to Lake Tahoe provides a mechanism for rapid shoreline fluctuation during drought years. The recessional and end moraines north of FLL have been incised by Taylor Creek, exposing moderately-to-poorly sorted sand, gravel and cobbles with occasional well-stratified silty layers (McCaughey, 2005) that may act as localized aquitards. A broad wetlands area located near Lake Tahoe and the mouth of Taylor Creek suggests year-round ground water seepage occurs through the end moraines. To better quantify the size of this flow, two comparative analyses were conducted. In the first, we performed a water balance calculation by combining measurements of Taylor Creek flow, changes in FLL stage (Hanes, 1981), evaporation off the lake surface and snow water content/precipitation records in the FLL watershed. We find a deficit between FLL inflow and Taylor Creek flow of approximately $1.5x10^7$ m^3/year. In the second, using measurements from 26 South Tahoe Public Utility District (STUPD) wells in the area (data courtesy of Ivo Bergsohn, STUPD) an average hydraulic conductivity was calculated at ~10 m/day, which is slightly higher than typically seen in glacial till (Freeze and Cherry, 1972). The conductivity multiplied by the cross sectional area of the flow (constrained by subsurface gravity modeling; Pearson, 1999) and the hydraulic gradient provides an estimate for the year round flow through the end moraine at $1.4x10^7$ m^3/yr. Therefore, the net ground water seepage from FLL through the end moraine and into Lake Tahoe is consistently ~$1.5x10^7$ m^3/year.

Trask and Fogg (Trask and Fogg, 2007) developed a regression model to look at the relationship between precipitation and streamflow in the Lake Tahoe and FLL watersheds, but they assumed that the net ground water outflow from both Lake Tahoe and FLL was zero. Adding the effect of groundwater seepage to the regression (Figure 3) translates the linear trend downward. It can be seen that the FLL yield will become negative when the precipitation falls below ~ 60% of normal (mean precipitation over water years 1969-1992), thus resulting in a drop in lake level. Normal levels of precipitation allow FLL to maintain its hydraulic head over Lake Tahoe while supplying flow through its end moraine and down Taylor Creek.

A simple comparison between the ratio of watershed area to lake area for Lake Tahoe (~1.6) and FLL (~7.6) might suggest that the FLL watershed has a significant advantage over the watershed of lake Tahoe especially during drought years (Trask and Fogg, 2007). The efficiency, or yield as a percentage of snowmelt input, for FLL is lowered dramatically due to the ground water seepage, making the FLL watershed less efficient than Lake Tahoe. In fact, greater than 140% of normal precipitation is required for the FLL watershed to become more efficient than Lake Tahoe. During periods of prolonged drought, FLL will drop faster than Lake Tahoe, making it more climate sensitive. This may explain the absence of unequivocal evidence for prolonged drought in Lake Tahoe, whereas the smaller, moraine bounded lakes higher in the watershed may be better recorders of prehistoric climate variability.

3.5 DISCUSSION

We offer a hydroclimatic scenario that accounts for prolonged changes FLL's shoreline and the growth and preservation of medieval trees. As with Mono Lake and Lake Tenaya (Stine, 1994), low runoff during medieval times provides the most plausible explanation for the drowned trees. At ~900 AD precipitation fell to less than 60% of normal and FLL began to drop relatively quickly, needing only a few decades to reach the same elevation as Lake Tahoe before being stabilized by groundwater exchange between the two lakes. After ~950 A.D. the two lakes remained at approximately the same elevation for several centuries, allowing trees to grow above their lowered shorelines. When drought conditions waned and precipitation increased, FLL rose 10’s of meters relatively quickly and drowned the trees. The same phenomenon occurred in Lake Tahoe, but the shoreline drop was less significant (10-15 m). Furthermore, several older, upright and rooted trees have also been discovered above the paleoshoreline in FLL. Two of these trees were radiocarbon dated at ~200 A.D. (Table 1) and one was dated at ~1545 B.C. This suggests that drought conditions in the FLL watershed may be recurring, and cyclic in nature. However a systematic sampling of all submerged trees is needed to extend the late-Holocene paleoclimate record and to determine the timing and duration of potential pre-medieval drought cycles.

If the older, upright trees record pre-medieval drought, how could they remain standing despite exposure during subsequent shoreline regressions? It appears that a process of permineralization occurs while the trees are submerged for many centuries. A 1.3 cm x 45.7 cm core sample of the tree recovered from FLL was examined using a scanning electron microscope. The pores of the wood appear to have accumulated calcium carbonate that is dissolved in the lake waters. To test the wood’s resistance to decay, several sections of ancient wood were placed in the open forest surrounding FLL. After three years of exposure, there is no evidence of decay and the wood remains untouched by insects, where modern dead trees nearby show significant signs of rot and insect attack. It appears the assimilation of the calcium carbonate makes the trees more resistant to rot and discourages insect consumption.

3.6 CONCLUSION

Our observations provide important constraints on short- and long-term variations of water availability in the high Sierra. By combining hydrogeology with radiocarbon dating of ancient trees, we provide an independent estimate of precipitation during medieval megadrought that can be compared to tree-ring proxies at other locations (Herweijer et al., 2007; Stahle et al., 2007; Stine, 1994). As the primary source of water to the Reno area, a multicentennial drought today would devastate the economies of communities dependent on Sierran runoff, particularly California and northern Nevada. Furthermore, as additional wood samples are collected, dated, and entered into the tree-ring chronology there is potential to construct a continuous, annually resolved record that could span several millennia. In central Europe, for example, a myriad of wood samples have provided tree-ring chronologies spanning the last 12,460 years (Helama et al., 2009). Alpine lakes similar to FLL bounded by glacial till may provide hydraulically sensitive environments ideal for studying Holocene climate variability. Future sampling in FLL and potential discoveries in other Sierran lakes may provide the data needed to extend tree ring records over the entire Holocene. In so doing, it may become possible to determine the recurrence of multi-centennial drought and begin to truly understand how such events develop and persist.

3.7 ACKNOWLEDGEMENTS

Funding for this work was provided by US Geological Survey/Desert Research Institute under Project ID# 2003NV39B, the Geological Society of America graduate research grant; student support was provided by the IRIS undergraduate internship program. We would like to thank Glenn and Grant Adams, Bill Craven, and John Rich for their generous help with data acquisition. We would also like to thank John Knezovich of Lawrence Livermore National Lab for assistance with the radiocarbon analysis, James Trask for the several discussions regarding the FLL water budget, and finally Scott Cassell and the crew of the Underwater Voyager Project for providing access to their

submersible.

3.8 REFERENCES

Benson, L., Kashgarian, M., Rye, R., Lund, S., Paillet, F., Smoot, J., Kester, C., Mensing, S., Meko, D., and Lindstrom, S., 2002, Holocene multidecadal and multicentennial droughts affecting Northern California and Nevada: Quaternary Science Reviews, v. 21, p. 659-682.

Biondi, F., Kleppe, J.A., Brothers, D.S., and Kent, G.M., 2006, Underwater dendrochronology of the Sierra Nevada: Testing the Medieval Mega-Drought hypothesis: Eos Trans. AGU, v. 87.

Birkeland, P.W., 1964, Pleistocene Glaciation of the Northern Sierra Nevada, North of Lake Tahoe, California: Journal of Geology, v. 72, p. 810-826.

Brothers, D.S., Kent, G.M., Driscoll, N.W., Smith, S.B., Karlin, R., Dingler, J.A., Harding, A.J., Seitz, G.G., and Harding, A.J., 2009, New Constraints on Deformation, Slip Rate, and Timing of the Most Recent Earthquake on the West Tahoe–Dollar Point Fault, Lake Tahoe Basin, California: Bulletin of the Seismological Society of America, v. 99, p. 499-519.

Cook, E.R., Seager, R., Cane, M.A., and Stahle, D.W., 2007, North American drought: Reconstructions, causes, and consequences: Earth-Science Reviews, v. 81, p. 93-134.

Cook, E.R., Woodhouse, C.A., Eakin, C.M., Meko, D.M., and Stahle, D.W., 2004, Long-term aridity changes in the western United States: Science, v. 306, p. 1015-1018.

Danforth, W.W., 1997, Xsonar/ShowImage: A Complete System for Rapid Side-scan-Sonar Processing and Display: U.S. Geological Survey Open-File Report, v. 97-686, p. pp.99.

Dingler, J.A., Kent, G., Driscoll, N., Babcock, J.M., Harding, A.J., Seitz, G.G., Karlin, R., and Goldman, C., 2009, A high-resolution seismic CHIRP investigation of active normal faulting across the Lake Tahoe Basin, California-Nevada: Geological Society of America Bulletin, v. 121, p. 1089-1107.

Freeze, R.A., and Cherry, J.A., 1972, Groundwater: Eglewood Cliffs, NJ, Prentice Hall, Inc.

Hanes, T., June (1981) Hydrologic analysis of the Fallen Leaf Lake watershed and operation plan for Fallen Leaf Lake: U.S. Forest Service Lake Tahoe Basin Management Unit report.

Helama, S., Merilainen, J., and Tuomenvirta, H., 2009, Multicentennial megadrought in northern Europe coincided with a global El Nino-Southern Oscillation drought pattern during the Medieval Climate Anomaly: Geology, v. 37, p. 175-178.

Herweijer, C., Seager, R., and Cook, E.R., 2006, North American droughts of the mid to late nineteenth century: a history, simulation and implication for Mediaeval drought: Holocene, v. 16, p. 159-171.

Herweijer, C., Seager, R., Cook, E.R., and Emile-Geay, J., 2007, North American droughts of the last millennium from a gridded network of tree-ring data: Journal of Climate, v. 20, p. 1353-1376.

Jones, T.L., and Schwitalla, A., 2008, Archaeological perspectives on the effects of medieval drought in prehistoric California: Quaternary International, v. 188, p. 41-58.

Kleppe, J.A., 2005, A Study of Ancient Trees Rooted 36.5M (120') Below the Surface Level of Fallen Leaf Lake: Nevada Water Resources Journal, Lake Tahoe Edition, v. Vol. 2, p. 29-40.

Lindstrom, S.G., 1990, Submerged tree stumps as indicators of mid-Holocene aridity in the Lake Tahoe region: Journal of California and Great Basin Anthropology, v. 12, p. 146-157.

McCaughey, J., 2005, Pleistocene Glaciation of the Southwest Tahoe Basin: MS Thesis,University of Nevada,Reno.

Mensing, S.A., Benson, L.V., Kashgarian, M., and Lund, S., 2004, A Holocene pollen record of persistent droughts from Pyramid Lake, Nevada, USA: Quaternary Research, v. 62, p. 29-38.

Pearson, D.a.J., Inc., 1999, Preliminary report: profile gravity modeling Lake Tahoe area.

Saucedo, G.J., Little, J.D., Watkins, S.E., Davis, J.R., Mascorro, M.T., Walker, V.D., and Ford, E.W., 2005, Geologic map of the Lake Tahoe Basin, California and Nevada: California Geological Survey, scale 1:100,000.

Stahle, D.W., Fye, F.K., Cook, E.R., and Griffin, R.D., 2007, Tree-ring reconstructed megadroughts over North America since AD 1300: Climatic Change, v. 83, p. 133-149.

Stine, S., 1994, Extreme and Persistent Drought in California and Patagonia during Medieval Time: Nature, v. 369, p. 546-549.

Swetnam, T.W., 1993, Fire History and Climate-Change in Giant Sequoia Groves: Science, v. 262, p. 885-889.

Trask, J., and Fogg, G., 2007, Tahoe basin precipitation and watershed streamwater outflow: inter-annual variability and explanatory variables: Tahoe Symposium.

Table 3-1: Radiocarbon data from submerged trees. All samples were analyzed at the Lawrence Livermore Center for Accelerator Mass Spectrometry and were calibrated using Radiocarbon Calibration Program CALIB 5.0.2 (http://calib.qub.ac.uk/calib/).

Table 1. Tree age and depth data

Tree #	**Samples**	**Depth below surface**	**Altitude of base (m)**	**Height of tree (m)**	**Lab age (year B.P.)**	**Cal age (year B.P.)**	**Death year (range)**	**Age of tree at death**
1	1-1, 1-2A	25.3	1918.2	20.8	790 ± 50, 825 ± 40	674-738, 691-765	1185-1276 AD	220
2	2-A, 2-C	36	907.8	26.7	810 ± 35, 830 ± 40	686-739, 694-769	1181-1264 AD	200
3	x	35.8	1907.7	5.5	x	x		
4	4-B, 4-C	35.4	1908.1	30.7	800 ± 35, 810 ± 35	686-733, 686-739	1211-1264 AD	200
5	9/18/06	36	1907	10.5	x	x		
6	7/10/03, 8/1/04	34.1	1908.1	6.1	1805 ± 40, 1815 ± 45	1703-1813, 1706-1818	132-247 AD	
7	7/31/04	33.2	1910.3	9.6	1930 ± 35	1826-1901	28-124 AD	
8	repeat sample							
9	8/8/04	30.5	1913	5	3230 ± 35	3399-3474	1524-1449 BC	
10	7/13/04	36.9	1906.7	N/A	960 ± 40	798-927	1023-1152 AD	202
11	7/4/03	N/A	N/A	N/A	2175 ± 40	2121-2305	355-232 BC	
12	7/10/03	N/A	N/A	15	200 ± 40	147-296	1654-1803 AD	
13	8/28/04	14.3	1929	12.3	780 ± 40	680-727	1223-1270 AD	

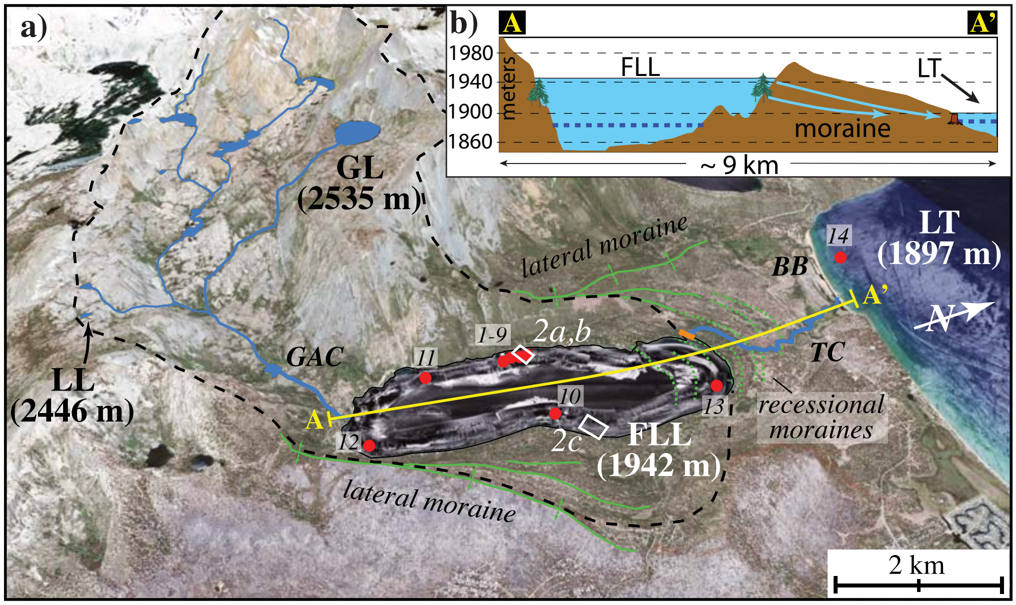

Figure 3-1: Fallen Leaf Lake watershed and local geomorphology. (a) Abbreviations: Fallen Leaf Lake, FLL; Lake Tahoe, LT; Lake Lucille, LL; Gilmore Lake, GL; Glen Alpine Creek, GAC; Taylor Creek, TC; Baldwin Beach, BB. Solid green lines are lateral moraines (arrows indicate valley-bounding moraine crests); dashed green lines are recessional moraines; red dots are sampled and dated trees (14 total); labeled white boxes are locations for Figure 2 panels. Texture over FLL is a sidescan sonar mosaic. (b) Topographic cross section and hydrogeologic schematic. Ancient trees in FLL are rooted at ~36 m below the surface. Submerged paleoshorelines are observed at ~60 m below the surface, approximately the same altitude as an ancient stump observed offshore Rubicon Point in Lake Tahoe. Tree 14 marks a cluster of submerged mid-Holocene stumps in Lake Tahoe(Lindstrom, 1990).

Figure 3-2: Sidescan sonar and submersible imagery of submerged trees and paleoshorelines. (a) Upright trees are seen as shadows in the sonar imagery. “grove” represents a cluster of trees 2, 3, 4 and 5 (Table 1). The root ball is visible in both upright and downed trees. Arrows point to downed trees on the lakefloor. Paleoshorelines are visible upslope. (b) Photo of Tree #1 taken from the Undersea Voyager Project submersible (taken by G. Kent). (c) Sonar image along eastern shore highlighting prehistoric submerged shorelines, berms and downed trees. Paleoshoreline features are seen up to 60 m depth, >20 m below root depth, suggesting trees were growing above an ancient shoreline.

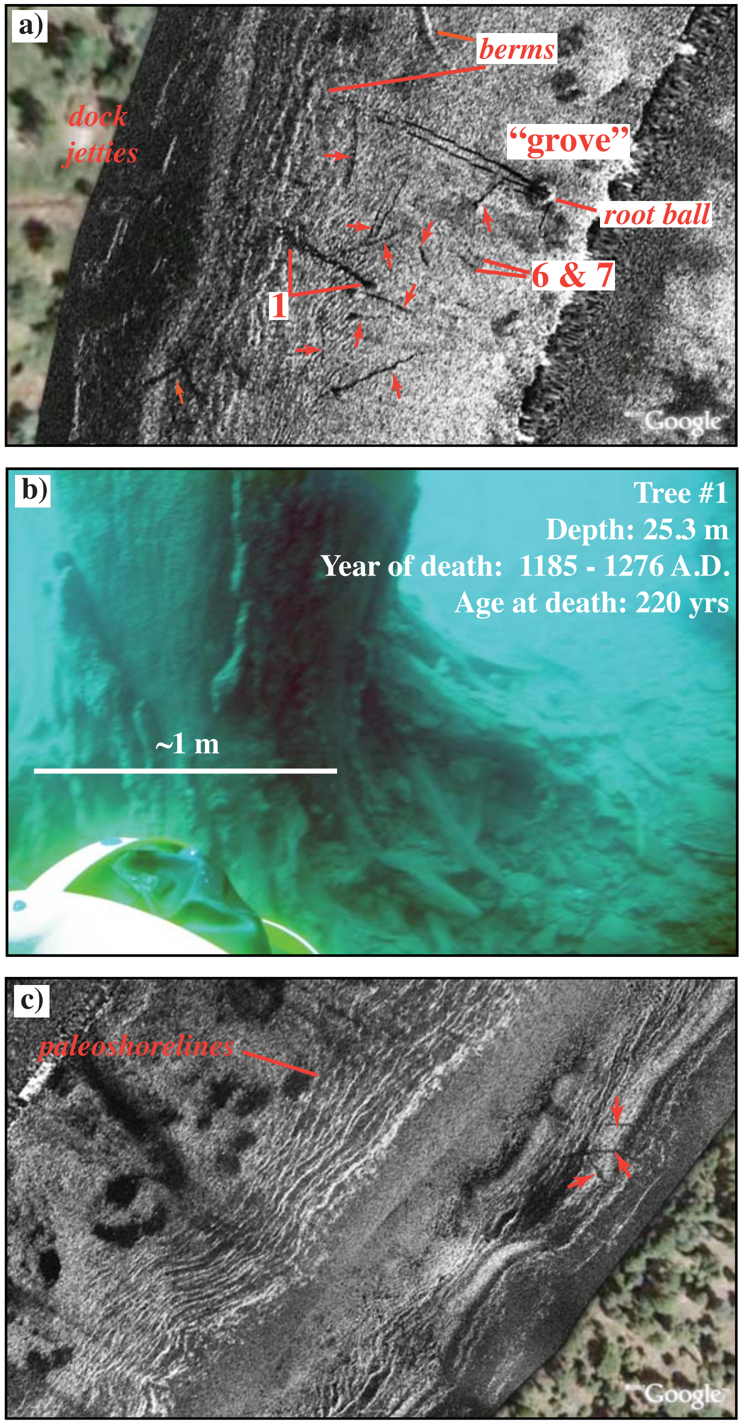
a)
berms
dock
jetties
"grove"
root ball
6 & 7
1
Google
b)
Tree #1
Depth: 25.3 m
Year of death: 1185 - 1276 A.D.
Age at death: 220 yrs
~1 m
c)
paleoshorelines
Google

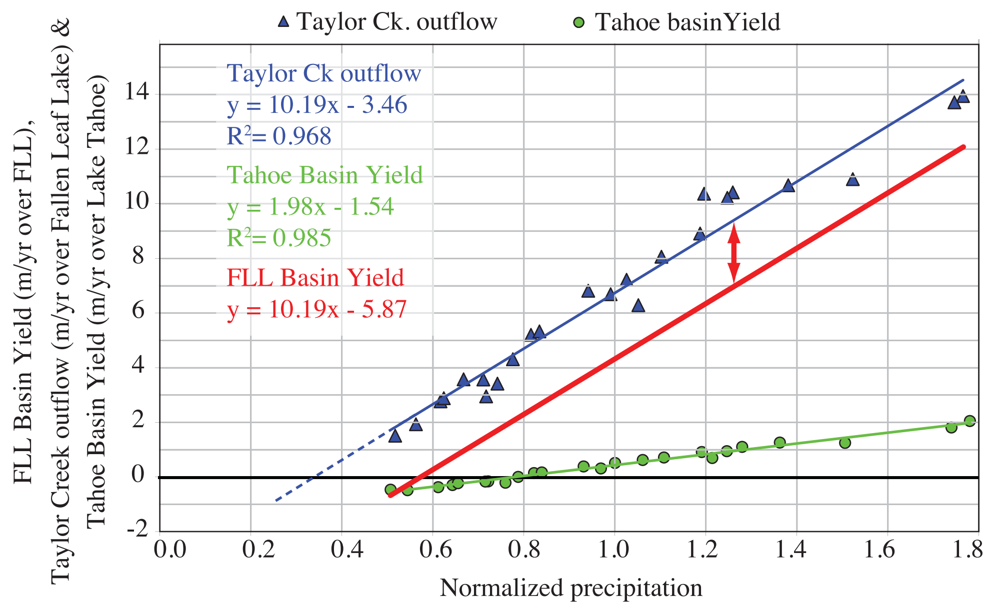

Figure 3-3: Taylor Creek stream outflow, Fallen Leaf Lake Basin annual water yield and Tahoe Basin annual water yield versus normalized precipitation; water years 1969-1992 (modified from Trask and Fogg, 2007). A value of 1.0 is considered "normal" and represents the WY 1969-92 mean precipitation over the FLL Basin normalized over the surface area of FLL. The FLL Basin watershed is less efficient than the Lake Tahoe Basin due to the "leak". The FLL yield becomes almost negative at 0.6 of normal precipitation due to the ground water seepage. This suggests that the precipitation in the FLL watershed was less than 0.6 of normal during medieval times, resulting in shoreline regression and allowing trees to grow below the modern shoreline for over 220 years.

4

Tectonic Evolution of the Salton Sea Inferred from Seismic Reflection Data

nature geoscience

LETTERS

PUBLISHED ONLINE: 26 JULY 2009 | DOI: 10.1038/NGEO590

Tectonic evolution of the Salton Sea inferred from seismic reflection data

D. S. Brothers[1]*, N. W. Driscoll[1], G. M. Kent[1], A. J. Harding[1], J. M. Babcock[1] and R. L. Baskin[2]

Oblique extension across strike-slip faults causes subsidence and leads to the formation of pull-apart basins such as the Salton Sea in southern California. The formation of these basins has generally been studied using laboratory experiments or numerical models[1–4]. Here we combine seismic reflection data and geological observations from the Salton Sea to understand the evolution of this nascent pull-apart basin. Our data reveal the presence of a northeast-trending hinge zone that separates the sea into northern and southern sub-basins. Differential subsidence (>10 mm yr^{-1}) in the southern sub-basin suggests the existence of northwest-dipping basin-bounding faults near the southern shoreline, which may control the spatial distribution of young volcanism. Rotated and truncated strata north of the hinge zone suggest that the onset of extension associated with this pull-apart basin began after ~0.5 million years ago. We suggest that slip is partitioned spatially and temporally into vertical and horizontal domains in the Salton Sea. In contrast to previous models based on historical seismicity patterns[5], the rapid subsidence and fault architecture that we document in the southern part of the sea are consistent with experimental models for pull-apart basins[1].

Our current understanding of the kinematics and evolution of pull-apart basins is based largely on laboratory[1–3] and numerical models[4], with few well-dated field studies examining the regional deformation patterns within active pull-apart basins. The San Andreas fault–Imperial fault (SAF–IF) transtensional step-over is an ideal locale to study the relationship between horizontal and vertical deformation in an active pull-apart basin using regional-scale, high-resolution geophysical methods[6]. This step-over delineates the northward transition from the obliquely divergent Gulf of California margin to transpressional deformation of the San Andreas fault system. Early crustal models suggested that much of the southern Salton Trough is underlain and intruded by young, mafic material[7,8]. Geophysical and thermal anomalies along with volcanism near the southern Salton Sea were attributed to a buried spreading centre between the SAF and IF (refs 7, 8). Later studies examined seismicity patterns and the kinematics of moderate-to-strong earthquakes in the region[9–11]. The complex ladder-like seismicity patterns of the Brawley Seismic Zone (BSZ; Fig. 1) and faulting to the west of the Salton Sea led to models of distributed dextral shear and block rotation between the SAF and San Jacinto fault (SJF; ref. 5). At present, a consistent model for basin evolution is needed that accounts for the high subsidence rates observed in this study, the seismicity patterns[11], the prominent northeast-trending thermal anomaly[12] and string of Quaternary volcanic buttes[13] (Fig. 1).

Between 2006 and 2008, we acquired over 1,000 line-km of high-resolution chirp seismic reflection data in the Salton Sea (Fig. 1). Sediments deposited during the late Holocene in Lake Cahuilla[14] (herein referenced as the Cahuilla Formation, CFm) blanket the basin and are defined by parasequence sets that have been radiocarbon dated at onshore sites[15]. The sedimentary packages record shoreline fluctuations of Lake Cahuilla, enabling us to correlate high- and low-amplitude reflectors offshore with dated sequences onshore. In the Salton Sea, the CFm records deformation for at least 12 transgression–regression cycles (~2–3 kyr BP). Numerous faults are identified in the CFm by vertically offset reflectors and occasionally by seafloor scarps. Potential correlations between onshore and offshore structures include the Extra fault zone[9,16] (EFZ) and possibly the Elmore Ranch fault[17] (ERF); both show sinistral slip west of the Salton Sea. Although historic seismicity is scarce along the newly mapped faults[5,11], palaeoearthquakes have produced over 1 m of vertical offset per event (see Supplementary Fig. S4). The average strike of faults in the southern sea (N15° E; Fig. 1c) is more northerly than the cross-faults west of the Salton Sea and the short (<5 km) ~N40° E trending seismicity lineaments in the BSZ.

The northeast-striking EFZ, expressed in the CFm as a series of down-to-the-southeast growth folds and faults, seems to be a structural hinge zone that separates the sea into northern and southern basins (Fig. 2). In the northern basin, an angular unconformity separates parallel, concordant reflectors of the CFm from underlying folded and faulted reflectors that we interpret as the Pleistocene Brawley Formation[16,18] (BFm) mapped west of the sea and at Durmid Hill (DH) (Fig. 1). BFm strata show a progressive increase in dip and fold frequency southward approaching the EFZ, then drop below the limits of acoustic penetration south of the EFZ. The fold geometry provides evidence for broad ~N/S-directed compression and uplift that was subsequently truncated, leaving a nearly flat unconformity surface. The trend of the compression seems to align with subtle topography associated with the San Felipe Anticline west of the sea[16] (Fig. 1). Nevertheless, we do not observe stratigraphic evidence within the CFm for differential subsidence or uplift north of the EFZ.

The EFZ marks the northern limit of active extension. South of the EFZ, CFm beds show marked divergence and evidence for syntectonic sedimentation. Average subsidence measured over the AD 830 time-horizon just south of the hinge zone is between 9 and 12 mm yr^{-1} (Fig. 2; Supplementary Fig. S3). The CFm beds continue to diverge to the southeast beyond our data coverage, suggesting that the above estimate is a minimum. Stratal divergence indicates that subsidence is equal to or slightly higher than sedimentation, where the average sedimentation rate in the southern basin has been nearly 19 mm yr^{-1} since ~AD 1360. The projected location of maximum subsidence is near the southern shoreline, approximately coincident with the locus of Quaternary volcanism and a northeast-trending band of very high heat flow. Farther south, the rapidly subsiding Mesquite Basin bounds the

[1]Scripps Institution of Oceanography, University of California, San Diego, 9500, Gilman Drive, La Jolla, California 92093, USA, [2]United States Geological Survey, 2329 West Orton Circle, West Valley City, Utah 84119, USA. *e-mail: dbrother@ucsd.edu.

 NATURE GEOSCIENCE DOI: 10.1038/NGEO590

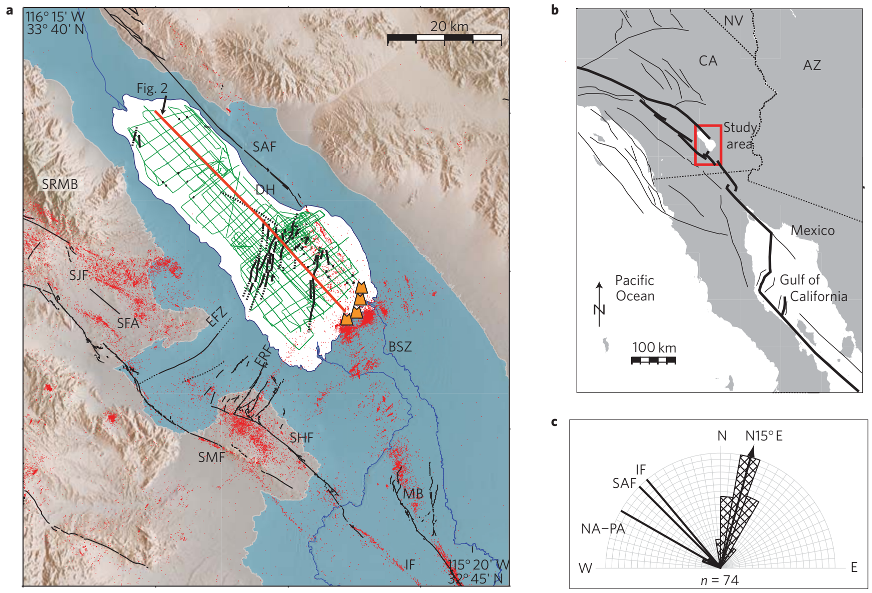

Figure 1 | Map of the Salton Sea region. a, Green lines represent seismic reflection profiles (the red line is the location for Fig. 2). Lake Cahuilla is shaded blue. Black lines denote Holocene faults, red dots are relocated earthquakes[11] and orange triangles are volcanic buttes. Abbreviations: SRMB, Santa Rosa mountain block; SJF, San Jacinto fault; EFZ, Extra fault zone; ERF, Elmore Ranch fault; BSZ, Brawley seismic zone; SAF, San Andreas fault; SHF, Superstition Hills fault; SMF, Superstition Mountain fault; IF, Imperial fault; DH, Durmid Hill; SFA, San Felipe anticline; MB, Mesquite basin. **b**, Regional map of study area. Abbreviations: CA, California; AZ, Arizona; NV, Nevada. **c**, Rose diagram of fault strikes. The average strike for faults in the sea is N15° E (see the Methods section). Other trends are the SAF, IF and North America–Pacific (NA–PA) plate motion vector at this latitude[30].

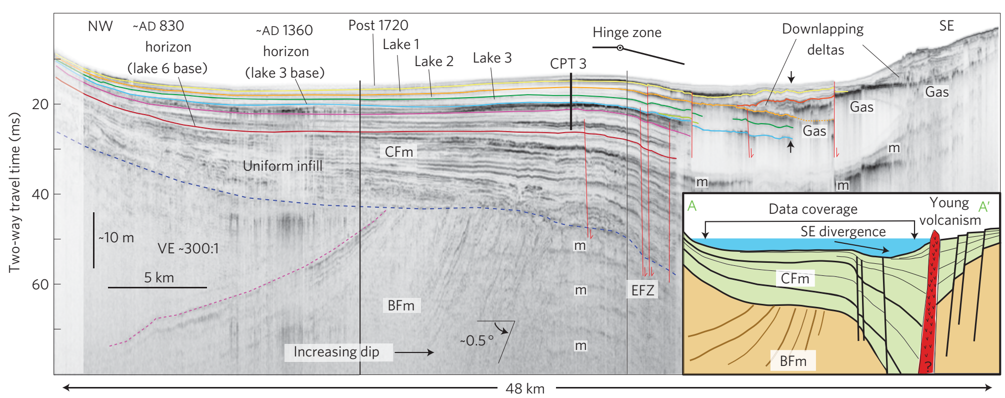

Figure 2 | Salton Sea long-axis seismic reflection profile. A truncation surface (dashed blue line) separates the Holocene CFm from the underlying Pleistocene BFm. Coloured horizons represent time horizons in the CFm; red lines denote faults; black arrows mark the location at which sedimentation rate was estimated; multiple reflections (acoustic artefacts) are identified by 'm'. The black pipe labelled CPT-3 represents cone penetration test data (see Supplementary Fig. S1). Inset, Interpretive cross-section. North of the EFZ, reflectors in the CFm are concordant and record little deformation. Reflectors in the BFm show evidence for ~N/S-oriented compression. South of the EFZ, layers diverge and thicken. We infer that maximum subsidence occurs near the southern shoreline and that extensional faults may provide fluid migration pathways for young volcanism.

northern terminus of the IF and seems to define a separate pull-apart basin[19,20] within the larger SAF–IF step-over (Fig. 1).

If we assume that subsidence is equal to or slightly greater than sedimentation (~20 mm yr^{-1}) and that an inferred boundary fault (assumed strike/dip = N30° E/60° N) accommodates most of the subsidence, then horizontal extension is calculated at 11.5 mm yr^{-1} in the direction N60° W (orthogonal to the boundary fault). Projected onto an azimuth parallel to the SAF, this yields ~11.2 mm yr^{-1} of dextral slip. Although long-term slip-rate estimates for the southern SAF are few and somewhat controversial, offset alluvial fans north of the Salton Sea provide a rate between 9 and 15 mm yr^{-1} over the past 45–50 kyr (ref. 21), whereas the short-term geodetic rate is 23.3 ± 0.5 mm yr^{-1} (ref. 22). Should the long-term rate be more representative, 75–100% of the horizontal

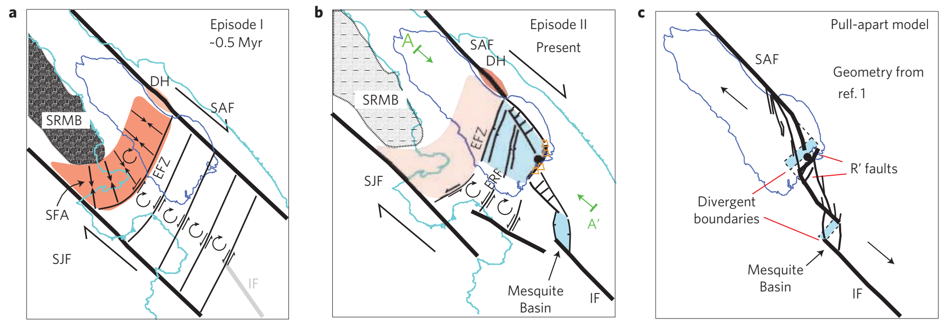

Figure 3 | Map-view models for the tectonic evolution of the Salton Sea. Bold faults represent the primary tectonic structures; orange triangles are volcanic buttes[13]. Blue shades are extensional domains; light-red zones are inactive compression; dark-red zones are active compression; the blue line is the Lake Cahuilla high-shoreline. Green arrows define the extent of the cross-sectional view in Fig. 2 (inset). **a**, Block rotation between the SAF and the SJF and compression north of the EFZ at ~0.5 Myr. **b**, Development of SAF–IF step-over and present-day configuration. **c**, Physical model of a pull-apart basin with mechanical layering[1] (superimposed on the Salton Sea). Extension is focused along R′ faults above the divergent boundary, forming an asymmetric basin. The Mesquite Basin represents a separate pull-apart basin within the SAF–IF step-over.

slip transferred from the SAF into the Salton Sea is accommodated by extension and subsidence, leaving less than 4 mm yr^{-1} for intrabasin strike-slip faulting and/or rotation. If we assume that the geodetic rate is more representative, then only ~50% of SAF slip is converted to extension in the sea. The ratio of horizontal slip to vertical subsidence constrains the relative importance of slip partitioning in this evolving pull-apart basin.

The EFZ and projected ERF show consistent down-to-the-east vertical displacement beneath the Salton Sea; these observations call into question the relationship between the onshore and offshore structures. If they represent the same fault segments, their trends and kinematics change as they extend into the SAF–IF step-over. Studies examining cross-faults west of the Salton Sea and seismicity in the BSZ (refs 5, 9, 23) would not have observed the large component of extension and subsidence occurring within the sea. We contend that the ~N15° E striking faults and inferred boundary fault in the southern sea produce relatively infrequent, but large, earthquakes (magnitude $M > 6$) that accommodate extension and subsidence, whereas the smaller events ($M < 5$) and microseismicity that define the BSZ are due to fracturing and block rotation within a narrow (<5-km-wide), dextral shear zone. In essence, the southern sea seems to be slip-partitioned into two separate tectonic domains. Contrary to previous models[5], we argue that block rotation alone cannot generate the observed rapid subsidence, the northeast-trending collection of volcanic buttes, and the thermal and geophysical anomalies along the southern shoreline[8,12,13]. These observations are more consistent with a large component of extension. Understanding the kinematics of the SAF–IF step-over may depend on the observation timescale. Extension and subsidence dominate over hundreds of years through ground-rupturing ($M > 6$) normal-oblique earthquakes, where the BSZ releases strain over decadal scales through numerous small-to-moderate earthquakes[10,11] and aseismic processes[24]. Sinistral cross-faults west of the Salton Sea have low slip-rates (~1 mm yr^{-1}; ref. 23) and seem to be secondary structures responding to rotation within the broader SAF–SJF strain field[5].

We propose a conceptual two-stage model for tectonic evolution for the Salton Sea. Though poorly understood, Episode I is characterized by the transpression observed north of the EFZ. Here, the EFZ may have started as a transpressional boundary between the SAF and SJF, before the development of the SAF–IF step-over (Fig. 3a). As the SJF formed, clockwise rotating blocks bounded by northeast-striking sinistral faults accommodated strain distributed between the SAF and SJF (ref. 5). One scenario is that block boundaries were not defined by simple, linear faults, but contained geometric complexities that produced vertical deformation. As rotation proceeded, block margins west of the Salton Sea are expected to have translated northward, impinging onto the Santa Rosa Mountains and resulting in ~N/S-oriented compression recorded in the sediments beneath the Salton Sea.

Episode II marks the onset of extension in the Salton Sea and development of the present-day transtensional regime (Fig. 3b). As the SAF–IF step-over formed, compression waned and some of the cross-faults that formed during Episode I began to accommodate normal slip. The differential subsidence and normal slip observed across northeast-striking faults began with the formation or northward propagation of the IF. Fault and subsidence patterns support bulk surface displacement being roughly parallel to plate motion. As extension progressed, subsidence became focused in the southern sea along an inferred north-dipping basin-bounding fault zone that we believe resembles R′ faults in physical models of pull-apart basins[1] (Fig. 3b,c). Maximum subsidence occurs in the hanging wall of R′ faults directly above the divergent boundary, producing hinge zone roll-over and stratal divergence[1]. These boundary faults may enhance decompression melting and provide migration pathways for volcanic and hydrothermal fluids (Fig. 2 (inset)). Similarities between observed structure and physical models suggest that the Salton Sea is in an early to mid-stage of development, but the overall SAF–IF step-over is relatively immature[1,2]. Short sinistral faults in the BSZ (ref. 5) may reflect internal deformation and rotation within strike-slip shear zones, as predicted in physical models[1] (Fig. 3b,c). Through time, deformation is expected to broaden where the Salton Sea and Mesquite Basin coalesce to form a composite pull-apart basin[25].

Although the absolute age of each deformational episode remains poorly constrained, this study provides relative ages for the deformation and an upper bound on the age of the SAF–IF step-over. In our model, the compression of the BFm beneath the angular unconformity is contemporaneous with, or postdates, the onset of deformation along the southern SJF zone (1.1–1.3 Myr; ref. 26). Subsequently, a structural reorganization that established N/S-directed compression to the west of the Salton Sea occurred at ~0.5–0.6 Myr (refs 16, 27), approximately the same time that deposition of BFm ended[16]. Assuming that the structural reorganization coincides with Episode I, we argue that the compression in the BFm north of hinge occurred sometime after ~0.5 Myr. Compression was then replaced by extension south of the EFZ, thus providing a maximum age for the formation of the SAF–IF step-over at ∼0.5 Myr. Erosion of onshore BFm strata may present a significant lacuna, therefore a late-Pleistocene[19] (∼0.1 Myr) age for the SAF–IF is possible.

In summary, our observations provide important constraints on the growth of an active pull-apart basin and the evolution of the southern SAF system. On the basis of our interpretive model we conclude the following. (1) Differential subsidence south of the EFZ has produced an asymmetric basin with strata thickening southward into a basin-bounding fault system. (2) Transtension beneath the Salton Sea is partitioned into distinct extensional and strike-slip domains. Extensional faults are at a high angle to the SAF, rupture during larger, less frequent earthquakes and should be considered seismically hazardous. The BSZ accommodates dextral shear transferred into the basin through internal deformation (for example secondary faulting and/or rotation). (3) The Salton Sea basin seems similar to young pull-apart basins in physical models and provides a comparative example on the basis of high-fidelity records of deformation. Our proposed model is the first to account for the rapid subsidence, elevated heat flow and profuse seismicity in the Salton Sea.

Methods

Seismic reflection data were collected using Scripps Institution of Oceanography's Edgetech 512i sub-bottom profiler, herein referred to as a chirp system. Each shot was digitally recorded and included real-time GPS navigation. Profiles were processed using SIOSEIS then imported into the Kingdom Suite and IVS Fledermaus software packages for interpretation. Vertical resolution between reflectors is ∼15–40 cm, depending on the source pulse and sediment velocity, and vertical penetration is up to ∼70 m. Time-to-depth conversions assumed a sediment velocity of 1,600 m s^{-1}. Seismic sections were interpreted using considerable vertical exaggeration (as in Fig. 2) to delineate subtle changes in stratal geometry and identify regional scale variation. All faults shown in Fig. 1 offset the CFm and typically dip between 50° and 70° (faults in Fig. 2 seem vertical owing to vertical exaggeration). Fault statistics (Fig. 1c) were not normalized by fault length because many faults extend beyond the data coverage.

The CFm consists of unconsolidated fluvio-lacustrine facies deposited during Colorado River diversions, but before the formation of the Salton Sea (1905). Between 2003 and 2006, United Research Services collected 17 sediment borings and 34 cone penetration tests in the Salton Sea[28]. These data provide information on the lithostratigraphy that can be correlated with the acoustic properties observed in chirp profiles. High-amplitude horizons correspond to lowered lake levels and the consequent increased silt/sand components detected by cone penetrometer tests[28]; low-amplitude horizons represent fine-grained high-stand lake deposits. Correlating the onshore[15] and offshore lake sequences enables us to establish a chronostratigraphic framework that is used to constrain the deformation history beneath the sea (see Supplementary Fig. S1). The most recent Lake Cahuilla high-stand occurred around AD 1680–1720 and up to six high-stands have been dated back to ∼AD 800 (refs 15, 29). Dated horizons were correlated spatially between chirp profiles to construct isopach maps and estimate differential subsidence rates.

Received 6 January 2009; accepted 30 June 2009; published online 26 July 2009

References

1. Basile, C. & Brun, J. P. Transtensional faulting patterns ranging from pull-apart basins to transform continental margins: An experimental investigation. *J. Struct. Geol.* **21**, 23–37 (1999).
2. Wu, J. E., McClay, K., Whitehouse, P. & Dooley, T. 4D analogue modelling of transtensional pull-apart basins. *Mar. Petrol. Geol.* (in the press).
3. McClay, K. & Dooley, T. Analog models of pull-apart basins. *Geology* **23**, 711–714 (1995).
4. Katzman, R., ten Brink, U. S. & Lin, J. A. 3-Dimensional modeling of pull-apart basins—implications for the tectonics of the dead-sea basin. *J. Geophys. Res.* **100**, 6295–6312 (1995).
5. Nicholson, C., Seeber, L., Williams, P. & Sykes, L. R. Seismic evidence for conjugate slip and block rotation within the San-Andreas Fault System, Southern California. *Tectonics* **5**, 629–648 (1986).
6. Seeber, L. *et al*. Rapid subsidence and sedimentation from oblique slip near a bend on the North Anatolian transform fault in the Marmara Sea, Turkey. *Geology* **34**, 933–936 (2006).
7. Elders, W. A., Biehler, S., Rex, R. W., Robinson, P. T. & Meidav, T. Crustal spreading in Southern California. *Science* **178**, 15–24 (1972).
8. Fuis, G. S., Mooney, W. D., Healy, J. H., Mcmechan, G. A. & Lutter, W. J. A seismic refraction survey of the Imperial-Valley Region, California. *J. Geophys. Res.* **89**, 1165–1189 (1984).
9. Hudnut, K. *et al*. Surface ruptures on cross-faults in the 24 November 1987 Superstition Hills, California, earthquake sequence. *Bull. Seismol. Soc. Am.* **79**, 282–296 (1989).
10. Hardebeck, J. L. & Shearer, P. M. Using S/P amplitude ratios to constrain the focal mechanisms of small earthquakes. *Bull. Seismol. Soc. Am.* **93**, 2434–2444 (2003).
11. Lin, G. Q., Shearer, P. M. & Hauksson, E. Applying a three-dimensional velocity model, waveform cross correlation, and cluster analysis to locate southern California seismicity from 1981 to 2005. *J. Geophys. Res.* **112**, B12309 (2007).
12. Newmark, R. L., Kasameyer, P. W. & Younker, L. W. Shallow drilling in the Salton-Sea Region—the thermal anomaly. *J. Geophys. Res.* **93**, 13005–13023 (1988).
13. Schmitt, A. K. & Vazquez, J. A. Alteration and remelting of nascent oceanic crust during continental rupture: Evidence from zircon geochemistry of rhyolites and xenoliths from the Salton Trough, California. *Earth Planet. Sci. Lett.* **252**, 260–274 (2006).
14. Waters, M. R. Late holocene lacustrine chronology and archaeology of ancient Lake Cahuilla, California. *Quat. Res.* **19**, 373–387 (1983).
15. Philibosian, B. *Paleoseismology of the San Andreas Fault at Coachella, California*. Master's thesis, Univ. Oregon (2007).
16. Kirby, S. M. *et al*. Pleistocene brawley and ocotillo formations: Evidence for initial strike-slip deformation along the San Felipe and San Jacinto fault zones, southern California. *J. Geol.* **115**, 42–62 (2007).
17. Hudnut, K. W., Seeber, L. & Pacheco, J. Cross-fault triggering in the November 1987 Superstition Hills earthquake sequence, Southern California. *Geophys. Res. Lett.* **16**, 199–202 (1989).
18. Burgmann, R. Transpression along the Southern San-Andreas Fault, Durmid Hill, California. *Tectonics* **10**, 1152–1163 (1991).
19. Larsen, S. & Reilinger, R. Age constraints for the present fault configuration in the Imperial Valley, California—evidence for Northwestward propagation of the Gulf of California Rift System. *J. Geophys. Res.* **96**, 10339–10346 (1991).
20. Johnson, C. E. & Hadley, D. M. Tectonic implications of the Brawley Earthquake Swarm, Imperial Valley, California, January 1975. *Bull. Seismol. Soc. Am.* **66**, 1133–1144 (1976).
21. Behr, W. *et al*. *SCEC Annual Meeting, Proceedings and Abstracts* Vol. 17, 87 (2007).
22. Meade, B. J. & Hager, B. H. Block models of crustal motion in southern California constrained by GPS measurements. *J. Geophys. Res.* **110**, B04402 (2005).
23. Hudnut, K. W., Seeber, L. & Rockwell, T. Slip on the Elmore Ranch Fault during the past 330 years and its relation to slip on the Superstition Hills Fault. *Bull. Seismol. Soc. Am.* **79**, 330–341 (1989).
24. Lohman, R. B. & McGuire, J. J. Earthquake swarms driven by aseismic creep in the Salton Trough, California. *J. Geophys. Res.* **112**, B04405 (2007).
25. Aydin, A. & Nur, A. Evolution of pull apart basins and their scale independence. *Tectonics* **1**, 91–105 (1982).
26. Steely, A. N., Janecke, S. U., Dorsey, R. J. & Axen, G. J. Early Pleistocene initiation of the San Felipe fault zone, SW Salton Trough, during reorganization of the San Andreas fault system. *Geol. Soc. Am. Bull.* **121**, 663–687 (2009).
27. Lutz, A. T., Dorsey, R. J., Housen, B. A. & Janecke, S. U. Stratigraphic record of Pleistocene faulting and basin evolution in the Borrego Badlands, San Jacinto fault zone, Southern California. *Geol. Soc. Am. Bull.* **118**, 1377–1397 (2006).
28. URS. Preliminary in-sea geotechnical investigation, Salton Sea Restoration Project Report (Riverside and Imperial Counties, 2004).
29. Meltzner, A. J., Rockwell, T. K. & Owen, L. A. Recent and long-term behavior of the Brawley Fault Zone, Imperial Valley, California: An escalation in slip rate? *Bull. Seismol. Soc. Am.* **96**, 2304–2328 (2006).
30. Kreemer, C., Holt, W. E. & Haines, A. J. An integrated global model of present-day plate motions and plate boundary deformation. *Geophys. J. Int.* **154**, 8–34 (2003).

Acknowledgements

Funding for this work was provided by the California Department of Water Resources, California Department of Fish and Game, UCSD Academic Senate, Scripps Institution of Oceanography, National Science Foundation (grants OCE-0112058 and EAR-0545250) and Southern California Earthquake Center (grant 2008-08127). We would like to thank B. Philibosian, D. Sandwell and D. Kilb for discussions, and V. Langenheim for a review.

Author contributions

D.S.B. planned field surveys, collected, analysed and interpreted the data and wrote the manuscript. N.W.D. and G.M.K. planned field surveys, collected and interpreted the data and provided extensive feedback on the manuscript. A.J.H., J.M.B. and R.L.B. collected data and provided feedback on the manuscript.

Additional information

Supplementary information accompanies this paper on www.nature.com/naturegeoscience. Reprints and permissions information is available online at http://npg.nature.com/reprintsandpermissions. Correspondence and requests for materials should be addressed to D.S.B.

5

Late-Holocene Earthquake and Sedimentary History Beneath the Salton Sea, Southern California

5.1 ABSTRACT

Marine paleoseismic investigations in the Salton Sea uncovered more than 15 vertical displacement events along a series of ~N15°E oriented faults. Seismic CHIRP profiles imaged more than fourteen Lake Cahuilla (LC) parasequences (2-3 kyr B.P.). Calendar age estimates for the six most recent parasequences (~830 AD - present) are obtained by correlating acoustic stratigraphy in the Salton Sea with onshore sequences that have been radiocarbon dated. Faults to the southwest of Bombay Beach have produced up to 10 events in the last 2-3 kyr. Since ~830 AD, vertical slip rates range from 1.1 to 3.4 mm/yr and average recurrence intervals range from 115 years to 460 years. Seafloor scarps and deformed Salton Sea sediments imply recent offset, possibly aseismic creep and/or triggered slip. Evidence for slip inversion suggests fault kinematics has changed over short timescales (<1000 years). As faults extend farther west their vertical displacement and recurrence intervals appear to decrease, but contain evidence for at least 2 events in the LC section. Faults discovered in the northern sea show evidence for at least two events in the LC section, but are generally less active. Only 2 of the last 5 events on the southern San Andreas Fault (SAF) were potentially synchronous with events offshore. Based on the relationship between flooding surfaces and fault displacements, it appears that ruptures on three offshore faults occur when the Colorado River floods the basin. Assuming strain is released seismically, faults in the Salton Sea can potentially generate M6-6.8 earthquakes, which could modulate stress on the southern SAF.

5.2 INTRODUCTION

5.2.1 Paleoseismology in the Salton Sea

The Salton Sea is a large (~970 km^2), shallow lake located in the central Salton Trough of Southern California that covers the southernmost extension of the San Andreas

Fault (SAF; Figure 1) and the northernmost transtensional step-over associated with Gulf of California oblique rifting. Brothers et al. (2009) mapped numerous faults and defined the shallow basin architecture. They proposed that rapid subsidence in the southern Salton Sea is due to oblique extension within the San Andreas Fault- Imperial Fault (SAF-IF) step-over, one of few places in the Salton Trough undergoing active lithospheric thinning, and that several faults in the Salton Sea have the potential to produce relatively frequent M>6 earthquakes. In this paper we expand on the results of Brothers et al. (2009) by performing a detailed investigation of paleoseismic deformation along faults in the Salton Sea. Several studies have suggested the southernmost SAF is overdue for a large-magnitude earthquake (Fialko, 2006). Comprehensive hazard assessments require regional studies that account for rupture along secondary faults and their potential to inhibit or promote failure on the SAF. Therefore, understanding the kinematic relationships and seismic cycling between the SAF and extensional faults beneath the Salton Sea is of utmost importance.

The Salton Sea offers an opportunity to perform marine paleoseismology along a 50 km-long section of the SAF system. Marine paleoseismology has been successfully applied in extensional domains (Brothers et al., 2009b; Bull et al., 2003; Kent et al., 2005; Lamarche et al., 2006; McHugh et al., 2006), but few places offer multi-event records at decadal-scale resolution. There are significant advantages to working in subaqueous over subaerial environments, namely that sedimentation tends to be more continuous in time and space allowing better preservation of deformed sediment horizons and anthropogenic disturbances are generally less underwater. In addition high-resolution geophysics can image deformation at sub-meter resolution, but with much greater spatial coverage than with onshore methods. The goals of this study are to define a detailed late-Holocene depositional framework and deformation history within the submerged portion of the San Andreas-Imperial Fault (SAF-IF) pull-apart basin (Figure 1). We examine coseismic deformation preserved in Lake Cahuilla sediments to obtain constraints on the earthquake history, slip-rates and sedimentation history using detailed analysis of > 1,000 line-km of seismic CHIRP profiles (Figure 2). We also compare paleoearthquake records beneath the Salton Sea with those observed along onshore fault systems, namely the SAF.

5.2.2 The Salton Trough Tectonics

As much as 80% of the contemporary North America-Pacific plate boundary motion is partitioned across the SAF, San Jacinto Fault (SJF) and Imperial Fault (IF) zones (Becker et al., 2005; Meade and Hager, 2005). Slip rates determined for the SAF and SJF vary depending on the study and the timescale. Geodetic studies place their combined rate at between 35 – 40 mm/yr (Fay and Humphreys, 2005; Meade and Hager, 2005), but rates based on geologic data are generally lower, but highly variable (Behr et al., 2007; Brothers et al., 2009a; Fletcher et al., 2007; Kendrick et al., 2002; Rockwell et al., 1990). At Bombay Beach the SAF takes a transtensional step towards the IF (Figure 1), forming the southern Salton Sea and the Mesquite pull-apart basins (Brothers et al., 2009a). The Salton Sea pull-apart appears asymmetric and is bounded to the north by the Extra Fault hinge-zone and to the south by an inferred boundary fault system near the southern shoreline (Brothers et al., 2009a). Subsidence approaches 20 mm/yr in the southern sea. The SJF splays into several dextral faults west of the Salton Sea, but deformation converges southward onto the Imperial Fault, which takes on the combined SAF and SJF slip-rates at 36 - 40 mm/yr (Lyons et al., 2002; Meade and Hager, 2005). Interseismic creep has been observed throughout the Salton Trough with temporally varying rates between 2 - 20 mm/yr (Lyons and Sandwell, 2003; Lyons et al., 2002; Sieh and Williams, 1990). Fault creep and triggered slip were observed following the Landers, Hector Mine, and Superstition Hills earthquakes (Hudnut et al., 1989b; Lyons and Sandwell, 2003).

The southernmost 200-km of the SAF has not produced a major rupture in ~300+ years despite evidence that the surrounding region continues to accumulate significant strain (Fialko, 2006; Fumal et al., 2002; Philibosian, 2007; Sieh and Williams, 1990). The potential for a M7.0 or greater rupture to nucleate in the Salton Sea and propagate northward along SAF is a major concern (Olsen et al., 2006), but has not been investigated in detail due to an absence of paleoseismic data in the Salton Sea. In addition, few sites along the southern SAF have produced reliable paleoseismic records. Philibosian (2007) presented the most detailed Lake Cahuilla history based on 82 radiocarbon dates and six earthquakes since ~ 800 AD. It is important to determine if faults in the Salton Sea play a role in modulating the earthquake cycle along the SAF.

5.2.3 Lake Cahuilla and the Salton Sea

During the Holocene, the Colorado River would occasionally flow northward into the isolated Salton Basin, forming Lake Cahuilla. When the river resumed flow to the Gulf of California, Lake Cahuilla would begin to evaporate and at times expose the basin to subaerial processes. The sediment record of these flooding-desiccation cycles has been studied along the banks of stream channels and in paleoseismic excavations surrounding the Salton Sea. The most thoroughly dated Lake Cahuilla section is at a paleoseismic site near Coachella, California (Philibosian, 2007), where seven Lake Cahuilla flooding-desiccation cycles were identified, six of which were precisely dated with radiocarbon analysis. The Coachella site is at 9 m elevation and records Colorado River diversions that completely filled the basin to an elevation of ~13 m, the height of the delta apex south of the international border (Figure 1). In general, the late-Holocene depositional environment cycled through periods of rapid flooding during Colorado River diversions, followed by lower energy lacustrine conditions, then shoreline regression, desiccation and subaerial exposure. Philibosian (2007) characterized parasequences by fine grained, deep water lacustrine facies deposited during Lake Cahuilla high-stands separated by sand and gravel rich fluvial beds associated with low-stand intervals and subaerial exposure. Prior to the present study, the only detailed information on the stratigraphy beneath the Salton Sea was based on bore holes and cone penetration test data (URS, 2004).

During spring runoff in 1905, canal construction weakened the Colorado River's natural levees allowing it to breach its banks and flow northward for 18 months, filling the depression that is now the Salton Sea. The present shoreline has been maintained at ~ 69 m below sea level by agricultural runoff in the Imperial and Coachella Valleys. Several factors combine to make the Salton Sea an ideal location to use marine geophysical methods to study regional depositional processes and tectonic deformation. First, the repeated flooding and desiccation cycles associated with Lake Cahuilla formed distinctive marker beds that can be correlated regionally. Second, onshore paleoseismic studies (Meltzner et al., 2006; Philibosian, 2007) have constrained the age of Lake Cahuilla sediments over the last ~6 flooding-desiccation cycles, providing a chronostratigraphic framework that can be extended offshore. Last, sedimentation rates in the sea are high, providing optimal conditions to preserve paleoearthquake evidence over multiple earthquake cycles.

One of the primary goals of this study is to use a chronostratigraphic model to quantify the timing and magnitude of tectonic deformation. In places, sediment accumulation averaged over the last ~1200 years is nearly 2 cm/yr, therefore the ~ 12 cm resolution of the 1-15 kHz CHIRP pulse has the potential to provide decadal-scale resolution during this interval. More than 20 fault segments were mapped beneath the Salton Sea (Figure 2). Some faults show sharp seafloor offset and/or stratigraphic growth down-section, while others are more subtly expressed as growth folds. In general, slip rates on individual faults are an order of magnitude less than sedimentation rates, allowing rapid burial and preservation of coseismic offset. To date, most paleoseismic work on faults is restricted to regions of deposition at a limited number of elevations. By systematically mapping the Salton Sea, we can assess the earthquake and sediment history at multiple elevations and across several fault systems and as such it provides an excellent approach to complement onshore paleoseismic excavations.

5.3 METHODS

Detailed geophysical surveys were conducted in the Salton Sea between 2006 and 2009 (Figure 2). Sub-bottom CHIRP profiles and sidescan sonar imagery were collected using Scripps Institution of Oceanography's Edgetech subscan systems aboard two vessels: a privately owned 50' pontoon vessel and the 23' R/V Stephens (operated by the USGS). Ancillary swath bathymetry surveys employed a Konsberg 3002 multibeam system aboard the R/V Stephens. This study is focused on the results from > 1,000 line-km sub-bottom data. All data were digitally recorded and included real-time GPS navigation with each shot, providing absolute location accuracy to within 5 m. JSF files were converted to standard SEGY format and subsequently processed using SIOSEIS, then imported into the Kingdom Suite and Fledermaus software packages for interpretation. Sidescan data were processed using xsonar (Danforth, 1997). Sub-bottom surveys employed different CHIRP pulses depending on sub-bottom conditions. The 0.7 – 3.0 kHz, 50 ms pulse provided greatest penetration (up to 60 m) while the 1.0 – 15.0 kHz, 30 ms pulse produced the highest vertical resolution (~15 cm).

Between 2003 and 2006, United Research Services Corporation (URS Corp.) collected 17 offshore borings and 34 cone penetration tests (CPT) from a self-propelled jack-up barge (URS, 2004). CPTs are primarily used for near-surface stratigraphic profiling. Soundings in the Salton Sea recorded measurements of cone bearing, sleeve friction, and dynamic pore water pressure at 2.5-cm intervals during penetration, thus providing a nearly continuous stratigraphic log in the upper ~20 m. Variations in these measurements can be used to infer changes in sediment type and/or grain size variations with depth (Robertson, 1990). Additionally, Schroeder et al. (2002) generated chemical profiles from a 0.5 m gravity core to identify the pre-Salton Sea sediment horizon and constrain the post-1905 sedimentation rates. Combined, these studies provide information on the lithostratigraphy that can be correlated with the acoustic properties observed in CHIRP profiles. We built a chronostratigraphic framework based on the correlation between radiocarbon-dated parasequences from Philibosian (2007) with offshore seismic stratigraphy. In so doing, the resulting offshore model is biased towards the stratigraphic ages defined by Philibosian (2007). Vertically offset horizons and/or hanging wall growth strata were used as paleoearthquake evidence. Lastly, horizons were correlated in three dimensions and isopach maps were constructed to understand the differential subsidence patterns and rates.

All depth measurements from seismic sections assumed a p-wave velocity of 1600 m/s to avoid overestimates. Several material index properties, including water content and void ratio were measured from bore samples, but these measurements were too sparsely distributed and did not show a consistent trend needed to correct depth measurements for compaction. Clay layers, particularly near the seafloor show water content between 50-80%. Deeper sediments show lower water content and void ratios, suggesting that significant compaction may have occurred. Because hanging wall strata along faults are several meters deeper than the correlative footwall strata, uncorrected compaction in the hanging wall results in underestimates for fault throw and slip-rate estimates. Due to the sparse sampling, we opted to avoid adding further assumptions into the depth measurements and did not apply a decompaction correction; therefore all depth measurements should be taken as underestimates. Nevertheless, CPT profiles superimposed on seismic sections (converted to depth sections assuming 1600 m/s velocity) provide good correlation between amplitude boundaries and lithologic boundaries, suggesting the assumed p-wave velocity and resulting depth measurements are reasonably accurate.

5.4 RESULTS

5.4.1 Sedimentary and Stratigraphic Framework

Type sections north and south of the hinge zone were used to identify parasequence sets and establish a basin-wide chronostratigraphy (Figures 3, 4). A CHIRP profile co-registered with an alignment of CPT soundings (Figures 3) was used as our initial type-section. CPT data confirmed the relationship between grain size and acoustic amplitude boundaries: high-amplitude layers correlate with increased silt/sand components deposited during low-stand or flooding events and the low-amplitude horizons represent fine-grained clays deposited during high-stand episodes. At least 14 parasequences are identified based on acoustic character correlated with CPT soundings and the first six are correlated with onshore stratigraphy at the Coachella site (Table 1). Throughout the basin, high-stand deposits tend to mimic underlying topography, but also show slight thickening in topographic lows. Low-stand deposits, however, record different processes to the north and south of the tectonic hinge zone (Brothers et al., 2009). North of the hinge, low-stand deposits tend to downlap onto the underlying strata, thicken shoreward and appear to be sourced from alluvial fans and local ephemeral streams (Figure 4 inset; Figure 5). Nearshore CHIRP profiles in the northern basin reveal distinct alternations between lacustrine facies and lenticular alluvial deposits. Ephemeral streams and washes drain the San Felipe Hills and Santa Rosa Mountains to the northwest as well as the Mecca Hills and Chocolate Mountains to the northeast. Some of the sand/silt rich facies show irregular erosional contacts with overlying deep-water deposits, particularly moving shoreward (Figure 3 inset). Away from shore, the fine-grained lacustrine layers comprise the majority of the LC section.

Sedimentation south of the hinge-zone is dominated by thick, coarse-grained fan delta facies that were deposited rapidly during Colorado River flooding. These layers tend to onlap the hinge zone and show marked thickening towards the southern shoreline (Figure 6), comprising more than 50% of the LC-section. Fine-grained deposition during high-stands and coarse-grained deposits record the differential subsidence in the southern sea in different ways. Fine-grained deposits, with lower acoustic amplitudes, are generally concordant across fault scarps and seafloor topography, where the coarse grained deposits tend to infill and obscure topographic relief. Near surface gas causes acoustic wipe-out zones (AWZ) throughout much of the southern sea and sub-bottom penetration was limited, particularly along the offshore extension of the SAF. In several places, vertical AWZs, "pipes", disrupt stratigraphic horizons and extend to the seafloor. Active venting is observed in the water column and at the lake surface. AWZs appear to be confined to certain stratigraphic horizons and exhibit steps or vertical offset across faults.

Parasequence sets are bounded by flooding surfaces (Van Wagoner and Bertram, 1995). South of the hinge-zone, distinguishing between the low-stand coarse grained facies and the coarse flood deposits that fine upward is difficult. Both have similar acoustic signatures, being high amplitude and infilling lows (Figures 5 and 6). To avoid ambiguity, we define basin-wide LC sequences based solely on amplitude boundaries. High-amplitude sections include both low-stand deposits and deposits emplaced during Colorado River flooding (Figures 3, 5 and 6). In correlating between onshore and offshore stratigraphy, we adopt similar nomenclature as Philibosian (2007), where each lake sequence is numbered and includes a coarsening upward lowstand ("S") and/or fining upward flood deposit ("F") followed by a fine-grained high-stand sequence ("L").

A transparent layer above an irregular high-amplitude reflector defines the youngest episode of lacustrine deposition. Based on borings, CPT soundings and gravity cores (Schroeder et al., 2002; URS, 2004), this layer consists of unconsolidated silt and clay deposited subsequent to the 1905-1907 creation of the Salton Sea. Salton Sea deposits (SS; e.g., Figures 3 and 4) are the most widely mapped of all units because the AWZs usually limits penetration and imaging of underlying layers. North of the hinge zone, parasequence sets display higher consistency in thickness and acoustic character than to the south (Figure 5). Salton Sea deposition (SS) since 1907 is less than ~0.5 cm/yr and pinches out in shallow areas, exposing the top of layer 1S at the seafloor (Figure 3). Sidescan images reveal meandering seafloor channels at the top of 1S. 1S has varied thickness and an irregular upper surface (Figure 3). Fine grained, low amplitude layers 1L, 2L and 3L are separated by relatively thin layers 2S and 3S. 2S and 3S downlap basinward and also thicken towards local sources onshore (Figure 3). CPT soundings detect 2S and 3S as distinct silt/sand layers along the shoreline, but they are not detected in the deepest portions of the basin (Figures 2 and 3). Evidence for erosional scour in 2S or 3S is not observed. Philibosian (2007) defined 4S as a thick accumulation of fluvial and aeolian deposits that was deposited during prolonged subaerial exposure. Profiles north of the hinge zone show distinct evidence for channelization, such as cut and fill structures during 4S (Figure 3). 6S and 9S also exhibit high amplitude acoustic reflectivity. Although layers 5S, 7S, 8S, 10S, 11S and 12S show an increase in acoustic reflectivity compared to high-stand layers, they are relatively thin. Below layer 9S, horizons become more difficult to correlate throughout the basin. Overall, low-stand episodes form lenticular-shaped lobes of coarse-grained material that thicken towards their respective drainages (Figures 3 and 5) and each parasequence contains essentially the same suite of acoustic character as the parasequences above and below.

SS deposits thicken considerably south of the hinge-zone, especially towards the southern shoreline where modern input from the New and Alamo Rivers is greatest. ~ 2 km north of the Salton Buttes, we observe a downlapping sediment wedge that is more than 4.7 m thick (Figure 5), yielding an average sedimentation rate of ~5 cm/yr since 1907. Layer 1S is thickest in the southern basin where the Colorado River formed a delta during flooding between 1905-1907. South of the hinge, we observe a gradational boundary between all high-stand deposits and the underlying flood facies (top low-stand layers). Layer 2S thickens from less than 0.5 m near the hinge to greater than 5.0 m south of the hinge and contains at least 5 internal layers (Figure 5), that progressively onlap and pinch out on the hinge. 2S does not extend as far north as some of the underlying high-amplitude units (4S, 6S, 9S; Figures 5, 6 and 7). Layer 3S is expressed as a single reflector throughout most of the lake and then thickens slightly south of the hinge zone. Layers 4S, 6S and 9S are thick, high amplitude marker beds that are easily correlated throughout the sea (Figures 3, 5, 6-8). Overall, moving south from the hinge zone, stratigraphic dip progressively increases down-section (Figure 5) and every coarse grained layer diverges and thickens systematically toward the southern shoreline (Brothers et al., 2009a). Sedimentation appears to be approximately 6-10 mm/yr during high stand and low-stand episodes, but during transgressive flooding and fan delta progradation from the Colorado River, sedimentation at times may exceed 30 cm/yr in the southern sea.

5.4.2 Faults and Earthquake Evidence

We will discuss the faults in the hinge zone from east to west. Other faults south of the hinge zone and north of the hinge zone will be discussed subsequently. For discussion purposes, we geographically grouped the faults into the following (Figure 2): the hinge-zone (“H”), southern (“S”) and northern (“N”) faults. Most faults located in the southern sea have an average trend of N15°E (Brothers et al., 2009a). AWZs limited our ability to image faulting throughout much of the southern sea, including the offshore projection of the SAF (Brothers et al., 2009a) and thus, any determination of fault lengths and scaling relationships would be biased. Irregular seafloor topography and disruption in the modern Salton Sea deposits provide some evidence for faulting in this area, but correlating these observations between profiles is difficult (Figure 2).

The hinge-zone defined by Brothers et al. (2009) contains a series of relatively short fault segments (Table 2) that bound the northern extent of active extension and subsidence in the SAF-IF pull-apart basin. Figure 5 illustrates the southward divergence and differential subsidence that is inferred to be bounded to the south by a northwest dipping fault zone (Brothers et al., 2009a). Deformation across the hinge zone is almost exclusively down-to-the-southeast and ranges from subtle fault propagation-folds in the west, to very abrupt vertical offset and seafloor scarps to the east (Figures 7 and 8).

5.4.3 Eastern Hinge-Zone

Well-defined vertical offsets are observed on faults H7, H8 and H9 (Figures 6-9). These faults provide the most complete paleoseismic records in the Salton Sea. Stratal thickness variations between the footwall and hanging wall contain information on fault movement and the rates and style of deposition. Detailed correlations between the footwall and hanging wall strata have provided over 25 piercing points from which displacements by individual earthquakes can be measured. The total throw measured over the top of 14L for faults H7, H8 and H9 is 7.1 m, 1.7 m and 4.2 m, respectively (Figures 6-8). Each of these faults offset the top of 1L. 1S onlaps the resulting scarp, suggesting each had an event within the last 300 years (Tables 1 and 2). H7, the most extensively mapped fault in the Salton Sea, shows evidence for displacement since it filled in 1907 (Figures 6 and 7). The average vertical displacements-per-event for the H7 and H8 are 0.7 ± 0.2 m and 0.4 ± 0.2 m; maximum offsets are 1.4 ± 0.2 m, 0.6 ± 0.2, respectively. The sense of slip on fault H9 was inverted after event *i* (Table 2; Figure 7). For example, the average displacement-per-event for the six most recent events is 0.5 ± 0.3 m and

-0.3 ± 0.2 m for the three oldest events. The maximum offset measured on H9 is 1.0 m. Paleoevent chronologies were constructed for events that occurred since the end of 7S deposition (Table 3). Using our best estimates for displacement timing, the following average recurrence intervals were calculated: (H7) 145 – 280 years over the last six events, (H8) 385 – 460 years over the last 3 events, and (H9) 115 -255 years over the last six events. The average vertical slip-rates since ~830 AD on H7, H8 and H9 are at least 3.4, 1.1, and 3.4 mm/yr respectively. Average slip rate estimates appear to have decreased from ~830 to present.

Based on acoustic character and infilling of the sequence on the hangingwall, we examine the timing of offset for the different events. Five events (i.e., *b, e, h, l, n*) are observed on H7, H8 and H9 appear to have occured coincidentally. To assess when the fault scarp formed, we flatten the stratigraphy on specific horizons (Figures 8 and 9). To demonstrate where the offset occurred we flatten on the top of the pre-event stratigraphy (Figure 8) and to determine the style of infill we flatten on a post-event layer (Figure 9). Cumulative offset from earthquakes *a-e* is shown in Figure 7c inset. To assess the offset of event *e*, we have to perform two functions. First, we flatten horizons that show no thickness variability across the hangingwall footwall boundary that are beneath the event horizon (Figure 8a). Based on our correlation with the onshore stratigraphy (Philibosian, 2007) the seafloor age at this time is 1260 AD. Next we flatten the horizon that fills the coseismic accommodation (Figure 8b). Such an approach shows that the event horizon, *e*, occurs in a layer of relatively low acoustic reflectivity immediately above a high-amplitude section (Figure 8, dashed red line).

Following this approach we flattened on horizons for events *b, e, h, l,* and *n* (Figure 9). For event *b*, the infilling stratigraphy exhibits high acoustic amplitude, onlaps the scarp and fills the coseismic accommodation. The (black) dashed line in Figure 9 represents the top of the sequence that fills the accommodation. Note the fault offset is at the top of the high amplitude acoustic package (1S) that represents the pre-event stratigraphy and shows no thickness variability across the fault (Figure 9a). For event *e*, the offset occurs above 4S within 3F within a unit of lower acoustic reflectivity (Figure 9b). Moving back in time, event *h* occurs at the top of 6S/5F. As mentioned above, it is often difficult to identify the boundary between the subaerial component of the previous lake and the initial flooding for the nascent lake (Figure 9c). Another event, *l*, is observed in 9S, where thin high-amplitude layers mantle a unit with low acoustic reflectivity (9L). Finally, the last of the five events observed on all three faults is event *n*, which occurs within 11L, a zone of low reflectivity. Flattening pre-event horizons and post-event infilling horizons yields insight into the style of deposition as well as the lake level when offset occurred (e.g., low-stand, S; flooding, F; high-stand, L).

5.4.4 Western Hinge-Zone

Vertical offset decreases towards the west as faults extend away from the SAF-IF extensional domain (Figures 10, 11 and 12). There also appears to be large differences in the earthquake recurrence interval from west to east. In the western hinge zone, because deformation is expressed as folding rather than distinct vertical offset, timing estimates were not straightforward and varied from line to line. Cumulative throw across 9S (Figure 11) provides comparisons of along-strike changes in vertical motion along the hinge zone.

Deformation distributed across H1-H6 is expressed as monocline folds rather than vertical offset (Figures 10 and 11). With the available data, it is difficult to distinguish between growth caused by multiple earthquakes, attenuation up-section into poorly consolidated material or from gradual infill of accommodation. Figure 12 is an example section that illustrates earthquake-timing estimates for faults H1 – H5. Seafloor offset on faults H3 and H4 is less than 20 cm, but can be correlated between profiles (Figure

11). Small offset and/or folding across the 1907 surface is observed on some faults (e.g., H2). Underlying fold growth is not detected until 3L or 4S, implying that prior to 1907 these faults do not show evidence for slip for several hundred years. The maximum displacement amongst faults H1-H4 measured over 6L-base (~830 AD) is ~1.7 m, yielding a vertical deformation-rate of ~1.5 mm/yr. Each of the faults in the western hinge (H1-H6) have nearly equal cumulative offset across the base of 9S of ~ 1.5 m with maximum displacement of ~2 m. The total subsidence since ~830 AD across faults H1-H5 is ~7.5 m, yielding a subsidence rate of ~6.3 mm/yr. Strata continues to diverge south of fault H5 (Figures 11 and 12). Alluvial fan aggradation in the northern portion of these profiles increases the relief (Figure 12). Areas of highly disturbed sediment, domes and sags are observed throughout the region (Figure 12).

5.4.5 Southern Faults

A series of faults to the southeast of the hinge-zone (S1-S4) offset stratigraphy in the upper 5 m, but deeper offsets are obscured by AWZs (Figures 7 and 13). Each of these faults exhibit down-to-the-southeast vertical offset. One segment, S2, has a clear seafloor scarp associated with the most recent event (MRE) that measured between 0.1 and 0.3 m in height (Figure 13). The scarp associated with fault S2 is steep with no overlying sediment. Total offset was measured on 15 profiles yielding an average of 0.4 ± 0.1 m. A CPT log near Figure 13 helps constrain the depth of sequence boundaries below the AWZ. Displacement during the penultimate event is observed across the top of layer 1L or bottom of 1S. Fault S1 shows subtle growth folding at the same displacement intervals as on S2. S1, S2 and a few additional un-named faults south of H9 (Figures 2 and 7) appear to have had multiple earthquakes in the post-1L sediments.

5.4.6 Northern Faults

Only a few faults are observed in the Holocene LC section to the north of the hinge zone. Numerous folds and faults, however, are observed in the underlying Brawley Formation (Brothers et al., 2009a). The age of these deformed strata is poorly constrained, but is inferred to be late Pleistocene. Reflections below the unconformity surface can be traced throughout most of the northern basin (Figures 3 and 14). Fault N1 (Figures 3) is expressed as a subtle syncline fold in the LC section but has significant deformation in the underlying Brawley Formation. This fault trends subparallel to the SAF for at least 16 km. Individual event offset and timing are difficult to ascertain, but appears to extend into 6L deposits and possibly younger. Burgman (1991) proposed a SAF parallel fault to explain transpression in Durmid Hill (Figure 1). Two north-trending faults along the northwestern shoreline (Figures 2 and 14) can be traced for only ~2.5 km before being obscured by AWZs. They predominantly deform layers below the LC section. Fold growth is observed in the LC section then increases dramatically in the underlying units. Based on growth patterns, N2 and N3 had at least 2 events during the last few thousand years (Figure 14). A subtle seafloor scarp on fault N4 near the northeastern shoreline is also observed.

5.4.7 Sediment Thickness and Subsidence

The regional bathymetry of the Salton Sea shows a northern and southern basin separated by a saddle. Isopach maps were constructed to examine the thickness of the various lake sequences (Figure 15c-e). Note the isopach maps are truncated to the south because shallow gas prevented imaging the lake sequences. Nevertheless, the spatial distribution revealed some interesting patterns. For example, the depocenter in all three isopach maps is shifted to the southeast from the present day deepest water depth (Figure 15). The sediment thickness in combination with the onshore stratigraphy were used to calculate the subsidence rates and sediment accumulation in the Salton Sea. Even though the depocenter for the lake sequences are offset from the bathymetry, it is clear the hinge-zone delineates the abrupt thickness increase to the south (Figure 15). Dipping strata appear to extend farther south towards the Salton Buttes and CPT soundings in the southern sea (Figure 16) indicate the stratigraphy continues to deepen to the south beneath the gas. Table 4 summarizes subsidence estimates over horizons 3L, 6L and 8L.

5.5 DISCUSSION

5.5.1 Lake Cahuilla Stratigraphy

The seismic CHIRP profiles capture the importance of Colorado River sedimentation in filling tectonic accommodation in the southern Salton Sea. The tectonic subsidence identified by Brothers et al. (2009) plays a large role in the deposition patterns observed in the Salton Sea. The regions north and south of the hinge-zone record different depositional processes due to differential relief and proximity to the Colorado River during lake-filling events. The region north of the hinge is mostly devoid of thick high acoustic amplitude packages inferred to be fan delta deposits (Figure 5). Ephemeral streams that drain local relief supply coarse-grained sediment to the northern basin during episodic storms. As such, the subaerial horizon in the northern part of the lake is a desiccation surface with locally derived fluvial sediment. In contrast in the southern sea, steep relief is far from the Salton Sea, and thus there is no mechanism to transport this coarse grained sediment from the distant relief to the basin (Figure 1).
In contrast, the rapidly subsiding southern sea is filled with proximal Colorado River deposits. Most of the sediment deposited by the Colorado River delta onlaps the hinge zone and back steps landward as the shoreline transgresses (Figure 5). Nevertheless, in lacustrine environments during arid episodes or when the Colorado River is not flowing, little sediment is supplied to the basin during lowstands. We surmise that the majority

of high amplitude packages that are observed at the base of each lake sequence in the southern Salton Sea are sourced from the Colorado River as flooding commences. Often it is difficult to identify the surface that separates the subaerial portion of the previous lake from the flooding stage of the nascent lake. Where possible we separate the subaerial component from flooding component of the strata, but in some units they are indistinguishable (e.g., 4S/3F and 6S/5F).

Assuming the entire flow of the Colorado River is diverted to the Salton Basin (Van De Kamp, 1973), the amount of time required to fill LC to high-shoreline is approximately 20 years. The transition from fan delta facies to deep-water lacustrine facies beneath the Salton Sea is probably coincident with the filling of the basin. Therefore, the base of each correlative lacustrine unit onshore and offshore is assumed to be equivalent in age. Van de Kamp (1973) estimated that once the Colorado River diverts back to the Gulf of California, Lake Cahuilla evaporates at ~1.8 m/yr, causing exposure beneath the Salton Sea to occur nearly 60 years later than at the high shoreline. Based on these relationships, we established a chronostratigraphic framework for the facies observed beneath the Salton Sea (Table 1). Based on the average sedimentation rate since ~830 AD the older, undated lake sequences are not expected to be older than 3,000 years.

Deposition is highly variable over century-long time scales. South of the hinge, 2S, 4S, 6S, and 9S are distinctive layers where thick, coarse-grained sediments appear to have accumulated very quickly. Based on the acoustic character and stratal geometry, it appears that 4S, 6S and 9S contain sediment that was deposited during flooding into a dry basin. The modern delta sedimentation rates and the estimated time required to fill Lake Cahuilla suggests that these coarse grained units accumulated in 10-20 years (Pratson et al., 2008). Intervals 2S, 3S, 5S, 7S, 10S, 11S, 12S and 13S are relatively thin, which suggests the Colorado River sediment was dispersed into a shallow lake. Migration of the Colorado River away from Lake Cahuilla is controlled by avulsion rather than the elevation of Lake Cahuilla's shoreline. Therefore, even though Lake Cahuilla may be full, the Colorado River may continue to supply sediment to the north for prolonged periods of time. Desiccation observed onshore at higher elevations does not always represent prolonged exposure at lower elevations, nor does it necessarily mean that a component of Colorado River flow did not still enter the basin. These intervals may simply record brief shoreline regressions at higher elevations around the basin (e.g., Coachella site at 3 m below the high-shoreline). For example, high-amplitude layers 2S and 3S appear to have been deposited when the LC shoreline dropped, resulting in basin-ward shift of coarse-grained material, but the deeper portions of the basin remained subaqueous.

Layer 2S thickens south of the hinge zone implying it formed when the Colorado River flow returned and deposited a thick fan delta sequence. Subunits within layers 2S and 4S fluctuate between high- and low-amplitude (Figures 5-7). These fluctuations are interpreted as localized parasequence sets formed during lobe-shifting and infilling of accommodation that results in along-shore variability between distal (low-amplitude) and proximal (high-amplitude) facies. Offshore imaging reveals at least six additional lake sequences that have not been logged at onshore sites (Philibosian, 2007). Longer paleoseismic records improve our estimates for recurrence intervals as well as fault interaction and distribution of strain. Coring beneath the Salton Sea and/or deeper excavation at the Coachella paleoseismic site to establish a depth transect at different elevations of Lake Cahuilla will provide a comprehensive stratigraphic model for constraining more paleoseismic events.

5.5.2 Earthquakes and Slip-Rates

To constrain the age of fault displacement, we locate the most recent event horizon, then flatten the entire section to that horizon in order to locate older displacement (Figures 8 and 9). Locating the event horizons also involved significant stratigraphic correlation and interpretation to identify onlap and divergence. Identifying event horizons was particularly difficult when offset occurred during high-stand intervals and displacement resulted in slight thickening of the fine-grained facies. Most accommodation was infilled during subsequent floods and coarse-grained deposition. The following measurements were made for faults H7, H8 and H9: (H7) 184 displacement measurements on 21 CHIRP sections, (H8) 16 measurements on 4 sections and (H9) 22 measurements on 4 sections. In total, we identified 25 vertical displacement events across these three faults since layer 14L was deposited.

Recurrence intervals for faults in the southern Salton Sea are relatively short (Table 2; Figures 16 and 17) and are comparable to recurrence estimates on the southern SAF (Philibosian, 2007). H7, H8, H9 and S1 each had events between ~1720 – 1907 that may have occurred around the same time as a number of paleoearthquakes on faults in and around the Salton Sea (Hudnut et al., 1989c; Hudnut and Sieh, 1989; Meltzner et al., 2006; Philibosian, 2007; Williams et al., 1990). Correlating the onshore events to offshore events is difficult and only a few events appear to be contemporaneous. We performed a detailed investigation of potential correlations, or synchronicity, between events offshore and events at the Coachella SAF site (Figures 16 and 17). From oldest to youngest, event h, observed on H7, H8 and H9 appears to correlate with event 5 observed on the SAF during flooding of lake 5 (Figures 16 and 17). Event 4 from Philibosian (2007) occurred during 5S may correlate with event f observed on H9. Given the best age estimates for onshore event 3 of 1280 and 1300 AD, and its position in the mid-section of 4S, this event does not appear to correlate with offshore event e (although this assumes a linear-rate of deposition during sub-aerial exposure). Event e is observed on H7, H8, and H9 and appears to occur at ~1360 AD, during lake 3 flooding. Nevertheless, the age estimate for event e is within uncertainty of event 3 from the onshore Coachella site. Of the five events observed on all three eastern hinge faults, only two potentially correlate with the onshore SAF events. Based on the youthful nature of the scarp across S2 during event a and the absence of overlying sediment drape, the MRE appears to have occurred during the last ~30-50 years. Folding of Salton Sea sediment on fault H7 also suggests recent deformation.

Clearly more investigations are required at different elevations in the basin to evaluate the coincident timing of events. The limited data precludes us from making any predictions about the hinge faults triggering the SAF or vise versa. There is potential for stress interaction between these fault systems (King et al., 1994). Stress triggering of the Superstition Hills Fault by events on cross-faults in the region has been observed (Hudnut et al., 1989b). Assuming strain is released seismically, the length and displacement-per-event on the hinge faults suggest they could produce events of magnitude 6.0-6.8. Simulations of such an event on H7 have shown that static shear stress along the SAF near Bombay Beach (Figure 1) would increase by more than 3 bars (Kilb et al., 2009). In our tectonic model, the hinge zone faults are accommodating, in large part, the extensional component of deformation and differential subsidence that is occurring in the southern Salton Sea. Consequently, these hinge faults may have a different recurrence interval and may not be coincident with events on the southern SAF. It is important to note, even amongst the hinge faults, events observed on one fault are not observed on adjacent faults, let alone the southern SAF.

Numerous crossings of multiple faults have revealed that the fault systems are complicated and three-dimensional. Paleoseismic studies need to examine multiple faults at different elevations within the Lake Cahuilla system. At this junction it is not possible to determine if the hinge faults trigger the southern SAF and thus control its rupture propagation direction. Despite limited correlation between onshore events and offshore events, the new data reveal a very robust correlation between events on the hinge zone faults and flooding events associated with Colorado River inflow (Figures 9, 16 and 17).

The Colorado River appears to also play an important role in modulating the earthquake cycle beneath the Salton Sea (Figures 9, 16 and 17). Rapid loading by sedimentation and water may change the stress conditions in the southern Salton Sea. Paleoearthquakes in the Salton Sea seem to cluster around times when the Colorado River was spilling into a dry basin causing a rapid transition from a subaerial to deep lacustrine environment. The correlation suggests a common process causes these faults to rupture in concert or release strain through clustered seismicity during flooding. Faults may be modulated more heavily by the flooding of the basin than by stress interaction amongst each other. Previous studies have noted similar recurrence intervals between earthquakes on the SAF and Lake Cahuilla high-stands (Luttrell et al., 2007).

Displacement timing in the western hinge-zone is difficult to constrain due to the subtle nature of deformation and absence of definitive event horizons (Figures 11 and 12). A strike-slip component of deformation is likely, but difficult to measure using two-dimensional profiles. Synclinal folding along faults may be evidence for strike-slip deformation, particularly along faults H8 and H9 (Figures 6 and 7), but the consistency in magnitude and direction of vertical displacement in the hinge zone suggests that extension is the dominant mode of deformation. Slip inversion and fold growth on H9 (Figure 7) may be evidence for a change in kinematics through time from an oblique-convergent to oblique-divergent sense of motion between 14L to 8L. H9 had an abrupt change in kinematics over an ~2,000 year time scale. This observation suggests that the style of deformation has changed quickly through time or faults alternate between different kinematic modes at different time periods.

The relationship between onshore and offshore faults remains poorly understood. Distinct 0.0 - 0.3 m high seafloor scarps along fault S2 and slight folds in Salton Sea sediments across faults S1, S3, and S4 suggest recent displacement. These faults trend ~N10°E and have a consistent down-to-the-southeast sense of slip. The1987 Elmore

Ranch Fault event recorded ~0.15 m of sinistral offset along a ~N40°E plane (Hudnut et al., 1989a; Sipkin, 1989). As the Elmore Ranch Fault enters the SAF-IF step-over its azimuth may adjust to accommodate extension, or these faults may be entirely independent of one another. Further mapping is required to understand the relationship of the southern faults to the Elmore Ranch Fault system. Aseismic creep and triggered slip have been observed on faults surrounding the Salton Sea, including the Extra Fault (Hudnut et al., 1989a; Lohman and McGuire, 2007; Lyons and Sandwell, 2003; Lyons et al., 2002; Meltzner et al., 2006). Some of the seafloor offsets observed, particularly along faults in the western hinge zone that project with the onshore Extra Fault, may be from triggered slip following large events in the region. Although evidence for fault displacement in the Salton Sea during discrete events is definitive, we cannot discount sudden aseismic slip as a possible slip mechanism. Such events have been observed in other extensional settings (Doubre and Peltzer, 2007) and given the high heat flux and young volcanic activity along the southern shoreline the Salton Sea may be experiencing similar processes.

The late Holocene to present deformation on the hinge-zone faults appears to be predominantly dip-slip in nature. The hinge faults trend approximately 50° oblique to the SAF and show consistent down-to-the-southeast vertical displacement despite minor along-strike jogs and bends. Furthermore, the vertical offset per event and vertical slip-rates are relatively large and thus accommodate a significant percentage of the strain transferred from the SAF to the Imperial Fault (Brothers et al., 2009a). The nearly flat sedimentary horizons deposited by Lake Cahuilla offer little opportunity for strike-slip faults to create topographic relief. To generate 7 m of throw by a strike-slip fault in this environment would require an unrealistic amount of horizontal offset during the given time interval. Nevertheless, we cannot exclude a component of strike-slip along these faults. In Figure 7, for example, fault H9 appears to have a component of strike slip in the region imaged by CHIRP profiles. The confluence of hinge faults and the SAF is expected to produce complicated deformation as strain is transferred between faults systems. Constraining the relative amounts of strike-slip versus dip-slip offset on faults in the Salton Sea requires further study.

Although many of the hinge faults have relatively high slip-rates, southward divergence and rotated beds indicate the basin is bounded by a down-to-the-northwest fault (or system of faults) with a significantly higher slip-rate. Brothers et al. (2009a) inferred subsidence rates up to 20 mm/yr during the last several hundred years. The ~10 mm/yr of subsidence across the hinge zone can be converted into ~6 mm/yr of horizontal extension (assuming 60° southeast dipping fault plane). In rift basins, between 20-50% of the total extension is typically distributed across secondary faulting in the hinge zone (Morley, 1995) implying between 12 – 30 mm/yr of extension is accommodated south of the hinge. It appears that at least 50% of the 23 mm/yr (Meade and Hager, 2005) of horizontal slip transferred across the SAF-IF pull-apart basin is accommodated by extension.

Faults discovered north of the hinge zone are poorly constrained and need to be studied further. N2 and N3 have had displacement during the last 2 kyr. Tight synclinal folding across fault N2 implies a large component of strike-slip. N3 may be a minor splay off the nearby SAF, whereas N2 may be a splay off the SAF that trends along the western side of the valley and east edge of the Santa Rosa Mountains. Onshore reconnaissance may improve mapping of these structures and their relationship to faults mapped in Pleistocene and older units (Dibblee, 1984). Farther southeast, fault N1 (Figure 3) is sub-parallel to the SAF and might help explain transpressional folding in Durmid Hill (Burgmann, 1991), although its slip rate appears relatively low.

5.6 CONCLUSIONS

This study has provided the first detailed look at Lake Cahuilla sedimentation and paleoseismic records in the Salton Sea. Future studies aimed at improving the age dating in sea are necessary to constrain the displacement history prior to ~830 AD. Deeper penetrating seismic reflection data will provide important constraints on the longer-term evolution of these faults and how they interact. The most significant results of this study are summarized below.

1. Correlation between high-amplitude reflections in CHIRP profiles and coarse-grained sediment layers in CPT soundings allow us to identify parasequences sets in Lake Cahuilla sediment beneath the Salton Sea. Correlative parasequences have been radiocarbon dated at onshore sites and provide a chronostratigraphic framework for acoustic stratigraphy back to ~830 AD. At least 14 Lake Cahuilla parasequences are observed in the Salton Sea. Not all Lake Cahuilla sequences are separated by desiccation events. Stratigraphic evidence suggests there were extending periods of lacustrine conditions that may have experience brief shoreline regressions.
2. Shoreline transgressions caused by Colorado River diversions into the Salton Basin result in rapid deposition that infills tectonically generated accommodation south of the hinge zone. Thick wedges of fan delta facies onlap the hinge zone and diverge southward.
3. Assuming strain is released seismically, the Salton Sea experiences moderate to large earthquakes every 100 - 200 years and the dominant mode of deformation is extension. Vertical slip rates along individual faults are over 3.4 mm/yr.
4. Displacement on hinge faults H7-H9 appears coincident with major flooding from the Colorado River. The onset of flooding appears to trigger events on the hinge faults within the sea. Earthquake 5 on the SAF appears to be synchronous with cross fault rupturing event h; earthquake 3 on the SAF appears to have preceded by several

decades rupturing of the cross faults during flooding event e, but this asynchronous behavior may not be true, but potentially explained by a rapid infilling of 4S at the Coachella site during the decade or so of rise time to highstand (e.g., storm driven sedimentation).

5. Given the proximity of these hinge faults to the SAF, static stress changes following displacement, either seismic or aseismic, on offshore faults may alter stress conditions along the southernmost SAF and promote a destructive northward propagating rupture (Olsen et al., 2006). Their roles as stress modulators need to be addressed by future research.

5.6 ACKNOWLEDGEMENTS

This work was funded by the State of California Department of Water Resources, Scripps Institution of Oceanography, UC Academic Senate, National Science Foundation (grants OCE-0112058 and EAR-0545250) and the Southern California Earthquake Center (grant 2008-08127). We would like to thank the Sonny Bono Salton Sea National Wildlife Refuge and the Salton Sea State Recreation Area for their hospitality and providing access to their facilities during data collection. We would also like to thank E. Aaron, L. Johnstone, J. McCullaugh, J. Dingler and numerous others for field assistance.

The text and figures from this chapter are being prepared for publication in: Brothers, D.S., Driscoll, N.W., Kent, G.M., Harding, A.J., Babcock, J.M, and Baskin, R.L., In Prep, Late Holocene earthquake and sedimentary history beneath the Salton Sea, Southern California. The dissertation author was the primary researcher and author of the submitted work. The co-authors directed and supervised that research, which forms the basis for this chapter.

5.7 REFERENCES

Becker, T.W., Hardebeck, J.L., and Anderson, G., 2005, Constraints on fault slip rates of the southern California plate boundary from GPS velocity and stress inversions: Geophysical Journal International, v. 160, p. 634-650.

Behr, W., Hudnut, K., Platt, J., Kendrick, K., Sharp, W., Fletcher, K., Finkel, R., and Rood, D., 2007, A revised slip rate estimate for the Mission Creek–Coachella Valley strand of the southern San Andreas fault at Biskra Palms Oasis, Indio, California: outhern California Earthquake Center Annual Meeting, Proceedings with Abstracts, v. 17.

Brothers, D.S., Driscoll, N.W., Kent, G.M., Harding, A.J., Babcock, J.M., and Baskin, R.L., 2009a, Tectonic evolution of the Salton Sea inferred from seismic reflection data: Nature Geoscience.

Brothers, D.S., Kent, G.M., Driscoll, N.W., Smith, S.B., Dingler, J.A., Harding, A.J., Seitz, G.G., Karlin, R., and Babcock, J.M., 2009b, New constraints on earthquake history and slip-rates on the West Tahoe-Dollar Point Fault, Lake Tahoe Basin, CA: Bulletin of the Seismological Society of America.

Bull, J.M., Minshull, T.A., Mitchell, N.C., Thors, K., Dix, J.K., and Best, A.I., 2003, Fault and magmatic interaction within Iceland's western rift over the last 9 kyr: Geophysical Journal International, v. 154, p. F1-F7.

Burgmann, R., 1991, Transpression Along the Southern San-Andreas Fault, Durmid Hill, California: Tectonics, v. 10, p. 1152-1163.

Danforth, W.W., 1997, Xsonar/ShowImage: A Complete System for Rapid Sidescan-Sonar Processing and Display: U.S. Geological Survey Open-File Report, v. 97-686, p. 99.

Dibblee, T.W., 1984, Stratigraphy and tectonics of the San Felipe Hlls, Borrego Badlands, Superstition Hills and vicinity: Imperial Basin- Tectonics, Sedimentation and Thermal Aspects; Society of Economic Paleontologists and Mineralogists, p. 31-44.

Doubre, C., and Peltzer, G., 2007, Fluid-controlled faulting process in the Asal Rift, Djibouti, from 8 yr of radar interferometry observations: Geology, v. 35, p. 69-72.

Fay, N.P., and Humphreys, E.D., 2005, Fault slip rates, effects of elastic heterogeneity on geodetic data, and the strength of the lower crust in the Salton Trough region, southern California: Journal of Geophysical Research-Solid Earth, v. 110, p. -.

Fialko, Y., 2006, Interseismic strain accumulation and the earthquake potential on the southern San Andreas fault system: Nature, v. 441, p. 968-971.

Fletcher, K.E., Sharp, W.D., Kendrick, K.J., and Hudnut, K., 2007, U-Series ages for the Biskra Palms alluvial fan and their implications for long-term slip-rate of the Coachella Valley segment of the San Andreas Fault, Southern California: GSA Annual Meeting, Paper No. 123-5.

Fumal, T.E., Rymer, M.J., and Seitz, G.G., 2002, Timing of large earthquakes since AD 800 on the Mission Creek strand of the San Andreas fault zone at Thousand Palms Oasis, near Palm Springs, California: Bulletin of the Seismological Society of America, v. 92, p. 2841-2860.

Hudnut, K., Seeber, L., Rockwell, T., Goodmacher, J., Klinger, R., Lindvall, S., and Mcelwain, R., 1989a, Surface Ruptures on Cross-Faults in the 24 November 1987 Superstition Hills, California, Earthquake Sequence: Bulletin of the Seismological Society of America, v. 79, p. 282-296.

Hudnut, K.W., Seeber, L., and Pacheco, J., 1989b, Cross-Fault Triggering in the November 1987 Superstition Hills Earthquake Sequence, Southern-California: Geophysical Research Letters, v. 16, p. 199-202.

Hudnut, K.W., Seeber, L., and Rockwell, T., 1989c, Slip on the Elmore Ranch Fault during the Past 330 Years and Its Relation to Slip on the Superstition Hills Fault: Bulletin of the Seismological Society of America, v. 79, p. 330-341.

Hudnut, K.W., and Sieh, K.E., 1989, Behavior of the Superstition Hills Fault during the Past 330 Years: Bulletin of the Seismological Society of America, v. 79, p. 304-329.

Kendrick, K.J., Morton, D.M., Wells, S.G., and Simpson, R.W., 2002, Spatial and temporal deformation along the northern San Jacinto fault, southern California: Implications for slip rates: Bulletin of the Seismological Society of America, v. 92, p. 2782-2802.

Kent, G.M., Babcock, J.M., Driscoll, N.W., Harding, A.J., Dingler, J.A., Seitz, G.G., Gardner, J.V., Mayer, L.A., Goldman, C.R., Heyvaert, A.C., Richards, R.C., Karlin, R., Morgan, C.W., Gayes, P.T., and Owen, L.A., 2005, 60 k.y. record of extension across the western boundary of the Basin and Range province: Estimate of slip rates from offset shoreline terraces and a catastrophic slide beneath Lake Tahoe: Geology, v. 33, p. 365-368.

Kilb, D., Brothers, D.S., Lin, G.Q., Kent, G.M., Newman, R., and Driscoll, N.W., 2009, On The Dichotomy Between Geologic And Seismologic Signatures in Data From the Salton Sea Region in Southern California Southern California Earthquake Center Annual Meeting, v. Proceedings and Abstracts.

King, G.C.P., Stein, R.S., and Lin, J., 1994, Static Stress Changes and the Triggering of Earthquakes: Bulletin of the Seismological Society of America, v. 84, p. 935-953.

Lamarche, G., Barnes, P.M., and Bull, J.M., 2006, Faulting and extension rate over the last 20,000 years in the offshore Whakatane Graben, New Zealand continental shelf: Tectonics, v. 25, p. -.

Lohman, R.B., and McGuire, J.J., 2007, Earthquake swarms driven by aseismic creep in the Salton Trough, California: Journal of Geophysical Research-Solid Earth, v. 112, p. -.

Luttrell, K., Sandwell, D., Smith-Konter, B., Bills, B., and Bock, Y., 2007, Modulation of the earthquake cycle at the southern San Andreas fault by lake loading: Journal of Geophysical Research-Solid Earth, v. 112, p. -.

Lyons, S., and Sandwell, D., 2003, Fault creep along the southern San Andreas from interferometric synthetic aperture radar, permanent scatterers, and stacking: Journal of Geophysical Research-Solid Earth, v. 108, p. -.

Lyons, S.N., Bock, Y., and Sandwell, D.T., 2002, Creep along the imperial fault, southern California, from GPS measurements: Journal of Geophysical Research-Solid Earth, v. 107, p. -.

McHugh, C.M.G., Seeber, L., Cormier, M.H., Dutton, J., Cagatay, N., Polonia, A., Ryan, W.B.F., and Gorur, N., 2006, Submarine earthquake geology along the North Anatolia Fault in the Marmara Sea, Turkey: A model for transform basin sedimentation: Earth and Planetary Science Letters, v. 248, p. 661-684.

Meade, B.J., and Hager, B.H., 2005, Block models of crustal motion in southern California constrained by GPS measurements: Journal of Geophysical Research-Solid Earth, v. 110, p. -.

Meltzner, A.J., Rockwell, T.K., and Owen, L.A., 2006, Recent and Long-Term Behavior of the Brawley Fault Zone, Imperial Valley, California: An Escalation in Slip Rate?: Bulletin of the Seismological Society of America, v. 96, p. 2304-2328.

Morley, C.K., 1995, Developments in the structural geology of rifts over the last decade and their impact on hydrocarbon exploration: From Lambiase, J.J. (ed), Hydrocarbon Habitat in Rift Basins, Geological Society Special Publications, v. 80, p. 1-32.

Olsen, K.B., Day, S.M., Minster, J.B., Cui, Y., Chourasia, A., Faerman, M., Moore, R., Maechling, P., and Jordan, T., 2006, Strong shaking in Los Angeles expected from southern San Andreas earthquake: Geophysical Research Letters, v. 33, p. -.

Philibosian, B., 2007, Paleoseismology of the San Andreas Fault at Coachella, California: Master's Thesis, University of Oregon.

Pratson, L., Hughes-Clarke, J., Anderson, M., Gerber, T., Twichel, D., Ferrari, R., Nittrouer, C., Beaudoin, J., Granet, J., and Crockettt, J., 2008, Timing and patterns of basin infilling as documented in Lake Powell during a drought: Geology, v. 36, p. 843-846.

Robertson, P.K., 1990, Soil Classification Using the Cone Penetration Test: Canadian Geotechnical Journal, v. 27, p. 151-158.

Rockwell, T., Loughman, C., and Merifield, P., 1990, Late Quaternary Rate of Slip Along the San-Jacinto Fault Zone near Anza, Southern California: Journal of Geophysical Research-Solid Earth and Planets, v. 95, p. 8593-8605.

Schroeder, R.A., Orem, W.H., and Kharaka, Y.K., 2002, Chemical evolution of the Salton Sea, California: nutrient and selenium dynamics: Hydrobiologia, v. 473, p. 23-45.

Sieh, K.E., and Williams, P.L., 1990, Behavior of the Southernmost San-Andreas Fault during the Past 300 Years: Journal of Geophysical Research-Solid Earth and Planets, v. 95, p. 6629-6645.

Sipkin, S.A., 1989, Moment-Tensor Solutions for the 24 November 1987 Superstition Hills, California, Earthquakes: Bulletin of the Seismological Society of America, v. 79, p. 493-499.

URS, 2004, Preliminary in-sea geotechnical investigation, Salton Sea Resoration Project Report, Riverside and Imperial Counties, California, p. 399.

Van De Kamp, P.C., 1973, Holocene Continental Sedimentation in Salton-Basin, California - Reconnaissance: Geological Society of America Bulletin, v. 84, p. 827-848.

Van Wagoner, J.C., and Bertram, G.T., 1995, Sequence Stratigraphy of Foreland Basin Deposits: Tulsa, American Association of Petroleum Geologists, 453 p.

Williams, P.L., Sykes, L.R., Nicholson, C., and Seeber, L., 1990, Seismotectonics of the Easternmost Transverse Ranges, California - Relevance for Seismic Potential of the Southern San-Andreas Fault: Tectonics, v. 9, p. 185-204.

Table 5-1: Lake Cahuilla flooding and desiccation cycles from Philibosian (2007). Offshore parasequences are expected to represent longer subaqueous intervals due to an ~60-year time difference between dessiccation at 9m and potential dessication deeper in the basin. The chronostratigraphic model represents the time required to deposit each layer based on radiocarbon dates and the estimated ages have significant uncertainty (see Philibosian, 2007).

Table 1: Onshore-Offshore Chronostratigraphic Correlation						
	Coachella Site (9 m elevation)			**Seafloor (-85 m elevation)**		
Layer	Depositional Interval (Calendar Date AD)		Duration (years)	Depositional Interval (Calendar Date AD)		Duration (years)
SS	N/A	N/A	N/A	1907	present	100
1S	Present	1720	290	1907	1720	190
1L	1720	1650	70	1720	1630	90
2S	1650	1620	30	Regression, but no desiccation		
2L	1620	1480	140	1680	1460	220
3S	1480	1460	20	Regression, but no desiccation		
3L	1460	1380	80	1520	1360	160
4S	1380	1200	180	1360	1260	100
4L	1200	1150	50	1260	1130	130
5S	1150	1000	150	1130	1060	70
5L	1000	?	?	1060	?	?
6S	?	?	?	?	?	?
6L	?	850	150	?	830	230
7S	850	?	?	830	?	?

*Assume 20 years are required to fill the lake to 13 m and at a desiccation rate of 1.8 m/yr, ~60 years are required to dry lake.
**1770 younger bound on 1L and 1720 older bound on 1S are based on reports from the 1770 Anza expedition, in which no lake existed in the basin (Philibosian, 2007).

Table 5-2: Paleoearthquake offset and timing estimates. *n* represents the number of measurements. The timing estimates are basded on the chronostratigraphic model presented in Table 1. Age bounds incorporate the total uncertainty for each given depositional unit at the Coachella site. Best estimates extrapolate a narrower age range based on the positioning of the event within a given stratigraphic unit.

Table 2. Earthquake Measurements: Offset and Timing Estimates

	Event	Layer	n	Mean offset (m)	Age Bounds (Year AD)*	Preferred Age (Year AD)	Comment
Fault: H7	a	SS	21	0.4 ± 0.2	1907 - 2006	Post 1980	Recent SS offset, seafloor folding
	b	1S	21	0.5 ± 0.2	1680 - 1905	1720 - 1905	Likely after subaerial deposition in 1S
	d	3L	21	0.8 ± 0.3	1380 - 1460	1430 - 1460	Upper third of 3L
	e	4S/3F	19	1.0 ± 0.2	1260 - 1380	1360 - 1380	During 3L flooding
	g	5L	19	0.6 ± 0.1	950 - 1060	970 - 1060	Mid section of 5L
	h	6S/5F	15	0.7 ± 0.1	830 - 1060	900 - 930	During 5L flooding
	i	8L	18	0.7 ± 0.2	?	?	Mid-section of 8L
	j	9S/8F	18	0.5 ± 0.3	?	?	During 8L flooding
	k	10L	16	0.8 ± 0.2	?	?	Later half of 10L
	l	11L	16	0.8 ± 0.2	?	?	Early part of 11L
Fault: H8	b	1S	4	0.3 ± 0.1	1680 - 1907	1720 - 1800	Early part of 1S
	e	4S/3F	4	0.5 ± 0.2	1260 - 1380	1360 - 1380	During 3L flooding
	h	6S/5F	4	0.3 ± 0.2	830 - 1060	900 - 930	During 5L flooding
	j	9S/8F	4	0.5 ± 0.1	?	?	During 8L flooding
	l	11L		0.5 ± 0.1	?	?	Within 11L
Fault: H9	b	1S	4	0.5 ± 0.2	1680 - 1905	1720 - 1905	Likely after subaerial deposition
	c	2L	4	0.5 ± 0.1	1480 - 1620	1480 - 1520	Early part of 2L
	e	4S/3F	4	0.6 ± 0.1	1260 - 1380	1360 - 1380	Later part of 4S, during flooding into 3L
	f	4L	3	0.9 ± 0.1	1150 - 1200	1130 - 1180	Early third of 4L
	g	5L	1	0.2 ± 0.1	950 - 1060	970 - 1060	Mid-section 5L
	h	6S/5F	1	0.4 ± 0.1	830 - 1060	850 - 950	Early 6S or upper 6L
	i	8L	2	0.1 ± 0.1	?	?	Mid-section of 8L
	j	9S/8F	2	-0.3 ± 0.2	?	?	During 8L flooding
	l	11L	1	-0.5 ± 0.1	?	?	Mid section of 11L
	m	13L	1	-0.4 ± 0.1	?	?	Mid section of 13L
Fault: E2	a	SS	15	0.4 ± 0.1	1907 - 2006	Post 1980	Well-defined seafloor scarp
	b	1S	10	0.4 ± 0.1	1680 - 1905	1720 - 1905	Appears to be within 1S

Table 5-3: Subsidence rates across profiles shown in Figure 15.

Table 3: Subsidence Rates				
Horizon	**Approx. Age (years)**	**Profile**	**Differential Subsidence**	**Subsidence Rate (mm/yr)**
3L	650	A	4.1	6.3
3L	650	B	6.7	10.3
6L	1180	A	11.4	9.7
8L	?	A	13.4	?

*Age is given as years before 2010, contrary to convention, because sedimentation has continued to present.

Figure 5-1: Regional map of the Salton Trough. Map units: active faults (black lines), seismicity since 1983 (red dots; Lin et al., 2007), selected paleoseismic sites (red stars), Coachella Paleoseismic site from Philibosian (2007; large red star), volcanoes (orange craters). The Lake Cahuilla high shoreline (light blue) and the Salton Sea occupy the northern trough, separted from the Gulf of California by the Colorado River delta. Inset (B): plate boundary schematic of the transition between transpression the San Andreas Fault (SAF) system (red shades) and transtension of the Gulf of California rifted margin (pull-apart basins shaded blue). The Salton Sea covers part of the pull-apart basin formed at a step-over between the SAF and Imperial Fault (IF). Abbreviations: San Jacinto Fault, SJF; Extra Fault Zone, EFZ; Elmore Ranch Fault, ERF; Cerro Prieto Fault, CPF; SD, San Diego.

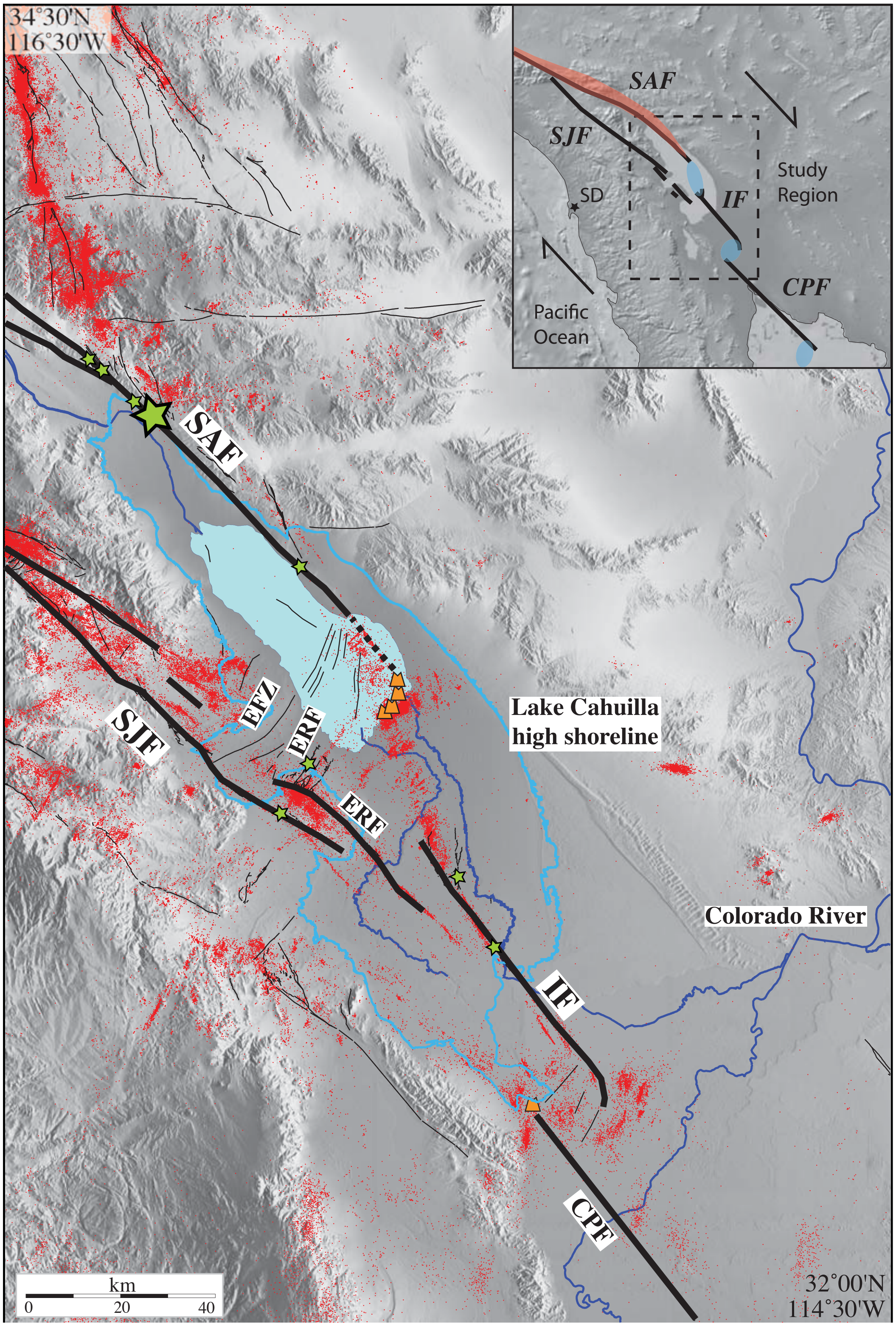

34°30'N
116°30'W
SAF
SJF
SD
IF
Study
Region
CPF
Pacific
Ocean
SAF
EFZ
ERF
ERF
SJF
Lake Cahuilla
high shoreline
Colorado River
IF
CPF
km
0
20
40
32°00'N
114°30'W

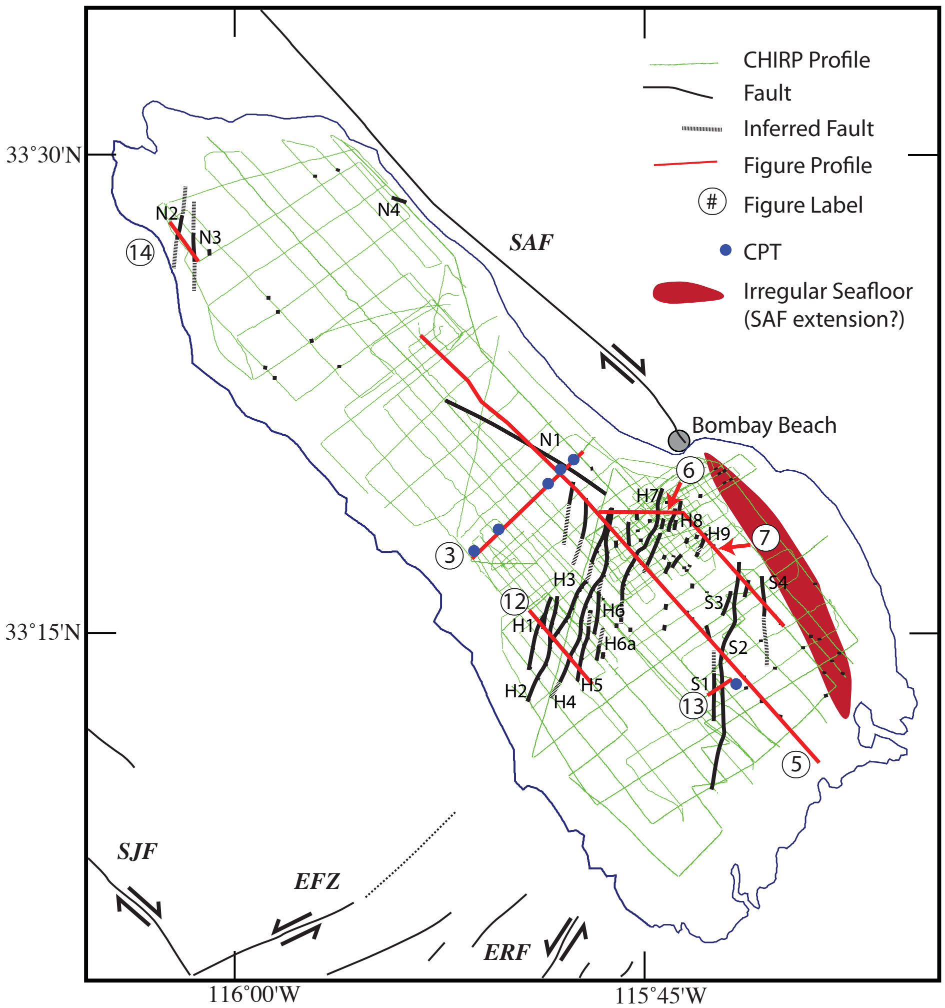

Figure 5-2: Survey map. Over 1,000 line-km of seismic CHIRP data were acquired between 2006 - 2009. Faults discovered in this study are labeled according to their geographic and/or structural position. "H" faults are considered part of the tectonic hinge-zone that bounds extension in the southern half of the Salton Sea (Brothers et al., 2009a). Southern ("S") and northern ("N") faults were also identified in sub-bottom sediments. Cone penetration test (CPT) data are from URS (2004) and were used to ground-truth sedimentary horizons imaged in seismic profiles. The (red) shaded region denotes a region of irregular seafloor topography and fluid venting. Numerous craters, pock marks and scarps in this region and may be related to the southernmost extension of the SAF. CHIRP profiles in forthcoming figures are numbered denoted as red lines.

Figure 5-3: Type section used to define Lake Cahuilla chronostratigraphy. A) Uninterpreted CHIRP profile with cone penetration test (CPT) logs superimposed on acoustic horizons. Inset shows location (thick black line). CPT logs contain two columns separated by vertical black lines. On the left is soil behavior type (SBT) and the right is normalized SBT. Normalized cone data (right column) account for increasing overburden stress with depth as measured by pore pressure changes (Robertson, 1990). Overall, both columns at each site reveal similar trends. CPTs show increased sand components moving shoreward, which that correlates with increased acoustic reflectivity in CHIRP profiles. B) Interpreted profile with CPT color key. Inset shows enlarged CHIRP section highlighting onlapping and downlapping coarse grained facies. Downlap records locally sourced sediment from ephemeral streams and fan deltas. Colors represent Lake Cahuilla sedimentary sequences and each sequence is number from 1-14. Stippled column highlights the high-stand (white with dashed lines) from low-stand and fan delta material (gray shaded layers). High-amplitude layers are interpreted as containing both coarse-grained low-stand deposits and fluvial fan-delta deposits associated with Colorado River flooding. Distinguishing between the two is difficult (see text). Dashed box is enlarged section in Figure 5. Dashed brown line marks the approximate boundary between Holocene Lake Cahuilla section (CFm) and Pleistocene (?) Brawley Formation (BFm). Folded strata along fault N1 (red lines) are observed in the CFm and BFm. Dashed box is section shown in Figure 4.

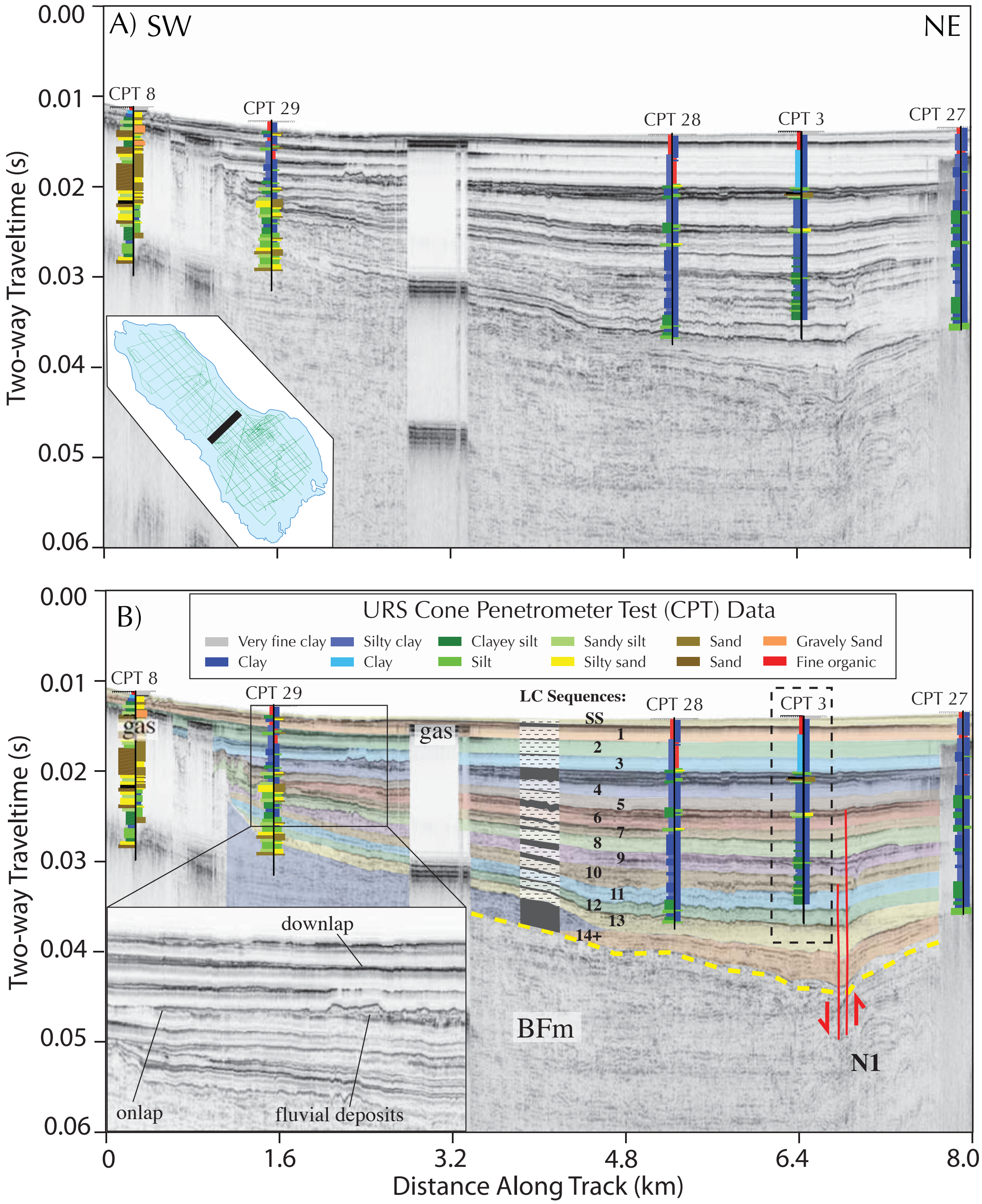

A) SW
NE
CPT 8
CPT 29
CPT 28
CPT 3
CPT 27
Two-way Traveltime (s)
0.00
0.01
0.02
0.03
0.04
0.05
0.06
B)
URS Cone Penetrometer Test (CPT) Data
Very fine clay
Clay
Silty clay
Clay
Clayey silt
Silt
Sandy silt
Silty sand
Sand
Sand
Gravely Sand
Fine organic
gas
LC Sequences:
SS
1
2
3
4
5
6
7
8
9
10
11
12
13
14+
downlap
onlap
fluvial deposits
BFm
N1
0
1.6
3.2
4.8
6.4
8.0
Distance Along Track (km)

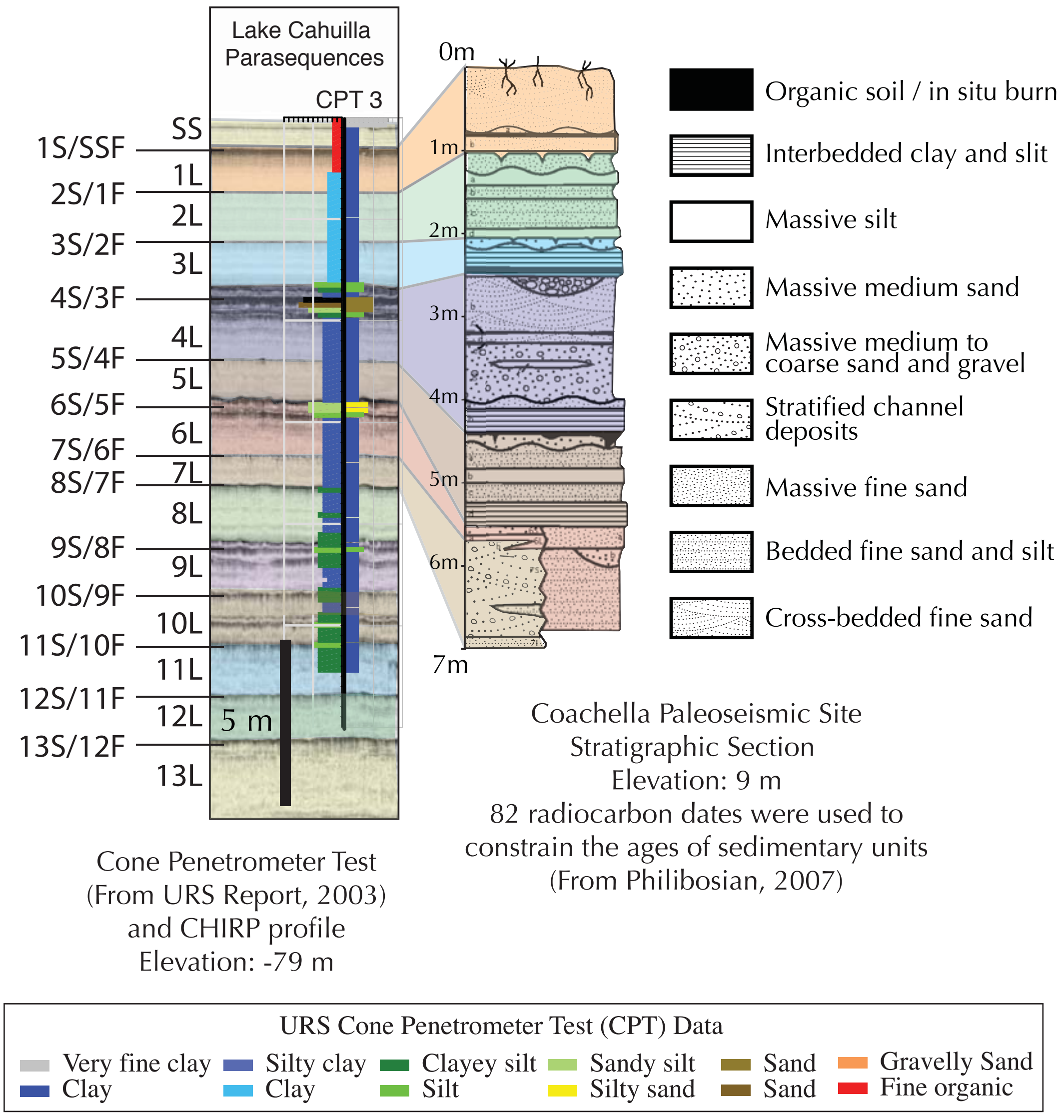

Figure 5-4: Chronostratigraphic correlations between seismic and lithostratigraphy in the Salton Sea and radiocarbon dated Lake Cahuilla sediments at the Coachella Paleoseismic site. Onshore stratigraphic column (right) is modified from Philibosian (2007). Within each Lake Cahuilla sequence, high stand deposits are labeled "L" and lowstand/flood deposits are labeled "S/F". Fine grained, low amplitude layers 1L, 2L and 3L are separated by relatively thin 2S/1F and 3S/2F layers. CPT soundings detect 2S/1F, 3S/2F and 5S/4F as distinct silt/sand layers closer to the shoreline (Figure 3), but they are not detected by CPTs at this location. Philibosian (2007) defined 4S onshore as a thick accumulation of fluvial and aeolian deposits that was deposited during prolonged subaerial exposure. Offshore, 4S/3F is also a distinct marker bed characterized by high reflectivity and sand/silt components. 6S/5F is the oldest layer that can be correlated to onshore deposits. See Table 1 for lake chronology.

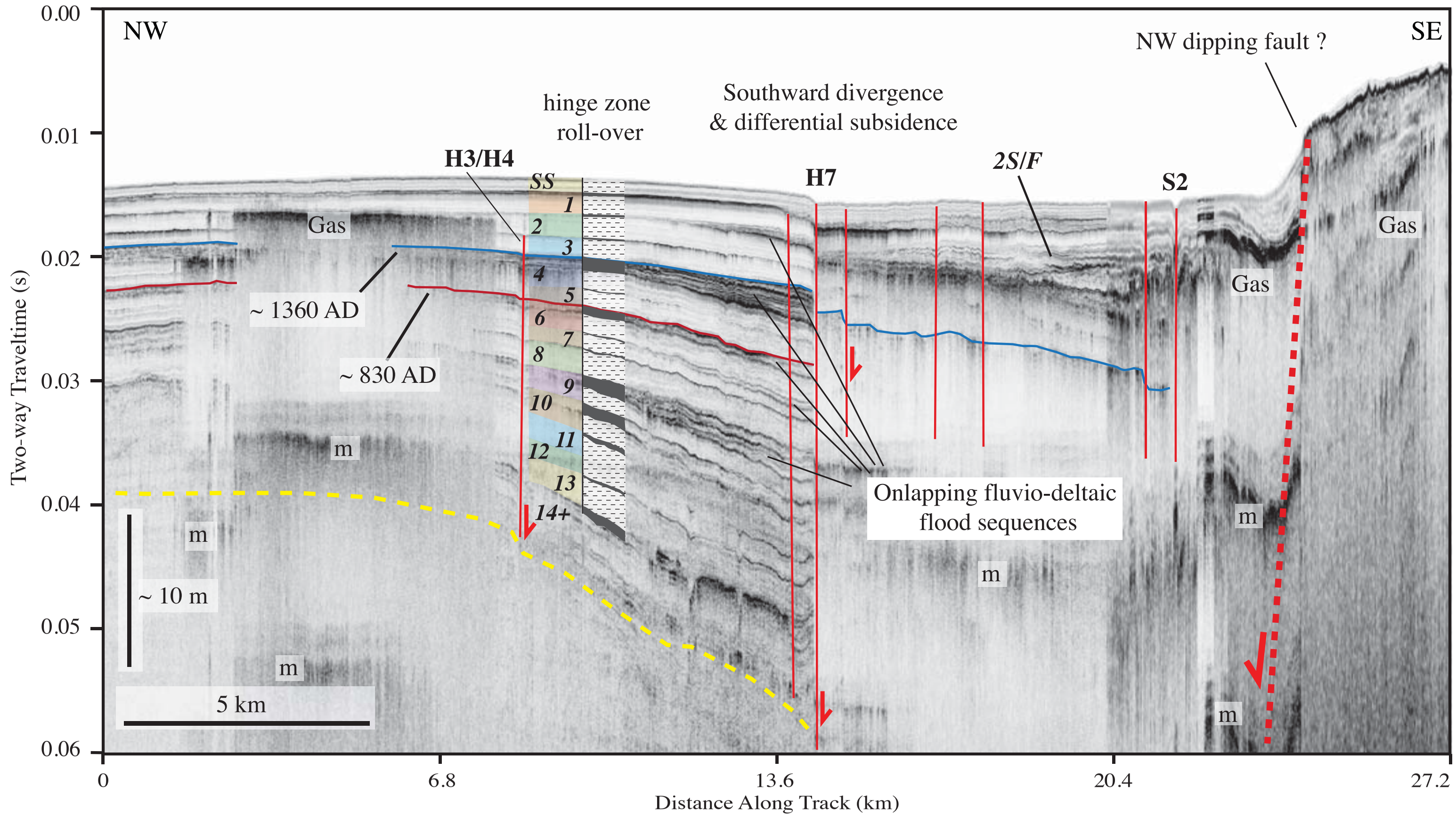

Figure 5-5: Profile spanning the tectonic hinge-zone and southern Salton Sea extension. Stratigraphy diverges south of the hinge, infilling differential subsidence and accommodation along an inferred down-to-the northwest normal fault system (Brothers et al., 2009a). Gas charged sediments limits penetration south of fault H7, but the 4S surface appears to continue to diverge (dark cyan).

Figure 5-6: Type section over faults H7 and H8. More than ten events are identified along H7 and five on H8 based on growth patterns. Large black arrows denote cumulative offset across the base of 13L. Alternating white and black arrows point to event horizons on the footwall and hangingwall. Earthquakes with the same lettering on separate faults appear to have occurred within the same stratigraphic interval. See Table 2 for earthquake timing and offset measurements.

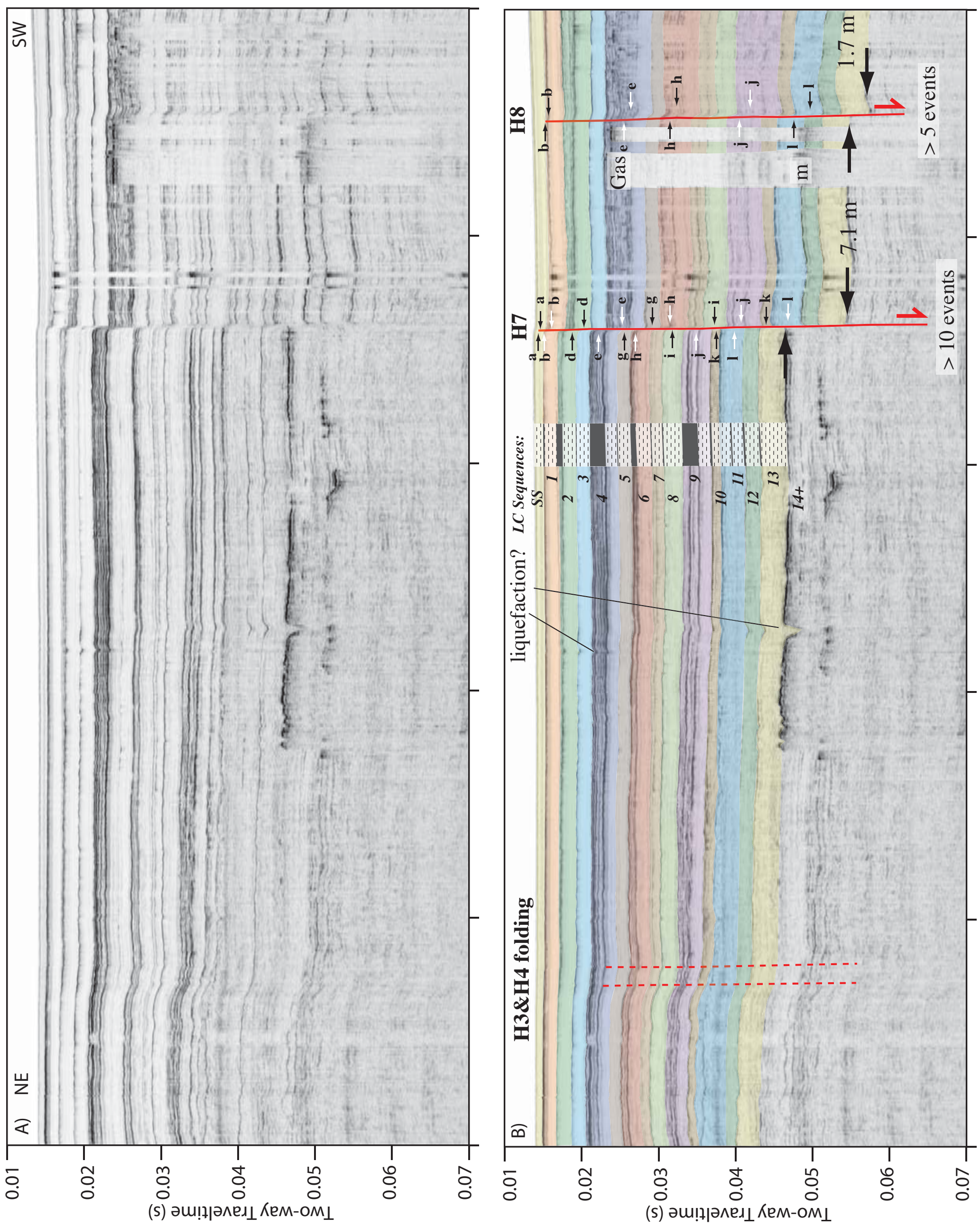

A)
NE
SW
Two-way Traveltime (s)
0.01
0.02
0.03
0.04
0.05
0.06
0.07
B)
H3&H4 folding
liquefaction?
LC Sequences:
SS
1
2
3
4
5
6
7
8
9
10
11
12
13
14+
H7
H8
Gas
m
> 10 events
> 5 events
7.1 m
1.7 m
Distance Along Track (km)
0
1.0
2.0
3.0
4.0
5.0

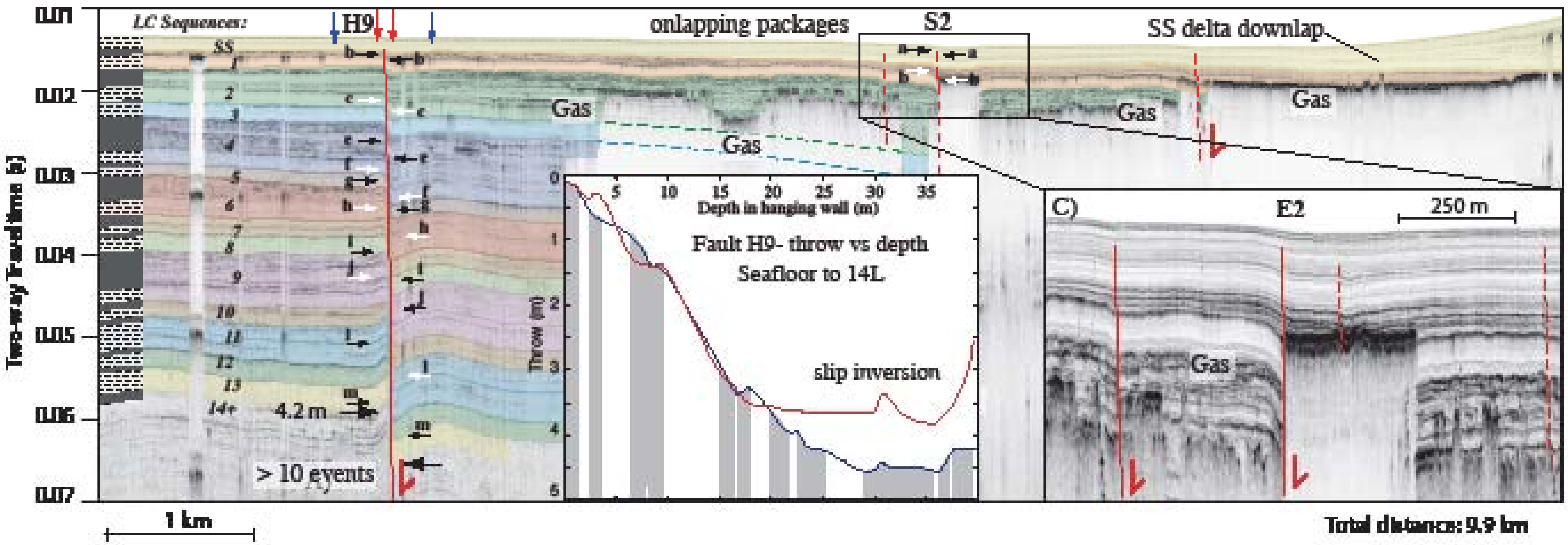

Figure 5-7: Type section of southern sea highlighting faults H9 and S2. Alternating white and black arrows point to event horizons on the footwall and hangingwall from which displacement-per-event estimates were made. Despite the limited penetration due to gas-charged sediment, the top of parasequence 1 (orange layer) has a southward dip at the end of the line, suggesting that rapid subsidence and southward divergence continues beneath the gas-prone sediment. (B) Throw versus depth plot highlighting the fold growth and slip inversion on fault H9 below Lake Cahuilla sequence 7, which may be indicative of strike-slip motion and/or a change from oblique-convergent to oblique-divergent deformation. White and gray shades represent lowstand/flood and highstand deposits, respectively. The blue and red lines correspond to the location of throw and depth measurements relative to the fault. The red profile was measured within 50 m of the fault plane (red arrows at top of CHIRP profile) and the blue profile was measured ~200 m away from the fault on either side. (C) Enlarged section of fault S2. The most recent event occurred within the Salton Sea time period (last 100 years). Gas termination at the fault suggests fault planes provide fluid migration pathways.

Figure 5-8: Enlarged section across fault H7 (Figure 6) to highlight displacement and sedimentary infill during 3S flooding. (A) Stratigraphic section prior to event *e* (dashed red-line). Layer 4S had been deposited (basal high-amplitude unit) and Lake 3 had begun to fill, depositing subunits 4S/3F-c and -b (See Figure 6). Hanging wall growth and/or onlap are not observed below the event horizon. (B) End of lake 3 flooding and coarse-grained deposition. Note the hangingwall onlap and thickening in 4S/3F-a,b that infilled accommodation that formed during event *e*. (C) Raw section representing present-day stratigraphy. Cumulative throw across event *e* horizon represents cumulative throw from events *a-e.* Based on the estimated amount of time required to fill Lake Cahuilla during Colorado River diversions and modern sedimentation rates in the Colorado River delta at Lake Powell (Pratson et al., 2008), the flood deposits may accumulate as quickly as 20 years.

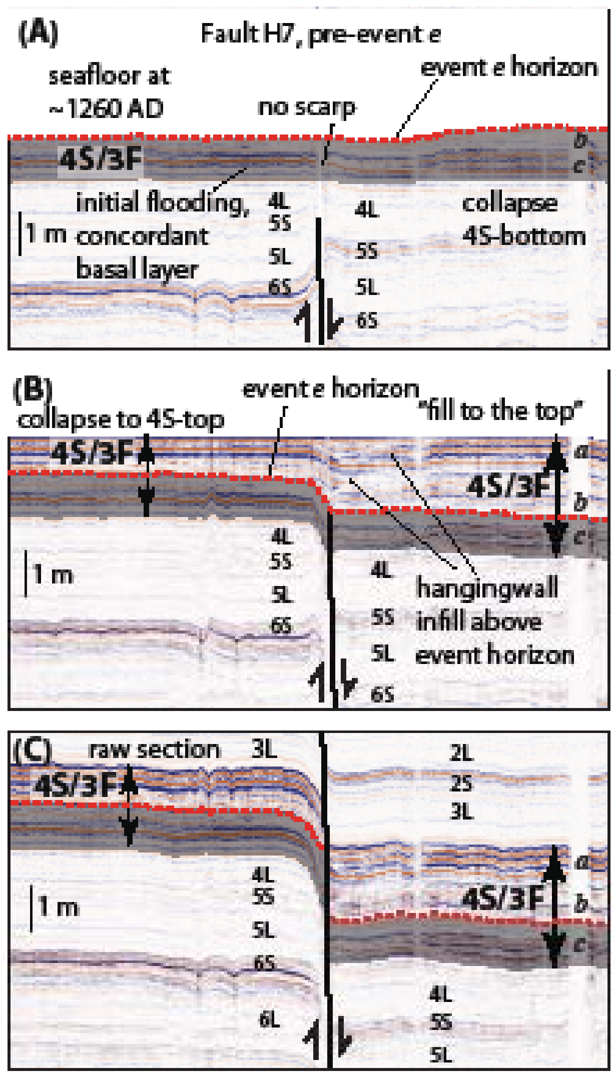
(A)
Fault H7, pre-event e
seafloor at ~1260 AD
event e horizon
no scarp
4S/3F
initial flooding, concordant basal layer
1 m
4L
5S
5L
6S
collapse 4S-bottom
(B)
event e horizon
collapse to 4S-top
"fill to the top"
4S/3F
hangingwall infill above event horizon
(C)
raw section
3L
2L
2S
6L

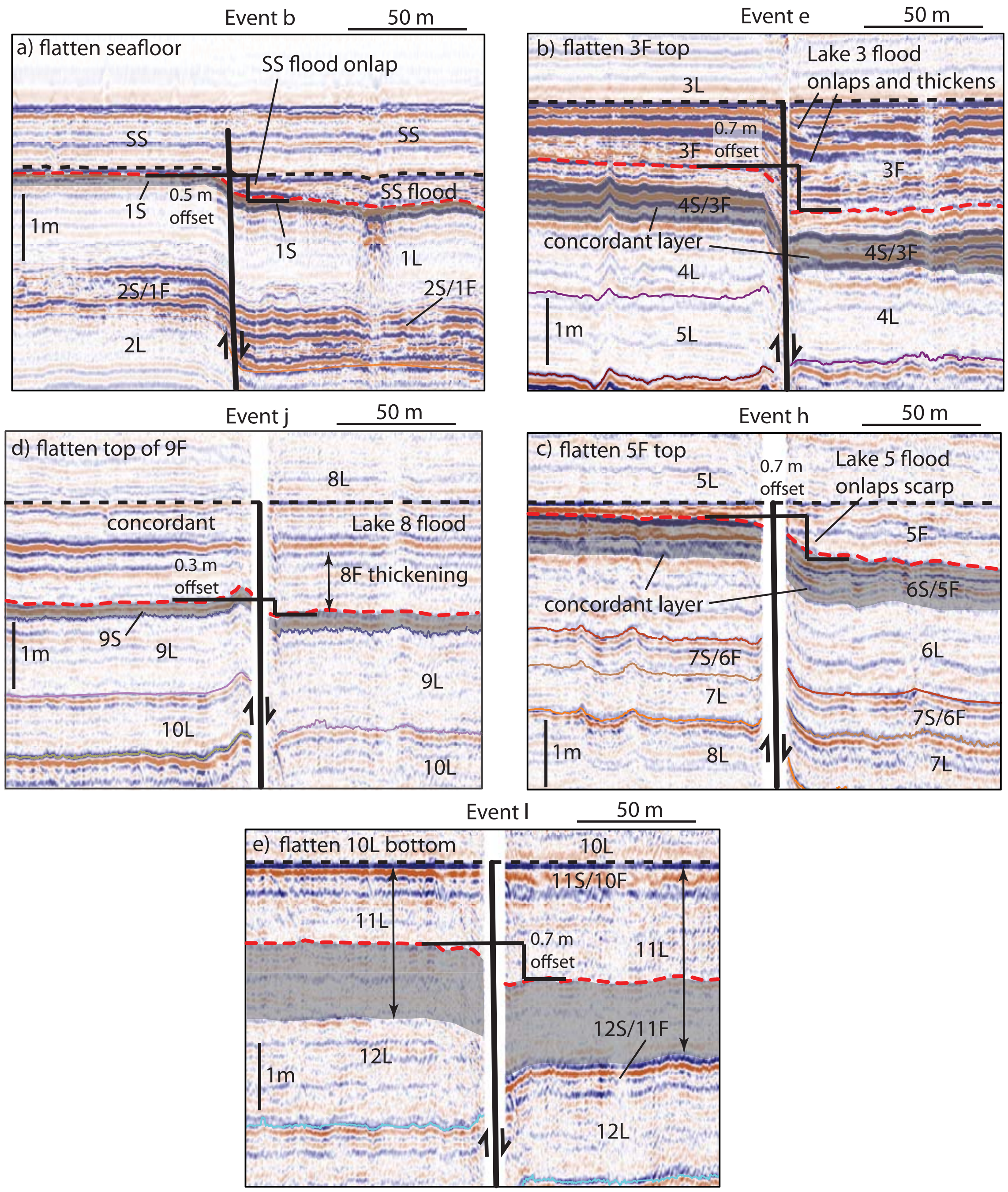

Figure 5-9: Example sections across fault H7 illustrating evidence for events *b*, *e*, *h* ,*j*, and *l*. Each of these events is observed on faults H7, H8 and H9. Event *b* is also observed on faults S1 and S2. Based on the stratal geometry and acoustic character, events *b*,*e*,*h*, and *j* appear to have occurred during flooding episodes. Event *l* occurred during prolonged high-stand episode 11L.

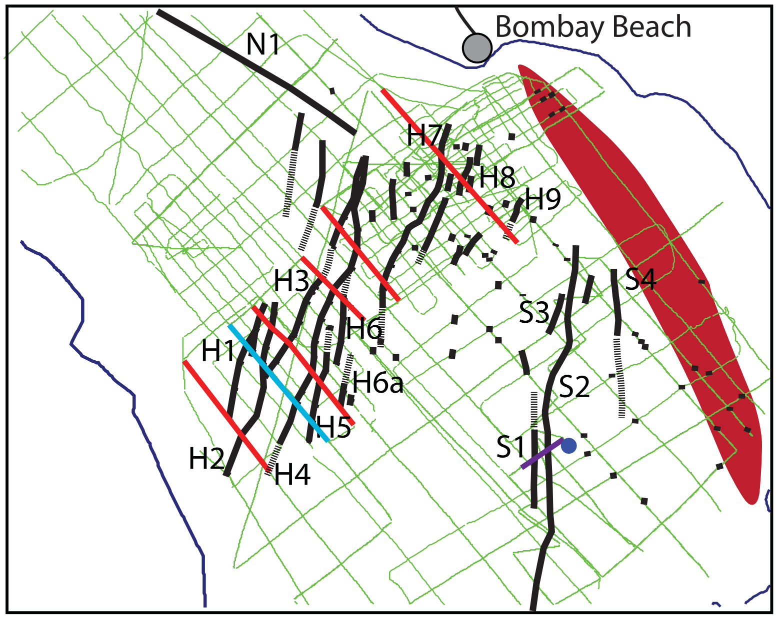

Figure 5-10: Location map for CHIRP profiles in Figures 11, 12 and 13. Red lines represent profiles shown in Figure 11. The Blue line over faults H1-H5 is shown in Figure 12 and the purple line over faults S1 and S2 is shown in Figure 13.

Figure 5-11: Panel of CHIRP profiles across hinge zone faults illustrating the structural variation from west (top) to east (bottom). Vertical exaggeration is not fixed between profiles. Fault segments and profile locations are shown in Figures 2 and 10. Colored lines highlight marker beds: 4S top (blue; 1360 AD) and 9S (Purple; age unknown). Faults to the west have less throw and do not exhibit the distinctive growth patterns seen along faults to the east. Subsidence is observed to increase from west to east as faults extend into the SAF-IF extensional step-over (Figure 1). Deformation in the western panels is expressed as subtle down-to-the-southeast monocline folds whereas deformation in the east is expressed as distinct faulting and vertically offset horizons. Minor deformation observed in Salton Sea sediments may be related to triggered slip observed on faults west of the Salton Sea (Hudnut et al., 1989a).

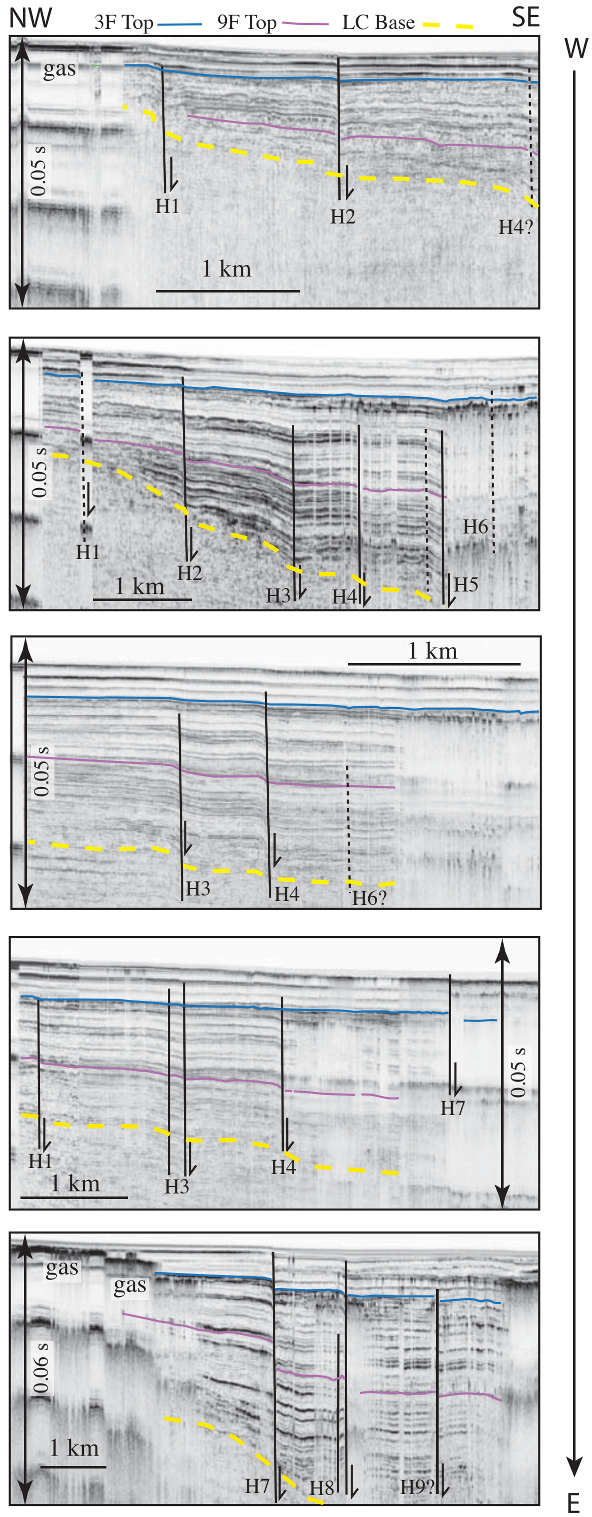

NW
3F Top
9F Top
LC Base
SE
W
E
gas
0.05 s
H1
H2
H4?
1 km
H3
H4
H5
H6
H6?
H7
0.06 s
H8
H9?

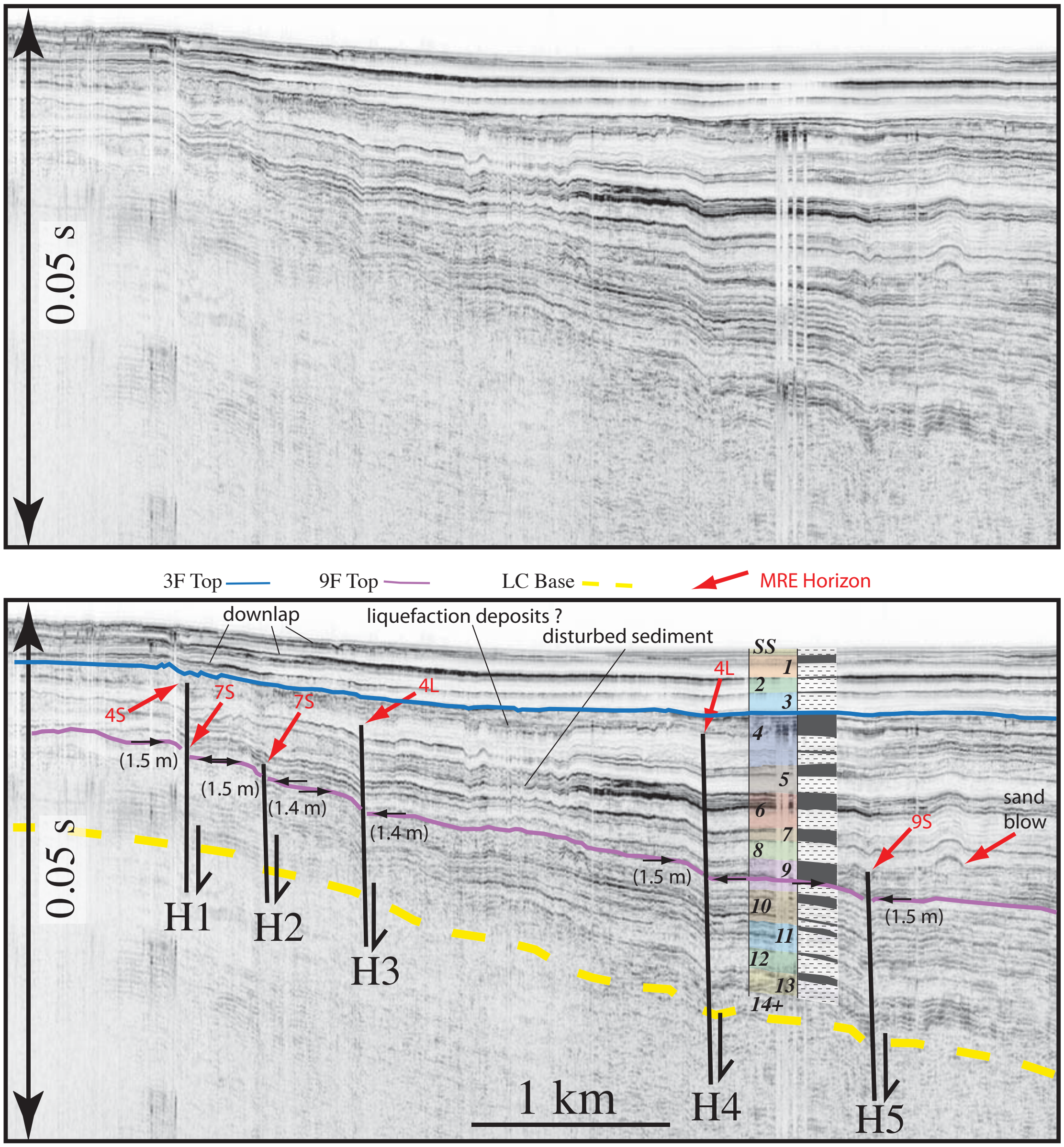

Figure 5-12: Type section across western hinge faults. Red arrows point to approximate event horizons. Due to the subtle nature of deformation, identifying event horizons is equivocal. Disturbed sediment and liquefaction dome (“sand blow”) may be seismically generated. Vertical folding over the base of 9S is consistently ~1.5 m for each fault.

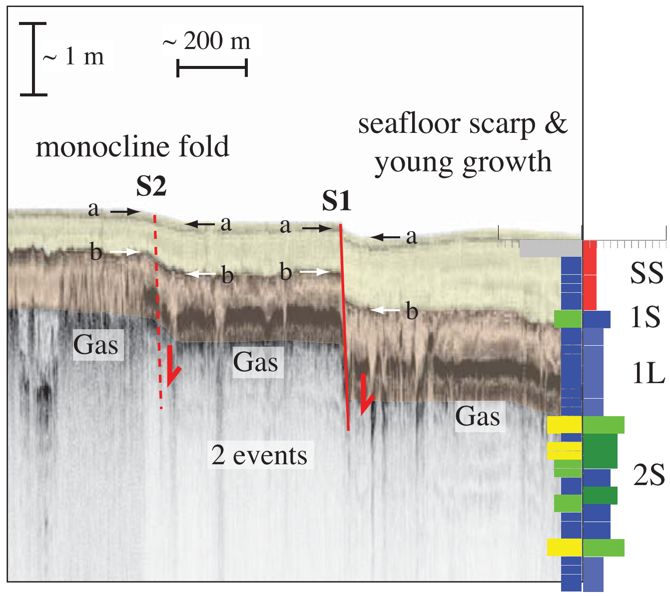

Figure 5-13: Most recent and penultimate offset along Faults S1 and S2. Distinctive seafloor scarps suggest displacement was recent, possibly coincident with the Elmore Ranch earthquake in 1987 (Hudnut et al., 1989b). However the relationship between onshore and offshore faults is not constrained. CPT soundings help define the stratigraphy obscured by acoustic wipeout zones (AWZs). Faults S1 and S2 may have experienced numerous earthquakes that are recorded in the deeper sediments below the AWZs.

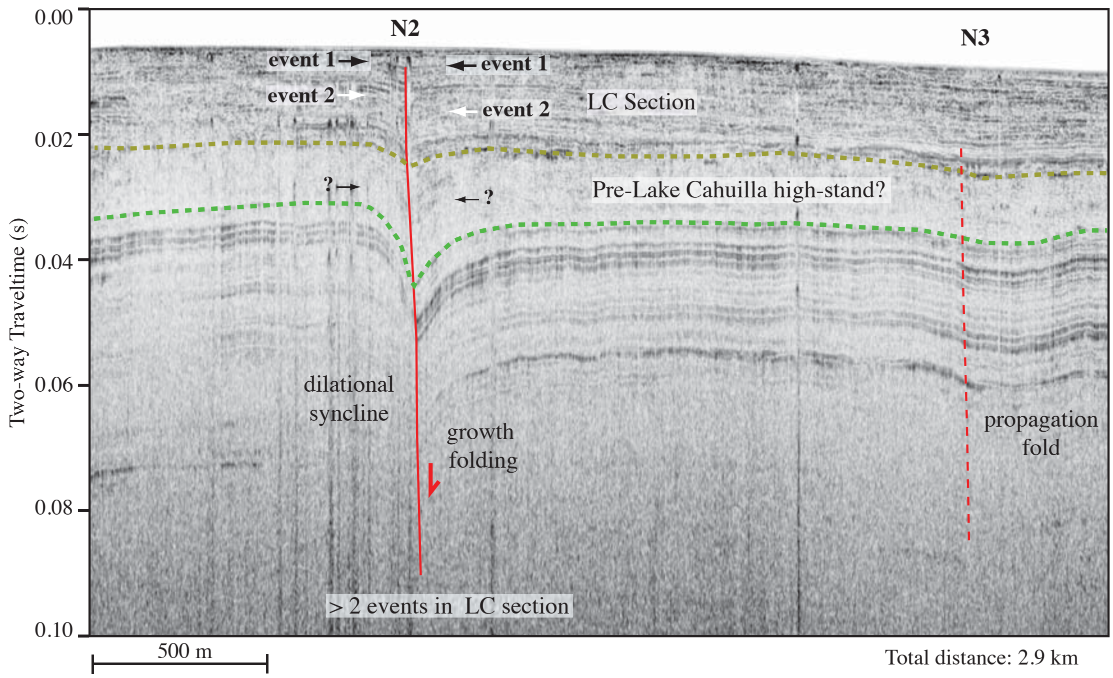

Figure 5-14: Northern faults N2 and N3. Growth folds have evidence for at least 2 events in the Lake Cahuilla section. Folding increases dramatically in the deeper section, which is inferred to be late Pleistocene in age. Based on the synclinal nature of deformation, fault N2 may accommodate a significant component of strike-slip motion.

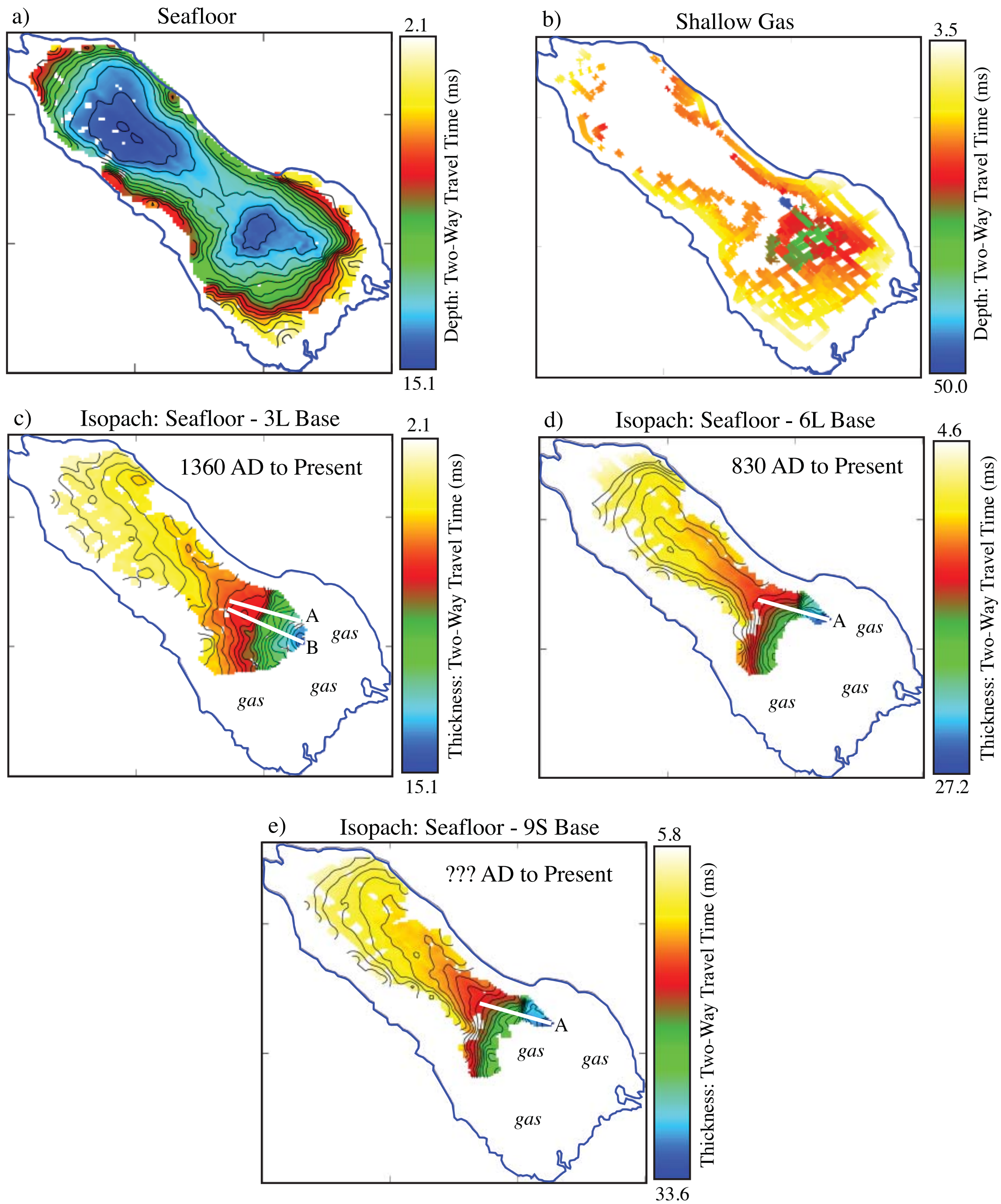

Figure 5-15: Contoured isopach calculations for 3 time horizons. Profiles A and B were used to calculate subsidence rates across the hinge zone. Rates are given in Table 3. We expect the subsidence measured here to be a minimum estimate. The inferred region of maximum subsidence to the south of the data coverage is closer to the sedimentation rate (~19 mm/yr), and based on the distinct topographic depression in the southern sea, we expect subsidence to outpace sedimentation.

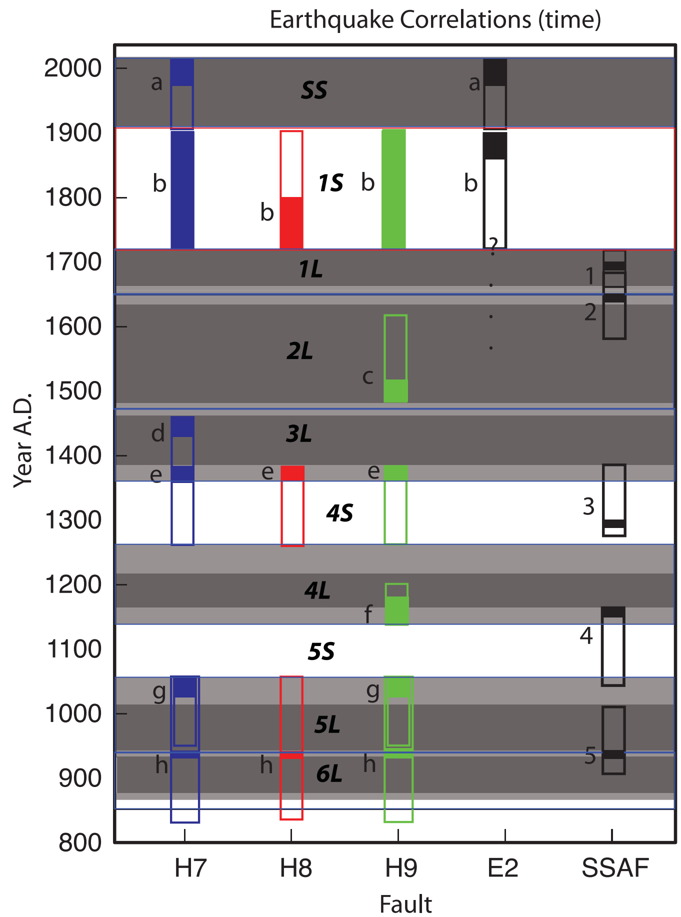

Figure 5-16: Comparison of earthquake chronologies between the Salton Sea and the Coachella site (following Philibosian, 2007). Filled rectangles are best estimates for timing, unfilled include the possible age range. Gray shades represent Lake Cahuilla high-stands. Dark shades are high-stands observed at 9m elevation (Philibosian, 2007) and light gray shades are times when shallow lakes persisted in the deeper portions of the basin. The best event correlation is between offshore event *h* and onshore event 5. Both appear to have occurred while lake 5 was flooding. Offshore event *f* and onshore event 4 are potential correlations. The rest of the events do not have unequivocal evidence for coincident timing. Events *e* and *c* occurred within the uncertainty bounds of onshore events 2 and 3. Despite close proximity of offshore faults and the SAF, the data do not show convincing evidence that these faults systems release strain in a synchronized manner. The most robust correlation is between offshore events and lake flooding (see Figure 9).

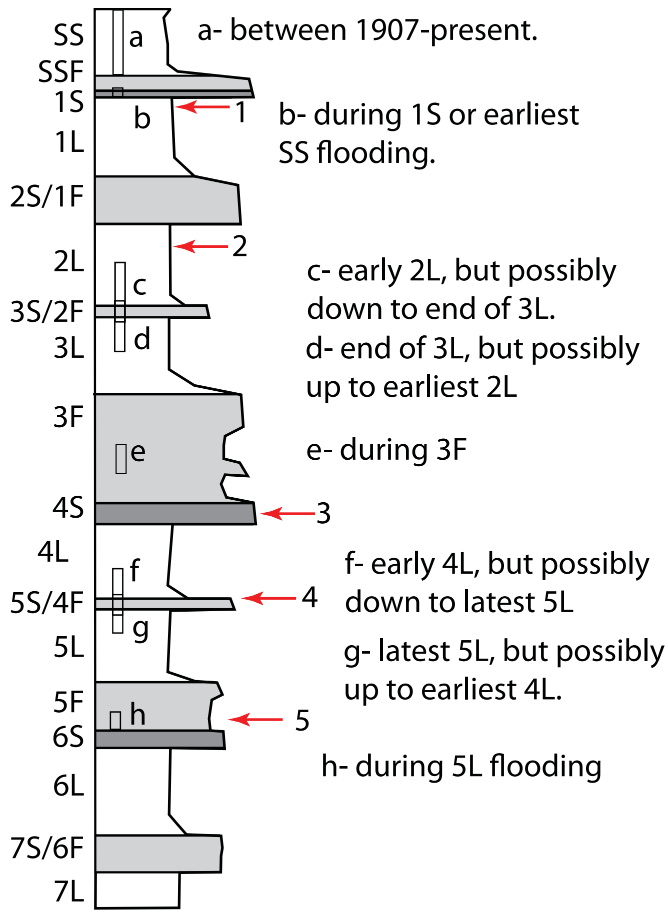

Figure 5-17: Relative stratigraphic positions between onshore (red arrows) and offshore (black rectangles) events. Event *b* occurred after a layer of subaerial coarse-grained material was deposited, suggesting it came several decades after event 1, which occurred when the high shoreline was still submerged in 1L. The lake would require ~60 years to desiccate before event *b* occurred. Events *c* and *d* appear to be distinct, taking place between the end of 3L and beginning of 2L, but their stratigraphic positions cannot be dissociated with complete certainty. Although event 2 occurred near the top of 2L and probably came after events *c* and *d*, the absolute timing differences cannot be resolved. Event *e* is seen during lake 3 flooding on faults H7, H8 and H9, but appears to have occurred after event 3, which is recorded in the mid-section of 4S. Events *f* and 4 correlate stratigraphically, as do events *h* and 5. It is important to note that events observed on one fault are often not observed on adjacent faults.

6

Geophysical Constraints on the Tectonic Evolution And Capture of the Baja California Microplate

6.1 ABSTRACT

Coincident wide-angle seismic refraction and multichannel seismic reflection surveys spanning the width of the of the southern Baja California Peninsula provide insight into the spatial and temporal evolution of microplate capture of the Baja California (BC) peninsula by the Pacific Plate. Stratigraphy in transtensional basins along the Magdalena Shelf records the onset of deformation along the Tosco-Abreojos and Santa Margarita/San Lazaro faults. Although age control of stratigraphy imaged in MCS data is uncertain, relationships between stratal geometry and acoustic character suggest that pre-rift sediment on the shelf may represent proximal facies of the material deposited above the Magdalena Fan along the base of the continental slope. If correct, this provides an upper bound of 12 Ma for the age of the pre-rift sediments and an age of ~8 Ma for the onset of extension across the borderlands, which is coincident with the cessation of seafloor spreading along the Magdalena Rise. Tomographic imaging of wide-angle ocean bottom seismic (OBS) and land-based RefTek seismometers reveals a heterogeneous upper crust that includes a high velocity basement block on the footwall of the Santa Margarita Fault. This block appears to be similar to the structure observed on Isla Santa Margarita ~50 north of Line 0 and contains a metamorphic subduction complex as well as ~6 Ma post subduction volcanics. Tomographic imaging provides evidence that remnant oceanic crust of the Magadalena microplate extends at least ~40 km east of the paleotrench. These observations, along with the presence of adakite volcanics at Isla Santa Margarita, suggest that the remnant slab beneath the western margin of Baja California may contribute to post subduction volcanism, uplift of the Magdalena Shelf by buoyancy forces and subsequent extension as the slab became coupled to the Pacific plate. The results of this study have implications for the plate boundary evolution and offers new insight into potential mechanisms associated with microplate capture and opening of the Gulf of California.

6.2 INTRODUCTION

The Baja California microplate (Figure 1) is a continental plate fragment that has been rifted from mainland Mexico and captured by the Pacific plate over a time period of ~10-15 Ma (Lonsdale, 1991; Nicholson et al., 1994; Stock and Lee, 1994; Demets, 1995; Michaud et al., 2006; Plattner et al., 2007;). The formation and subsequent capture of continental microplates at subducting margins is controlled in some fashion by the underlying oceanic slab, possibly through basal traction or distributed shear transmitted across the plate interface (Bohannon and Parsons, 1995; Nicholson et al., 1994). Understanding the dynamics of microplate capture requires knowledge of the plate kinematics leading up to capture, the geometry and rheology of the slab/upper plate interface, and the lithospheric architecture of the microplate. Baja California presents an ideal place to study the importance of shear across the plate interface because the kinematic evolution of the plate boundary is relatively well defined since ~12 Ma (Atwater and Stock, 1998; Fletcher et al., 2007; Michaud et al., 2006; Michaud et al., 2004; Stock and Hodges, 1989), the microplate is a structurally intact block that has experienced only minor late Cenozoic deformation (Stock and Lee, 1994) and it is now completely severed from North America. Interactions between Baja California and remnants of the Farallon plate (Figure 2), which broke into several oceanic microplates during the mid-Miocene, are inferred from marine magnetic anomalies, bathymetry, drilling and seafloor sampling (Lonsdale, 1991; Michaud et al., 2006). Basal shear applied to the continental margin of North America by stalled and captured Farallon oceanic microplates may have constituted a key influence in the dynamic evolution of the Baja California microplate and its subsequent capture by the Pacific plate (Nicholson et al., 1994). However, the presence of partially subducted slab beneath Baja California was not well established before this experiment.

Petrological data have been used to infer that post-subduction melts are derived, in part, from a relic Farallon slab beneath Baja California (Calmus et al., 2003; Defant and Drummond, 1990). Seismic imaging of the crust and uppermost mantle offer another method for quantifying the structural architecture and spatial extent of relic slab. Here we present the results of a multichannel seismic (MCS) reflection and wide-angle seismic refraction experiment that was conducted as a pilot profile as part of the PESCADOR seismic survey (Lizarralde et al., 2007) aboard the R/V Maurice Ewing in Fall 2002. Seismic data were acquired in two sections that formed a 343 km-long seismic profile (Figure 2) spanning the width of the Baja California microplate from the former Farallon trench on the west edge, to the Farallon Basin on the east. Air-gun shots on either side of the microplate were recorded by ocean bottom and land-based seismometers. In this paper, we report on the crustal and upper mantle structure from tomographic analysis of seismic refraction and stratigraphic relationships as seen on MCS reflection data. Stratigraphy imaged on the Magdalena Shelf records the transition from a convergent to a transtensional plate margin on the western edge of the Baja Peninsula. Tomographic imaging provides evidence that remnant oceanic crust of the Magadalena microplate extends at least 30 km east of the paleotrench. These results have implications for the plate boundary evolution and offers new insight into potential mechanisms that lead to microplate capture and opening of the Gulf of California.

6.3 BACKGROUND

6.3.1 Tectonics

The structure and morphology of the Pacific margin of Baja California have been shaped by three successive and distinctive Cenozoic tectonic episodes. Late Mesozoic and early Cenozoic subduction of the oceanic Farallon plate that ceased in the Miocene, Around 29 Ma (Early Oligocene), the Pacific-Farallon Ridge began to approach the trench and the plate margin began to transition from a convergent to a transform boundary (Atwater and Stock, 1998). As the East Pacific Rise approached the western edge of Baja, the intervening Farallon plate was bifurcated by the Shirley Fracture Zone into the Magdalena and Guadalupe microplates between 20-16 Ma (Lonsdale, 1991). Pacific-Magdalena spreading slowed dramatically by 12 Ma and rotated to align closely with Pacific Plate motion (Michaud et al., 2006), as if the Magdalena plate became partly coupled to western North America (Nicholson et al., 1994), and a dextral transform boundary began to form (Fletcher et al., 2007; Michaud et al., 2006; Michaud et al., 2004; Spencer and Normark, 1979). The onset of oblique dextral slip west of Baja California is broadly constrained to between ~12-6 Ma (Fletcher and Munguia, 2000; Lonsdale, 1991; Michaud et al., 2004; Spencer and Normark, 1979). Nevertheless, the cumulative dextral offset west of Baja remains debated, but appears to be much less than 150 km (Fletcher et al., 2007; Sutherland et al., submitted). The present-day Pacific margin of Baja California shows a distinctive change in morphology and structure to the north and south of the Vizcaino Peninsula; the north is characterized by basin-and-ridge topography typical of the California continental borderlands, whereas the south is generally more subdued with localized basin-and-ridge morphology. In both areas, the morphology primarily related to Miocene deformation along the Tosco-Abreojos and Santa Margarita-San Lazaro fault systems (Fletcher et al., 2007; Michaud et al., 2004; Spencer and Normark, 1979). There is evidence for ongoing deformation along these fault systems since at least 5 Ma and possibly since 8-7 Ma (Fletcher et al., 2007; Michaud et al., 2004).

The cumulative dextral displacement between the Pacific and North American plates is approximately 700 km since 14 Ma (Stock and Hodges, 1989), but how the motion has been partitioned across various fault systems on either side of the Baja peninsula is not well-constrained. Initially, a two-stage model was proposed for the Gulf of California evolution that ascribes ~300 km of dextral slip on the Tosco-Abreojos fault system between 12- 6 Ma (Stock and Hodges, 1989). At the same time, small amounts of E-W oriented extension occurred in the Gulf of California. At 6 Ma, strike-slip motion is thought to have jumped landward and initiated oblique-divergence in the Gulf of California. Conversely, recent studies of the Magdalena Fan (Figure 2) and basin analysis across the Alarcon corridor (Sutherland et al., submitted) support a model in which cumulative dextral slip across faults in the Magdalena Shelf may be as little as 50 km (Fletcher et al., 2007) with the onset of extension in the gulf beginning by ~12 Ma or earlier (Gans, 1997). This model requires at least 200 km of NW-SE extension and dextral slip between 14/12 – 6 Ma, which may have occurred to the east of the Gulf of California in Sonora, Mexico (Gans, 1997).

To the west of Baja, the Guadalupe and Magdalena microplates ceased subducting before the Farallon-Pacific spreading centers were recycled beneath North America, leaving behind fragments that became incorporated into the Pacific plate (Michaud et al., 2006). Spreading directions on the Monterrey and Magdalena spreading centers changed dramatically after ~12 Ma and minor spreading appears to have continued along the western margin of the Magdalena microplate until ~8 Ma (Michaud et al., 2006). Most likely, the Farallon slab detached from the microplate fragments before or during the cessation of spreading (Ferrari, 1995; Michaud et al., 2006), but it is not known where the detachments occurred and how much of the young slab remains coupled to the overriding continental crust (Ferrari, 1995; Martin et al., 2000; Pallares et al., 2007).

6.3.2 Volcanism

The transition from Farallon subduction to microplate capture and oblique divergence in the Gulf of California is recorded in volcanic rocks on Baja California. The early-mid Miocene calc-alkaline Comondú Group was emplaced within the Gulf and along the eastern edge of what is now the Baja California Peninsula as the volcanic arc migrated westward (Umhoefer et al., 2001). The Comondú Arc volcanism ceased at ~12 Ma; however, there appears to be a dramatic decrease in arc volcanism after ~15 Ma. Post-subduction and syn-rift volcanism (ca. 12 Ma- Holocene) on the Baja California Peninsula is found between 25N and 27°N, however, no post-Comondú volcanism is observed south of ~25°N on the Baja California peninsula.

Post-subduction magmatism produced a suite of rocks with adakitic signatures. Adakites are andesitic-dioritic or dacitic-granodioritic rocks that are depleted in heavy rare earth elements and have higher Sr/Y ratios relative to equivalent calc-alkaline rocks (Defant and Drummond, 1990). The origin of adakites has been attributed to slab melting often in hot subduction settings, such as subduction of mid-ocean ridges or subduction of very young (<5 Ma) oceanic crust (Bourgois et al., 1996; Lagabrielle et al., 1994). Baja California's magnesian andesites, referred to as "bajaites", display adakitic affinities, suggesting that slab melt persist in post-subduction Baja California magmatism (Bonini and Baldwin, 1998; Calmus et al., 2003; Defant and Drummond, 1990; Pallares et al., 2007; Saunders et al., 1987). Adakites and bajaites, however, have also been attributed to processes other than slab melting (Castillo, 2008). 6–5 Ma erupted adakites have been sampled at Santa Margarita Island (Bonini and Baldwin, 1998), approximately 50 km north of our seismic transect, along the footwall block of the Santa Margarita Fault (Figure 2). In general, the anomalous magmatism occurs □100–250 km inboard of the paleo-trench (Bonini and Baldwin, 1998; Pallares et al., 2007). The location of post-subduction volcanism may provide a proxy for the spatial and temporal evolution of Farallon slab detachment.

6.4 METHODS

6.4.1 Seismic Reflection and Refraction

The 2002 wide angle survey consisted of a seismic transect spanning the BC

Peninsula, from the trench on the west to the Pescadero transform fault on the east (Figure 2). This pilot transect was designed to capture the structure of the BC crust and uppermost mantle. Five ocean bottom seismometers (OBS) provided seismic records along the western continental shelf, eight RefTek seismometers were situated onshore, and eight more OBS instruments were deployed in the Gulf of California (Figure 2). Shot locations and MCS profiles are split into two lines, 0W and 0E, and both were shot twice: once at 50 m shot spacing for the seismic reflection survey and once at 150 m spacing for the refraction survey. Reflection data was recorded on the R/V Maurice Ewing's 6-km-long, 480-channel seismic streamer with 12.5 m receiver groups. Both data sets were shot with the Ewing's 20-gun, 140-L source array.

On this 343 km-long line, the OBS receivers did not record shots from the opposites side of the peninsula. OBS's on the western shelf were spaced ~25 km apart, land instruments were spaced between 6 and 13 km apart, and OBS's in the Gulf of California were spaced ~17 km apart. The eight land-based RefTek seismometers were set in alignment with the offshore profiles and, with the exception of one instrument (Land 02), recorded shots from both sides of BC. OBS and RefTek data were minimum-phase bandpass filtered 4-15 Hz. Data over the continental shelf were relatively noisy due to seafloor multiples. The survey was designed to capture the velocity structure in the crust and upper mantle, and the receiver spacing was generally not dense enough to resolve lateral velocity structure within the sedimentary basins without including MCS data. Although some information was extracted from the near-offset arrivals, the basement topography and sediment velocities were constrained using the MCS data. Velocity analysis using constant velocity stacks, supergather normal moveout calculations and semblance techniques were carried out approximately every 100 common mid-points (CMPs) on the 50 m shot-spacing data. The data were bandpass filtered, normal move-out was applied and the data were stacked. Post-stack time migration was followed by gain correction. Upper crustal faults, basins and sediment-basement interfaces are well imaged, but no lower crustal or Moho reflections are observed. We used the results from post-stack time migrated data to assess fault and stratigraphic structures along the Magdalena Shelf (Figure 2) and to inspect the basement structure and sediment velocities that were incorporated into the starting tomographic velocity model.

6.4.2 Travel Time Tomography

The primary aims of this study are to constrain the crustal and upper mantle velocity structure between the former Farallon trench and the active divergent plate boundary in the Gulf of California. To achieve this, we used seismic tomography as a tool for interpreting wide-angle travel time data (Van Avendonk et al., 2006; Van Avendonk et al., 2004). Travel time data contain information on both the seismic velocities and the reflection boundaries. The following section is summarized from Van Avendonk et al. (2004) and provides a basic description of the tomographic approach that was employed. The technique requires a starting model that roughly corresponds to the number of large-scale velocity changes seen in the receiver gathers. Next, seismic rays are traced between the sources and receivers through the starting model and travel time residuals δti, between the picked arrivals and predicted arrivals for each source-receiver pair are used in a linearized inversion. Using Fermat's principle, δt_i , can be expressed in a linear combination of perturbations of slowness δu and changes in the layer boundaries δ_{rk} at each reflector k.

$$\delta t_i \approx \int_i \delta u(x,z)ds + \sum_k \Gamma_{i,k}(x)\delta r_k$$

The integration of δu (x,z) is carried out over the ith ray path in the reference model, and $\Gamma_{i,k}(x)$ represents the expression for the Frechet derivatives for reflector depth $r_k(x)$.

We explicitly defined the step across seismic velocity across layer boundaries and the slowness grid $u(x,z)$ was split into separate layers on either side of these boundaries (Van Avendonk et al., 2004).

$$u(x,z) = u_0(x,z) + u_k(x)$$

Gradual slowness variations, or vertical gradients in $u(x,z)$ within a layer, are represented by $u_0(x,z)$ whereas $u_k(x)$ is a step in the $u_0(x,z)$ across the kth layer boundary in the model. Substituting equation (2) in equation (1) yields

$$\delta t_i \approx \int_i \delta u_0(x,z)ds + \sum_{k=1}\int_{k,i} \delta u_k(x)ds + \sum_k \Gamma_{i,k}(x)\delta r_k$$

The integration of $\delta u_0(x,z)$ is carried out over the entire ray path i. The integration of pertubations $\delta u_k(x)$ is carried out over the segment of the ith ray path that lies within layer k. Finally, the equation above can be expressed in matrix form as

$$\mathbf{d} = \mathbf{G}\delta\mathbf{m}$$

where data vector d contains the travel time residuals, matrix G is the Frechet matrix and the model perturbation δm is a vector that includes δu_0, δu_k, and δr_k. Prior to solving for matrix m, we used a form of "layer stripping" through the inversion by fixing the sedimentary basins and upper crustal structure when solving for the lower crustal and upper mantle travel time arrivals. Next, minimization of travel time residuals was accomplished through an iterative process of raytracing and least squares inversion that solved for m. Horizontal and vertical velocity gradients are minimized in the model by adjusting a term for the relative strength of smoothing (see Van Avendonk, 2004). This processed continued until the χ^2 data misfit approached a value of 1.

6.5 RESULTS

6.5.1 Multichannel Seismic Data

MCS data provided important constraints for the tomographic modeling, but also on the fault architecture and sedimentary basin evolution that occurred between the late Miocene to present. As we are most interested in interaction between the relic slab and overlying continental crust, detailed description of MCS data is given only for line 0W along the western margin of BC. From west to east (Figure 3), line 0W crosses the fossil trench that has been infilled by the Magdalena Fan and younger shelf derived detritus (Fletcher et al., 2007; Yeats and Haq, 1981) and continues up the continental slope onto the highly deformed Magdalena Shelf. Based on the acoustic character observed along the base of the continental slope, the contact between sediment and basaltic oceanic crust of the Farallon plate is easily identified (Figure 3). The acoustic character of reflectors reveals changes in sediment type that can be correlated with DSDP Site 471 (Yeats and Haq, 1981). Above the basaltic crust (purple line in Figure 3) lies a sedimentary sequence containing distal turbidites of the 13-14.5 Ma Magdalena Fan (Yeats and Haq, 1981). The orange layer in Figure 3B delineates the boundary between lower amplitude continuous reflectors below, from irregular high amplitude layers above.

On the Magdalena Shelf, two prominent NW trending fault systems displace sediments and appear to control shelf morphology (Figure 3A): the Tosco-Abreojos Fault (TAF) and San Lazaro-Santa Margarita Fault (SLMF). To the east of the TAF, a major unconformity surface separates older, highly deformed sediment from younger, less deformed sediment (orange line, Figure 3). The unconformity shoals from west to east and throughout most of this section, acoustic energy is not returned from below this horizon. The one area that produces a reliable image below the unconformity shows a pronounced syncline (Figure 3). The unconformity progressively increases in amplitude moving eastward from the syncline toward the hangingwall of the SLF, then disappears below the basin fill. Although the age of these sediments is unknown, Fletcher et al. (2007) suggested the unconformity represents a Miocene abrasion surface that was exposed subaerially as a consequence of subducting of young, buoyant oceanic crust.

The TAF and SLSMF zones are associated with relatively deep, asymmetric basins that contain divergent and rotated stratigraphic packages. Both basins have down to the east deformation. Syn-rift sedimentary sequences are defined by thickening and divergence of sedimentary units towards the fault indicating that deposition filled tectonically-induced accommodation. Note that post- and/or pre-rift sequences exhibit little to no thickening of units towards the bounding faults. Thus, on the western margin of BC, the change from pre-rift to syn-rift sediments marks the onset of basin formation and extension along the Tosco-Abreojos Fault (TAF) and San Lazaro-Santa Margarita Fault (SLMF).

The TAF zone appears to have two primary faults, labeled splay 1 and splay 2 in Figure 4. The exact location of Splay 1 is inferred based on the stratal geometry and the escarpment to the west. Based on amplitude signatures and stratal geometry, we identify three stratigraphic packages that can be correlated across the TAF. Pre-rift sediments are represented by high-amplitude, seaward prograding and downlapping sequences. Although packages B and C show no signs of thickening or divergence into either fault, the thickness changes on either side of splay 2. Package B has apparent thickening toward splay 1, but closer inspection reveals truncation along its eastern extent, suggesting that B thins upslope, rather than downslope. Individual layers within B do not exhibit divergence and thickening toward splay 2. Package A (green line) thickens into both fault splays.

The Santa Margarita Fault basin is bounded to the west by two uplifted footwall blocks that outcrop at the seafloor. In contrast, all sediment imaged in the SLF basin thickens toward the fault. The basin-bounding fault is obscured by shallow, high-amplitude horizons, but its location is inferred based on the down-to-the-east surface scarp (Figure 3C) and data recorded by OBS 3. Due to truncation and pinch-outs of the basin fill sediments, we are unable to unequivocally correlate the stratigraphy between the two major basins. Based on amplitude boundaries, we have assigned packages A, B and C in the SMF basin. As in the TAF basin, packages B and C do not show thickening and divergence within individual layers, but instead show pinchout and truncation shoreward.

The line 0E MCS transect extends from the northeastern edge of La Paz bay (north of Espiritu Santo) to southeastern edge of the Farallon basin (Figure 5). The bathymetry of this extended continental terrain is hummocky with several localized basins and ridges. Numerous faults offset sedimentary layering, but few exhibit unequivocal seafloor offset. We image two major basins that appear tectonically active based on seafloor scarps and near-surface deformation. The first basin is bounded on the west by the dramatic east-facing Espiritu Santo escarpment and on the east by a hummocky ridge. The basin is asymmetric and contains two down-to-the west normal faults (Figure 5A). As with basins on line 0W, the syn-rift sedimentary sequences are defined by a thickening and divergence of sedimentary units towards an apparent fault. Although we do not observe stratigraphic evidence for faulting along the western escarpment, we do not image to the basin floor and cannot rule out older episodes of faulting. The second major basin is the southeastern edge of the Farallon Basin, which appears slightly asymmetric at this location based on the more pronounced divergence to the west. Again, the seismic energy attenuates before providing a coherent image of the basement interface. Vertical offset along faults in the basin is quite low. Between the two major basins are several faults strands that extend very near the seafloor, and possibly offset the seafloor. Seismic horizons show mismatches across faults and in some cases do not show divergence into faults despite vertically offset horizons. This suggests some of these faults may accommodate strike-slip shearing that is distributed away from the primary transform boundary.

Sedimentary layers either thin dramatically or are absent on areas of higher relief. Layers generally downlap onto the plain located between Isla Espiritu Santo and the Farallon Basin, but also infill basement lows. The acoustic basement on line 0E shows variation along strike. To the west, acoustic character is similar to that described by Sutherland et al. (submitted) along a NW-SE trending seismic profile that nearly intersects line 0E. The top of basement along much of the reflection profile has a distinctive ropey seismic character, which is interpreted to be of volcanic origin (Sutherland et al., submitted) and must have been emplaced either prior to, or during the early stages of extension. Sutherland et al. (submitted) performed detailed velocity analysis of this layer and determined it has a relatively low velocity of 2.5 – 2.8 km/s, and a thickness of 250 – 500 m. They inferred this layer to be volcaniclastic in origin. Across the Baja California margin, this ropey layer is observed throughout much of the Baja margin in the southern Gulf of California. Based on the results from Sutherland et al. (submitted), we assign the ropey basement reflections to be part of the Comondú volcaniclastics or early rift volcanics (Figures 5 and 6). However, to the east as the profile approaches areas of highly extending crust in the Farralon Basin, the Comondú layer is less apparent and is replaced by highly irregular, high-amplitude layering that sometimes extends into the sediment column (Figure 6). In our initial velocity model, we treat the top of the inferred Comondú deposits and define an approximate layer boundary for the irregular, high-amplitude reflections as the sediment-basement interface. To the east, however, as the profile approaches areas of highly extending crust in the Farralon Basin, the Comondú layer is less apparent and is replaced by highly irregular, high-amplitude layering that sometimes extends into the sediment column (Figure 6). These reflectors may be sill intrusions, but are not expected to significantly alter the location of the basement interface.

6.5.2 Seismic Refraction Data

The analyses and modeling of the seismic data included arrival phase identification, correlation, and travel time picking followed by iterative forward and inverse travel time modeling using the method described by Van Avendonk et al. (2004). A total of 13,614 picks were initially made, but this number was scaled back for the final model due to uncertainty and inconsistencies between picks, particularly for PmP secondary arrivals. The remaining 10,007 picks (Pg and Pn) were used to constrain the velocities and interfaces in the final model. Errors assigned to the data ranged from 24 to 250 ms, depending on the strength and coherency of the signal. Arrivals at far offsets were assigned greater uncertainty than near offsets. All receivers recorded useful data except OBS 5. Raypaths through the starting model (Figure 10) and final model (Figure 11) illustrate data coverage and the associated travel time residuals between picked arrivals and predicted arrivals are shown in Figures 12 and 13. To first order, the velocity information of a particular diving-wave travel time pick is concentrated toward the bottoming point of its associated ray, however, derivative weight sum (DWS) data is a useful measure of ray density in the neighborhood of model nodes (Toomey and Foulger, 1989). DWS for a node is similar to the ray hit count, but weighted by the ray-node separation and raypath length in the vicinity of the node (Figure 10).

The initial line 0 velocity model is 343 km long, 36 km deep and (Figure 11A) includes three layers: sediment (1.55 km/s in the near surface layers to 2.75 km/s in deeper basins; average velocity = 1.8 km/s), crust (4.7 km/s to 6.5 km/s; average velocity = 6.1 km/s) and mantle (constant 8.1 km/s velocity throughout). The model is parameterized using a 0.1 km vertical spacing and 0.5 km horizontal spacing. MCS data were used to constrain the geometry of sedimentary basins and wide-angle travel times were used to model basins that were not fully imaged in MCS profiles. Once the upper crustal structure was constrained, 25 iterations between ray tracing and inversion produced a model (Figure 14) with a $\chi 2$ data misfit equal to 2.5 and an RMS misfit of 0.08 s, suggesting the model does a fairly good job at representing the data. The upper crust on the Magdalena Shelf is very heterogeneous. The uppermost sedimentary packages A, B and C (Figures 3 and 4) were assigned velocities using a compaction model of 0.55 km/s, which fit well in the trench and the TAF basin, but was too low for the SMF basin, where the gradient was increased to ~0.71 km/s with a maximum of 2.5 km/s. The model required an additional layer with a velocity of 3.0 km/s to be added in the vicinity of the syncline (Figure 3). These older sediments below the unconformity appear to extend to almost 2 km depth. Once this layer was added, the model was able to resolve a basement block on the footwall of the SMF with velocities of ~ 5 km/s. The SMF basin is more than 3.5 km deep. Pg rays turning in the lower crust along the western margin reveal a 6-7 km wide HVZ along the trench and extending ~40 km beneath the shelf. Although we cannot resolve the HVZ below 17 km depth, its disappearance is about 5 km above a change in Moho dip (Figure 14). Moho structure is constrained by Pn rays recorded on the land instruments (Figure 11C).

The basement interface on the eastern margin in the Gulf of California did not require significant modification from the MCS data. Velocities beneath the “ropey” layer imaged in MCS profiles are relatively low (3.0-3.5 km/s), which is consistent with volcaniclastic material proposed by Sutherland et al. (submitted). The velocity and Moho structure along the eastern margin is consistent with the Alarcon transect of the PESCADERO experiment (Lizarralde et al., 2007). The basement structure beneath the onshore extent of the profile is poorly constrained, but the data do not require shallow basement beneath any of the receivers. The basin along the Pescadero transform fault is the most significant structural feature in the velocity model and exhibit crustal thickness of ~13 km.

6.6 DISCUSSION

The primary objective of this research is to evaluate the role of relic slab beneath Baja California, and as such, the following discussion focuses on the structure and tectonic history of the western margin of the peninsula. Although samples and/or age control for sedimentary rocks on the shelf are not available, there is potential to correlate sedimentary units on the shelf with units at the base of the slope that have been dated at DSDP Site 471. The boundary marked with a red line in Figure 3B is inferred to represent the unconformity between Magdalena Fan deposits and the overlying upper middle Miocene porcelanite and porcelaneous silty claystone documented at Site 471. There is a drastic change in sedimentation rate across this boundary, which reflects a decrease in supply of terrigenous material to the region of the drill site. The higher acoustic amplitude, lenticular shaped reflectors and occasionally chaotic character near the base of the continental slope suggests that these layers represent localized deposition emplaced by debris flows. This sequence diverges into the relic trench, infilling topography as expected by coarse-grained gravity emplaced flows. Small, locally sourced debris flows are not expected to produce large turbidity flows that would extend to Site 471, which is located ~45 km to the west. Based on thickness of the sedimentary section in Figure 3B, post-13 Ma sedimentation rates at the base of the slope appear to have approximately the similar accumulation rates as the Magdalena Fan. Furthermore, the orange line drawn in Figure 3B is inferred to represent the end of subduction, where post-subduction sedimentation infilled the inactive trench.

Above the prominent angular unconformity (orange horizon), the prograding sequences observed in package C on the shelf (Figure 4) record thermal subsidence and the creation of accommodation. We interpret these deposits to be coeval with the uppermost deposits of unit B offshore (Figure 3B). If correct, this places important constraints on the timing of extension along the TAF and SMF, and potentially, on the amount of cumulative dextral motion along the BC borderland. In our interpretation, the base of A is offset more than the bases of the underlying packages due to the combination of spatial thickness variations of sediments and strike-slip motion along splay 2. Unless extension on the TAF and SMF began after dextral strike-slip, packages A and B were deposited prior to the onset of faulting and offer potential piercing points to estimate the cumulative dextral slip. The nature of the interfingering sequences of unit C (Figure 4) suggests that this unit was a seaward prograding sequence that was deposited after the Magdalena Fan subduction ceased, but prior to extension and formation of the TAF and SMF basins. In this scenario, subduction ceased at at ~13 Ma and the onset of borderland extension in the forearc occurred at ~8 Ma. Michaud et al. (2006) show a rapid decrease in spreading along the Magdalena Rise from ~12 Ma to 8-7 Ma. The approximately 4 million year time lag between the end of full-rate subduction and the end of spreading could represent a gradual reorganization of the plate boundary that first uplifted the shelf due to increased buoyancy following slab breakoff and the subduction of young oceanic lithosphere, then a gradual subsidence as the underplated slab and adjacent young mid-ocean ridge cooled.

The angular unconformity observed in Figure 3 records the uplift and wave-base erosion of the platform. The eroded sediment would be deposited offshore along the margin. Much of the sediment that had previously made its way to Site 471 was now being sequestered near the margin as debris flows and slumps. The chaotic acoustic character (Unit B) observed above the well laminated regional sequences (Unit A) record the change in deposition emplaced by turbidity flows from the overlying more locally sequestered debris flows (Figure 3B). As the plate cooled and the shelf gradually subsided, the prograding units infilled this accommodation (Figure 4). Much of the sediment that would have previously made its way to the margin (Unit B; Figure 3B) was now being sequestered on the shelf. The rapid decrease in accumulation rate and change in terrigenous component between Unit B and overlying Unit C is a result of the onshelf sequestering. We cross-correlated the prograding shelf package with the top of Unit B offshore and this yields an approximate age of 8 Ma for the prograding shelf unit. The high amplitude reflectors are uplifted, rotated, and truncated in the footwall block of the TAF and SMF suggesting they are prerift and place important constraints on the onset of oblique extension along the forearc. Then, as spreading ceased at the ridge, deformation along the TAF and SMF began and formed transtensional basins that captured more sediment. The age of rifting post-dates the deposition of the high-amplitude prograding unit (~8 Ma), an age that is consistent with other data from the region (Michaud et al., 2006).

Surface wave tomography of the Gulf of California region shows a phase velocity transition in the mantle that coincides with the location of Line 0 (Zhang et al., 2007). Phase velocity maps in the 50-80 s period range, which represent a range of maximum sensitivity between ~50-150 km depth, show high phase velocity north of Line 0 (interpreted to be remnants of the stalled Magdalena microplate) and low phase velocity to the south of Line 0, suggesting shallow asthenosphere beneath southernmost Baja (Zhang et al., 2007). Our results indicate that the remnant slab, or the proxy of fast velocities, does not extend beyond 30 km depth in the mantle, or 40 km east of the fossil trench. Our velocity model (Figure 14) for the western Magdalena Shelf and lower crust may have geodynamic implications for the evolution of the Baja margin and for the onset of rifting in the Gulf of California. In our preferred model, the slab is broken at the Moho slope change (Figure 15a). This interpretation suggests the subducting plate had a relatively high dip in order to reach the amphibolite instability depth (Plank and Langmuir, 1988) and generate arc melts in line with the axis of the Comondú arc. Nevertheless, further modeling that includes PmP arrivals will be required to test the robustness of the Moho depth, and forward modeling of slab reflections can provide additional supporting evidence in the wide angle data. Opening of the Gulf of California may be related to slab detachment and traction forces along the slab interface as the Baja California microplate became coupled to the underlying slab. As spreading along the Magdalena Rise ultimately ceased around 8-7 Ma, the slab acquired Pacific plate motion. This may have led to transtensional deformation along the Magdalena Shelf that waned as more extension was accommodated in the gulf. It is possible that the localization of rifting in the Gulf of California was caused by the combination of traction forces along the base of the Baja microplate and localized drop in compression after slab detachment ~350 km inboard of the trench; this in turn may have caused lithospheric weakening in the present Gulf in a manner analogous to back arc rifting in the Lau (Burkett and Billen, 2009). Upwelling and replacement of mantle material during slab roll-back and detachment may have provide additional forces to "push" the Baja peninsula toward Pacific plate velocities, which may explain, in part, how Baja California was "pulled" by a hot, weak oceanic lithosphere.

6.7 CONCLUSIONS

The results of this study provide the first detailed constraints on crustal structure of the Baja California microplate. Line 0 demonstrates the feasibility of using active source seismic imaging to constrain the crustal structure across a continental plate fragment. Future studies with increased spatial coverage in wide-angle refraction data, dense grids of MCS data on the Magdalena shelf and drilling of pre- and syn-rift sediments on the shelf will provide additional constraints on the evolution of this plate boundary as well as the mechanisms that lead to microplate capture and continental rifting. Dating the sediments imaged on the shelf will provide age constraints on deformation along the TAF and SMF. Dense MCS grids across the shelf also have the potential to constrain the cumulative strike-slip and extension accommodated by these faults, helping to resolve a long-standing debate. The result of this research will be important for dynamic modeling efforts (Burkett and Billen, 2009), where future calculations should incorporate divergent plate motion and northwestward pull along the slab-microplate interface. Traction forces at the base of the Baja microplate may provide a mechanism for extension and culminate in seafloor spreading in the Gulf of California, along with a "push" force on the Baja peninsula resulting from mantle flow infilling the space left by slab rollback and detachment.

Additional work is need to test for robustness of the velocity model shown in Figure 15A. PmP picks will be improved and used in future inversions to add constraints on the Moho depth. In addition, forward modeling can test for end member models in places where turning rays cannot accurately resolve the velocity structure. Forward modeling allows one to select a particular structure from a set of permissible structures based on subjective criteria. A slab interface will be added and forwarded modeling will be used simulate reflected arrivals off the slab. These will be plotted on the seismograms to search for evidence that such arrivals are recorded in the data, and if so, they will place additional constraints on the extent of the subducted slab beneath Baja California. offsets.

6.8 REFERENCES

Arrowsmith, J.R., Campbell, B., Kim, H.S., and Crosby, C., 2006a, Tectonic geomorphology and earthquake geology of the 1857 reach of the San Andreas Fault: a new look from Airborne Laser Swath Mapping: 2006 SCEC Annual Meeting Proceedings and Abstracts, v. 16, p. 70.

Atwater, T., and Stock, J., 1998, Pacific North America plate tectonics of the Neogene southwestern United States: An update: International Geology Review, v. 40, p.

375-402.

Bohannon, R.G., and Parsons, T., 1995, Tectonic Implications of Post-30 Ma Pacific and North-American Relative Plate Motions: Geological Society of America Bulletin, v. 107, p. 937-959.

Bonini, J.A., and Baldwin, S.L., 1998, Mesozoic metamorphic and middle to late Tertiary magmatic events on Magdalena and Santa Margarita islands, Baja California Sur, Mexico: Implications for the tectonic evolution of the Baja California continental borderland: Geological Society of America Bulletin, v. 110, p. 1094-1104.

Bourgois, J., Martin, H., Lagabrielle, Y., LeMoigne, J., and Jara, J.F., 1996, Subduction erosion related to spreading-ridge subduction: Taitao peninsula (Chile margin triple junction area): Geology, v. 24, p. 723-726.

Burkett, E.R., and Billen, M.I., 2009, Dynamics and Implications of Slab Detachment Due to Ridge-Trench Collision: Journal of Geophysical Research-Solid Earth, In Press.

Calmus, T., Aguillon-Robles, A., Maury, R.C., Bellon, H., Benoit, M., Cotten, J., Bourgois, J., and Michaud, F., 2003, Spatial and temporal evolution of basalts and magnesian andesites (“bajaites”) from Baja California, Mexico: the role of slab melts: Lithos, v. 66, p. 77-105.

Castillo, P.R., 2008, Origin of the adakite-high-Nb basalt association and its implications for postsubduction magmatism in Baja California, Mexico: Geological Society of America Bulletin, v. 120, p. 451-462.

Defant, M.J., and Drummond, M.S., 1990, Derivation of Some Modern Arc Magmas by Melting of Young Subducted Lithosphere: Nature, v. 347, p. 662-665.

Demets, C., 1995, Plate Motions and Crustal Deformation: Reviews of Geophysics, v. 33, p. 365-369.

Ferrari, L., 1995, Miocene Shearing Along the Northern Boundary of the Jalisco Block and the Opening of the Southern Gulf of California: Geology, v. 23, p. 751-754.

Fletcher, J.M., Grove, M., Kimbrough, D., Lovera, O., and Gehrels, G.E., 2007, Ridge-trench interactions and the Neogene tectonic evolution of the Magdalena shelf and southern Gulf of California: Insights from detrital zircon U-Pb ages from the Magdalena fan and adjacent areas: Geological Society of America Bulletin, v. 119, p. 1313-1336.

Fletcher, J.M., and Munguia, L., 2000, Active continental rifting in southern Baja California, Mexico: Implications for plate motion partitioning and the transition to seafloor spreading in the Gulf of California: Tectonics, v. 19, p. 1107-1123.

Gans, P.B., 1997, Large-magnitude Oligo-Miocene extension in southern Sonora: Implications for the tectonic evolution of northwest Mexico: Tectonics, v. 16, p. 388-408.

Lagabrielle, Y., Lemoigne, J., Maury, R.C., Cotten, J., and Bourgois, J., 1994, Volcanic Record of the Subduction of an Active Spreading Ridge, Taitao Peninsula (Southern Chile): Geology, v. 22, p. 515-518.

Langenheim, V.E., and Jachens, R.C., 2003, Crustal structure of the Peninsular Ranges batholith from magnetic data: Implications for Gulf of California rifting: Geophysical Research Letters, v. 30.

Lizarralde, D., Axen, G.J., Brown, H.E., Fletcher, J.M., Gonzalez-Fernandez, A., Harding, A.J., Holbrook, W.S., Kent, G.M., Paramo, P., Sutherland, F., and Umhoefer, P.J., 2007, Variation in styles of rifting in the Gulf of California: Nature, v. 448, p. 466-469.

Lonsdale, P.F., 1991, Structural patterns of the Pacific floor offshore of Peninsular California: in Dauphlin, J. P., and Simoneit, B. R. T., eds., The Gulf and Peninsular Province of the Californias: American Association of Petroleum Geologists Memoir, v. 47.

Martin, A., Fletcher, J.M., Lopez-Martinez, M., and Mendoza-Borunda, R., 2000, Waning Miocene subduction and arc volcanism in Baja California: the San Luis Gonzaga volcanic field: Tectonophysics, v. 318, p. 27-51.

Michaud, F., Royer, J.Y., Bourgois, J., Dyment, J., Calmus, T., Bandy, W., Sosson, M., Mortera-Gutierrez, C., Sichler, B., Rebolledo-Viera, M., and Pontoise, B., 2006, Oceanic-ridge subduction vs. slab break off: Plate tectonic evolution along the Baja California Sur continental margin since 15 Ma: Geology, v. 34, p. 13-16.

Michaud, F., Sosson, M., Royer, J.Y., Chabert, A., Bourgois, J., Calmus, T., Mortera, C., Bigot-Cormier, F., Bandy, W., Dyment, J., Pontoise, B., and Sichler, B., 2004, Motion partitioning between the Pacific plate, Baja California and the North America plate: The Tosco-Abreojos fault revisited: Geophysical Research Letters, v. 31.

Nicholson, C., Sorlien, C.C., Atwater, T., Crowell, J.C., and Luyendyk, B.P., 1994, Microplate Capture, Rotation of the Western Transverse Ranges, and Initiation of the San-Andreas Transform as a Low-Angle Fault System: Geology, v. 22, p. 491-495.

Oskin, M., Stock, J., and Martin-Barajas, A., 2001, Rapid localization of Pacific-North America plate motion in the Gulf of California: Geology, v. 29, p. 459-462.

Pallares, C., Maury, R.C., Bellon, H., Royer, J.Y., Calmus, T., Aguillon-Robles, A., Cotten, J., Benoit, M., Michaud, F., and Bourgois, J., 2007, Slab-tearing following ridge-trench collision: Evidence from Miocene volcanism in Baja California, Mexico: Journal of Volcanology and Geothermal Research, v. 161, p. 95-117.

Persaud, P., Perez-Campos, X., and Clayton, R.W., 2007, Crustal thickness variations in the margins of the Gulf of California from receiver functions: Geophysical Journal International, v. 170, p. 687-699.

Plank, T., and Langmuir, C.H., 1988, An Evaluation of the Global Variations in the Major Element Chemistry of Arc Basalts: Earth and Planetary Science Letters, v. 90, p. 349-370.

Plattner, C., Malservisi, R., Dixon, T.H., LaFemina, P., Sella, G.F., Fletcher, J., and Suarez-Vidal, F., 2007, New constraints on relative motion between the Pacific Plate and Baja California microplate (Mexico) from GPS measurements: Geophysical Journal International, v. 170, p. 1373-1380.

Saunders, A.D., Rogers, G., Marriner, G.F., Terrell, D.J., and Verma, S.P., 1987, Geochemistry of Cenozoic Volcanic-Rocks, Baja-California, Mexico - Implications for the Petrogenesis of Postsubduction Magmas: Journal of Volcanology and Geothermal Research, v. 32, p. 223-245.

Spencer, J.E., and Normark, W.R., 1979, Tosco-Abreojos Fault Zone - Neogene Transform Plate Boundary within the Pacific Margin of Southern Baja-California, Mexico: Geology, v. 7, p. 554-557.

Stock, J.M., and Hodges, K.V., 1989, Pre-Pliocene Extension around the Gulf of California and the Transfer of Baja California to the Pacific Plate: Tectonics, v. 8, p. 99-115.

Stock, J.M., and Lee, J., 1994, Do Microplates in Subduction Zones Leave a Geological Record: Tectonics, v. 13, p. 1472-1487.

Sutherland, F., Kent, G., Harding, A., Umhoefer, P., Lizarralde, D., Driscoll, N., Fletcher, J., Axen, G., Holbrook, W.S., Gonzalez-Fernandez, A., and Lonsdale, P.F., 2009, Mid-Miocene to early Pliocene Oblique Extension in the southern Gulf of California: Journal of Geophysical Research-Solid Earth, submitted.

Toomey, D.R., and Foulger, G.R., 1989, Tomographic inversion of local earthquake data from the Hengill-Grensdalur Central Volcano Complex, Iceland: Journal of Geophysical Research-Solid Earth, v. 94, p. 17,497-17510.

Umhoefer, P.J., Dorsey, R.J., Willsey, S., Mayer, L., and Renne, P., 2001, Stratigraphy and geochronology of the Comondu Group near Loreto, Baja California sur, Mexico: Sedimentary Geology, v. 144, p. 125-147.

Van Avendonk, H.J.A., Holbrook, W.S., Nunes, G.T., Shillington, D.J., Tucholke, B.E., Louden, K.E., Larsen, H.C., and Hopper, J.R., 2006, Seismic velocity structure of the rifted margin of the eastern Grand Banks of Newfoundland, Canada: Journal of Geophysical Research-Solid Earth, v. 111.

Van Avendonk, H.J.A., Shillington, D.J., Holbrook, W.S., and Hornback, M.J., 2004, Inferring crustal structure in the Aleutian island arc from a sparse wide-angle seismic data set: Geochemistry Geophysics Geostystems, v. 5, p. doi:10.1029/2003GC000664.

Yeats, R., and Haq, B., 1981, Deep-sea drilling off the Californias: Implications of Leg 63: Initial Reports DSDP, v. 63, p. 949-961.

Zhang, X., Paulssen, H., Lebedev, S., and Meier, T., 2007, Surface wave tomography of the Gulf of California: Geophysical Research Letters, v. 34.

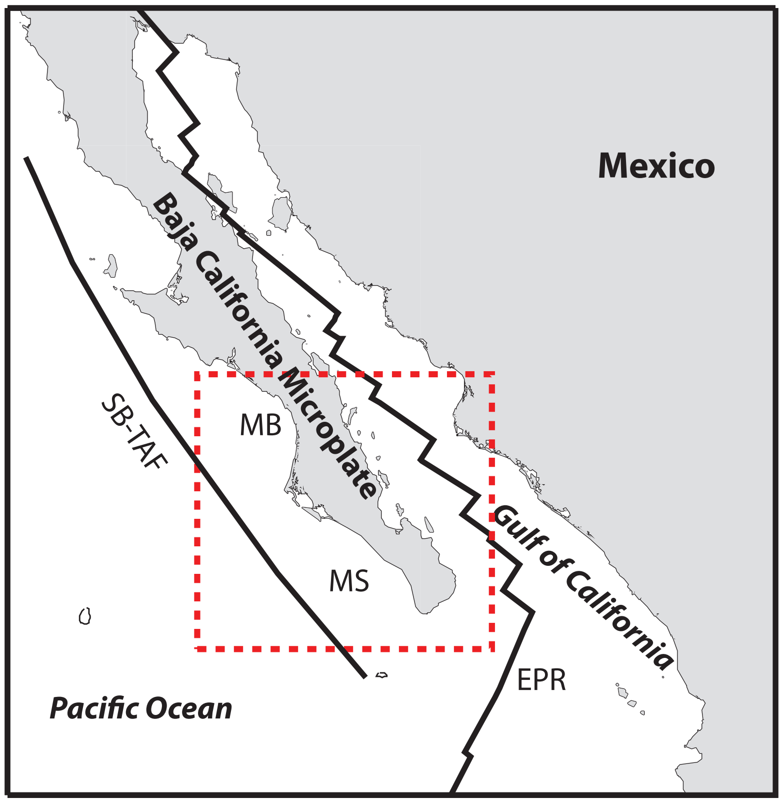

Figure 6-1: Baja California map showing major fault systems (black lines) and primary study region (red box). San Benito-Tosco Abreojos Fault, SBTAF; Magdalena Bay, MB; Magdalena Shelf, MS; East Pacific Rise, EPR.

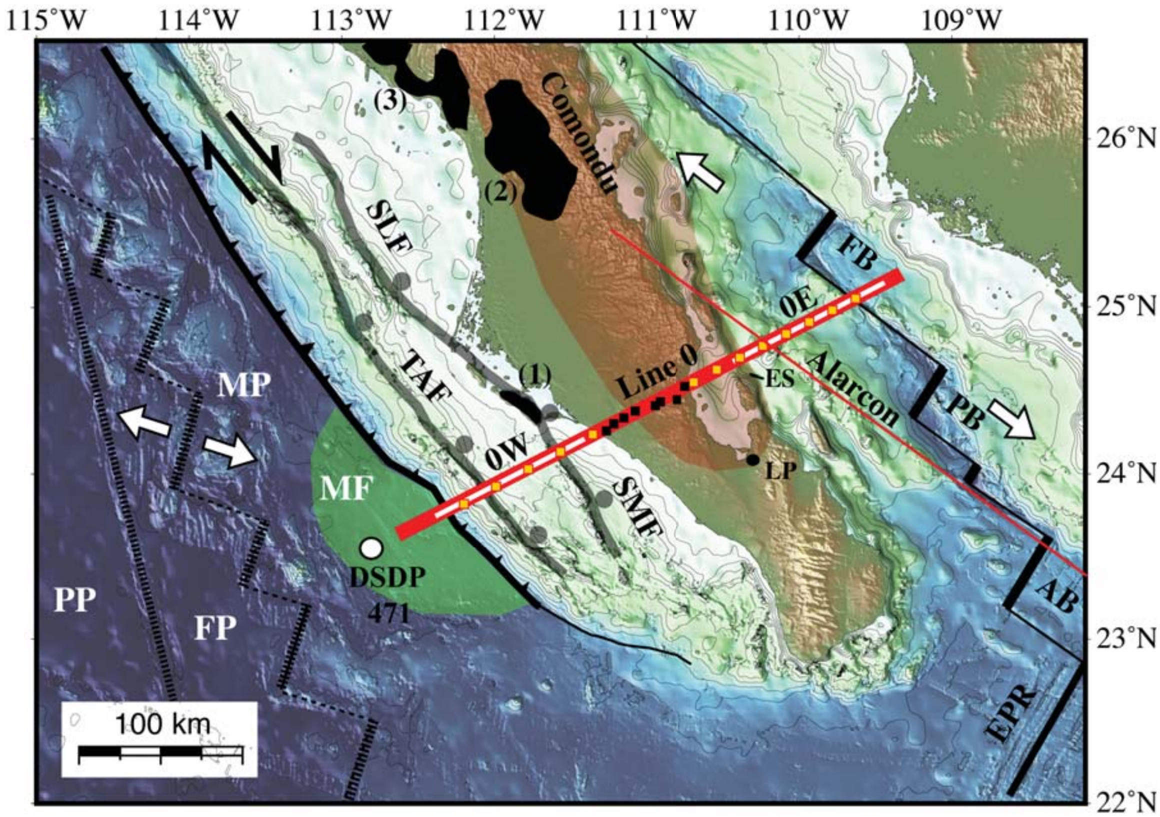

Figure 6-2: Baja California Sur map showing major geologic and tectonic features. Line 0 (red line) with the western (0W) and eastern (0E) multichannel seismic profiles are shown in white. Ocean-bottom seismometers are shown as yellow squares and land-based RefTek seismometers are shown as black squares. Thin red line labeled "Alarcon" is the seismic profile presented in Lizarralde et al. (2007) and Sutherland et al. (2009). On the west, Line 0 extends from the Magdalena Fan (MF) and fossil Magdalena trench at the base of the continental slope and across the continental shelf, which includes the Tosco Abreojos and Santa Margarita faults. On the east, the line extends from the Espiritu Santo (ES) escarpment and across the southern edge of the Farallon Basin (FB). Tectonic features include the former spreading boundary between the Pacific Plate (PP) and the Farallon Plate (FP), shore ridge segments between the FP and Magdalena microplate (MP). Dashed lines are inactive spreading centers. Deep Sea Drilling Program Site 471 is marked on the distal portion of the MF. The East Pacific Rise (EPR) enters the Gulf of California and is segmented in to a serried of active spreading boundaries (thick black lines; Alarcon Basin, AB; Pescador Basin, PB) separated by transform faults. Four volcanic provinces are highlighted on the peninsula: (1) 6.2 ± 0.1 and 4.9 ± 0.1 Ma adakites on Isla Santa Margarita (Bonini and Baldwin, 1998), (2) 9.7 – 8.8 Ma La Purisima magnesian andesites ("bajaites") and (3) 8.5 – 13.3 Ma San Ignacio tholeiite lavas. Region blanketed by Miocene Comondú volcanics is shaded in red.

Figure 6-3: Seismic reflection profiles 0W. (A) Complete line (total length = 111 km) with locations for OBS receivers 1-5. Stratigraphic correlations between sediment at the base of the continental slope and pre-rift sedimentary packages on the shelf are based on acoustic character and stratal geometry. The red line in inset (B) represents the transition from Magdalena Fan deposits to localized debris deposits and coarse-grained irregular bedding. Estimates for stratal ages are based on correlation with DSDP Site 471 (Yeats and Haq, 1981). Prograding and downlapping sediment deposited on the shelf prior to opening of the TAF and SMF basins may be correlative to facies deposited above the Magdalena Fan (orange horizon). Magdalena Fan reflectors are regionally laminated and low amplitude, layers above are acoustically chaotic and high amplitude. If this correlation is correct, the onset of extension on the shelf occurred ~8 Ma. The "*" in panel (A) marks a fault that appears to have significant strike-slip offset based on mismatched reflectors. Dredge samples of mid-Miocene age were obtained from the scarp of the TAF (Spencer and Normark, 1979). (C) Enlarged section over the SMF basin.

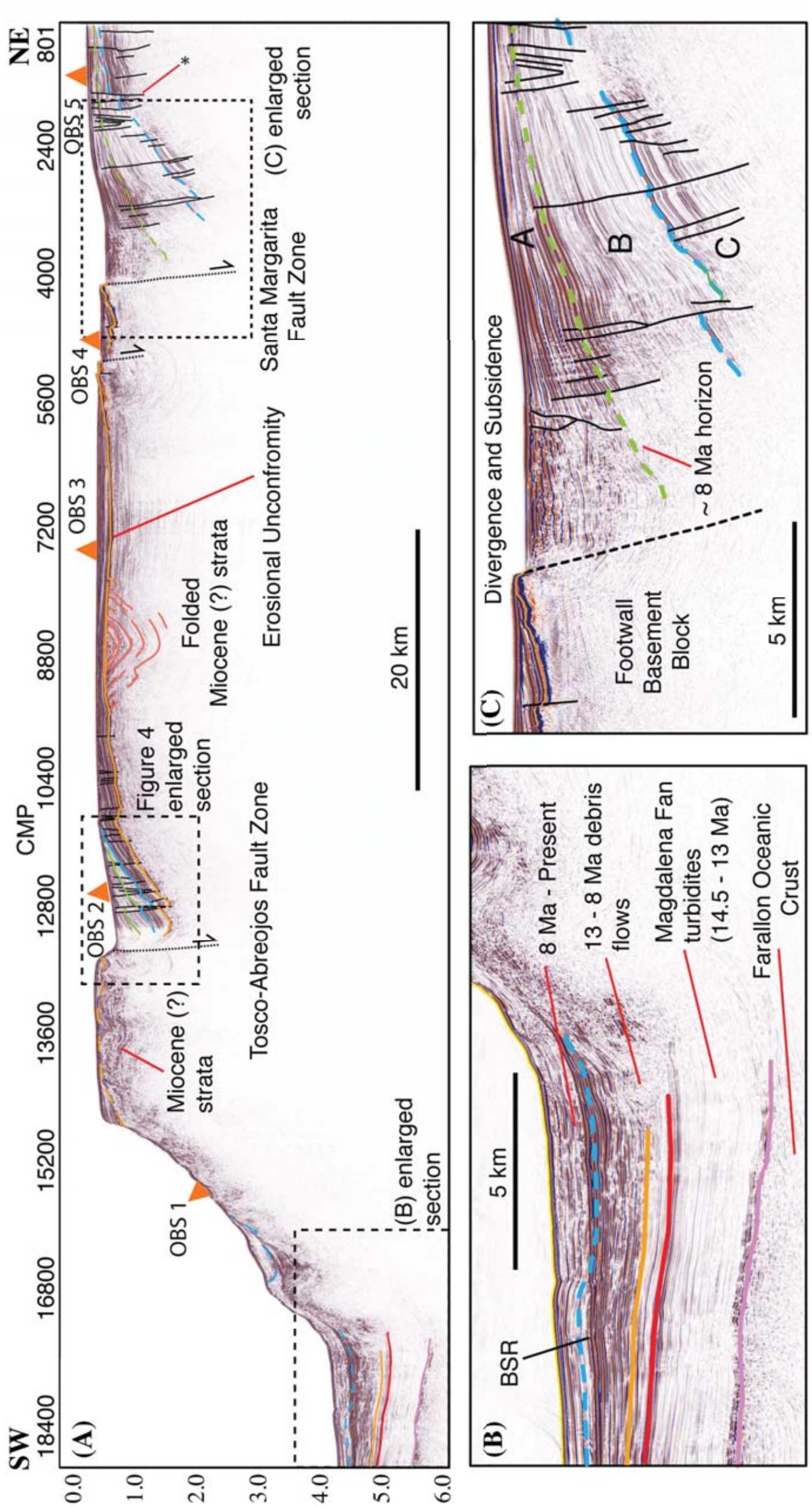
SW
NE
CMP
18400
16800
15200
13600
12800
10400
8800
7200
5600
4000
2400
801
Two Way Travel Time (s)
0.0
1.0
2.0
3.0
4.0
5.0
6.0
(A)
OBS 1
OBS 2
OBS 3
OBS 4
OBS 5
(B) enlarged section
Miocene (?) strata
Tosco-Abreojos Fault Zone
Figure 4 enlarged section
Folded Miocene (?) strata
Erosional Unconfromity
Santa Margarita Fault Zone
(C) enlarged section
20 km
(B)
BSR
5 km
8 Ma - Present
13 - 8 Ma debris flows
Magdalena Fan turbidites (14.5 - 13 Ma)
Farallon Oceanic Crust
(C)
Footwall Basement Block
5 km
Divergence and Subsidence
~ 8 Ma horizon
A
B
C

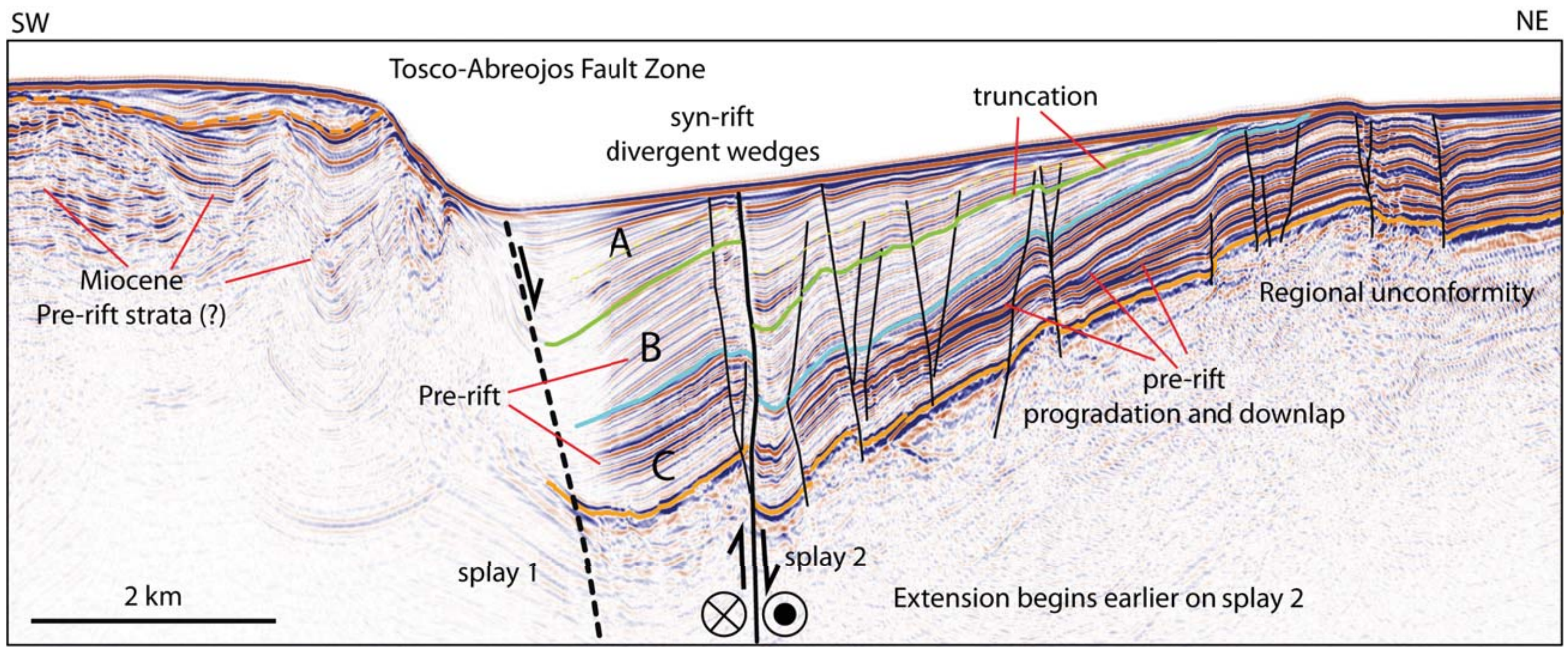

Figure 6-4: Enlarged MCS section of the Tosco-Abreojos fault zone. The unconformity surface separates younger (post 13 Ma), unconsolidated sediment from older (pre 13 Ma), highly consolidated sediment and basement rock. Stratigraphic horizons can be correlated across faults based on amplitude signatures. Stratal divergence to the west is indicative of syntectonic deposition. Package A (green line) represents syn-rift sediment and contains wedges of thickened strata adjacent to splay 2. Although the exact location of splay 1 is inferred, subsidence appears to have started at approximately equivalent time on both splays. Mismatches in layer thickness and greater offset upsection on splay 2 suggests this fault has a significant strike-slip component. Packages B and C represent a pre-rift sequences that do not show divergence of individual layers. Although the vertical resolution of this data does not preclude fault offset along the seafloor, we do not observe offset in the uppermost horizons. See text for detailed interpretation.

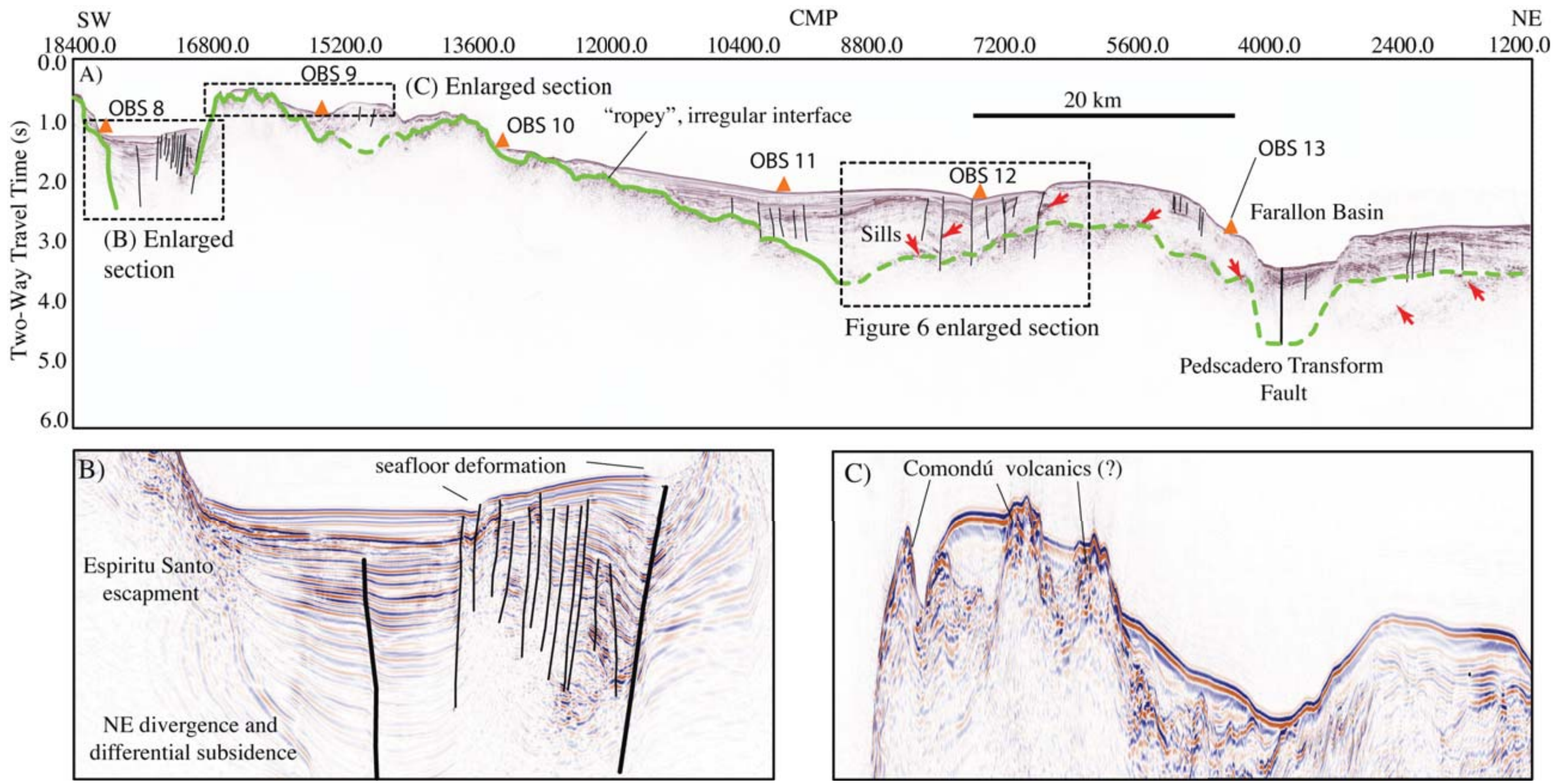

Figure 6-5: Seismic reflection profile 0E. (A) Complete line (total length = 111 km) with locations for OBS receivers 6-13. Green line represents the approximate sediment/basement boundary used in the tomographic model. The basement interface is interpreted to be a contact between sediment and Miocene volcaniclastic deposits of the Comondú Group (Sutherland et al., 2009), but becomes highly irregular near the active plate boundary. Short, discontinuous high-amplitude reflectors (red arrows) may be volcanic sills and dikes. (B) Enlarged section of the basin below the Espiritu Santo escarpment. Stratal divergence and seafloor scarps show a history of extension here that continues to present. (C) Enlarged section highlighting the "ropey" nature of the sediment/basement interface.

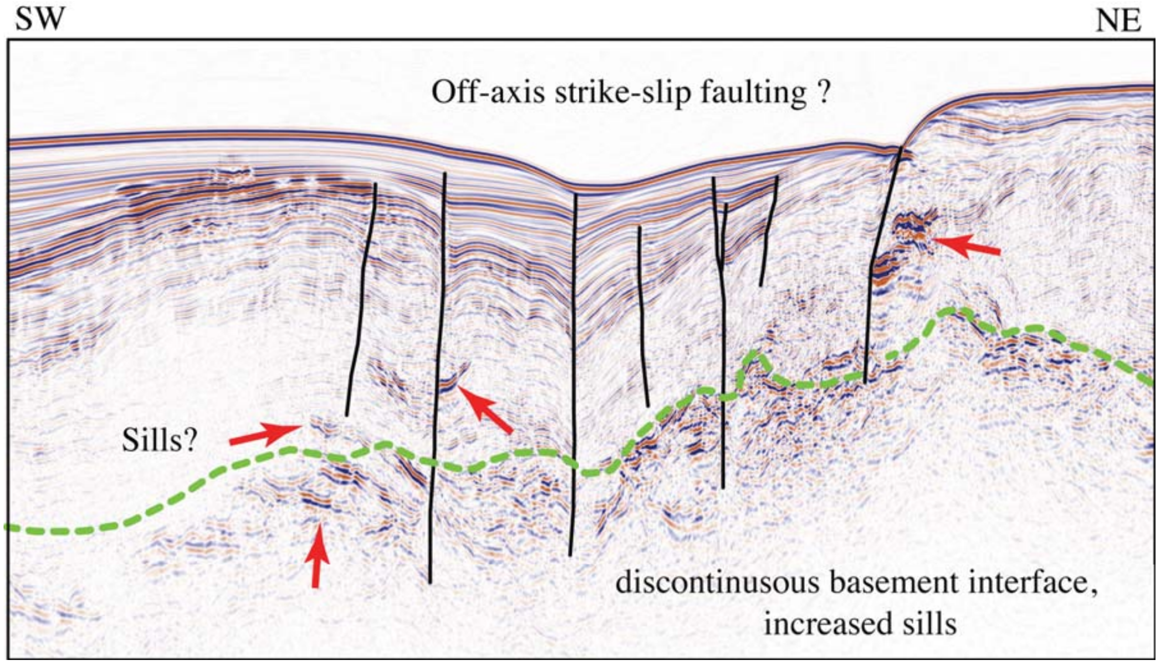

Figure 6-6: Enlarged section from Figure 5 highlighting potential sills and faulting. Based on folded strata these faults appear to be normal-oblique.

Figure 6-7: Example record sections for OBSs 1 and 3 on the Magdalena Shelf. Solid lines are arrival picks and dashed lines are predicted arrivals based on raytracing through the final velocity model. Magenta lines are Pg (crustal) arrivals, green are Pn (mantle) arrivals and blue lines are reflections off the moho. Pa picks (yellow) on OBS 3 represent refractions through the older compacted sediments of the syncline feature seen in Figure 3. PmP picks were not used in the inversion due to inconsistencies in data quality between receivers, but will be added in the future. Data quality for Pg arrivals is generally good for shot-receiver offsets of 50 km and less and 70 km and less for Pn arrivals.

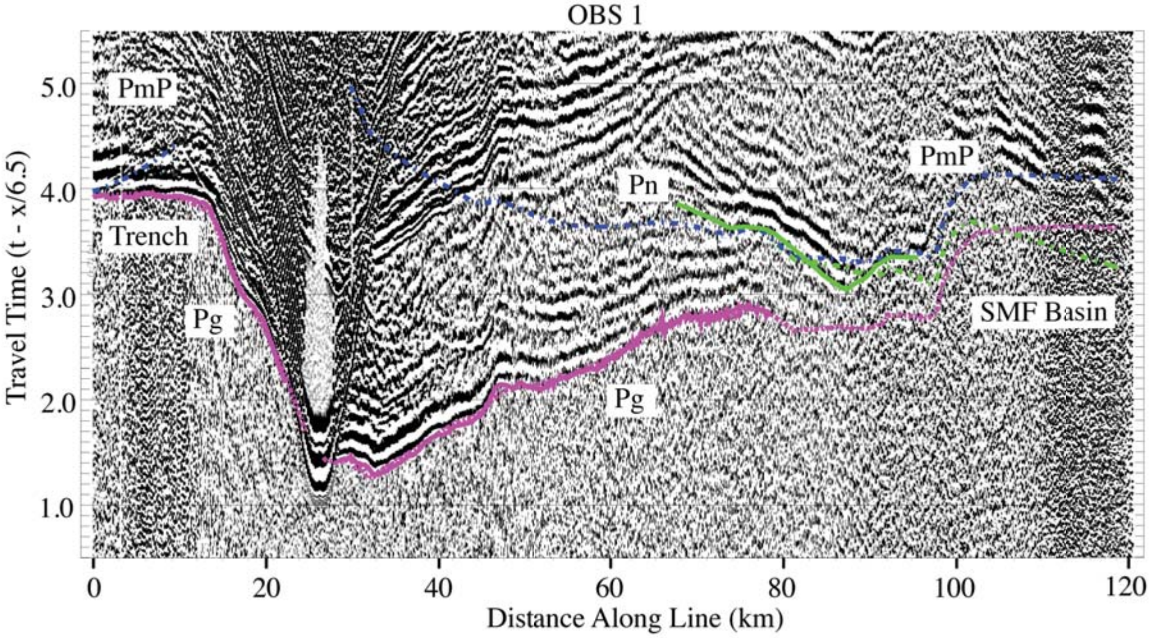
OBS 1
Travel Time (t - x/6.5)
5.0
4.0
3.0
2.0
1.0
PmP
Trench
Pg
Pn
PmP
SMF Basin
Pg
0
20
40
60
80
100
120
Distance Along Line (km)

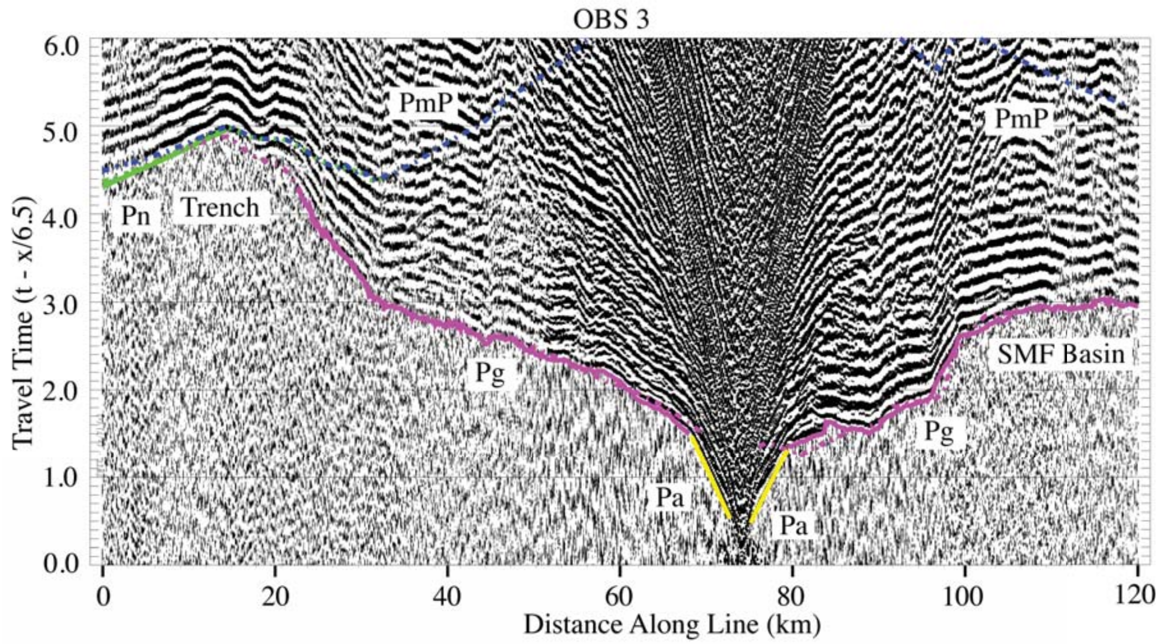
OBS 3
Travel Time (t - x/6.5)
6.0
5.0
4.0
3.0
2.0
1.0
0.0
PmP
PmP
Pn
Trench
Pg
SMF Basin
Pg
Pa
Pa
0
20
40
60
80
100
120
Distance Along Line (km)

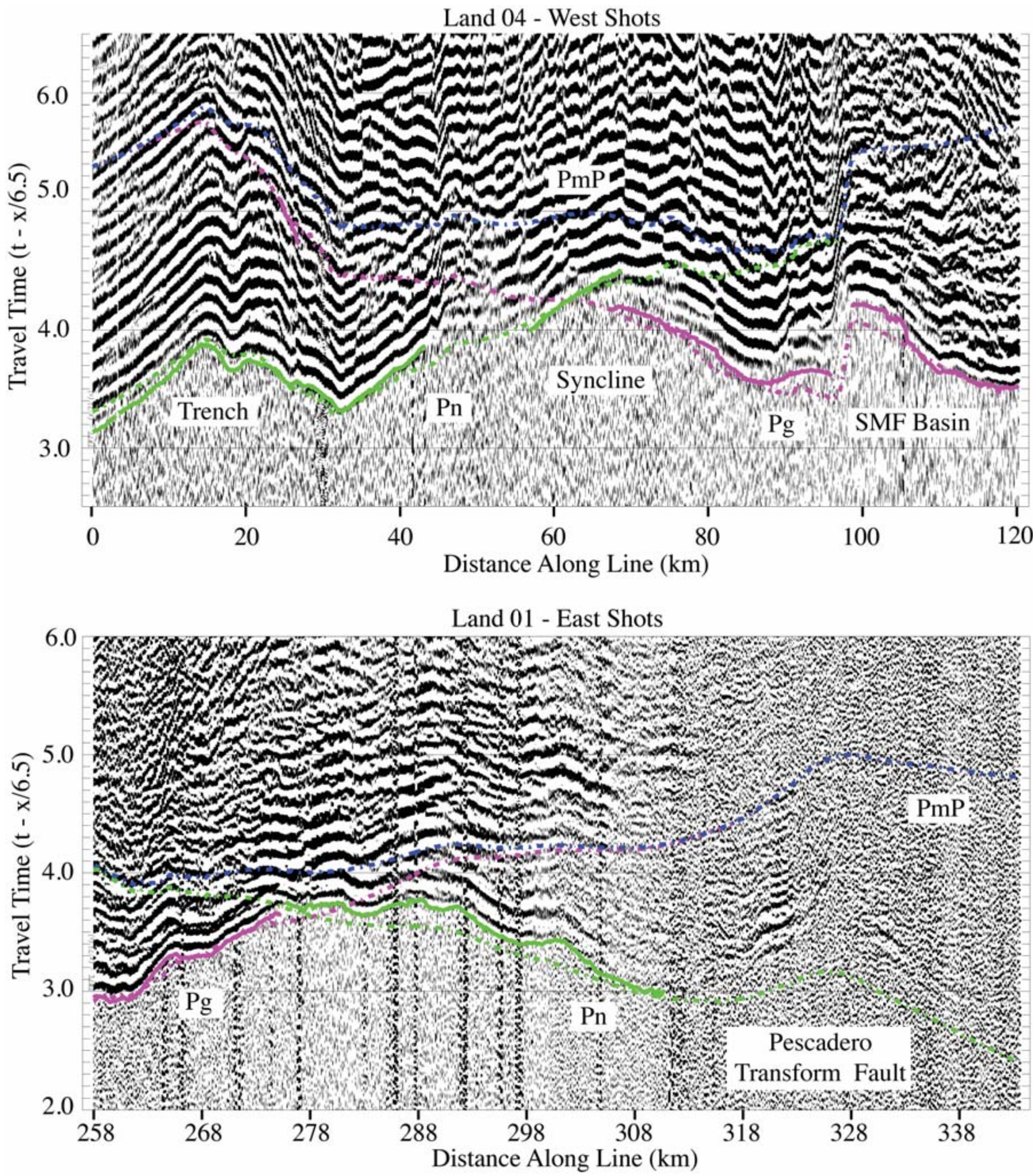

Figure 6-8: Example record sections for land receivers 4 (western shots) and 1 (eastern shots). Land 04 recorded excellent data for shots up to 120 km away from the receiver.

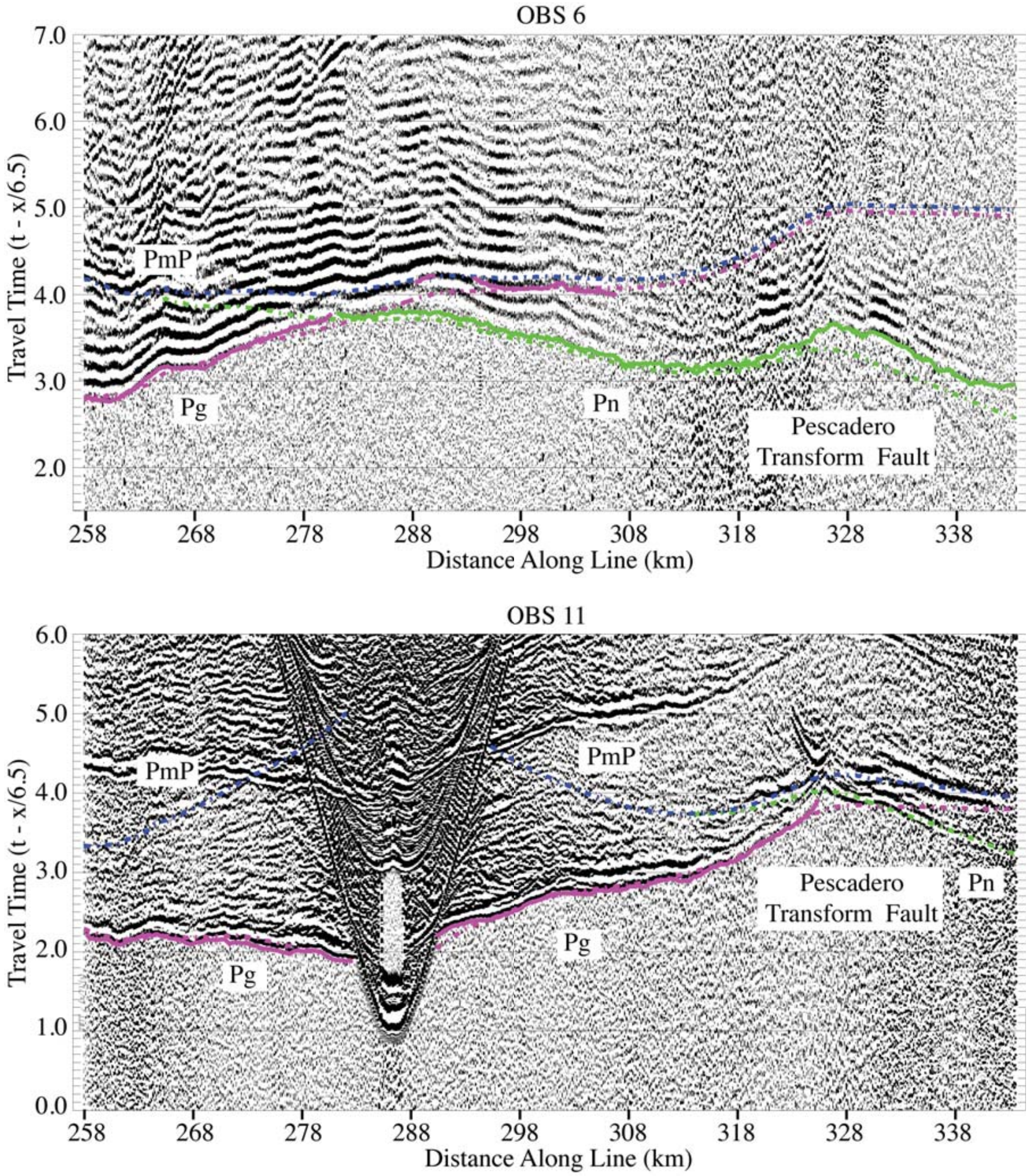

Figure 6-9: Example record sections for OBS receivers 6 and 11 in the Gulf of California. The most prominent feature in the data is the basin surrounding the Pescadero Transform Fault.

Figure 6-10: Initial velocity models and ray tracing. The initial starting velocity model (A) was modified to obtain reasonably accurate interface boundaries before inverting for velocity structure and fine scale heterogeneity along the interfaces. (B) The second starting model comprises 4 layers: low velocity sediment (gradient between 1.55 and 2.75 km/s), high velocity sediment (3.0 km/s), crust (4.7 – 6.5 km/s) and mantle (8.1 km/s). (C) Ray paths for Pg and Pn arrival time picks from all instruments. Only the deepest point of the crustal root is not constrained by the data. Improved picks at far offset distance may improve the image of the lowermost moho boundary.

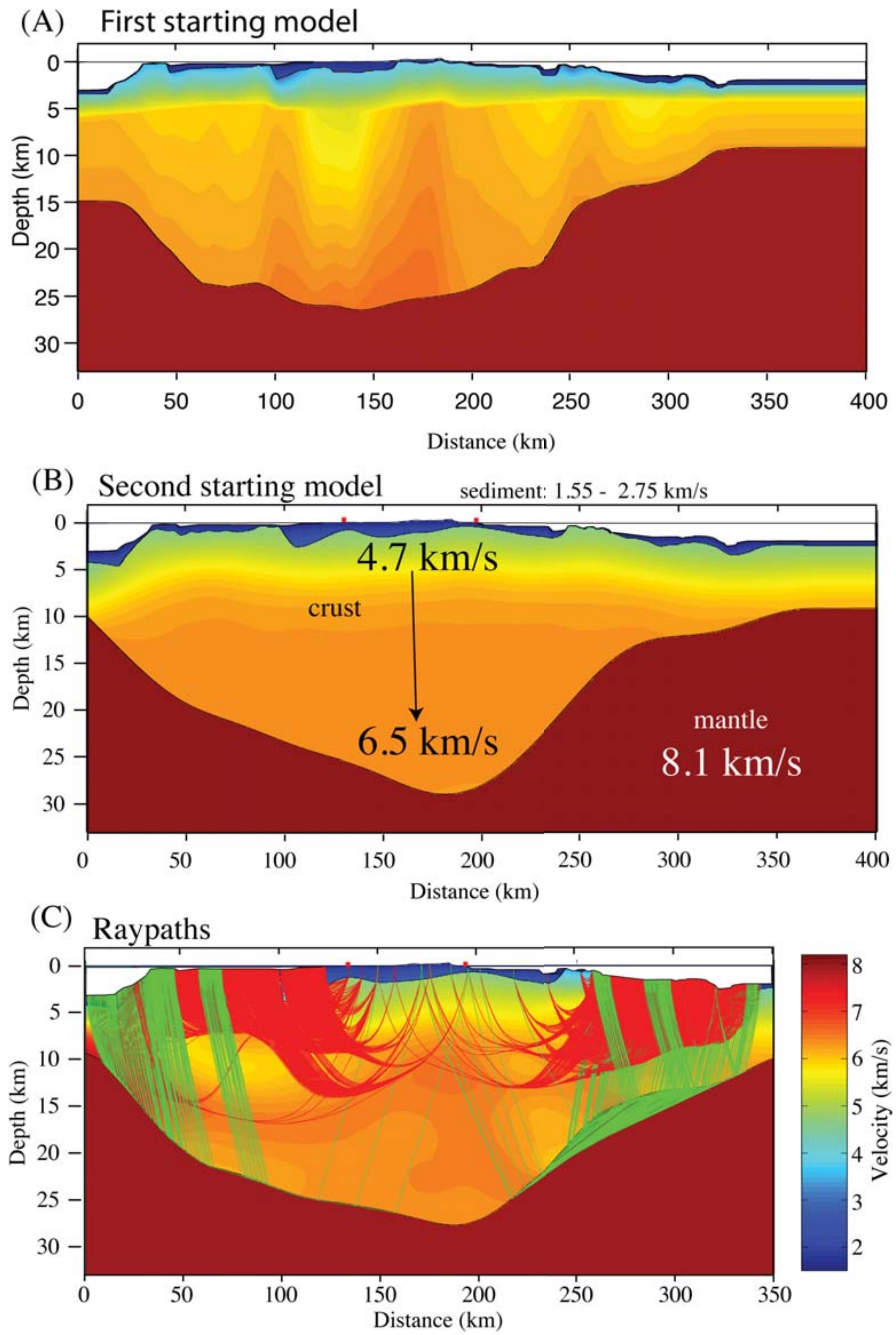
(A) First starting model
Depth (km)
0
5
10
15
20
25
30
0
50
100
150
200
250
300
350
400
Distance (km)
(B) Second starting model
sediment: 1.55 - 2.75 km/s
4.7 km/s
crust
6.5 km/s
mantle
8.1 km/s
Depth (km)
Distance (km)
(C) Raypaths
Depth (km)
Distance (km)
Velocity (km/s)
2
3
4
5
6
7
8

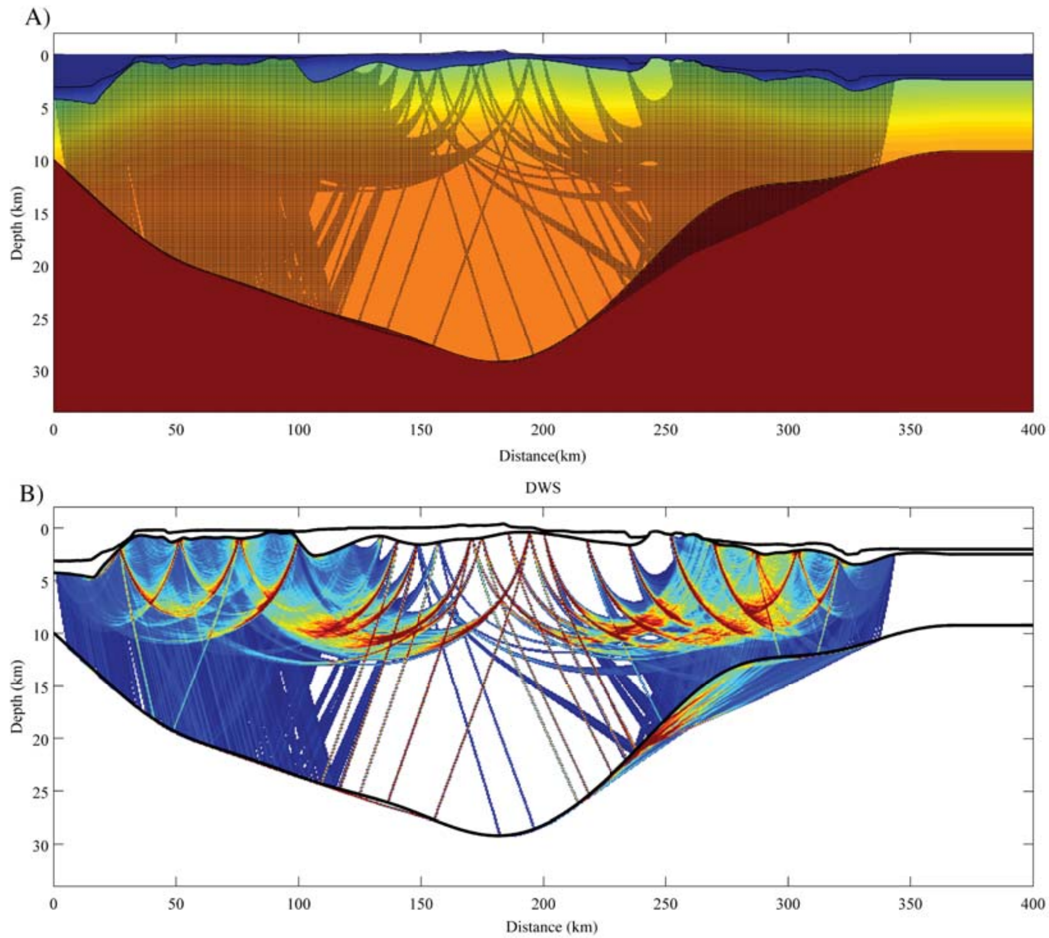

Figure 6-11: Derivative weight sum (DWS) plot of the final model (Toomey and Foulger, 1989). DWS demonstrates the ray coverage (A) and relative resolution between various regions of the velocity model (B). White regions are unconstrained by the raypaths.

Figure 6-12: Picked (dashed lines) and predicted (solide lines) travel time curves. The model produced good agreement between picks and predictions. The $\chi 2$ data misfit for the final model was 2.5.

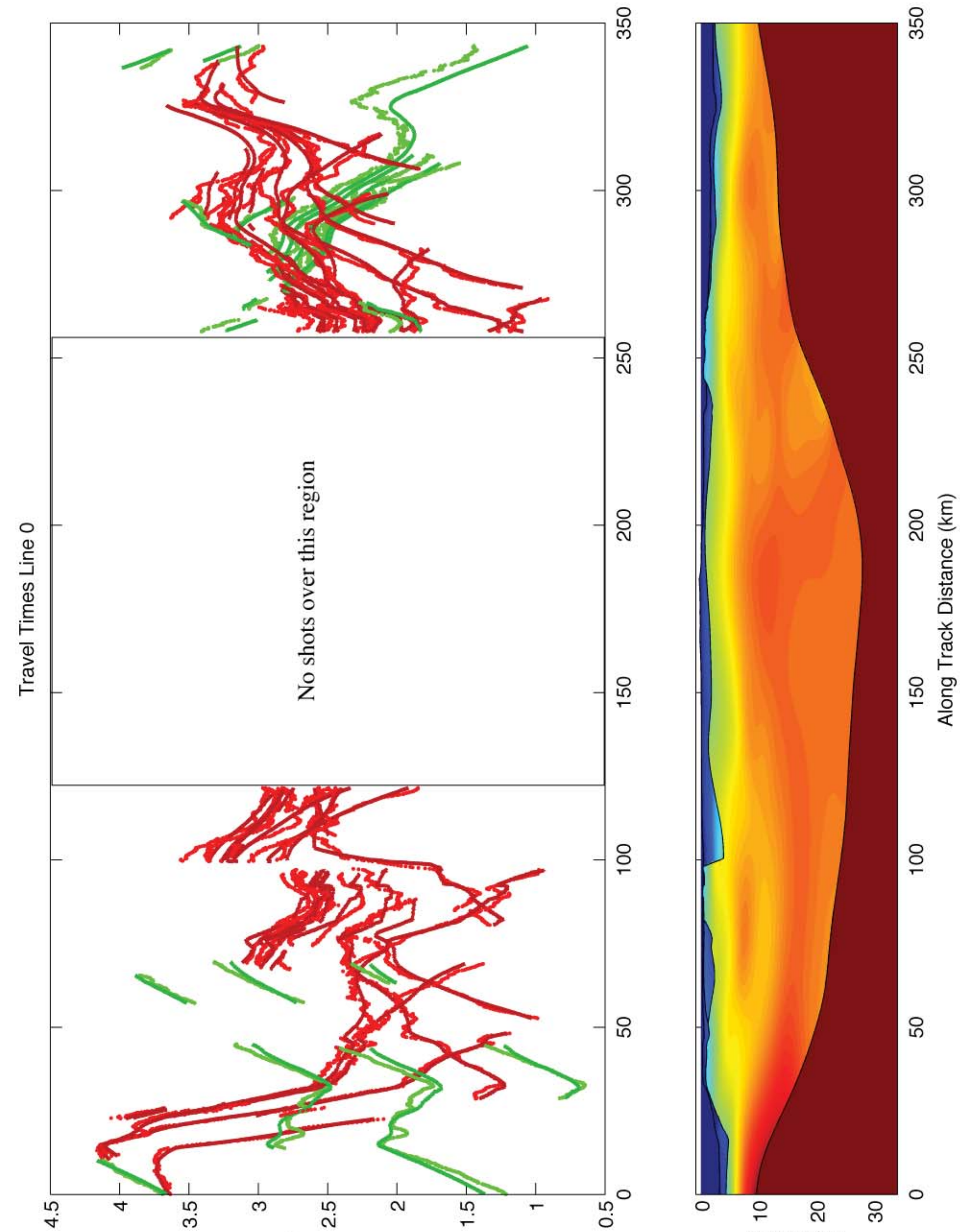
Travel Times Line 0
No shots over this region
t - x/6.5 (s)
Depth (km)
Along Track Distance (km)

Figure 6-13: Travel time residuals between picked arrivals and predicted arrivals.

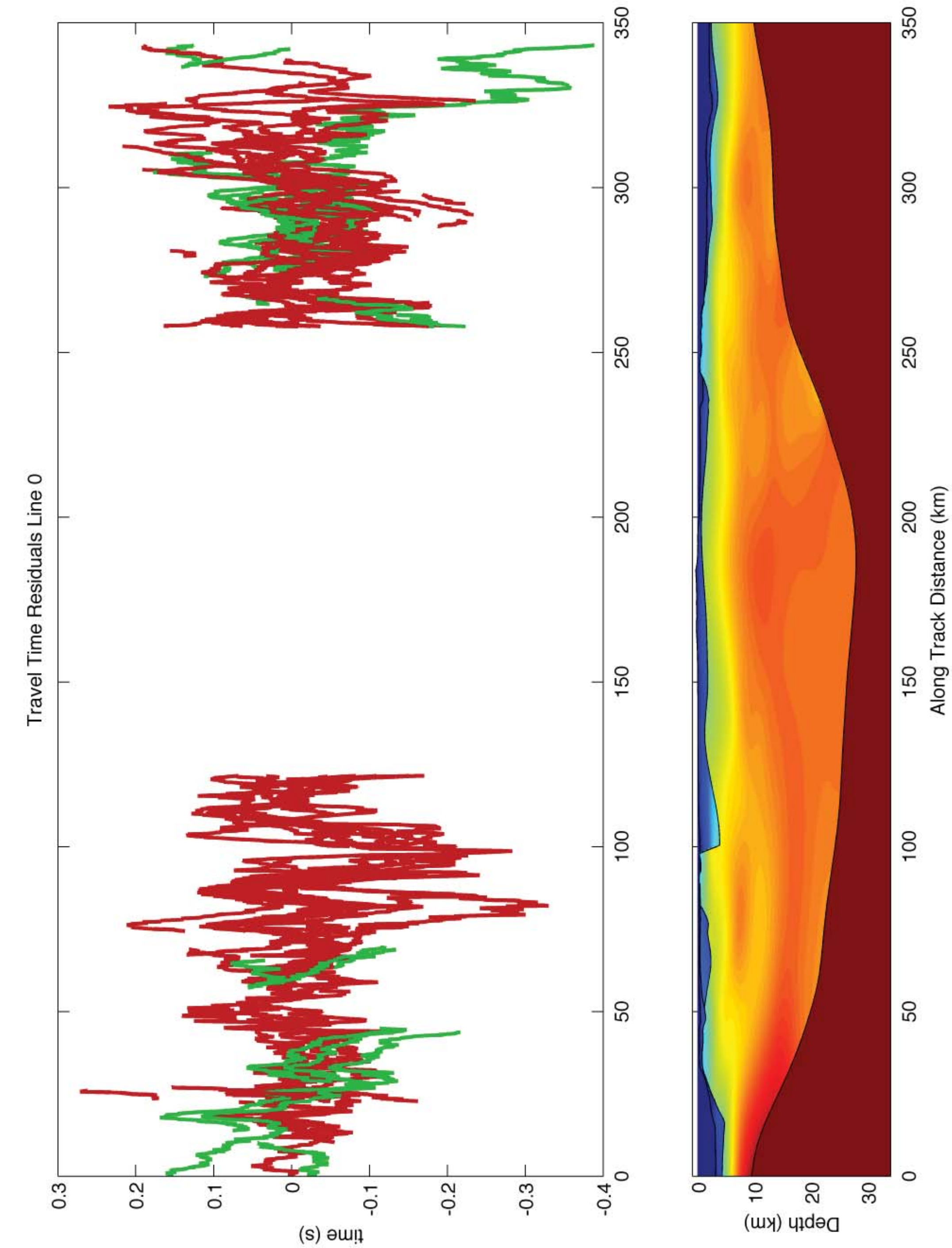

Travel Time Residuals Line 0
time (s)
0.3
0.2
0.1
0
-0.1
-0.2
-0.3
-0.4
0
50
100
150
200
250
300
350
Depth (km)
0
10
20
30
Along Track Distance (km)

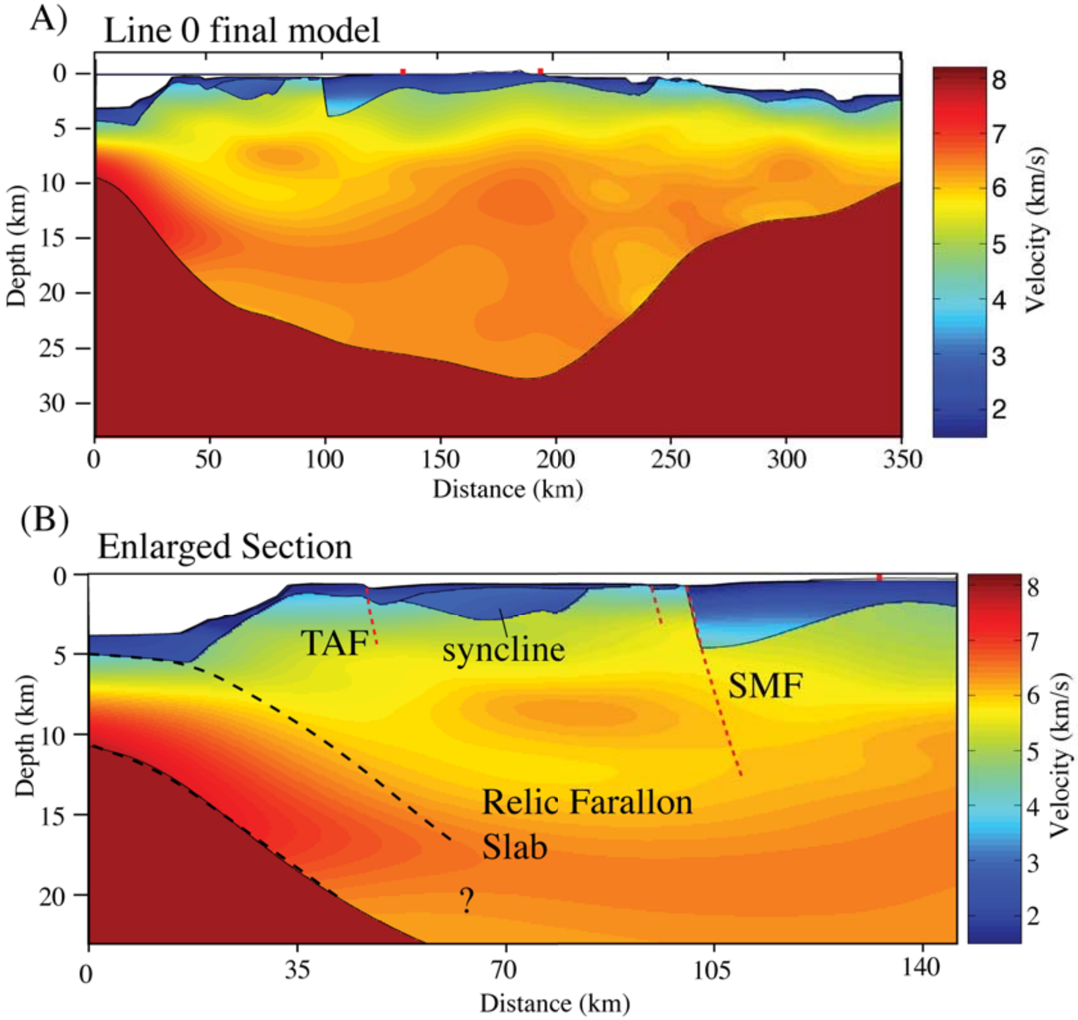

Figure 6-14: Final velocity model and enlarges section of the western margin of the Baja peninsula. A high velocity zone extends beneath the western half of the Magdalena shelf and is interpreted to be Farallon oceanic crust. The edge of the high velocity zone is nearly coincident with a change in moho dip at ~50 km from the western edge of the model. Moho depth at the western shoreline is ~26 km, slightly shallower than the crustal thickness determined using receiver functions (Persaud et al., 2007). The relatively high velocity material towards the central crust may represent the core of the Peninsular Ranges Batholith (Langenheim and Jachens, 2003), but further tests are required to determine if this feature is robust.

Figure 6-15: Schematic cross-section of the Baja microplate. (A) Preferred model. TAF, Tosco Abreojos Fault; SMF, Santa Margarita Fault; PTF, Pescador Transform Fault. We cannot unequivocally show where the slab pinches off, but based on the high-velocity zone and the change in moho dip, it appears likely that the older, denser Farallon slab broke from the younger, weaker and more buoyant slab very near the interface with the overriding continental crust. Furthermore, panel (A) is consistent with depth to amphibole breakdown and melt generation (Plank and Langmuir, 1988) below the axis of the Comondú volcanic arc (black arrows). Furthermore, the slope break in the moho interface is directly below the TAF and the inferred easternmost tip of the slab is below the hanging wall block of the SMF basin. Hot, buoyant slab, combined with reverse motion of the Farallon lithosphere as it became coupled with the Pacific plate may have let to uplift and extension along the Magdalena Shelf. Post subduction adakites are observed on the hanging wall of the SMF ~50 km north of Line 0 (Bonini and Baldwin, 1998), which may suggest there is a relationship between the breakoff point of the slab and the generation post subduction slab melts.

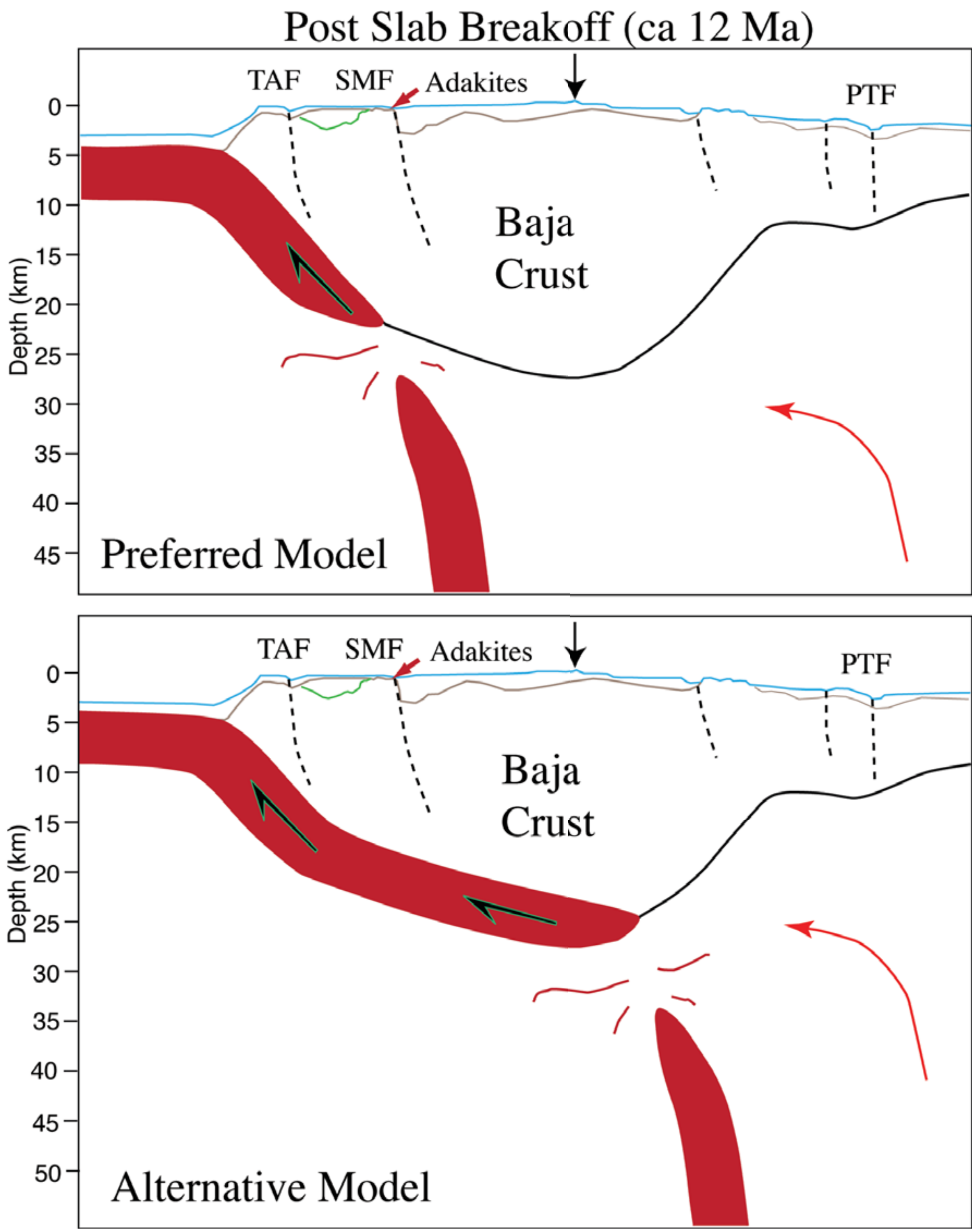

Post Slab Breakoff (ca 12 Ma)
TAF
SMF
Adakites
PTF
Baja Crust
Depth (km)
0
5
10
15
20
25
30
35
40
45
Preferred Model
TAF
SMF
Adakites
PTF
Baja Crust
Depth (km)
0
5
10
15
20
25
30
35
40
45
50
Alternative Model

7

Conclusions

The research presented in the preceding chapters has improved our understanding of the tectonic, stratigraphic and hydroclimatic processes that have shaped three regions along the North America-Pacific plate boundary. Central to this research was the acquisition of new data. In order to advance our general understanding of earth processes, we need to collect innovative, multidisciplinary data sets that provide the information needed to address fundamental scientific questions. Each of the five preceding chapters presented new geophysical and geological data. The following paragraphs summarize the major accomplishments of this research.

The tectonic and glacial histories of the LTB make it an ideal place to study tectonic geomorphology and hydroclimatic change. Based on seismic CHIRP surveys and sediment coring in Fallen Leaf Lake and Lake Tahoe, we determined that the West Tahoe-Dollar Point Fault (WTDPF) has the potential to generate M ≥7.0 ruptures. The most recent event occurred between 4.1 – 4.5 kyr ago and the vertical slip rate is estimated at 0.4–0.8 mm/yr, which suggests that the WTDPF is one of the most active normal faults in the northern Walker Lane Belt. The new constraints on timing and slip across the WTDPF are important for hazard assessment in the LTB, as well as Carson City and Reno, Nevada.

While studying the WTDPF in Fallen Leaf Lake, an ancillary paleoclimate study began through collaboration with other scientists working in the area. We conducted sidescan sonar surveys in Fallen Leaf Lake to image submerged paleoshorelines and medieval trees on the lakefloor. Prolonged Lake level fluctuations are related to changes in precipitation and ground water seepage through the end moraine that bounds Fallen Leaf Lake. We estimate that Fallen Leaf Lake's shoreline begins to drop when precipitation dips below 60% of normal, suggesting that such conditions persisted in the LTB for 250 years, allowing trees to grow below the modern shoreline. These observations give important constraints on short- and long-term variations of water availability in the high Sierra. By combining hydrogeology with radiocarbon dating of ancient trees, we provide an independent estimate of precipitation during medieval megadrought that can be compared to tree-ring proxies at other locations. As the primary source of water to several metropolitan areas, a multi-centennial drought today would devastate the economies of California and Nevada. Future sampling in FLL and potential discoveries in other Sierran lakes may provide the data needed to extend high-resolution paleoclimate records over the entire Holocene. In so doing, it may become possible to determine the recurrence of multi-centennial drought and begin to truly understand how such events develop and persist.

Our research in the Salton Sea led to numerous discoveries of faults, gas vents, sedimentary structures and paleoseismic history along the southernmost San Andreas Fault. Our regional-scale observations provide important constraints on the growth of an active pull-apart basin and the evolution of the southern SAF system. New seismic CHIRP data gave us the information needed to propose a new tectonic model for the region that includes the following characteristics. (1) Differential subsidence in the southern Salton Sea has produced an asymmetric basin with strata thickening southward into a basin-bounding fault system. (2) transtension beneath the Salton Sea is partitioned into distinct extensional and strike-slip domains. Extensional faults are at a high angle to the SAF, rupture during larger, less frequent earthquakes and should be considered seismically hazardous. The Brawley Seismic Zone accommodates dextral shear transferred into the basin through internal deformation (for example, secondary faulting and/or rotation). (3) Lastly, the basin architecture suggests the Salton Sea basin is similar to young pull-apart basins studied in physical models. Our proposed model is the first to account for the rapid subsidence, elevated heat flow and profuse seismicity in the Salton Sea.

In addition, our work in the Salton Sea has developed the first high-resolution record of Lake Cahuilla sedimentation and paleoseismic history in a region inaccessible to traditional land-based methods. Based on the total number of events identified in the sea, we have developed some of the largest event records for individual faults anywhere in North America. Future studies aimed at improving the age dating in sea are necessary to constrain the displacement history prior to ~830 AD and deeper penetrating seismic reflection data will provide important constraints on the longer-term evolution of these faults and how they interact. The most significant results of this study are the following. (1) Correlation between high-amplitude reflections in CHIRP profiles and coarse-grained sediment layers in CPT soundings allow us to identify parasequence sets in Lake Cahuilla sediment beneath the Salton Sea. Correlative parasequences have been radiocarbon dated at onshore sites and provide a chronostratigraphic framework for the acoustic stratigraphy back to ~830 AD, and at least 14 Lake Cahuilla parasequences are observed in the Salton Sea. (2) Assuming strain is released seismically, the Salton Sea experiences moderate to large earthquakes every 100 - 200 years and the dominant mode of deformation is extension. Vertical slip rates along individual faults are over 3.4 mm/yr. (3) Displacement on three of the normal faults appears coincident with flooding in the basin from the Colorado River and two events on the San Andreas Fault may be synchronous with rupture on faults beneath the sea. Static stress changes following displacement, either seismic or aseismic, on offshore faults may alter stress conditions along the southernmost SAF and promote a destructive northward propagating rupture. The role that faults in the sea play as stress modulators needs to be addressed by future research.

The final project, a study of microplate capture and transfer of the Baja California peninsula from the North American plate to the Pacific plate, provided the first successful wide-angle seismic refraction data across the Baja California microplate. Seismic reflection and refraction data demonstrate the feasibility of using active source seismic imaging to constrain the crustal structure across a continental plate fragment.

Stratigraphy in transtensional basins along the Magdalena Shelf record the onset of deformation along the Tosco-Abreojos and Santa Margarita faults. Although age control of stratigraphy imaged in MCS data is uncertain, relationships between stratal geometry and acoustic character suggest an upper bound of 12 Ma for the age of pre-rift sediments and an age of ~8 Ma for the onset of extension, which is coincident with the cessation of seafloor spreading along the Magdalena Rise. Tomographic imaging reveals a very heterogeneous upper crust that includes a high velocity basement block on the footwall of the Santa Margarita Fault. This block appears to be the same structure that is observed on Isla Santa Margarita that contains outcrops of ~6 Ma post subduction adakite volcanics. Tomographic imaging also provides evidence that remnant oceanic crust of the Magdalena microplate extends ~40 km east of the paleotrench. Traction forces at the base of the Baja microplate may provide a mechanism for focused weakening, extension and eventually rifting in the Gulf of California. Future studies with increased spatial coverage in wide-angle refraction data, dense grids of MCS data on the Magdalena Shelf and drilling of pre- and syn-rift sediments on the shelf will yield improvements in our fundamental understanding of the evolution of this plate boundary. Dating the sediments imaged on the shelf will provide age constraints on deformation along the TAF and SMF. Dense MCS grids across the shelf have the potential to constrain the cumulative strike-slip and extension accommodated by these faults.